

© 2023 Dipobrato Sarbapalli

ELECTROCHEMICAL ANALYSIS OF INTERFACE STRUCTURES AND  
FUNCTIONALIZATION IN GRAPHITIC CARBONS FOR NA-ION AND FLOW  
BATTERY ELECTRODES

BY

DIPOBRATO SARBAPALLI

DISSERTATION

Submitted in partial fulfillment of the requirements  
for the degree of Doctor of Philosophy in Materials Science and Engineering  
in the Graduate College of the  
University of Illinois Urbana-Champaign, 2023

Urbana, Illinois

Doctoral Committee:

Associate Professor Daniel Shoemaker, Chair  
Associate Professor Joaquín Rodríguez-López, Director of Research  
Professor Paul Braun  
Assistant Professor Yingjie Zhang

# Abstract

The current state of energy storage in the world currently relies heavily on the use of relatively mature technologies such as Li-ion batteries. However, with scarcities of raw Li reserves and supply chain constraints, future electrochemical energy storage scenario involves having a diverse set of batteries, each dedicated to its niche application, thereby creating a holistic electrochemical energy storage ecosystem. These new technologies need to be developed with earth-abundant materials such as carbon. The objective of my Ph.D. dissertation is to focus on understanding how carbon interfaces influence electron and ion transfer within two upcoming energy storage technologies: Na-ion (NiBs) and non-aqueous redox flow batteries (NRFBs). Electrochemical analysis of these new systems necessitates robust experimental setups, with the reference electrode often a shortcoming in non-aqueous measurements. Chapter 2 of this thesis describes the use of a polypyrrole solid-state reference which can be utilized across non-aqueous systems, and in harsh oxidizing/reducing environments. To incorporate graphite anodes in Na-ion batteries, Chapter 3 describes a fluorine-surface modifier approach, which stabilizes sodium intercalated graphite structures. Likewise, Chapter 4 compares how interphases evolve in terms of graphite electrode passivation in Li, Na, and K electrolytes, which is critical in understanding performance limitations of Na-ion and K-ion batteries, compared to Li-ion. Chapter 5 focuses on NRFBs; specifically on understanding how interfacial processes affect electron transfer using *in situ* scanning electrochemical microscopy and atomic force microscopy. Chapter 6 describes a rapid, SECM-based “spot-analysis” approach to obtain a quantitative understanding of electron-transfer kinetics as a function of electrode potential. Finally, Chapter 7 explores the interplay between graphite electrode structure and heterogeneous electron transfer kinetics.

In summary, this dissertation is written to improve the understanding of how carbon surface structure and functionalization affect the electron and ion transfer at the electrode-electrolyte interface of nascent battery technologies such as NiBs and NRFBs.

# Acknowledgments

As I wrap up my dissertation and prepare for a journey outside of academia, I wish to thank everyone who has been a part of my life in graduate school. First and foremost, my adviser, Prof. Joaquin Rodriguez-Lopez, for accepting me in his research group and for enabling me to develop professionally with zero bounds. The experiences I have gained with him will serve me well in the future, and I thank him for being a very supportive adviser, especially during the pandemic. His manner of handling my situations during such tumultuous times has been exceptional, and this has been critical in helping me get over the line with my dissertation research. Likewise, I thank my committee members for their valuable feedback over the course of the dissertation. I have known Prof. Daniel Shoemaker for over five years now; his calm, relaxed style of advising has helped me face tough situations, and he has always provided sound advice for my research. Prof. Paul Braun has been instrumental in helping me think about my research – his advice during my preliminary examinations about having clear boundaries about the nature of the work I am doing is something I will forever carry with me. Prof. Yingjie Zhang’s questions about the nature of graphene used in my research have given me a fresh focus when approaching my experiments.

I am proud to have had three amazing mentors in my doctoral research journey: Dr. Jingshu Hui, Dr. Michael J. Counihan, and Dr. Zachary T. Gossage. I have had the pleasure of observing them closely for multiple years. Their dedication, sharp focus, boundless energy, and technical expertise are something that I have tried to take away as I progressed through the years. While I may not have succeeded in emulating their best qualities, they will always inspire me. Their attitude of never giving up has always helped me tide over hard times. I consider myself to be extremely lucky that I have spent a significant

time working with them, it has helped me set a high standard for myself, and I will always try to become better because of them.

Likewise, I have found myself in a great peer group in Prof. Rodriguez-Lopez's lab, and I thank them all for their support during my time in the lab. Especially, I want to thank Dr. Kendrick O. Hatfield who is an absolute gem of an individual; I have no words to express my gratitude for his patience and diligence in holding up the entire lab almost singlehandedly at times. His tireless actions have always ensured that the entire lab works smoothly with no barriers, and his work has impacted everything I have gained. His selfless nature is something very rare in today's world, and I would like to thank him for everything he has done. I also thank Sanja Pudar for illustrating resilience and reminding me of the privilege I carry. Never have I observed a person who has carried on with doctoral research with a lot of struggles, and whenever I have faced tough times, her spirit and enthusiasm have always reminded me to carry on and overcome my troubles. Equally amazing are the younger group members, and I would like to thank Abhiroop Mishra for being a fantastic source of professional and personal support. His potential is limitless, and his cheery spirit has always helped me get out of bed and push myself forward. I thank him for allowing me to collaborate in his research, I have learned a lot from him, and my experience with him has been nothing short of inspiring. I especially thank Raghuram Gaddam for being a wonderful collaborator in my research. Similarly, I have been fortunate to work alongside Dr. Sazzad Hossein, Michael Pence, Curtis Althaus, Michelle Zorigt and Dong Ok Kim. Their energy, talent, and passion are amazing; they have served as great sources of support, entertainment, and inspiration at various points in my grad school journey. I am also indebted to Dr. Nusrat Jahan and Dr. Sazzad Hossein for hosting fantastic, mouthwatering dinners with traditional bengali cuisine, which have kept my home hunger cravings at bay while being unable to travel during the pandemic. I will always cherish these moments, and her thoughtful gifts of homemade goodies.

Equally important in my research journey has been my internship experience, with Alexander Kosyakov at Natrion Inc. It has been a life-changing experience working under him, the man has redefined all boundaries that I thought were humanely possible with regard to getting tasks done and moving forward. I look at my professional objectives in a completely different way than what I used to. More importantly, I have managed to narrow down my goals and interests, which is something that takes work and time. I cannot thank him enough for letting me flourish and find myself outside of graduate school. The level of commitment, passion, and the sacrifice he exhibits daily is something I can never emulate, but his actions will always serve as an inspiration to keep improving, to keep pushing forward, and to give my absolute best in every single thing I do professionally. I wish him nothing but the very best as he takes his company forward and I will celebrate every single success they have. I wish to thank everyone at Natrion, especially Valeria Cruz for making the internship a fun and easy experience for me with her humor and robust skills in cell building. I also thank Gavin Depew, Connor Kniaz, Soheil Malekpour and Prof. Dah-Shyang Tsai for providing a lot of entertainment and elucidating many concepts during my time there.

I have been fortunate to have great collaborators over the course of my Ph.D. studies. I thank Prof. Jose Luis Mendoza-Cortes and his team: Yu-Hsiu Lin, Dr. Sean Stafford, and Dr. A. Nijamudheen; they have worked with me seamlessly on multiple projects, and it has always been an enjoyable experience. I thank Dr. Jason Howard, working with him has been equally easy and enlightening. I thank Dr. Rajeev Assary, Dr. Larry Curtiss, Dr. Lu Zhang, Dr. Yichao Yan, and Dr. Melanie Sanford for providing support with computational resources and synthesizing molecules which helped me further my research. Special mention goes to Dave Williams at the SCS machine shop for working with me on numerous cell designs. Interactions with Dave have always been fun, and his presence will be missed. Equally important in my research is Dr. Richard T. Haasch for assisting me with my XPS measurements and critiquing my XPS analysis and inferences. I

have learnt a lot from him and the wealth of knowledge he possesses.

My friends and family have always kept my spirit up over the past years in Urbana-Champaign. I would like to thank Bhavesh for being a constant, solid, calm, and reassuring presence throughout my entire time here in the US. My childhood friends Shiladitya and Sabyasachi have been omnipresent support systems, and have made my final defense a memorable experience. I have also been well-supported by Kamalendu, Gaurav, Shubham, and Shradha; the times spent with them have been nothing short of memorable. My friends from my MS and undergraduate years: Abishek, Ivana, Aditya, Parikshit, and Bharadwaj have always been there for me whenever needed, and I thank them for their presence and support. My cousin brother, Sudeep has also been another strong source of support for all my endeavors. One of his most important contributions has been in transforming me into a fan of Liverpool F.C., more on that later. I also thank Elicia Hunt for being a solid source of support during difficult times. My family, especially my brother, has made numerous sacrifices looking after my parents and ensuring things at home are stable owing to which I have never had any issues with focusing on my research. These are actions which I can never thank him enough for. Similarly, my parents have always given their full support and understanding, owing to which I have never felt stressed from the outside. Their love and support are one of the reasons for me being where I am today. I also thank my family in Chicago for their care and support throughout my time here in the US; they have always ensured that I am never alone here.

Lastly I would like to thank all my past teachers and mentors: Mr. Subhasish Chatterjee, Mr. Anirban Biswas, Dr. Bishwajit Bhattacharjee, Dr. Kaustav Sarkar, Dr. Xu Chen, Dr. John Popovics, Dr. Paramita Mondal, and Dr. Leslie Struble, for imparting invaluable lessons and for their patience in molding me into a researcher. I would like to thank Dr. Sravanthi Puligilla, she was my first mentor when I came to graduate school, and I owe a lot of my training, mindset, and philosophy to her mentorship. I thank the staff

at Materials Research Lab, Beckman and Holonyak Micro and Nano-technology institute for their assistance in my research. I thank Ashley Phillips Smith for providing support for meeting departmental requirements. Lastly, I would like to thank Gayle Adkisson, who has gone out of her way to look after my academic progress and requirements and has been a savior in many a tough time with room reservations and getting other miscellaneous things addressed. Despite being a complete stranger and agnostic to my existence, I wish to thank Jürgen Klopp, Manager, Liverpool F.C., for providing countless instances of sheer motivation and willpower through his actions and interviews; they have kept me going on and on. The man is a miracle and the most normal human being in the limelight. I am deeply apologetic if I have missed out on names; I sincerely appreciate all the kindness and assistance I have received over the last five years. I thank NSF DMR and JCESR for funding my doctoral research.

# Table of contents

<b>Chapter 1</b>	<b>Introduction</b>	<b>1</b>
1.1	Interfaces in EESS	2
1.2	Electrochemical analysis of interfaces	3
1.3	Electrode interface structure and functionalization	12
1.4	Organization of the thesis	15
<b>Chapter 2</b>	<b>Pt/Polypyrrole Quasi-References: Robustness and Application in Electrochemical Energy Storage Research</b>	<b>24</b>
2.1	Experimental methods	26
2.2	Results	28
2.3	Conclusions	34
<b>Chapter 3</b>	<b>A Surface Modification Strategy Towards Reversible Na-ion Intercalation on Graphitic Carbon Using Fluorinated Few-Layer Graphene</b>	<b>37</b>
3.1	Methods and Materials	40
3.2	Results and discussion	47
3.3	Conclusions	58
<b>Chapter 4</b>	<b>Tracking Passivation and Cation Flux at Incipient Solid-Electrolyte Interphases on Multi-Layer Graphene using High Resolution Scanning Electrochemical Microscopy</b>	<b>64</b>
4.1	Results and discussion	66
4.2	Conclusions	79
4.3	Experimental section	80
<b>Chapter 5</b>	<b>A combined SECM and electrochemical AFM approach to probe interfacial processes affecting molecular reactivity at redox flow battery electrodes</b>	<b>89</b>
5.1	Materials and methods	92
5.2	Results and discussion	96
5.3	Conclusions	109
<b>Chapter 6</b>	<b>An SECM-based spot analysis for redoxmer-electrode kinetics: identifying redox asymmetries on model graphitic carbon interfaces</b>	<b>115</b>

6.1	Experimental methods . . . . .	118
6.2	Results and discussion . . . . .	121
6.3	Conclusions . . . . .	141
<b>Chapter 7</b>	<b>Reactivity of redoxmers on sp<sup>3</sup> carbon electrodes: Hydrogenated graphene and boron-doped diamond . . . . .</b>	<b>147</b>
7.1	Methods and materials . . . . .	149
7.2	Results and discussion . . . . .	152
7.3	Conclusions . . . . .	161
<b>Appendix A</b>	<b>Supplementary Information for Chapter 3 . . . . .</b>	<b>165</b>
A.1	Synthesis and characterization of tetrakis(decyl)ammonium hexfluorophosphate [N(C <sub>10</sub> H <sub>21</sub> ) <sub>4</sub> ](PF <sub>6</sub> ) . . . . .	165
A.2	Pt padding on Si wafer . . . . .	165
<b>Appendix B</b>	<b>Supplementary Information for Chapter 4 . . . . .</b>	<b>181</b>
<b>Appendix C</b>	<b>Supplementary Information for Chapter 5 . . . . .</b>	<b>197</b>
C.1	Materials and methods . . . . .	197
C.2	Macrodisk electrochemistry . . . . .	204
C.3	SECM: Comparing C1 and C7 on MLG with LiBF <sub>4</sub> . . . . .	209
C.4	Filming on MLG . . . . .	211
C.5	AFM: Comparing C1 and C7 on HOPG . . . . .	214
C.6	SECM: SLG vs. HOPG edge planes . . . . .	216
C.7	SECM: Comparing C1 and C7 on MLG with LiTFSI . . . . .	220
C.8	AFM: Comparing C1 and C7 on MLG with LiTFSI . . . . .	222
C.9	SECM k <sub>f</sub> quantification . . . . .	223
C.10	Summary of SECM experiments . . . . .	224
<b>Appendix D</b>	<b>Supplementary Information for Chapter 6 . . . . .</b>	<b>226</b>

# Chapter 1

## Introduction

*Some of the content in this chapter has been adopted from the following published works:*

- Jingshu. Hui, Zachary. T. Gossage, **Dipobrato Sarbapalli**, Kenneth Hernández-Burgos, and Joaquín. Rodríguez-López. “Advanced electrochemical analysis for energy storage interfaces” *Anal. Chem.* **2019**, *91*, 60–83. DOI: [10.1021/acs.analchem.8b05115](https://doi.org/10.1021/acs.analchem.8b05115)
- Michael J. Counihan, **Dipobrato Sarbapalli**, and Joaquín Rodríguez-López. “Picture Your Electrode: A Primer on Scanning Electrochemical Microscopy” *Electrochem. Soc. Interface.* **2020**, *29*, 30–32. DOI: [10.1149/2.f03203if](https://doi.org/10.1149/2.f03203if)
- Abhiroop Mishra, Zachary T. Gossage, **Dipobrato Sarbapalli**, Yuanya Zhao, and Joaquín Rodríguez-López. *Methods and Instrumentation in Energy Storage* in *Encyclopedia of Electrochemistry*, Wiley-VCH, **2021**. DOI: [10.1002/9783527610426.bard030111](https://doi.org/10.1002/9783527610426.bard030111)
- **Dipobrato Sarbapalli**, Abhiroop Mishra, Zachary T. Gossage, Kendrick Hatfield, and Joaquín Rodríguez-López. *Scanning Electrochemical Microscopy: A Versatile Tool for Inspecting the Reactivity of Battery Electrodes* in *Batteries: Materials Principles and Characterization Methods*, IOP Science, **2021**. DOI: [10.1088/978-0-7503-2682-7ch9](https://doi.org/10.1088/978-0-7503-2682-7ch9)

The 2019 Nobel Prize in Chemistry for the development of Li-ion batteries (LiBs) highlights the impact of battery technology on modern lifestyle. However, it is critical to keep in mind that no single battery chemistry can fulfill all requirements of electrochemical energy storage systems (EESS). In the bigger picture, grand challenges exist in developing EESS for areas such as grid-level energy storage.<sup>[1]</sup> With current lithium reserves being insufficient<sup>[2, 3]</sup> for such a mammoth demand, more low-cost and versatile battery technologies are needed, prepared with earth-abundant materials.

Carbon is an example of an abundant and low-cost resource, available in various forms such as synthetic graphite, artificial graphite, carbon black, activated carbons, and pyrolyzed carbon, among others.<sup>[4]</sup> In LiBs, graphitic carbon materials are used as the anode material where it stores energy by reversible intercalation reactions with  $\text{Li}^+$  at low

potentials. Similarly, carbon materials are also used in other battery technologies. For example, non-graphitizable carbons (otherwise referred to as hard carbons) are utilized as anode materials for Na-ion batteries. Na-ion batteries (NiBs) are similar to LiBs, with the greater availability and low cost of Na raw materials being its greatest advantage over LiBs.<sup>[5]</sup> Likewise, graphitic carbons are an inexpensive candidate for use as current collector electrodes in non-aqueous redox flow batteries (nRFBs), an upcoming candidate for grid-level energy storage.<sup>[6–8]</sup> In nRFBs, energy storage takes place by (dis)charge of redox-active organic molecules, oligomers, and polymers, henceforth referred to as redoxmers, in solution. A key advantage of the redox-flow battery configuration is that it allows the power and energy capacity of the battery to be decoupled, making it inherently scalable for large-scale energy storage applications such as the grid.<sup>[1]</sup> While there are numerous other electrochemical energy storage technologies/chemistries (potassium ion, zinc ion, super-capacitors, etc.), my thesis focuses broadly on nRBFs and NiBs, which are emerging technologies *beyond Li-ion*.

## 1.1 Interfaces in EESS

One of Wolfgang Pauli's, 1945 Nobel Prize in Physics, most popular quotes reads “God made the bulk; the surface was invented by the devil.”<sup>[9]</sup> When it comes to energy storage, interfaces - structures created between dissimilar media, such as liquids and solids, and interphases - structures arising in between these dissimilar media - inherit this notorious reputation. Indeed, the high-energy density chemical systems comprising the most attractive energy storage technologies are host to a plethora of dynamic processes<sup>[10]</sup> - including electron transfer, ion transfer and migration, nucleation and dissolution, side reactions, and (de)solvation processes to name a few, that significantly alter their landscape. This presents a fascinating challenge to the analysis of the interfacial region, increasing its complexity from a problem of surface-sensitivity, to now include aspects of time and transient behavior, measurement across scales, through materials, and with the inherent need of coupling with electrochemical techniques. Despite the great diversity of energy technologies, spanning

phenomena of ion intercalation, adsorption, and plating for batteries and supercapacitors, the interface between the electrode and electrolyte is a common structure that plays an indispensable role in efficient electronic and ionic mobility.[11, 12] Therefore, fundamental studies with model systems and real devices are both desirable and complementary. For an operating energy storage system, it is important to keep a balance between dimension, morphology, porosity, tortuosity, and chemically specific electronic interactions at the dominating interfaces.[13] Ion diffusion/intercalation and reactivity mechanisms in solid-state materials are often multi-step and rely on the structure, overpotential, and any modification at the material surface.[12] Likewise, while there are numerous material developments for anodes, cathodes, and separators for batteries, integrating them into practical devices, and characterizing them within, is often a challenge. A primary reason is that battery components are sealed in inert atmospheres, in the absence of water and oxygen, preventing conventional approaches for their characterization. In addition, battery operation requires the prior formation of interphases, *in situ*. For example, the 'formation' step in LiB production chains involves parasitic reactions with electrolytes to form interphases on the anode, which largely influences battery performance and safety.[14] Often, while individual components of a battery maybe optimized, it is these very interfaces and interphases that limit overall device performance. ***Therefore, I have chosen my doctoral research to focus on a two-pronged approach for i) developing analytical techniques and ii) tailoring interfaces on carbon materials, to advance the understanding of electrode-electrolyte interfaces in beyond Li-ion batteries.***

## 1.2 Electrochemical analysis of interfaces

Electrochemical techniques involving classical amperometric and potentiometric electrochemical analysis provide indirect information on the electrode materials' response towards external changes of solvent, electrolyte, and surface modification. Electrochemical techniques, including cyclic voltammetry (CV),[15] galvanostatic charge-discharge,

electrochemical impedance spectroscopy (EIS),<sup>[16]</sup> potentiostatic intermittent titration (PITT), and galvanostatic intermittent titration (GITT)<sup>[17]</sup> are widely used methods for energy-related applications. These techniques are typically used directly to the bulk energy storage materials to obtain information about their charge storage mechanisms, charge diffusion, capacity, cyclability, and stability.<sup>[18]</sup>

Macroscopic techniques like CV and EIS typically describes electrode performance in terms of single-valued, averaged measurements: a peak current, a charge transfer resistance, a capacitance, a charge capacity. However, these characterizations escape the complexity of most practical materials. Electrodes are not idealized current collectors but rather heterogeneous surfaces on which individual features strongly influence device performance by dictating local charge transfer. Thus, it would be desirable to understand reactivity at such a locality, whatever its length scale. In this regard, electrochemical scanning probe techniques (ESPTs) are uniquely positioned to address these needs. ESPTs are interface-sensitive by nature and enable high spatiotemporal resolution for investigating interfacial processes in realistic battery environments. One such ESPT to visualize electrode heterogeneity and quantify reactivity *in situ* is scanning electrochemical microscopy (SECM).<sup>[19–21]</sup> SECM is a versatile technique with various modes for exploring the electrochemistry underlying sustainable technologies: from interrogating electrodes for batteries, to those for fuel cells and electrolyzers, as reviewed in recent years.<sup>[20, 22]</sup> SECM measurements have been developed to study local electron transfer at varying electrode interfaces, and a brief description of its working principles is also provided below.

### 1.2.1 Cyclic voltammetry, CV

Cyclic voltammetry (CV) is a well-established potential controlled technique in the electroanalytical chemistry community for over half a century.<sup>[23, 24]</sup> This technique is heavily used while studying redox-active species under the conditions of semi-infinite diffusion.<sup>[23, 25]</sup> These conditions are relevant to technologies such as redox-flow batteries,

wherein energy is stored in the form of dissolved redox-active molecules in solution. However, for solid-state electrode reactions, such as those involving ion-intercalation, conditions of semi-infinite diffusion in solution no longer apply on the relevant timescales of electrode operation. Instead, there is finite diffusion of ions into solid electrodes via various mechanisms, including intercalation and alloying reactions, each leading to different behavior according to Gibb's phase rule.[26, 27]

While CVs can quickly identify redox potentials for such finite-diffusion reactions involved in energy storage, they also provide mechanistic insight, which becomes invaluable when characterizing new electrode materials. This is because the shape of voltammograms can often distinguish between electron transfer (Faradaic processes) and electrode charging (non-Faradaic processes), although recently there has been significant discussion on this topic.[28–30] A schematic of such responses is shown in **Figure 1.1a-c**. Such mechanistic details can be critical in discerning charge storage mechanisms in battery materials. For example, galvanostatic characterization can yield materials capacities that largely exceed the theoretical expectations of materials such as graphite.[31] In those cases, evaluation of the CV and comparison to the cases shown in **Figure 1.1**, could elucidate which charge storage mechanism is dominating. Likewise, CV has been used to study additional phenomena relevant to battery operation, such as parasitic reactions,[32–34] ion diffusion,[35, 36] and interphase formation.[37]

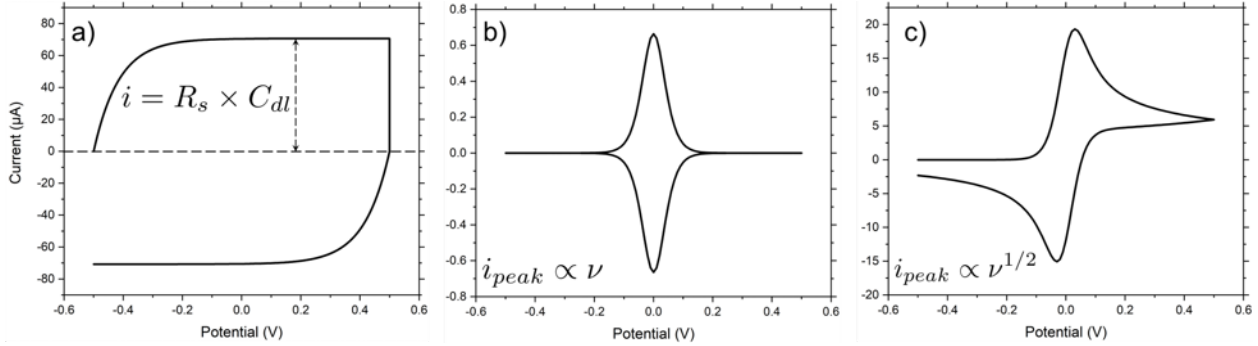


Figure 1.1: Simulations of voltammograms resulting purely from a) non-faradaic double layer charging, b) faradaic charging of surface bound redox-active species, and c) redox active species dissolved in solution on a 3 mm diameter electrode. Parameters used: Scan rate = 0.1 V/s, resistance of solution,  $R_{soln} = 1000 \Omega$ , double layer capacitance,  $C_{dl} = 0.1 \text{ F/cm}^2$ , standard heterogeneous electron transfer rate constant,  $k^0 = 1 \times 10^{-3} \text{ m/s}$ , Diffusion coefficient of species,  $D = 1 \times 10^{-9} \text{ m}^2/\text{s}$ , initial concentration of reduced species in solution,  $C_{red} = 1 \text{ mM}$ , Initial concentration of surface-bound reduced species  $\gamma_{red} = 1 \times 10^{-6} \text{ mol/m}^2$ .

CV also yields powerful thermodynamic and mechanistic details of faradaic charge transfer processes. For example, some of the earliest investigations in Li-ion battery electrodes utilized slow scan CVs in the order of  $\mu\text{V/s}$  as shown in [Figure 1.2](#).

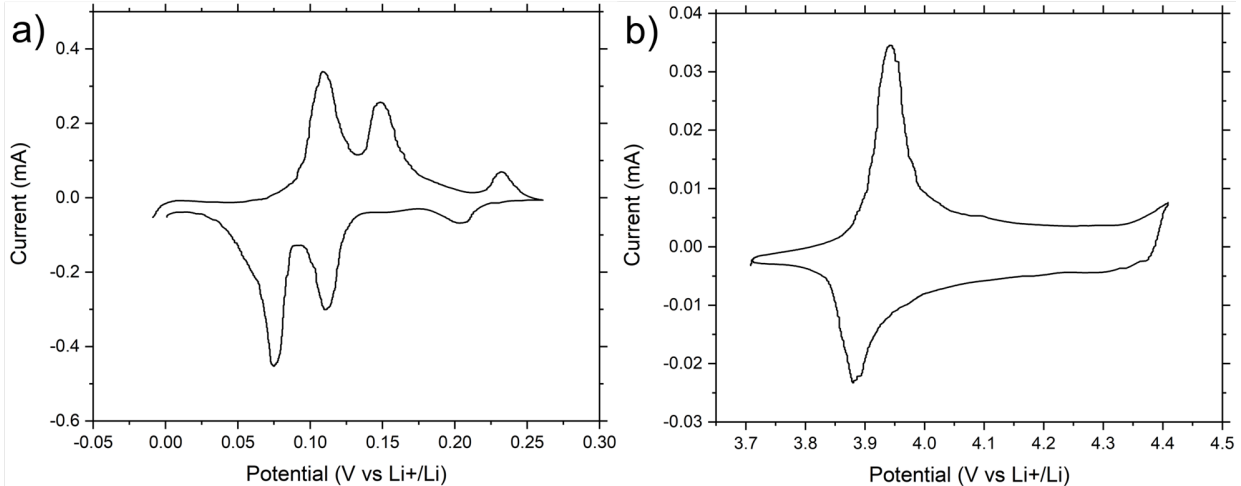


Figure 1.2: Cyclic voltammograms at slow scan rates for a) graphite anode and b)  $\text{LiCoO}_2$  cathode.[\[38, 39\]](#)

Considering the voltammogram in [Figure 1.2a](#), multiple peaks are observed in the graphite electrode, which indicates phase transitions. Indeed, when correlated with in

situ XRD measurements, it was revealed that the intercalation of  $\text{Li}^+$  follows a staging mechanism in which ions progressively fill interlayers.[4, 39] While the specific details of structure are only elucidated using XRD, notably the simplicity of the CV method in suggesting these complex mechanisms makes it a powerful analytical tool. Similarly, in the case of  $\text{Li}^+$  (de)intercalation in  $\text{LiCoO}_2$  cathodes (**Figure 1.2b**), a primary peak associated with the transition of  $\text{LiCoO}_2$  between two hexagonal phases is observed.[38] Therefore, peaks in voltammograms of such electrodes provide thermodynamic information in the form of electrode potentials at which these reversible phase transformations take place.

### 1.2.2 Principles of scanning electrochemical microscopy (SECM)

The SECM probe is often, but not necessarily, a flat disc ultramicroelectrode (UME) positioned close to a surface of interest. Henceforth, the SECM probe is referred to as the “tip” or “probe” and the analyte material as the “substrate.” Ultramicroelectrodes are typically electrodes with their largest dimension less than 25  $\mu\text{m}$ .[23] Key to the operation of UMEs is their ability to attain a mass-transfer limited steady-state current, as shown in **Figure 1.3**. Such a response results in a time-invariant current due to the formation of a radial diffusion layer of electrogenerated species, unlike electrodes of larger dimensions ( $>> 25\mu\text{m}$ ) which display a transient response.[23] Redox-active species in solution are described as the “redox mediator,” or, the “mediator.” A typical SECM experiment involves rastering the SECM tip across the substrate while measuring the tip and/or substrate currents due to electrochemical reactions. For further detail and description, readers can peruse through the SECM textbook,[20] and several reviews.[19, 21, 40] Experiments in this thesis utilized three modes of SECM, described as follows.

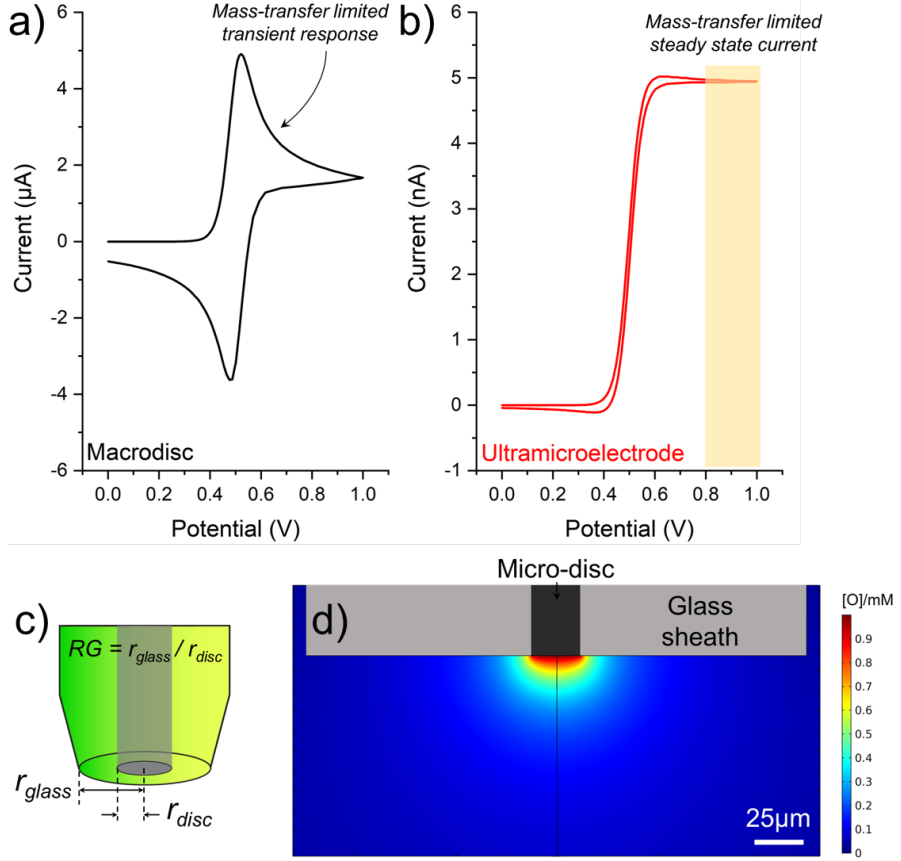


Figure 1.3: COMSOL finite element simulations of cyclic voltammograms (CVs) with a) 2.5 mm diameter macrodisc electrode and b) 25  $\mu$ m diameter UME for a single electron oxidation of  $R \longrightarrow O$  with standard potential ( $E^0$ ) of 0.5 V. Mass transfer limited steady state current is illustrated in the CV. c) RG, a geometric parameter relating UME disc radius to the radius of the insulating glass sheath. d) A COMSOL simulation of the radial diffusion layer generated under mass transfer-limited conditions. Color variation represents concentration of the generated O species when the initial concentration of R is 1 mM.

### Approach curves

Approach curves are used to position the SECM tip at a known distance from the substrate via the use of a redox mediator such as the O/R redox pair described in **Figure 1.3** (examples of mediators used with SECM highlighted in Ref. [40]). In this mode, the tip is biased to a potential such that oxidation/reduction of the mediator is limited only by mass transfer (i.e. diffusion) of the mediator to the electrode surface. As the tip is brought near the substrate (shown in **Figure 1.4a**), the tip current ( $i_T$ ) deviates from the value obtained in

bulk solution ( $i_{T,\infty}$ ). The tip current can increase or decrease depending on the nature of the substrate. An insulating substrate hinders diffusion of the mediator to the tip, causing the tip current to decrease from  $i_{T,\infty}$  (**Figure 1.4b**), a conducting substrate can donate/accept electrons to/from the mediator (**Figure 1.4c**), forming the original charge state and leading to a “feedback loop” which results in a current higher than  $i_{T,\infty}$ . This operation is termed “feedback mode”, with “negative feedback” occurring over ideal insulators and “positive feedback” occurring over ideal conductors.

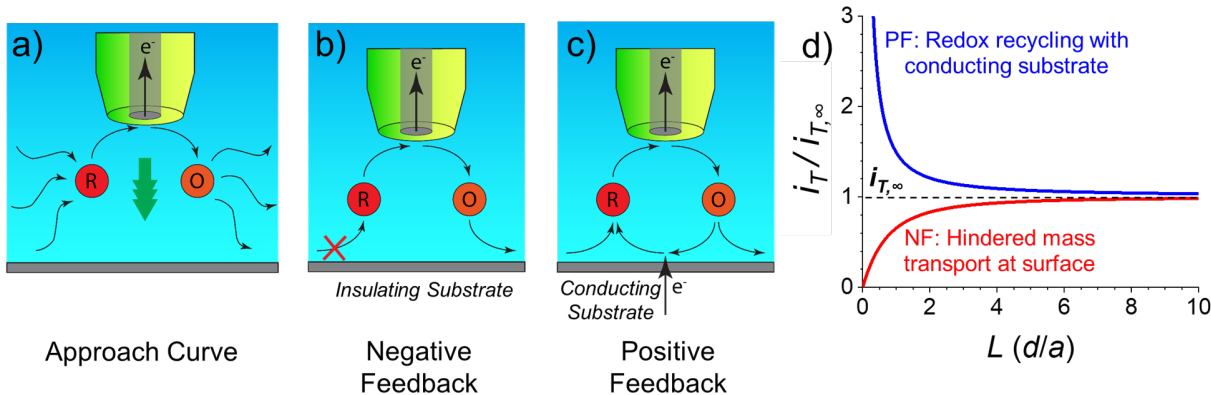


Figure 1.4: Operation of the feedback mode. a) Schematic of an approach curve experiment, b) Negative feedback (NF) due to hindered diffusion of species R, c) Positive feedback (PF) due to recycling of species O  $\longrightarrow$  R by the substrate, d) NF and PF approach curves showing deviation of tip currents  $i_T$  from  $i_{T,\infty}$  as the tip is brought near the substrate.

Approach curves are often plotted as normalized tip current ( $i_T / i_{T,\infty}$ ) vs. normalized tip-substrate distance,  $L (= d/a$ , where  $d$  is the distance from tip to substrate and  $a$  is the tip radius) as shown in **Figure 1.4d**. While an absolute  $d$  value is unknown at the beginning of an experiment, the data can be fitted to previously developed analytical expressions,[41] yielding final tip-substrate distance. The approach speed should be low enough to ensure there is no convection in solution so that diffusion is the only form of mass transfer present.[41] In a positive feedback approach curve, the tip current is a function of the substrate’s ability to transfer an electron to/from the mediator in solution and ultimately back to the UME. Therefore, fitting positive feedback approach curves can

yield the heterogeneous electron transfer rates, or  $k_f$ , between the mediator and substrate.

**Figure 1.5** shows how approach curves change with different  $k_f$  values. Standard rate constants,  $k^0$ , can also be determined by collecting and fitting multiple approach curves while applying different substrate potentials.[42–45]

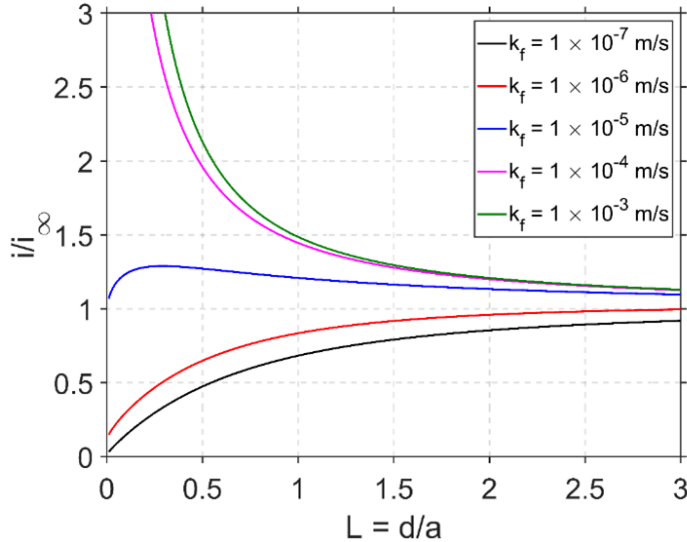


Figure 1.5: Analytical approach curves for different electrochemical kinetics  $k_f$  between substrate and mediator. Diffusion coefficient of mediator,  $D = 1 \times 10^{-10} \text{ m}^2/\text{s}$ , tip radius,  $a = 12.5 \mu\text{m}$ , RG = 3.

Good practice before any SECM experiment is to perform negative feedback approach curves over flat insulated substrates to determine an accurate RG of the tip. While **Figure 1.3** defines RG explicitly, practical RG values will deviate from the definition by some extent due to the microdisc being off-centered, glass sheath not perfectly shaped, among other reasons. Fitting these approach curves ( $i_T/i_{T,\infty}$  vs.  $L$ ) to the analytical expressions, which are a function of  $L$  and RG,[41] yields RG for that particular SECM tip. Prior knowledge of RG subsequently leads to an accurate measurement of  $k_f$  from positive feedback curves, since  $k_f$  is the only unknown parameter.

### Feedback imaging

Feedback imaging is performed by measuring the tip current resulting from

electrolysis of a redox mediator while the probe is rastered near a substrate. The tip-substrate distance must be on the order of the thickness of the diffusion layer generated at the tip to modify  $i_T$ . Feedback imaging provides a way to visualize electrochemically active and inactive regions (i.e. conductive vs. insulating) on the substrate.[46] If the substrate is flat and tip-substrate distance is known through approach curves, feedback imaging can be used to map kinetics of electron transfer. This can be achieved by converting  $i_T/i_{T,\infty}$  values in the feedback image into  $k_f$  by using analytical expressions.[41] In practice, this enables in-situ mapping of passivating processes, e.g. interphase formation.

#### *Redox competition and ion-sensitive SECM*

In this mode, the tip and substrate are held at potentials to perform the same redox reaction while measuring tip current.[47] Electrochemically active regions of the substrate will consume redox species, leaving the tip unable to perform redox reactions near that area, resulting in a decreased tip current. However, if the substrate region exhibits sluggish kinetics, the tip current will experience a lesser effect, thus giving rise to contrast in SECM images.

The concept of redox competition has been extended to ion-flux detection at battery interfaces. Here, a Hg SECM probe is used to quantify local ionic flux changes.[48, 49] The flux is monitored by amalgamation and stripping of alkali ions ( $\text{Li}^+$ ,  $\text{Na}^+$ ,  $\text{K}^+$ ) at the tip (**Figure 1.6**). The measured amalgamation and stripping currents are correlated to the concentration of ions near the probe. Fluxes can be detected by monitoring changes in the tip current; for example, if a substrate is actively consuming ions, the tip current would decrease. Therefore, competition for ions between tip and substrate can inform the user about the activation of ion-consuming or ion-releasing processes at the substrate.[50, 51]

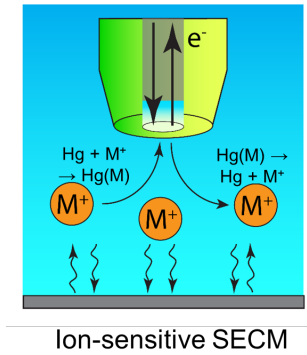


Figure 1.6: Schematic illustrating ion-sensitive SECM.

### 1.3 Electrode interface structure and functionalization

The fundamental processes at electrode-electrolyte interfaces for batteries are electron and ion transfer. For example, in nRFBs, electron-transfer at the electrode-electrolyte interfaces is essential for proper battery functioning,[52, 53] on the other hand, electron transfer is detrimental to LiB operation and is blocked by solid-electrolyte interphases (SEI) formed during initial cycling of the battery. [54] These SEI structures form due to the irreversible decomposition of Li-electrolyte, and prevent further loss of active electrolyte species, while enabling facile  $Li^+$  transfer across the interphase.[54] These two examples highlight completely different outcomes of electron-transfer processes occurring at the electrode-electrolyte, which is critical to battery operation. In this section, a brief description of carbon electrode structure and functionalization is provided, which may influence these interfacial processes in various ways.

Carbon electrodes are ubiquitous in the field of electrochemistry, and are used in multiple forms ranging from graphite, boron doped diamonds, fullerenes, vapor-deposited carbon among others.[55] Both the bulk and surface structure of carbon influences the properties and electrochemical performance of electrode materials, as has been comprehensively highlighted by McCreery in 2008.[55] In this thesis, one of the primary carbon materials studied was chemical vapor deposition (CVD) grown multi-layer graphene.

Graphene refers to a two-dimensional structure of carbon in a hexagonal lattice. Graphitic structures ultimately consist of stacks of graphene, leading to the formation of basal planes (i.e. plane perpendicular to the c axis containing the hexagonally ordered carbon atoms) and edge planes (parallel to the c axis). These structures possess distinct electrochemical reactivity, as has been reviewed by McCreery<sup>[55]</sup> and others<sup>[56–59]</sup>. Therefore, the electrode structure provides a possible path in improving electron transfer kinetics at the electrode-electrolyte interface, which is relevant to battery technologies like RFBs. However, the structural features of carbon electrodes have also been recently identified to influence processes relevant in intercalation type electrochemical reactions, for example, improved electronic insulation and thicker SEIs were observed to form on step edges and edge planes of carbon anodes for LiBs.<sup>[11, 60, 61]</sup> However, correlating the electrode structure to electrochemical behavior is not straightforward as these observations could vary based on the electrochemical techniques. For example, bulk techniques such as CV have reported that basal planes are relatively inert when it comes to heterogeneous electron transfer<sup>[55]</sup>. Recently, microscopic measurements with scanning probe techniques has brought these differences in reactivity under review.<sup>[62–64]</sup> Therefore, it is important to evaluate local electrochemical behavior at the electrode-electrolyte interface, which is addressed to some extent by using SECM measurements, in this dissertation.

Consequently, while the carbon electrode interface structure influences electrochemical properties at interfaces, I hypothesized that functionalized carbon interfaces also hold the potential to dictate local electrochemical behavior. However, in heterogeneous electron-transfer reactions, this may not always hold true. Experimentally, there is a distinction made between “outer-sphere” and “inner-sphere” electron transfer, wherein, for the former, the electrode surface structure and functionalization does not affect the rates of electron-transfer. This is observed practically in aqueous redox reactions with species like hydroxymethyl ferrocene and hexamine ruthenium – with Pt, Au and C electrodes producing the same electrochemical behavior.<sup>[65]</sup> On the other hand, inner sphere electron transfer

proceeds with a strong interaction of reactant or product with the electrode surface, which ultimately enables the redox reaction.[65] In the field of flow batteries, the early technologies based on vanadium RFBs (VRFBs) involve catalytic reactions with carbon current collectors, and surface functionalization has been utilized to improve electron-transfer rates in VRFB systems.[66–68] However, in non-aqueous media, there lacks a comprehensive understanding of the electrode’s structure and functionalization on electron-transfer rates, therefore making this an unexplored area of practical relevance in nRFBs. This research gap is one of the two areas explored in this thesis.

Likewise, surface-modification of electrode materials, especially carbon for use in LiBs has been widely described in literature.[69, 70] In general, surface modification has been reported to improve the reversible capacity and decrease the first-cycle capacity loss in graphitic carbon anodes. Within our research group, we have studied the effect of modifying the interface between single-layer graphene and  $\text{SiO}_2/\text{Si}$  substrate with metals such as Au and Pt to observe its effect on electrochemical and electrocatalytic behavior.[37, 71] In the case of outer sphere electron-transfer reactions,[71] a pronounced kinetic improvement ( $\approx$  5 times) was observed over the graphene/Au which was attributed to an electron-donating effect from the metal sub-surface, which enhances the electron density of states and Fermi level of graphene. Consequently, it is hypothesized that the electrostatic and electronic modulations introduced by external ionic modifiers at the electrode-electrolyte interface can result in changes in the electrode potential at which intercalation processes are observed. This hypothesis has been validated by computational simulations, which suggest covalently bound fluorine surface modifiers may stabilize thermodynamically unstable structures, such as Na-intercalated graphene.[72] Likewise, the properties of the interphase forming on alkali-ion batteries are a strong function of the solution identity,[73, 74] and there exists little understanding of the electronic insulation offered by SEIs forming across different alkali-ion electrolytes. Therefore, the second area explored in this dissertation is understanding effects of surface functionalization on Na-ion intercalation and comparing SEI formation in  $\text{Li}^+$ ,

$\text{Na}^+$  and  $\text{K}^+$ -electrolytes.

## 1.4 Organization of the thesis

This thesis is organized into six chapters. The first three chapters deal with electrochemical analysis of interfaces and interphases in *beyond Li-ion* batteries. The final three chapters examine electron-transfer at carbon interfaces relevant to nRFBs. A brief description of each chapter is presented below. Appendices with supplemental info and characterization is also provided.

### 1.4.1 Chapter 2

Choosing reference electrodes for non-aqueous electrochemical measurements, especially in energy storage research, is challenging due to lengthy experiments ( $>1$  day), the lack of alternatives to the commonly used  $\text{Ag}/\text{Ag}^+$  reference electrode (RE), the introduction of junction potentials, and the possibility of sample contamination. Often, quasi-reference electrodes (QREs) such as Ag wire and Li metal strip are used, but small changes in electrolyte composition can cause large potential drifts, and their surfaces may be reactive to the solution. Here, we propose an alternative QRE based on polypyrrole electrodeposited on Pt wire (PPyQRE) encased in a glass tube with the open end sealed with commercial frits. While freestanding PPyQRE wires have been reported in literature, simple encasing of the PPyQRE overcomes the above-mentioned drawbacks of QREs while providing a reliable reference potential that is closer to the performance of an RE. During cyclic voltammetric and bulk electrolysis testing of a redox mediator in solution, the encased PPyQRE exhibited stable reference potentials over multiple charge/discharge cycles with minimal drift ( $\approx 5$  mV) after  $\approx 2.25$  days of operation. We also tested the reliability of our reference during the testing of multi-layer graphene Li-ion anodes, which often involve cycling samples at highly reducing potentials ( $< 3$  V vs.  $\text{Fc}/\text{Fc}^+$ ) over long durations ( $>1$  day). While in the same testing conditions the  $\text{Ag}/\text{Ag}^+$  electrode led to observable Ag deposits on the graphene

and large potential drifts ( $\approx$ 50 mV), the PPyQRE exhibited no measurable drift, revealing changes in voltammetric features that were obscured by reference drift when using Ag/Ag<sup>+</sup>. Minor reference drifts of  $\approx$ 30 mV over long usage of the QRE ( $\approx$ 2 months) can be addressed by calibration with a ferrocene couple at the end of experiments. These results highlight the advantages of using an encased PPyQRE as a simple and practical reference electrode for electrochemical measurements in the field of non-aqueous energy storage research.

#### 1.4.2 Chapter 3

Na-ion batteries (NIBs) are proposed as a promising candidate for beyond Li-ion chemistries, however, a key challenge associated with NIBs is the inability to achieve intercalation in graphite anodes. This phenomenon has been investigated and is believed to arise due to the thermodynamic instability of Na-intercalated graphite. We have recently demonstrated theoretical calculations showing it is possible to achieve thermodynamically stable Na-intercalated graphene structures with a fluorine surface modifier. Here, we present experimental evidence that Na<sup>+</sup> intercalation is indeed possible in fluorinated few-layer graphene (F-FLG) structures using cyclic voltammetry (CV), ion-sensitive scanning electrochemical microscopy (SECM) and in situ Raman spectroscopy. SECM and Raman spectroscopy confirmed Na<sup>+</sup> intercalation in F-FLG, while CV measurements allowed us to quantify Na-intercalated F-FLG stoichiometries around NaC<sub>14-18</sub>. These stoichiometries are higher than the previously reported values of NaC<sub>186</sub> in graphite. Our experiments revealed that reversible Na<sup>+</sup> ion intercalation also requires a pre-formed Li-based SEI in addition to the surface fluorination, thereby highlighting the critical role of SEI in controlling ion-transfer kinetics in alkali-ion batteries. In summary, our findings highlight the use of surface modification and careful study of electrode-electrolyte interfaces and interphases as an enabling strategy for NIBs.

### 1.4.3 Chapter 4

The solid electrolyte interphase (SEI) is a dynamic, electronically insulating film that forms on the negative electrode of Li<sup>+</sup> batteries (LiBs) and enables ion movement to/from the interface while preventing electrolyte breakdown. However, there is limited comparative understanding of LiB SEIs with respect to those formed in Na<sup>+</sup> and K<sup>+</sup> electrolytes for emerging battery concepts. We used scanning electrochemical microscopy (SECM) for the *in situ* interfacial analysis of incipient SEIs in Li<sup>+</sup>, K<sup>+</sup> and Na<sup>+</sup> electrolytes formed on multi-layer graphene. Feedback images using 300 nm SECM probes and ion-sensitive measurements indicated a superior passivation and highest cation flux for a Li<sup>+</sup>-SEI in contrast to Na<sup>+</sup> and K<sup>+</sup>-SEIs. Ex situ X-ray photoelectron spectroscopy indicated significant fluoride formation for only Li<sup>+</sup> and Na<sup>+</sup>-SEIs, enabling correlation to *in situ* SECM measurements. While SEI chemistry remains complex, these electroanalytical methods reveal links between chemical variables and the interfacial properties of materials for energy storage.

### 1.4.4 Chapter 5

Redox flow batteries are attractive technologies for grid energy storage since they use solutions of redox-active molecules that enable a superior scalability and the decoupling of power and energy density. However, the reaction mechanisms of the redox active components at RFB electrodes are complex, and there is currently a pressing need to understand how interfacial processes impact the kinetics and operational reversibility of RFB systems. Here, we developed a combined electrochemical imaging methodology rooted in scanning electrochemical microscopy (SECM) and atomic force microscopy (AFM) for exploring the impact of electrode structure and conditioning on the electron transfer properties of model redox-active dialkoxybenzene derivatives, 2,5-di-tert-butyl-1,4-bis(2-methoxyethoxy)benzene (C1) and 2,3-dimethyl-1,4-dialkoxybenzene (C7). Using AFM and secondary-ion mass spectrometry (SIMS), we observed the formation of interfacial films with distinct mechanical

properties compared to those of cleaved graphitic surfaces, and exclusively during reduction of electrogenerated radical cations. These films had an impact on the median rate and distribution of the electron transfer rate constant at the basal plane of multilayer and single layer graphene electrodes, displaying kinetically-limited values that did not yield the activation expected per the Butler–Volmer model with a transfer coefficient  $\approx 0.5$ . These changes were dependent on redoxmer structure: SECM showed strong attenuation of C7 kinetics by a surface layer on MLG and SLG, while C1 kinetics were only affected by SLG. SECM and AFM results together show that these limiting films operate exclusively on the basal plane of graphite, with the edge plane showing a relative insensitivity to cycling and operation potential. This integrated electrochemical imaging methodology creates new opportunities to understand the unique role of interfacial processes on the heterogeneous reactivity of redoxmers at electrodes for RFBs, with a future role in elucidating phenomena at high active concentrations and spatiotemporal variations in electrode dynamics.

#### 1.4.5 Chapter 6

Redox-flow battery (RFB) operation revolves around electron transfer (ET) between a current collector electrode and redoxmers in solution. Here, we present an approach utilizing scanning electrochemical microscopy (SECM) to evaluate interfacial ET kinetics between redoxmers and various electrode materials of interest at desired locations. This spot-analysis method relies on the measurement of heterogeneous electron transfer rate constants ( $k_f$  or  $k_b$ ) as a function of applied potential ( $E - E^0$ ). Our method enabled the identification of inherent asymmetries in the ET kinetics of oxidation and reduction for ferrocene-based redoxmers in propylene carbonate. These occurred on a wide variety of carbon electrodes such as multi-layer graphene, highly ordered pyrolytic graphite, glassy carbon and chemical vapor deposition grown graphite films, but not Pt or in water. We demonstrate operation of our spot analysis at concentrations up to 100 mM of redoxmer, which is critical for evaluating redoxmer/electrode/solvent systems for high-performance

redox-flow batteries.

#### 1.4.6 Chapter 7

Carbon structures come in numerous forms, and their surface structure is known to influence electron transfer (ET) kinetics between the electrode and redox-active species in the solution. However, little is known about the interdependencies of carbon surface structure and electron-transfer kinetics in non-aqueous media, with such knowledge being relevant to non-aqueous redox-flow batteries. In this study, we focus on comparing ET kinetics across carbon surfaces with  $sp^2$ ,  $sp^3$  hybridization, and with defects. Such carbon structures are represented by single-layer graphene (SLG) and hydrogenated SLG (H-SLG). Bulk  $sp^3$  carbon such as boron-doped diamond is also utilized as a bulk substrate material. Defects are introduced by Ar/H<sub>2</sub> and Ar plasma exposure. Scanning electrochemical microscopy (SECM) with ferrocene redox mediators revealed fast electron-transfer kinetics over  $sp^3$  hybridized carbon, consistent with Butler-Volmer theory of electron transfer over H-SLG and BDD. However, kinetically limited behavior was observed over  $sp^2$  carbon. Likewise, a higher energy dialkoxybenzene molecule (2,3-dimethyl-1,4-dialkoxybenzene, or C7) was observed to exhibit faster ET kinetics over  $sp^3$  carbon than  $sp^2$  carbon, although its ET rates deviated from expected theoretical behavior for all cases. This result is not surprising since C7 is known to form interfacial films over carbon electrodes during cycling. In all likelihood, such structures are still forming but posing a lesser inhibition to ET kinetics over  $sp^3$  carbon.

### Bibliography for Chapter 1

- (1) Trahey, L. et al. *Proceedings of the National Academy of Sciences* **2020**, *117*, 12550–12557, DOI: [10.1073/pnas.1821672117](https://doi.org/10.1073/pnas.1821672117).
- (2) Chayambuka, K.; Mulder, G.; Danilov, D. L.; Notten, P. H. L. *Advanced Energy Materials* **2020**, *10*, 2001310, DOI: [10.1002/aenm.202001310](https://doi.org/10.1002/aenm.202001310).
- (3) Speirs, J.; Contestabile, M.; Houari, Y.; Gross, R. *Renewable and Sustainable Energy Reviews* **2014**, *35*, 183–193, DOI: [doi.org/10.1016/j.rser.2014.04.018](https://doi.org/10.1016/j.rser.2014.04.018).

- (4) Dahn, J. R.; Zheng, T.; Liu, Y.; Xue, J. S. *Science* **1995**, *270*, 590–593, DOI: [10.1126/science.270.5236.590](https://doi.org/10.1126/science.270.5236.590).
- (5) Abraham, K. M. *ACS Energy Letters* **2020**, *5*, 3544–3547, DOI: [10.1021/acsenergylett.0c02181](https://doi.org/10.1021/acsenergylett.0c02181).
- (6) Wong, A. A.; Aziz, M. J. *Journal of The Electrochemical Society* **2020**, *167*, 110542, DOI: [10.1149/1945-7111/aba54d](https://doi.org/10.1149/1945-7111/aba54d).
- (7) Forner-Cuenca, A.; Brushett, F. R. *Current Opinion in Electrochemistry* **2019**, *18*, 113–122, DOI: [10.1016/j.coelec.2019.11.002](https://doi.org/10.1016/j.coelec.2019.11.002).
- (8) Chakrabarti, M.; Brandon, N.; Hajimolana, S.; Tariq, F.; Yufit, V.; Hashim, M.; Hussain, M.; Low, C.; Aravind, P. *Journal of Power Sources* **2014**, *253*, 150–166, DOI: [10.1016/j.jpowsour.2013.12.038](https://doi.org/10.1016/j.jpowsour.2013.12.038).
- (9) Jamtveit, B.; Meakin, P. In *Growth, Dissolution and Pattern Formation in Geosystems*, Jamtveit, B., Meakin, P., Eds.; Springer Netherlands: Dordrecht, 1999, pp 1–19, DOI: [10.1007/978-94-015-9179-9\\_1](https://doi.org/10.1007/978-94-015-9179-9_1).
- (10) Hernández-Burgos, K.; Barton, Z. J.; Rodríguez-López, J. *Chemistry of Materials* **2017**, *29*, 8918–8931, DOI: [10.1021/acs.chemmater.7b02243](https://doi.org/10.1021/acs.chemmater.7b02243).
- (11) Yu, X.; Manthiram, A. *Energy & Environmental Science* **2018**, *11*, 527–543, DOI: [10.1039/C7EE02555F](https://doi.org/10.1039/C7EE02555F).
- (12) Gauthier, M.; Carney, T. J.; Grimaud, A.; Giordano, L.; Pour, N.; Chang, H.-H.; Fenning, D. P.; Lux, S. F.; Paschos, O.; Bauer, C.; Maglia, F.; Lupart, S.; Lamp, P.; Shao-Horn, Y. *The Journal of Physical Chemistry Letters* **2015**, *6*, 4653–4672, DOI: [10.1021/acs.jpclett.5b01727](https://doi.org/10.1021/acs.jpclett.5b01727).
- (13) Nitta, N.; Wu, F.; Lee, J. T.; Yushin, G. *Materials Today* **2015**, *18*, 252–264, DOI: [10.1016/j.mattod.2014.10.040](https://doi.org/10.1016/j.mattod.2014.10.040).
- (14) Wood, D. L.; Li, J.; An, S. J. *Joule* **2019**, *3*, 2884–2888, DOI: [10.1016/j.joule.2019.11.002](https://doi.org/10.1016/j.joule.2019.11.002).
- (15) Elgrishi, N.; Rountree, K. J.; McCarthy, B. D.; Rountree, E. S.; Eisenhart, T. T.; Dempsey, J. L. *Journal of Chemical Education* **2018**, *95*, 197–206, DOI: [10.1021/acs.jchemed.7b00361](https://doi.org/10.1021/acs.jchemed.7b00361).
- (16) Orazem, M. E.; Tribollet, B., *Electrochemical impedance spectroscopy*, 2008, pp 383–389.
- (17) Levi, M. D.; Aurbach, D. In *Characterization of Materials*; John Wiley & Sons, Ltd: 2012, pp 1–21, DOI: [10.1002/0471266965.com125](https://doi.org/10.1002/0471266965.com125).
- (18) Talaie, E.; Bonnick, P.; Sun, X.; Pang, Q.; Liang, X.; Nazar, L. F. *Chemistry of Materials* **2017**, *29*, 90–105, DOI: [10.1021/acs.chemmater.6b02726](https://doi.org/10.1021/acs.chemmater.6b02726).
- (19) Amemiya, S.; Bard, A. J.; Fan, F.-R. F.; Mirkin, M. V.; Unwin, P. R. *Annual Review of Analytical Chemistry* **2008**, *1*, 95–131, DOI: [10.1146/annurev.anchem.1.031207.112938](https://doi.org/10.1146/annurev.anchem.1.031207.112938).
- (20) *Scanning Electrochemical Microscopy*; Bard A.J. and Mirkin, M., Ed.; CRC Press: 2022, DOI: [10.1201/9781003004592](https://doi.org/10.1201/9781003004592).

- (21) Counihan, M. C.; Sarbapalli, D.; Rodriguez-Lopez, J. *The Electrochemical Society Interface* **2020**, *29*, 30, DOI: [10.1149/2.F03203IF](https://doi.org/10.1149/2.F03203IF).
- (22) Sarbapalli, D.; Mishra, A.; Hatfield, K. O.; Gossage, Z. T.; Rodríguez-López, J. In *Batteries*; 2053-2563; IOP Publishing: 2021, 9-1 to 9-44, DOI: [10.1088/978-0-7503-2682-7ch9](https://doi.org/10.1088/978-0-7503-2682-7ch9).
- (23) Bard, A.; Faulkner, L., *Electrochemical Methods*, 2nd; John Wiley & Sons, New York: 2001.
- (24) Delahay, P., *New Instrumental Methods in Electrochemistry – Theory, Instrumentation, and Applications to Analytical and Physical Chemistry*; Interscience Publishers: 1954.
- (25) Nicholson, R. S.; Shain, I. *Analytical Chemistry* **1964**, *36*, 706–723, DOI: [10.1021/ac60210a007](https://doi.org/10.1021/ac60210a007).
- (26) Gao, J.; Shi, S.-Q.; Li, H. *Chinese Physics B* **2015**, *25*, 018210, DOI: [10.1088/1674-1056/25/1/018210](https://doi.org/10.1088/1674-1056/25/1/018210).
- (27) Huggins, R. A., 2009, DOI: [10.1007/978-0-387-76424-5](https://doi.org/10.1007/978-0-387-76424-5).
- (28) Costentin, C. *The Journal of Physical Chemistry Letters* **2020**, *11*, 9846–9849, DOI: [10.1021/acs.jpclett.0c02667](https://doi.org/10.1021/acs.jpclett.0c02667).
- (29) Costentin, C.; Savéant, J.-M. *Chemical Science* **2019**, *10*, 5656–5666, DOI: [10.1039/C9SC01662G](https://doi.org/10.1039/C9SC01662G).
- (30) Costentin, C.; Porter, T. R.; Savéant, J.-M. *ACS Applied Materials & Interfaces* **2017**, *9*, 8649–8658, DOI: [10.1021/acsami.6b14100](https://doi.org/10.1021/acsami.6b14100).
- (31) Lian, P.; Zhu, X.; Liang, S.; Li, Z.; Yang, W.; Wang, H. *Electrochimica Acta* **2010**, *55*, 3909–3914, DOI: [10.1016/j.electacta.2010.02.025](https://doi.org/10.1016/j.electacta.2010.02.025).
- (32) Ruetschi, P. *Journal of Power Sources* **1977**, *2*, 3–120, DOI: [10.1016/0378-7753\(77\)85003-9](https://doi.org/10.1016/0378-7753(77)85003-9).
- (33) Smith, A. J.; Burns, J. C.; Trussler, S.; Dahn, J. R. *Journal of The Electrochemical Society* **2009**, *157*, A196, DOI: [10.1149/1.3268129](https://doi.org/10.1149/1.3268129).
- (34) Smith, A. J.; Burns, J. C.; Dahn, J. R. *Electrochemical and Solid-State Letters* **2010**, *13*, A177, DOI: [10.1149/1.3487637](https://doi.org/10.1149/1.3487637).
- (35) Markovsky, B.; Levi, M. D.; Aurbach, D. *Electrochimica Acta* **1998**, *43*, 2287–2304, DOI: [10.1016/S0013-4686\(97\)10172-4](https://doi.org/10.1016/S0013-4686(97)10172-4).
- (36) Levi, M. D.; Salitra, G.; Markovsky, B.; Teller, H.; Aurbach, D.; Heider, U.; Heider, L. *Journal of The Electrochemical Society* **1999**, *146*, 1279, DOI: [10.1149/1.1391759](https://doi.org/10.1149/1.1391759).
- (37) Hui, J.; Schorr, N. B.; Pakhira, S.; Qu, Z.; Mendoza-Cortes, J. L.; Rodríguez-López, J. *Journal of the American Chemical Society* **2018**, *140*, 13599–13603, DOI: [10.1021/jacs.8b08907](https://doi.org/10.1021/jacs.8b08907).
- (38) Aurbach, D.; Levi, M. D.; Levi, E.; Teller, H.; Markovsky, B.; Salitra, G.; Heider, U.; Heider, L. *Journal of The Electrochemical Society* **1998**, *145*, 3024, DOI: [10.1149/1.1838758](https://doi.org/10.1149/1.1838758).

- (39) Levi, M. D.; Aurbach, D. *Journal of Electroanalytical Chemistry* **1997**, *421*, 79–88, DOI: [10.1016/S0022-0728\(96\)04832-2](https://doi.org/10.1016/S0022-0728(96)04832-2).
- (40) Polcari, D.; Dauphin-Ducharme, P.; Mauzeroll, J. *Chemical Reviews* **2016**, *116*, 13234–13278, DOI: [10.1021/acs.chemrev.6b00067](https://doi.org/10.1021/acs.chemrev.6b00067).
- (41) Lefrou, C.; Cornut, R. *ChemPhysChem* **2010**, *11*, 547–556, DOI: [10.1002/cphc.200900600](https://doi.org/10.1002/cphc.200900600).
- (42) Kiani, A.; Alpuche-Aviles, M. A.; Eggers, P. K.; Jones, M.; Gooding, J. J.; Paddon-Row, M. N.; Bard, A. J. *Langmuir* **2008**, *24*, 2841–2849, DOI: [10.1021/la702811t](https://doi.org/10.1021/la702811t).
- (43) Bard, A. J.; Mirkin, M. V.; Unwin, P. R.; Wipf, D. O. *The Journal of Physical Chemistry* **1992**, *96*, 1861–1868, DOI: [10.1021/j100183a064](https://doi.org/10.1021/j100183a064).
- (44) Skaanvik, S. A.; Stephens, L. I.; Gatemann, S. M.; Geissler, M.; Mauzeroll, J. *Analytical Chemistry* **2022**, *94*, 13852–13859, DOI: [10.1021/acs.analchem.2c02498](https://doi.org/10.1021/acs.analchem.2c02498).
- (45) Ritzert, N. L.; Rodríguez-López, J.; Tan, C.; Abruña, H. D. *Langmuir* **2013**, *29*, 1683–1694, DOI: [10.1021/la3042549](https://doi.org/10.1021/la3042549).
- (46) Bard, A. J.; Fan, F.-R. F.; Pierce, D. T.; Unwin, P. R.; Wipf, D. O.; Zhou, F. *Science* **1991**, *254*, 68–74, DOI: [10.1126/science.254.5028.68](https://doi.org/10.1126/science.254.5028.68).
- (47) Eckhard, K.; Chen, X.; Turcu, F.; Schuhmann, W. *Physical Chemistry Chemical Physics* **2006**, *8*, 5359–5365, DOI: [10.1039/B609511A](https://doi.org/10.1039/B609511A).
- (48) Barton, Z. J.; Rodríguez-López, J. *Analytical Chemistry* **2017**, *89*, 2716–2723, DOI: [10.1021/acs.analchem.6b04022](https://doi.org/10.1021/acs.analchem.6b04022).
- (49) Barton, Z. J.; Rodríguez-López, J. *Analytical Chemistry* **2014**, *86*, 10660–10667, DOI: [10.1021/ac502517b](https://doi.org/10.1021/ac502517b).
- (50) Gossage, Z. T.; Hui, J.; Sarbapalli, D.; Rodríguez-López, J. *Analyst* **2020**, *145*, 2631–2638, DOI: [10.1039/C9AN02637A](https://doi.org/10.1039/C9AN02637A).
- (51) Gossage, Z. T.; Hui, J.; Zeng, Y.; Flores-Zuleta, H.; Rodríguez-López, J. *Chemical Science* **2019**, *10*, 10749–10754, DOI: [10.1039/C9SC03569A](https://doi.org/10.1039/C9SC03569A).
- (52) Noack, J.; Roznyatovskaya, N.; Herr, T.; Fischer, P. *Angewandte Chemie International Edition* **2015**, *54*, 9776–9809, DOI: [10.1002/anie.201410823](https://doi.org/10.1002/anie.201410823).
- (53) Nguyen, T.; Savinell, R. F. *The Electrochemical Society Interface* **2010**, *19*, 54, DOI: [10.1149/2.F06103if](https://doi.org/10.1149/2.F06103if).
- (54) Winter, M.; Barnett, B.; Xu, K. *Chemical Reviews* **2018**, *118*, 11433–11456, DOI: [10.1021/acs.chemrev.8b00422](https://doi.org/10.1021/acs.chemrev.8b00422).
- (55) McCreery, R. L. *Chemical Reviews* **2008**, *108*, 2646–2687, DOI: [10.1021/cr068076m](https://doi.org/10.1021/cr068076m).
- (56) Velický, M.; Toth, P. S.; Woods, C. R.; Novoselov, K. S.; Dryfe, R. A. W. *The Journal of Physical Chemistry C* **2019**, *123*, 11677–11685, DOI: [10.1021/acs.jpcc.9b01010](https://doi.org/10.1021/acs.jpcc.9b01010).
- (57) Pavlov, S. V.; Kislenko, S. A. *Journal of Physics: Conference Series* **2018**, *1092*, 012112, DOI: [10.1088/1742-6596/1092/1/012112](https://doi.org/10.1088/1742-6596/1092/1/012112).

- (58) Brownson, D. A. C.; Kampouris, D. K.; Banks, C. E. *Chemical Society Reviews* **2012**, *41*, 6944–6976, DOI: [10.1039/C2CS35105F](https://doi.org/10.1039/C2CS35105F).
- (59) Ambrosi, A.; Chua, C. K.; Bonanni, A.; Pumera, M. *Chemical Reviews* **2014**, *114*, 7150–7188, DOI: [10.1021/cr500023c](https://doi.org/10.1021/cr500023c).
- (60) Martín-Yerga, D.; Kang, M.; Unwin, P. R. *ChemElectroChem* **2021**, *8*, 4240–4251, DOI: [10.1002/celc.202101161](https://doi.org/10.1002/celc.202101161).
- (61) Zaghib, K.; Nadeau, G.; Kinoshita, K. *Journal of Power Sources* **2001**, *97-98*, Proceedings of the 10th International Meeting on Lithium Batteries, 97–103, DOI: [10.1016/S0378-7753\(01\)00596-1](https://doi.org/10.1016/S0378-7753(01)00596-1).
- (62) Lai, S. C. S.; Patel, A. N.; McKelvey, K.; Unwin, P. R. *Angewandte Chemie International Edition* **2012**, *51*, 5405–5408, DOI: [10.1002/anie.201200564](https://doi.org/10.1002/anie.201200564).
- (63) Zhang, G.; Kirkman, P. M.; Patel, A. N.; Cuharuc, A. S.; McKelvey, K.; Unwin, P. R. *Journal of the American Chemical Society* **2014**, *136*, 11444–11451, DOI: [10.1021/ja505266d](https://doi.org/10.1021/ja505266d).
- (64) Güell, A. G.; Cuharuc, A. S.; Kim, Y.-R.; Zhang, G.; Tan, S.-y.; Ebejer, N.; Unwin, P. R. *ACS Nano* **2015**, *9*, 3558–3571, DOI: [10.1021/acsnano.5b00550](https://doi.org/10.1021/acsnano.5b00550).
- (65) Bard, A. J. *Journal of the American Chemical Society* **2010**, *132*, 7559–7567, DOI: [10.1021/ja101578m](https://doi.org/10.1021/ja101578m).
- (66) Sivakumar, B. M.; Prabhakaran, V.; Duanmu, K.; Thomsen, E.; Berland, B.; Gomez, N.; Reed, D.; Murugesan, V. *ACS Applied Energy Materials* **2021**, *4*, 6074–6081, DOI: [10.1021/acsaelm.1c00912](https://doi.org/10.1021/acsaelm.1c00912).
- (67) Kim, K. J.; Kim, Y.-J.; Kim, J.-H.; Park, M.-S. *Materials Chemistry and Physics* **2011**, *131*, 547–553, DOI: [10.1016/j.matchemphys.2011.10.022](https://doi.org/10.1016/j.matchemphys.2011.10.022).
- (68) Li, W.; Liu, J.; Yan, C. *Carbon* **2013**, *55*, 313–320, DOI: [10.1016/j.carbon.2012.12.069](https://doi.org/10.1016/j.carbon.2012.12.069).
- (69) Fu, L.; Liu, H.; Li, C.; Wu, Y.; Rahm, E.; Holze, R.; Wu, H. *Solid State Sciences* **2006**, *8*, 113–128, DOI: [10.1016/j.solidstatesciences.2005.10.019](https://doi.org/10.1016/j.solidstatesciences.2005.10.019).
- (70) Mauger, A.; Julien, C. *Ionics* **2014**, *20*, 751–787, DOI: [10.1007/s11581-014-1131-2](https://doi.org/10.1007/s11581-014-1131-2).
- (71) Hui, J.; Zhou, X.; Bhargava, R.; Chinderle, A.; Zhang, J.; Rodríguez-López, J. *Electrochimica Acta* **2016**, *211*, 1016–1023, DOI: [10.1016/j.electacta.2016.06.134](https://doi.org/10.1016/j.electacta.2016.06.134).
- (72) Nijamudheen, A.; Sarbapalli, D.; Hui, J.; Rodríguez-López, J.; Mendoza-Cortes, J. L. *ACS Applied Materials & Interfaces* **2020**, *12*, 19393–19401, DOI: [10.1021/acsami.9b23105](https://doi.org/10.1021/acsami.9b23105).
- (73) An, S. J.; Li, J.; Daniel, C.; Mohanty, D.; Nagpure, S.; Wood, D. L. *Carbon* **2016**, *105*, 52–76, DOI: [10.1016/j.carbon.2016.04.008](https://doi.org/10.1016/j.carbon.2016.04.008).
- (74) Nie, M.; Lucht, B. L. *Journal of The Electrochemical Society* **2014**, *161*, A1001, DOI: [10.1149/2.054406jes](https://doi.org/10.1149/2.054406jes).

# Chapter 2

## Pt/Polyppyrrole Quasi-References: Robustness and Application in Electrochemical Energy Storage Research

*This work has been published. Citation: Dipobrato Sarbapalli, Abhiroop Mishra and Joaquín Rodríguez-López. “Pt/Polyppyrrole Quasi-References Revisited: Robustness and Application in Electrochemical Energy Storage Research” *Anal. Chem.* **2021**, *93*, 14048–14052. DOI: [10.1021/acs.analchem.1c03552](https://doi.org/10.1021/acs.analchem.1c03552)*

*Credit statement:* D.S. and J.R-L. conceptualized the study. D.S. and A.M. performed experiments. D.S. wrote the manuscript with assistance from A.M., all authors reviewed the manuscript.

Reference electrodes (REs) enable the measurement or control of the working electrode (WE) potential, which is a cornerstone of any electrochemical experiment. An ideal RE has a stable and well-defined electrochemical potential dictated by the Nernst equation. However, in practice the potential of the reference can shift, leading to ambiguous and misleading results. Therefore, the choice of REs is often of critical concern in experiment design. While in aqueous media, there are many reliable, well-established reference electrodes such as Ag/AgCl and calomel electrodes,[1–4] non-aqueous electroanalytical measurements commonly utilize Ag/Ag<sup>+</sup> RE[2, 3, 5] or quasi-reference electrodes (QREs) such as Ag wire.[2, 6] In particular, electrochemical measurements in the domain of energy storage technologies such as Li-ion batteries (LIBs) rely commonly on Li metal strip or Li transition metal oxides as QREs.[5, 7, 8] Issues associated with the use of QREs include i) unknown poising reaction (i.e. undefined terms in the Nernst equation) and ii) drift in reference potential when the solution composition is changed (for instance, upon adding an internal standard such as ferrocene for calibration) among others.[1, 2, 7] While the Ag/Ag<sup>+</sup> RE avoids this issue,

its use in non-aqueous media can lead to the development of junction potentials due to dissimilar solution compositions across the RE frit.[1–3, 5] Furthermore, the use of high reactivity REs and QREs such as Li metal limits their use in nonaqueous solvents such as acetonitrile,[9, 10] wherein byproducts such as methane gas are generated.[11] Additionally, in our own experience of using the Ag/Ag<sup>+</sup> RE, we have observed dark precipitates forming on the frit upon extended use, possibly due to photoreactivity of Ag<sup>+</sup>. Other issues include the possibility of Ag<sup>+</sup> leakage out of the RE, which could lead to reference potential drifting over long experiments, as well as the risk of solution contamination with Ag, and Ag electrodeposition on the working electrode.[3] Therefore, the identification of a robust non-aqueous reference electrode for energy storage research is often a challenge.

A possible solution to this challenge lies in the use of solid-state QREs. These electrodes have been reported in literature since the 2000s, and are typically based on conducting polymers.[12] An example from this class of QREs are polypyrrole (PPy) quasi-references (PPyQRE). A detailed investigation into these QREs was reported by Ghilane et al.,[13] and since then the PPyQRE has been used in several electroanalytical measurements involving electrodeposition, scanning electrochemical microscopy, and other areas.[14–22] The poising reaction for such polypyrrole QREs is based on the doping reaction of PPy as shown in Eq. 2.1, with A<sup>−</sup> being the counter-ion:



The study by Ghilane et al.[13] revealed the unique advantages obtained by using such references in electroanalytical measurements. First, the electrode can be easily calibrated by the ferrocene couple. In addition, since the reference is solid-state, there is no issue of junction potentials arising upon its use. Moreover, it was demonstrated that the PPyQRE showed great promise as a stable reference when tested in voltammetric experiments. However, Ghilane et al.,[13] also reported that the PPyQRE was unstable

in highly oxidizing/reducing solutions as a result of interference with the redox reaction described by **Eq. 2.1**. Such interfering conditions are often amplified in experiments involving dramatic changes in the redox state of the solution, such as those in bulk electrolysis (BE), a technique widely used in redox flow battery research.[23, 24] Additionally, by varying the anion in supporting electrolyte, they revealed shifts in the reference potential. Therefore, it is clear that the identity of solution controls the reference potential for PPyQRE. To overcome this problem, we propose a simple modification: encasing the PPyQRE in a glass tube with its open end covered by a commercial frit (henceforth referred as “encased PPyQRE”). While this simple strategy is often used in many other RE’s,[25] the scope of this note is to highlight the advantages of such encased PPyQREs, compared to a freestanding PPyQRE, for energy storage research. We show long term (>1 day) stability of the QRE, and its performance during bulk electrolysis experiments (BE) where the redox potential of the solution is changed. We further demonstrate the use of such encased PPyQRE in Li-ion battery research.

## 2.1 Experimental methods

### 2.1.1 Chemicals

Tetrabutylammonium hexafluorophosphate (TBAPF<sub>6</sub>, 99%), pyrrole reagent (98%), acetonitrile (MeCN, HPLC grade, 99.8%), propylene carbonate (PC, 99.7%, anhydrous), ethylene carbonate (EC, 99%, anhydrous) and lithium tetrafluoroborate (LiBF<sub>4</sub>, 98%) were procured from Sigma Aldrich and used as received. 0.5 mm diameter Pt wire (99.99%) was procured from SurePure Chemetals. Ferrocene (Fc, 98%) was procured from Sigma Aldrich and recrystallized twice out of hexane before use.

### 2.1.2 Deposition and assembly of PPyQREs

The deposition of polypyrrole on Pt wire was performed using the same cyclic voltammetry (CV) protocol as described by Ghilane et al.[13] In brief, Pt wire was cycled

in 10 mM pyrrole in 100 mM TBAPF<sub>6</sub> (dissolved in MeCN) between -0.6 V to 1.2 V vs. Ag/AgCl for 50 cycles, using a CHI760 potentiostat. The CV was terminated at a potential of 0.45 V (during the anodic sweep) to have part of the electrodeposited PPy doped to PPy<sup>+</sup>, as shown in **Figure 2.1a**. Subsequently, the Pt wire covered with polypyrrole was gently rinsed in MeCN and allowed to air dry overnight before use. The use of MeCN as solvent and rinse is a precaution to prevent water contamination of the box and of experiments where this electrode is used; furthermore, we observed that air drying was key to preventing cracking of the PPy film during vacuum transfer into a glovebox. Finally, the electrode was encased in a glass tube with one end covered by a chemically resistant rubber cap (Product 6448K76, McMaster-Carr, USA), as shown in **Figure 2.1b**. The other end of the glass tube was sealed with a glass Vycor frit (Biologic USA, Product 092-VYC4) and PTFE heat shrink (Zeus Inc.).

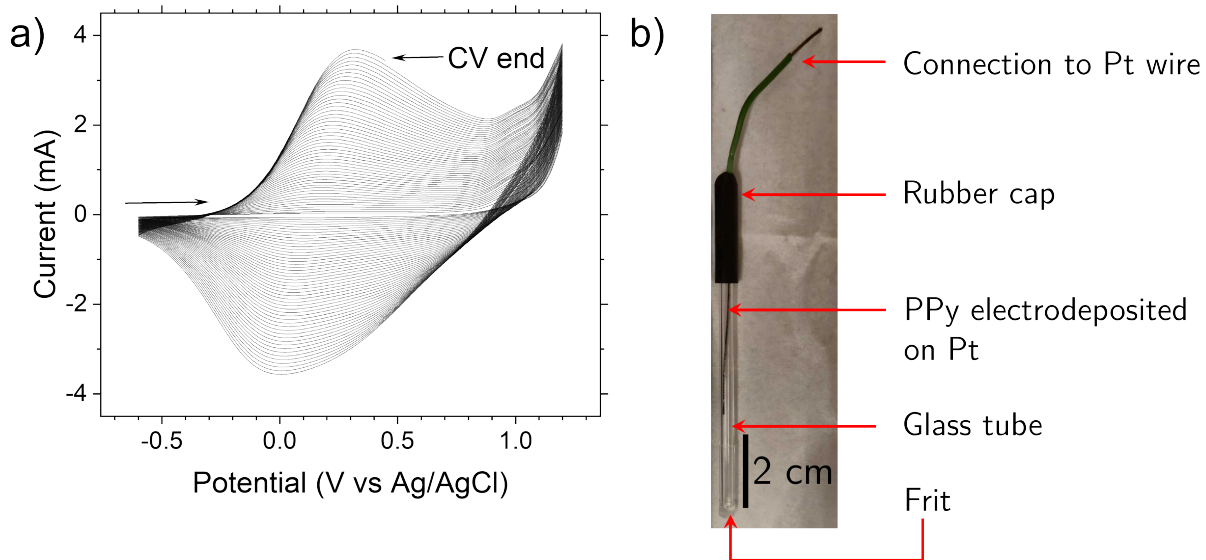


Figure 2.1: Deposition and construction of polypyrrole quasi-reference electrode (PPyQRE). a) Voltammogram depicting deposition of polypyrrole (PPy) on Pt wire and b) construction of the quasi-reference electrode, with  $\approx$ 3.5 cm of Pt wire coated with PPy.

### 2.1.3 Electrochemical and experimental measurements

All experiments using PPyQREs were performed in gloveboxes under Ar atmospheres with O<sub>2</sub> and H<sub>2</sub>O levels < 0.1 ppm using either a CHI920D bipotentiostat or a CHI760E potentiostat. W-cells for bulk electrolysis were procured from Adams and Chittenden Scientific Glass with P5 frits (1.0-1.6  $\mu\text{m}$  pore size). Scanning electron microscopy (SEM) and energy dispersive spectroscopy (EDS) was carried out in a Hitachi S4700 SEM equipped with an iXRF EDS detector (Oxford Instruments).

## 2.2 Results

In order to demonstrate the stability of encased PPyQREs, we performed cyclic voltammetry (CV) and bulk electrolysis (BE) measurements. **Figure 2.2a** illustrates CVs of 1 mM ferrocene (Fc) solution cycled for approximately 2.25 days, with a Pt ultramicroelectrode (UME). **Figure 2.2a** reveals only a slight drift after continuous operation during 15,000 CV cycles.  $E_{1/2}$  calculations for each cycle, as shown in **Figure 2.2b** reveal the majority of values to lie within a range of 55 to 64 mV (mean,  $\mu = 59 \text{ mV}$ , standard deviation,  $\sigma = 3 \text{ mV}$ ). We calculate a small drift of 0.08 mV/h (1.9 mV/day) throughout 56 h of operation. However, one should keep in mind that the diffusion layer generated at such UMEs during voltammetry have characteristic lengths similar to the diameter of the microdisk (25  $\mu\text{m}$  in our case).[1] Therefore, the identity of the solution remains virtually unchanged, especially around the reference electrode. This condition is not met sometimes in electrochemical measurements involving larger electrodes and is clearly not the case in BE.

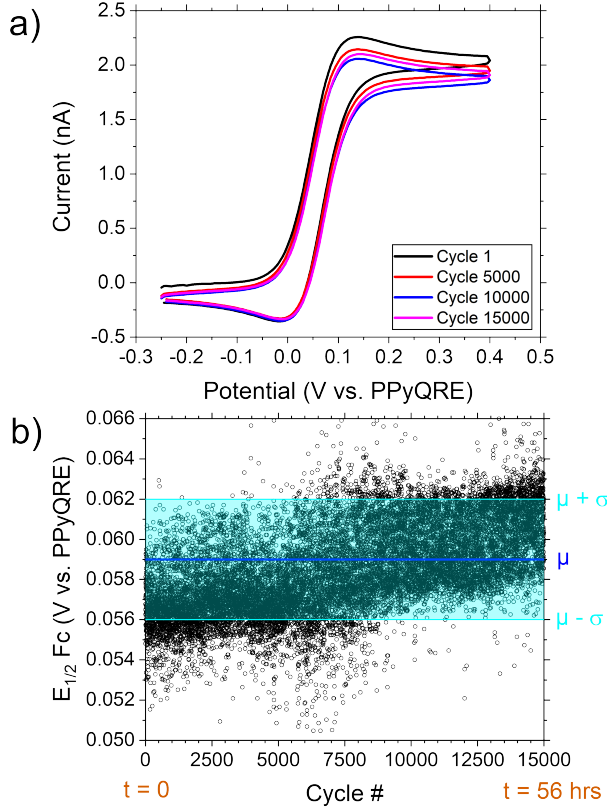


Figure 2.2: Long term ( $> 2$  days) cycling performance of PPyQRE. a) Select voltammograms of ferrocene as observed during cycling b)  $E_{1/2}$  of ferrocene as a function of cycle number. Working electrode: 25  $\mu\text{m}$  Pt UME; Reference electrode: PPyQRE; Counter Electrode: Graphite; Solution: 1 mM Fc in 0.1 M LiBF<sub>4</sub> dissolved in 1:1 PC/EC (by vol); scan rate 100 mV/s.

To prove that the encased PPyQRE assembly maintains a stable reference potential, we compared its performance during BE of Fc with polypyrrole electrodeposited on Pt wire (referred henceforth as “bare PPyQRE”). We utilized a W- and H-cell configuration in the BE experiment. In W cells, the RE, WE and counter electrodes were separated by P5 frits whereas in H-cells, the WE and RE were in the same compartment. During BE, we utilized a second working electrode, a 25  $\mu\text{m}$  Pt UME to measure the  $E_{1/2}$  of Fc as a function of state-of-charge (SOC, SOC = 0 means all Fc is in the native state, SOC = 1 means all Fc is converted to Fc<sup>+</sup>). **Figure 2.3** summarizes the results from these experiments.

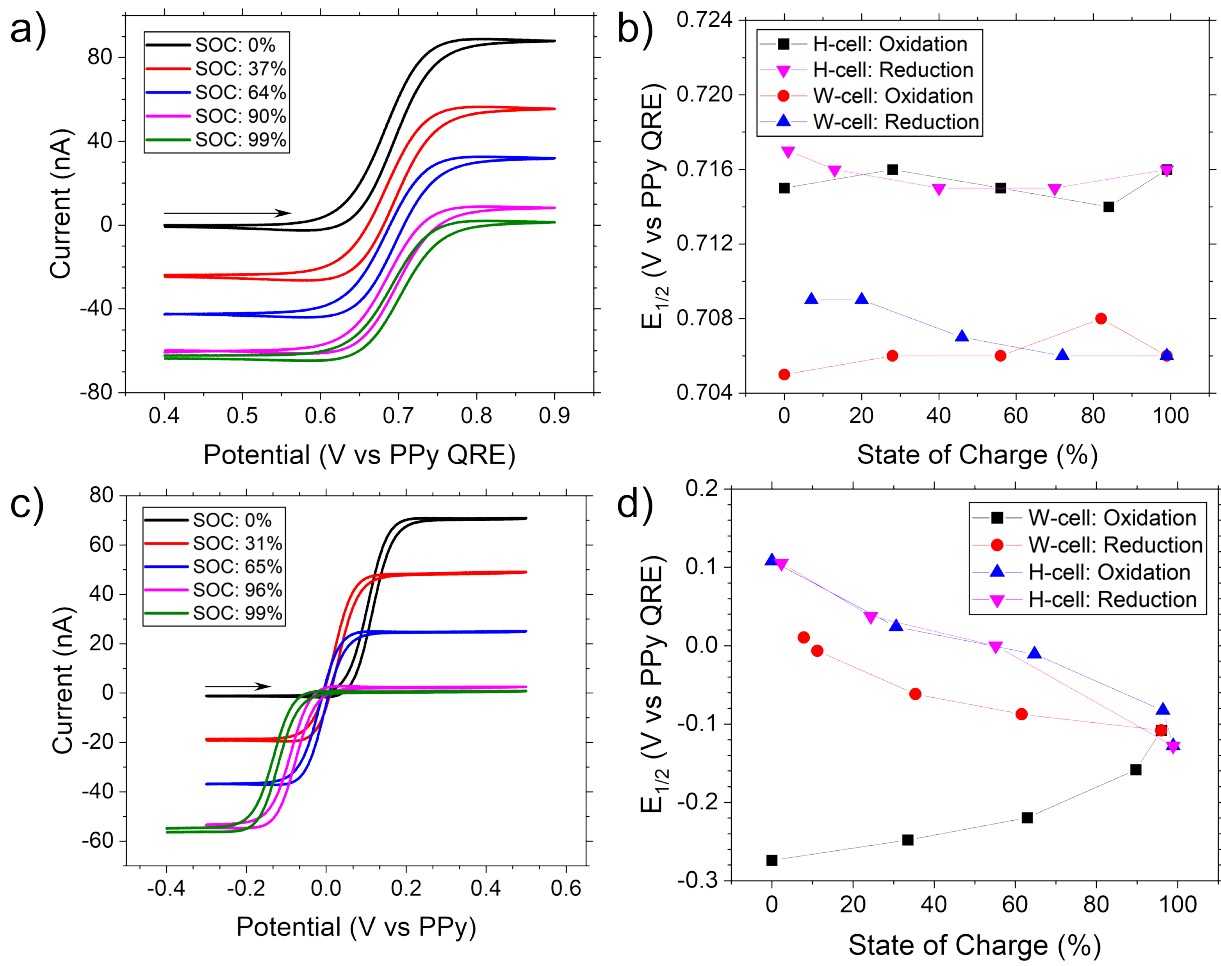


Figure 2.3: Bulk electrolysis of ferrocene in different configurations. a) UME CVs during  $\text{Fc}$  to  $\text{Fc}^+$  oxidation in an H-cell configuration and b)  $E_{1/2}$  during  $\text{Fc}$  oxidation and  $\text{Fc}^+$  reduction with an encased PPyQRE. c) and d) same as a) and b) respectively but with bare PPyQRE. Initial solution composition: 8 mM  $\text{Fc}$  in 0.5 M  $\text{TBAPF}_6$  dissolved in MeCN. Pt flag electrodes were used as working and counter electrodes for the BE of  $\text{Fc}$ . Scan rate in voltammetric experiments was 100 mV/s.

The robust performance of the encased PPyQRE is evident from the voltammograms and  $E_{1/2}$  data in **Figure 2.3a** and **2.3b**. There is a drift of  $\pm 5$  mV over the course of the BE measurements, irrespective of whether the reference was tested in a W or H-cell configuration. In comparison, when we use a bare PPyQRE, we observe a reference shift in the order of  $\approx 200$  mV when testing in a H-cell configuration and  $\approx 300$  mV in a W cell configuration (**Figures 2.3c** and **2.3d**). This result highlights that the frit used in the construction of the encased PPyQRE was able to preserve the identity of the

solution inside the glass tube, therefore preventing the reference potential from shifting over the seven-hour duration of BE experiments. As in other reference electrodes, the ultimate performance of the PPYQRE might be determined by the quality and porosity properties of the frit used.[26]

Now that we have demonstrated the stability of PPYQRE in non-aqueous electrochemical measurements of CV and BE concerning redox species in solution, we now highlight two examples illustrating their performance in Li-ion battery research. We targeted experiments using multi-layer graphene (MLG) electrodes as Li-ion battery anodes.[27–30]

A first experiment compares the use of an Ag/Ag<sup>+</sup> RE vs. encased PPYQRE in a potentiostatic intermittent titration (PITT) measurement to characterize solid-state Li-ion diffusion in MLG. In brief, PITT experiments involve characterizing the current-time behavior of electrodes over small potential increments, leading to the quantification of diffusion coefficients with respect to applied potential on the electrode.[31] The current-time measurements need to be run until equilibrium, and therefore, a PITT experiment runs for long duration (around 10 hours in our case). In practice, we run multiple PITT experiments while running voltammograms of Li<sup>+</sup> (de)intercalation in between. **Figure 2.4a** and **2.4b** illustrate these CVs with the Ag/Ag<sup>+</sup> RE and encased PPYQRE, respectively. As observed in **Figure 2.4a**, over the course of the PITT measurement, there is a reference potential drift of 50 mV when we use an Ag/Ag<sup>+</sup> RE. This can be explained by possible Ag<sup>+</sup> leakage and development of junction potentials across the frit in the RE. Ag<sup>+</sup> leakage modifies the concentration of Ag<sup>+</sup> in contact with the Ag wire, thus modifying its Nernst potential. Additionally, it is a concern in the electrochemical measurements at the MLG electrode, which is biased to strongly reducing potentials for Li<sup>+</sup> intercalation, therefore leading to the possibility of Ag plating. We have observed such Ag contamination arising from plating on the surface of MLG anodes after CV and PITT measurements when analyzing them ex situ using SEM-EDS. **Figure 2.4c** illustrates the EDS spectra at select points of a sample,

which revealed significant Ag metal presence, thereby proving that Ag metal plating is in fact realistically expected when using the Ag/Ag<sup>+</sup> RE in such Li<sup>+</sup> intercalation measurements in anodes. On the other hand, there are no major concentration gradients across the ends of the frit when using an encased PPyQRE since the solution inside and outside the glass tube are the same. This fact, combined with the low-reference drift characteristics of the PPyQRE results in excellent long-term control over working electrode potentials as shown in **Figure 2.4b**. In fact, the improved voltammograms in **Figure 2.4b** exhibit a small but clear peak splitting as the sample ages during operation, suggesting changes in the kinetics of charge transfer during the experiment. These details are largely obscured by the uncertainty introduced by reference potential drifts when using Ag/Ag<sup>+</sup> reference.

A second example highlighting the applicability of the PPyQRE with MLG samples is shown in **Figure 2.4d**, consisting of Li<sup>+</sup> (de)intercalation behavior captured via CV on various MLG samples at different times over two months, with the same encased PPyQRE. We expect the intercalation potentials to be consistent across measurements since it is a thermodynamic parameter. Kinetic complications are not expected, especially with our recent evidence of Nernstian behavior being observed with the staging peak potentials on such MLG electrodes.[27] Therefore, the fact that we are able to see consistent cathodic staging peak potentials in **Figure 2.4d** vs. PPyQRE attests to the robustness of the encased setup. It should be noted that the peak splitting in such electrodes depend heavily on factors such as cycling history and charge transfer kinetics, and therefore, we do not utilize the anodic staging peaks for estimating reference potential drift.[32] The minor drifts observed between these experiments ( $\approx$ 20-30 mV) could be easily solved via calibration to Fc/Fc<sup>+</sup>. In these experiments we performed such calibration after each run, and verified that within each measurement the reference potential does not drift significantly, consistent with the data reported above. This observation has also been consistent with the use of various PPyQREs in our laboratory for the past two years.

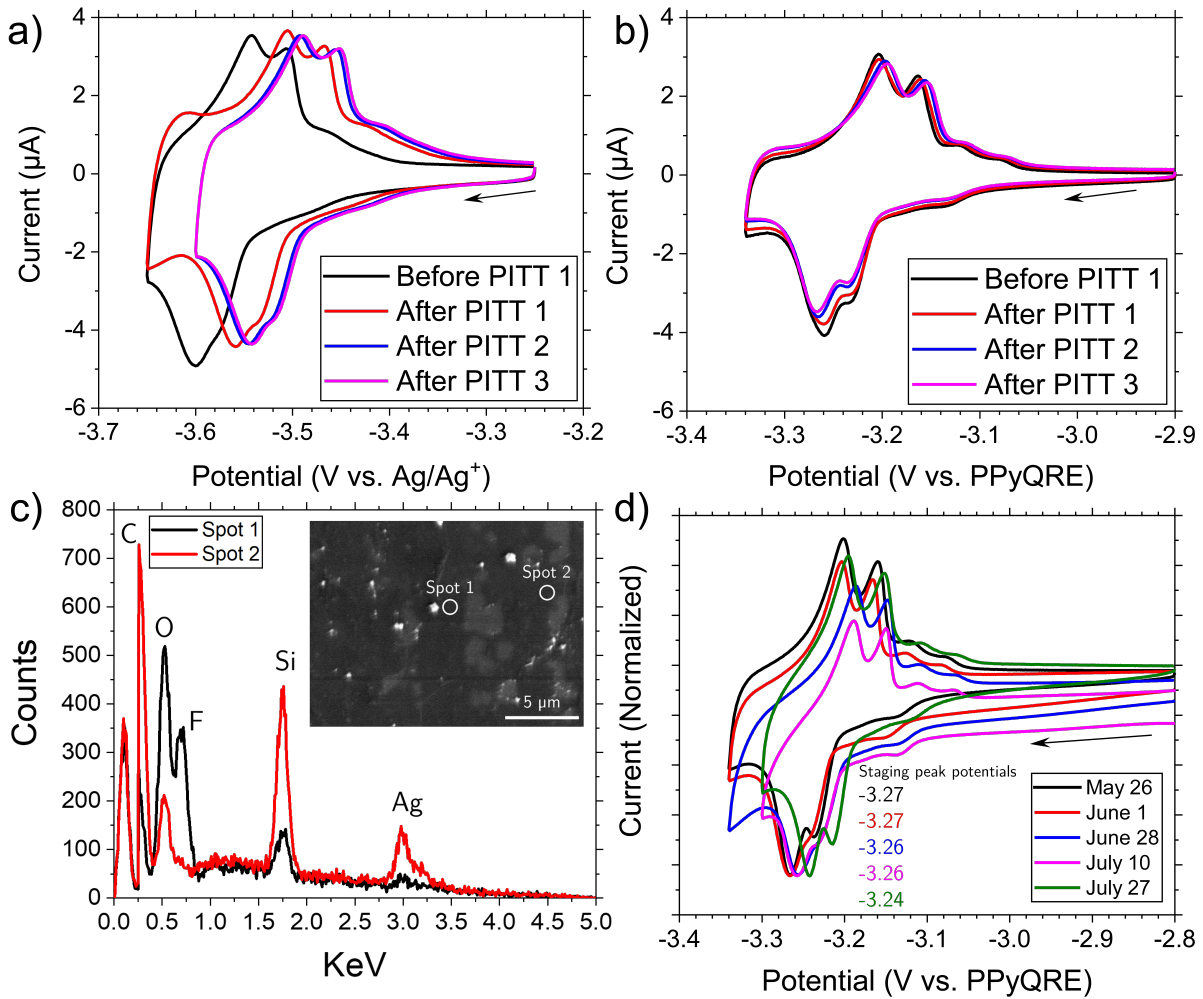


Figure 2.4: Performance of Ag/Ag<sup>+</sup> RE and encased PPyQRE characterized with Li<sup>+</sup> (de)intercalation experiments; macro-disc MLG working electrode, scan rate 1 mV/s, electrode area 7.1 mm<sup>2</sup>. a) CV using a Ag/Ag<sup>+</sup> RE ([Ag<sup>+</sup>] = 0.1 M) reference and b) using a PPyQRE after three PITT measurements (denoted as PITT1, PITT2, PITT3). c) SEM-EDS measurement of the MLG surface after CV and PITT measurements with the Ag/Ag<sup>+</sup> RE. d) Li<sup>+</sup> (de)intercalation CVs obtained with different MLG electrodes across two months. The potential corresponding to highest current peak in the cathodic sweep is reported inset (current axis is normalized to this peak value).

We have successfully used the PPyQRE in a variety of non-aqueous solvents: propylene carbonate, ethylene carbonate, acetonitrile, diethylene carbonate, dimethylformamide, and tetraglyme. Supporting electrolytes used in some of these solvents were: LiBF<sub>4</sub>, TBAPF<sub>6</sub>, KPF<sub>6</sub>, NaPF<sub>6</sub>, and LiPF<sub>6</sub>. The reference potential of encased

PPyQRE does not drift when exposed to oxygen, whereas the presence of dissolved oxygen has been previously reported to affect the potentiometric response of freestanding PPYQRE wires.[33] In any case, the lack of dissolved oxygen in most non-aqueous electrochemical energy storage measurements is an added support for the stability of PPYQREs. Additional experimental literature detailing the use of PPYQREs are described in many papers which cite Ref [13] (some of which have been highlighted earlier). It is also to be noted that there remain unidentified challenges in the use of such PPYQREs. For example, we have observed in our experiments that the construction of a PPYQRE in a solution containing lithium bis(trifluoromethanesulfonyl)imide immediately results in the polypyrrole flaking off the Pt wire, therefore rendering it ineffective in the presence of such salts.

### 2.3 Conclusions

We proposed the use of a Pt/polypyrrole electrode within a glass tube with fritted end to make a stable quasi-reference electrode for electrochemical energy storage research. Our results clearly prove the advantages of using such a RE for measurements wherein the bulk solution redox potential changes significantly, for example in bulk electrolysis. Practical electroanalytical measurements on Li-ion battery materials also highlight the utility of the encased PPYQREs. We hope that the work reported here aids the energy storage research community to address the challenge of identifying a suitable non-aqueous reference electrode for electroanalytical measurements.

### Bibliography for Chapter 2

- (1) Bard, A.; Faulkner, L., *Electrochemical Methods*, 2nd; John Wiley & Sons, New York: 2001.
- (2) Smith, T. J.; Stevenson, K. J. In *Handbook of Electrochemistry*, Zoski, C. G., Ed.; Elsevier: Amsterdam, 2007, pp 73–110, DOI: [10.1016/B978-044451958-0.50005-7](https://doi.org/10.1016/B978-044451958-0.50005-7).
- (3) Bott, A. *Current Separations* **1995**, *14*, 64–69.

- (4) Spitzer, P.; Wunderli, S.; Maksymiuk, K.; Michalska, A.; Kisiel, A.; Galus, Z.; Tauber, G. In *Handbook of Reference Electrodes*, Inzelt, G., Lewenstam, A., Scholz, F., Eds.; Springer Berlin Heidelberg: Berlin, Heidelberg, 2013, pp 77–143, DOI: [10.1007/978-3-642-36188-3\\_5](https://doi.org/10.1007/978-3-642-36188-3_5).
- (5) Izutsu, K. In *Handbook of Reference Electrodes*, Inzelt, G., Lewenstam, A., Scholz, F., Eds.; Springer Berlin Heidelberg: Berlin, Heidelberg, 2013, pp 145–187, DOI: [10.1007/978-3-642-36188-3\\_6](https://doi.org/10.1007/978-3-642-36188-3_6).
- (6) Inzelt, G. In *Handbook of Reference Electrodes*, Inzelt, G., Lewenstam, A., Scholz, F., Eds.; Springer Berlin Heidelberg: Berlin, Heidelberg, 2013, pp 331–332, DOI: [10.1007/978-3-642-36188-3\\_14](https://doi.org/10.1007/978-3-642-36188-3_14).
- (7) Mozhzhukhina, N.; Calvo, E. J. *Journal of The Electrochemical Society* **2017**, *164*, A2295, DOI: [10.1149/2.0341712jes](https://doi.org/10.1149/2.0341712jes).
- (8) La Mantia, F.; Wessells, C.; Deshazer, H.; Cui, Y. *Electrochemistry Communications* **2013**, *31*, 141–144, DOI: [10.1016/j.elecom.2013.03.015](https://doi.org/10.1016/j.elecom.2013.03.015).
- (9) Xu, K. *Chemical Reviews* **2014**, *114*, 11503–11618, DOI: [10.1021/cr500003w](https://doi.org/10.1021/cr500003w).
- (10) Widmaier, M.; Krüner, B.; Jäckel, N.; Aslan, M.; Fleischmann, S.; Engel, C.; Presser, V. *Journal of The Electrochemical Society* **2016**, *163*, A2956, DOI: [10.1149/2.0421614jes](https://doi.org/10.1149/2.0421614jes).
- (11) Zheng, D.; Yang, X.-Q.; Qu, D. *Chemistry – An Asian Journal* **2011**, *6*, 3306–3311, DOI: [10.1002/asia.201100422](https://doi.org/10.1002/asia.201100422).
- (12) Kisiel, A.; Marcisz, H.; Michalska, A.; Maksymiuk, K. *Analyst* **2005**, *130*, 1655–1662, DOI: [10.1039/B510868C](https://doi.org/10.1039/B510868C).
- (13) Ghilane, J.; Hapiot, P.; Bard, A. J. *Analytical Chemistry* **2006**, *78*, 6868–6872, DOI: [10.1021/ac060818o](https://doi.org/10.1021/ac060818o).
- (14) Ghilane, J.; Fan, F.-R. F.; Bard, A. J.; Dunwoody, N. *Nano Letters* **2007**, *7*, 1406–1412, DOI: [10.1021/nl070268p](https://doi.org/10.1021/nl070268p).
- (15) Fontaine, O.; Ghilane, J.; Martin, P.; Lacroix, J.-C.; Randriamahazaka, H. *Langmuir* **2010**, *26*, 18542–18549, DOI: [10.1021/la103000u](https://doi.org/10.1021/la103000u).
- (16) Leroux, Y.; Schaming, D.; Ruhlmann, L.; Hapiot, P. *Langmuir* **2010**, *26*, 14983–14989, DOI: [10.1021/la101294s](https://doi.org/10.1021/la101294s).
- (17) Noël, J.-M.; Zigah, D.; Simonet, J.; Hapiot, P. *Langmuir* **2010**, *26*, 7638–7643, DOI: [10.1021/la904413h](https://doi.org/10.1021/la904413h).
- (18) Lhenry, S.; Leroux, Y. R.; Hapiot, P. *Analytical Chemistry* **2013**, *85*, 1840–1845, DOI: [10.1021/ac303226e](https://doi.org/10.1021/ac303226e).
- (19) Duarte-Guevara, C.; Swaminathan, V. V.; Burgess, M.; Reddy, B.; Salm, E.; Liu, Y.-S.; Rodriguez-Lopez, J.; Bashir, R. *Analyst* **2015**, *140*, 3630–3641, DOI: [10.1039/C5AN00085H](https://doi.org/10.1039/C5AN00085H).
- (20) Kai, T.; Zhou, M.; Duan, Z.; Henkelman, G. A.; Bard, A. J. *Journal of the American Chemical Society* **2017**, *139*, 18552–18557, DOI: [10.1021/jacs.7b08702](https://doi.org/10.1021/jacs.7b08702).

- (21) Thompson, A. C.; Simpson, B. H.; Lewis, N. S. *ACS Applied Materials & Interfaces* **2020**, *12*, 11551–11561, DOI: [10.1021/acsami.9b21134](https://doi.org/10.1021/acsami.9b21134).
- (22) Isaev, V. V.; Sergeev, A. V.; Zakharchenko, T. K.; Itkis, D. M.; Groß, A.; Yashina, L. V. *Journal of The Electrochemical Society* **2021**, *168*, 030520, DOI: [10.1149/1945-7111/abe6ec](https://doi.org/10.1149/1945-7111/abe6ec).
- (23) Weber, A. Z.; Mench, M. M.; Meyers, J. P.; Ross, P. N.; Gostick, J. T.; Liu, Q. *Journal of applied electrochemistry* **2011**, *41*, 1137–1164, DOI: [10.1007/s10800-011-0348-2](https://doi.org/10.1007/s10800-011-0348-2).
- (24) Kwabi, D. G.; Ji, Y.; Aziz, M. J. *Chemical Reviews* **2020**, *120*, 6467–6489, DOI: [10.1021/acs.chemrev.9b00599](https://doi.org/10.1021/acs.chemrev.9b00599).
- (25) Zampardi, G.; Ventosa, E.; La Mantia, F.; Schuhmann, W. *Chemical Communications* **2013**, *49*, 9347–9349, DOI: [10.1039/C3CC44576C](https://doi.org/10.1039/C3CC44576C).
- (26) Mousavi, M. P. S.; Saba, S. A.; Anderson, E. L.; Hillmyer, M. A.; Bühlmann, P. *Analytical Chemistry* **2016**, *88*, 8706–8713, DOI: [10.1021/acs.analchem.6b02025](https://doi.org/10.1021/acs.analchem.6b02025).
- (27) Hui, J.; Nijamudheen, A.; Sarbapalli, D.; Xia, C.; Qu, Z.; Mendoza-Cortes, J. L.; Rodríguez-López, J. *Chemical Science* **2021**, *12*, 559–568, DOI: [10.1039/DOSC03226C](https://doi.org/10.1039/DOSC03226C).
- (28) Gossage, Z. T.; Hui, J.; Sarbapalli, D.; Rodríguez-López, J. *Analyst* **2020**, *145*, 2631–2638, DOI: [10.1039/C9AN02637A](https://doi.org/10.1039/C9AN02637A).
- (29) Hui, J.; Schorr, N. B.; Pakhira, S.; Qu, Z.; Mendoza-Cortes, J. L.; Rodríguez-López, J. *Journal of the American Chemical Society* **2018**, *140*, 13599–13603, DOI: [10.1021/jacs.8b08907](https://doi.org/10.1021/jacs.8b08907).
- (30) Hui, J.; Burgess, M.; Zhang, J.; Rodríguez-López, J. *ACS Nano* **2016**, *10*, 4248–4257, DOI: [10.1021/acsnano.5b07692](https://doi.org/10.1021/acsnano.5b07692).
- (31) Levi, M. D.; Aurbach, D. In *Characterization of Materials*; John Wiley & Sons, Ltd: 2012, pp 1–21, DOI: [10.1002/0471266965.com125](https://doi.org/10.1002/0471266965.com125).
- (32) Levi, M.; Aurbach, D. *Electrochimica Acta* **1999**, *45*, 167–185, DOI: [10.1016/S0013-4686\(99\)00202-9](https://doi.org/10.1016/S0013-4686(99)00202-9).
- (33) Bobacka, J.; Gao, Z.; Ivaska, A.; Lewenstam, A. *Journal of Electroanalytical Chemistry* **1994**, *368*, 33–41, DOI: [10.1016/0022-0728\(93\)03081-Y](https://doi.org/10.1016/0022-0728(93)03081-Y).

# Chapter 3

## A Surface Modification Strategy Towards Reversible Na-ion Intercalation on Graphitic Carbon Using Fluorinated Few-Layer Graphene

*This work has been published. Citation: Dipobrato Sarbapalli, Yu-Hsiu Lin, Sean Stafford, Jangyup Son, Abhiroop Mishra, Jingshu Hui, A Nijamudheen, Adolfo I. B. Romo, Zachary T. Gossage, Arend M. van der Zande, Jose L. Mendoza-Cortes, Joaquín Rodríguez-López. “A Surface Modification Strategy Towards Reversible Na-ion Intercalation on Graphitic Carbon Using Fluorinated Few-Layer Graphene” *J. Electrochem. Soc.* **2022**, *169*, 106522. DOI: [10.1149/1945-7111/ac9c33](https://doi.org/10.1149/1945-7111/ac9c33)*

*Credit statement:* D.S. fabricated, characterized samples and performed all electrochemical experiments under the guidance of J.R-L. D.S. analyzed all data, prepared figures and wrote the manuscript with assistance from J.H. and J.R-L. Y-H.L., S.S., A.N. performed simulations under the guidance of J. L. M-C. J.S. and A.M.v.d.Z. provided fluorinated graphene and associated recipes. A.M. and Z.T.G. fabricated HgUMEs, and assisted in SECM measurements. A.I.B.R. synthesized and characterized TkDAPF<sub>6</sub>. All authors reviewed the manuscript.

The demand for Li-ion batteries (LIBs) is ever increasing owing to their beneficial performance and cost characteristics for applications ranging from consumer electronics to vehicular transportation.<sup>[1, 2]</sup> However, research into the Li raw material reserves are predicting shortages,<sup>[3]</sup> along with limitations on logistics associated with LIB supply chains.<sup>[2, 4, 5]</sup> Therefore, beyond Li-ion chemistries are attracting increased attention,<sup>[4, 6–8]</sup> along with different battery architectures such as flow batteries.<sup>[1]</sup> Some examples of these beyond Li-ion battery technologies include Na-ion (NIB) and K-ion battery (KIB) chemistries.<sup>[7]</sup> Focusing specifically on NIBs, Yabuuchi et al.,<sup>[8]</sup> comprehensively reviewed developments in the field and highlighted the importance of NIBs over LIBs,

including (i) widespread abundance and consequently, low cost of sodium, (ii) comparable theoretical capacities, (iii) and weaker desolvation energies associated with  $\text{Na}^+$ , leading to energetically beneficial intercalation processes and solid state  $\text{Na}^+$  diffusion, among others.[6, 9] Thus, there is potential of NIBs being a candidate for practical beyond Li-ion battery technologies.[10]

Current Na-ion batteries utilize intercalation electrodes; cathodes are based on transition metal oxides which are structurally similar to LIB cathodes (for example those based on O<sub>3</sub>-type  $\text{NaMO}_2$  crystal structures, where M represents certain transition metals)[11, 12] among others such as Prussian Blue.[13] On the anode side, unlike LIBs, NIBs utilize use hard/non-graphitizable carbons with reversible capacities  $>200 \text{ mAh g}^{-1}$ .[14–16] However, hard carbons are influenced by their source materials and preparation method and can show large irreversible capacities during initial cycles.[17] Commercial LIBs utilize either natural or artificial forms of graphite as the anode material, owing to its high storage capacity and excellent (de)intercalation characteristics.[18] Given the well-established use of graphite in a commercial LIB battery, it is desirable to use the same materials and open a new field of anode materials of NIBs. This point is even more critical because implementing alternative Na-metal anodes currently face challenges owing to high reactivity, leading to unstable solid-electrolyte interphases and dendrite growth.[19, 20]

However, one of the major issues for extending the use of graphite to NIB anodes is the low  $\text{Na}^+$  storage capacity within graphitic carbons. Dahn and co-workers reported graphite to be a poor intercalation host for  $\text{Na}^+$  ions, with the experimentally measured stoichiometry being  $\text{NaC}_{186}$ ,[21] compared to the  $\text{LiC}_6$  or  $\text{LiC}_8$  stoichiometries in LIBs.[22–24] Subsequently, it has been reported that the origin of poor intercalation capacity stems from unfavorable interactions between intercalated Na and C atoms in graphite.[25, 26] We hypothesized that these unfavorable interactions could be overturned by using 2D materials with distinct surface electronic properties that create the conditions

for  $\text{Na}^+$  intercalation.[24] Thus, we recently presented theoretical calculations[24] which highlighted that a fluorine surface modifier built over a thin, 4-layer graphene structure (**Figure 3.1a**) resulted in multiple Na-intercalated structures (**Figure 3.1b**) becoming thermodynamically stable, as shown in **Figure 3.1c**. Experimental realization of this theoretical work could have significant impacts on the fundamental understanding of  $\text{Na}^+$  intercalation in graphitic carbons. Therefore, the scope of this paper is focused on the experimental investigation of  $\text{Na}^+$  intercalation in modified CVD-grown few-layer graphene (FLG) structures. Fluorine surface modification on FLG (F-FLG) was achieved by exposure to  $\text{XeF}_2$  gas.[27, 28] We utilized cyclic voltammetry (CV), ion-sensitive scanning electrochemical microscopy (SECM), and in situ Raman spectroscopy to probe  $\text{Na}^+$  charge storage capacity and associated mechanisms in F-FLG electrodes. Finally ex situ scanning electron microscopy (SEM) and X-ray photoelectron spectroscopy (XPS) were performed to characterize interphases forming on these F-FLG electrodes. Our results revealed that  $\text{Na}^+$  intercalation takes place with reversible stoichiometries higher than previously reported using a modified interface and SEI, seeding new directions for developing graphitic carbons as NIB anodes.

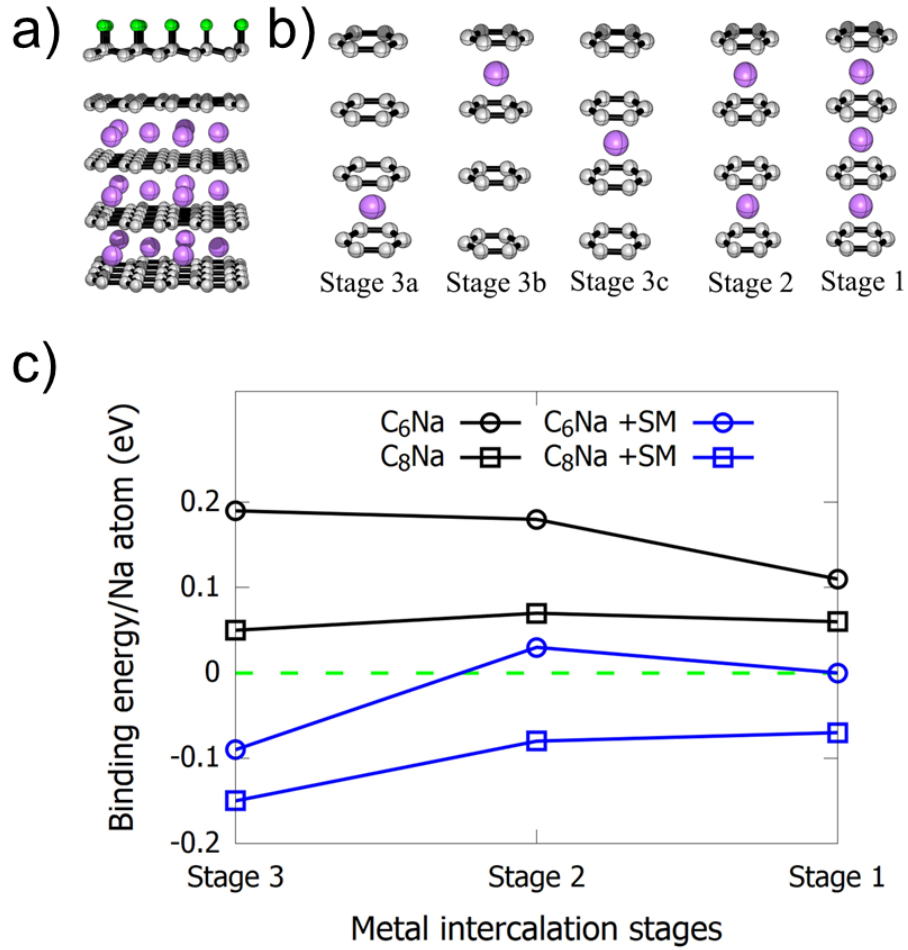


Figure 3.1: Simulations characterizing thermodynamic stability of Na-intercalated structures. a) Illustration of a Stage 1 Na-intercalated structure. b) Illustration of different staging structures. c) Binding energies of Na-intercalated structure with (blue line) and without (black line) fluorine surface modifiers (SM). Silver atoms depict carbon, purple atoms depict Na, and green atoms depict fluorine.

### 3.1 Methods and Materials

#### 3.1.1 Chemicals

All chemicals were purchased from commercial sources and used as received. Propylene carbonate (PC, anhydrous, 99.7%), ethylene carbonate (EC, anhydrous, 99%), lithium tetrafluoroborate ( $\text{LiBF}_4$ , 98%), ferrocene (Fc, 98%), acetone (99.5%), isopropyl alcohol (IPA 99.5%), glacial acetic acid (99.5%), N, N, N',

$N'$ -tetramethyl-p-phenylenediamine (TMED, 99%) and ethylenediaminetetraacetic acid disodium salt dihydrate ( $Na_2EDTA \cdot 2H_2O$ , 99.0%), Poly (Bisphenol A carbonate), with an average Mw of 45000, were all purchased from Sigma-Aldrich. Tetrakis(decyl) ammonium hexafluorophosphate ( $TkDAPF_6$ ) was synthesized in house using tetrakis(decyl)ammonium bromide (99%, TCI) and silver hexafluorophosphate (98%, Sigma); synthesis and characterization is reported in **Section A.1** of Appendix A. 25  $\mu m$  thick copper foil was purchased from Alfa Aesar. Copper etchant was purchased from Transene Company.  $SiO_2/Si$  wafer (3 in. B-doped P-type Si wafer with 300 nm wet thermal oxide) was purchased from University Wafer.

### 3.1.2 FLG synthesis, transfer and fluorination

FLG was synthesized through chemical vapor deposition (CVD) on pretreated copper foil catalyst following previously reported procedures.[29–31] The Cu foil was treated in solvents in the following order, to remove any organic contaminants and surface oxides: acetone (10 s), water (10 s), glacial acetic acid (10 min), water (10 s), acetone (10 s), and IPA (10 s). FLG was grown on Cu foil in a quartz tube, under atmospheric pressure at 960°C (Ramp time from room temperature to 960°C in 1.5 h), 10 sccm  $CH_4$  and 30 sccm  $H_2$  for 2.5 min. FLG was transferred on  $SiO_2/Si$  wafer and quartz coverslips through a wet transfer method,[32] using poly(bisphenol A carbonate). After Cu etching, transfer steps involved four rinsing steps floating the FLG on DI water, 2 h treatment with 0.1 M  $Na_2EDTA$  aqueous solution, and four additional rinse steps with DI water again to fully remove any metal residue. After transfer to Pt padded  $SiO_2/Si$  wafer (for mitigating conductivity issues in fluorinated FLG, **Section A.2**, Appendix A) and drying in a vacuum desiccator, samples were immersed in chloroform overnight to remove the polycarbonate protecting layer. For FLG fluorination, we used a  $XeF_2$  etcher (Xactix etching system) with expansion chamber partial pressure of  $XeF_2$  set to 3 torr at room temperature. We exposed the FLG over 12 cycles of fresh  $XeF_2$  at 1.3 torr specimen chamber pressure for 30 s each cycle. Fluorination

extent was  $\approx$ 56%, as characterized using single layer graphene as proxy (**Figure A.2**).

### 3.1.3 Graphene characterization

FLG was characterized through SEM, Raman spectroscopy and transmittance microscopy. The absorbance of graphene to radiation between 500–700 nm wavelengths is known to be 2.3% per layer.[33] Transmittance micrographs (**Figure 3.2a**) obtained at 561 nm was subsequently used to obtain layer number distribution maps (**Figure 3.2b**). SEM of FLG (**Figure 3.2c**) was performed on a Hitachi S4800 field emission microscope. Raman spectral maps were collected using a Nanophoton Laser Raman Microscope (RAMAN-11, Japan). XPS was performed using a Kratos Axis Ultra X-ray photoelectron spectrometer. Resulting characterization of FLG graphene is shown in **Figure 3.2**.

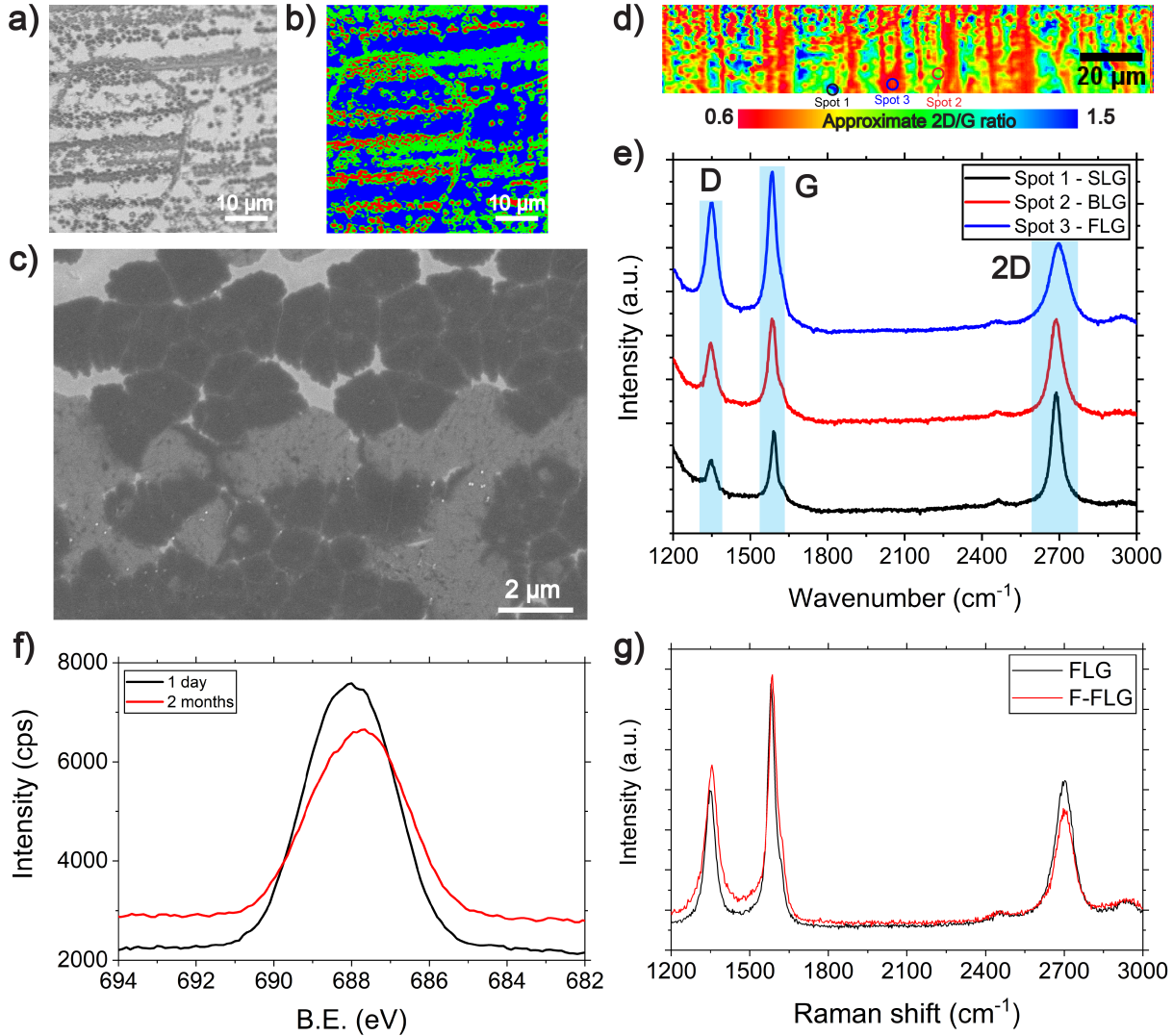


Figure 3.2: Characterization of FLG samples. (a) Transmittance micrograph of FLG on borosilicate coverslips obtained with 561 nm laser, and (b) corresponding layer number distribution map.  $\approx 48\%$  area is  $< 5$  layers. (c) SEM micrograph of FLG illustrating grain sizes  $\approx 1 \mu\text{m}$ . (d) Raman map illustrating approximate 2D/G ratios (calculated without baseline correction) across the sample, with (e) areas highlighting single layer graphene (SLG), bilayer graphene (BLG) and few layer graphene (FLG). D, 2D and G peak is illustrated in (e). (f) XPS F 1 s spectra of F-FLG after storage in Ar-glovebox for 1 day and 2 months. (g) Raman spectra comparing FLG and F-FLG.

**Figures 3.2b, 3.2d and 3.2e** illustrate heterogeneity in terms of grain sizes and layer numbers, leading to the presence of edge planes and grain boundaries in the FLG structure. The presence of edge planes and grain boundaries is critical for the electrochemical

intercalation experiments. This is because, ion intercalation primarily occurs through edge planes, as demonstrated in earlier work for similar graphitic carbon films.[29] XPS spectra confirm the fluorination of FLG (**Figure 3.2f**), with the trend of decreased Raman 2D peak intensity and increased D peak intensity (**Figure 3.2g**) agreeing with those observed in literature for the fluorination of graphene materials.[27, 28, 34]

### 3.1.4 Electrochemical methods

Cyclic voltammetry and galvanostatic cycling were performed in a VTI glovebox ( $O_2, H_2O < 1 \text{ ppm}$ ) using a CHI 760E potentiostat. The graphene electrodes were assembled in an open Teflon cell with Viton o-rings to isolate a 3 mm region ( $\approx 7.1 \text{ mm}^2$  area) and flooded with  $\approx 1 \text{ ml}$  of electrolyte for measurements. 0.1 M LiBF<sub>4</sub> in 1:1 PC-EC (propylene carbonate:ethylene carbonate, by vol, henceforth referred as Li electrolyte solution) was used to form the Li-SEI on FLG electrodes. For Na<sup>+</sup> intercalation experiments we used 0.1 M NaPF<sub>6</sub> in 1:1 PC-EC (by vol., henceforth referred as Na electrolyte solution). The choice of 0.1 M LiBF<sub>4</sub> was made on the basis of previous work in our group,[29–31] which highlights stable cyclability and SEI formation capabilities of the electrolyte. To maintain concentration comparisons, we subsequently chose 0.1M NaPF<sub>6</sub> for investigating Na<sup>+</sup> intercalation. All measurements were performed with a polypyrrole quasi-reference[35, 36] (PPyQRE) given Na-metal references can interfere in electrochemical measurements,[37] and 0.5 mm diameter Pt wire as counter electrode. The PPyQRE reference potential was calibrated to ferrocene (Fc/Fc<sup>+</sup>) externally, using the same solution as that used in the experiment (albeit with the addition of  $\approx 1 \text{ mM}$  Fc). Ion-sensitive SECM measurements used a CHI-920D bipotentiostat, with an Ag wire as quasi-reference, and Pt wire as counter electrode. Potentials were calibrated internally and reported vs ferrocene. Potentials in the in situ Raman measurements were calibrated by adding ferrocene internally, after all Raman measurements were completed. All electrochemical measurements on graphene inside a glovebox were replicated across multiple samples to ensure reproducibility. In situ Raman

measurements were performed at two spots within a single experiment using a Horiba LabRAM HR 3D spectrometer, with a 532 nm laser operating at a power level of  $\approx$ 1.5 mW. Spectra were collected with 3 s exposure, with an average of 3 scans measured. These conditions translate to acquisition of Raman spectra every 75 mV during in situ Raman experiments coupled with CV.

### 3.1.5 Fabrication of Hg probes for ion-sensitive SECM

Sphercapped Hg-UMEs (HgSC, **Figure S.A.3**) were prepared following previous work.<sup>[38, 39]</sup> 25  $\mu$ m diameter Pt UMEs were sharpened, polished and etched while sonicating in a saturated CaCl<sub>2</sub>/HCl solution by applying an AC waveform with a peak-to-peak voltage of 2.7 V using a Variac transformer and a graphite counter electrode. Probes were etched for 30 s followed by sonication in DI water. Hg was electrodeposited at 0 V vs Ag/AgCl from a 10 mM solution of Hg(NO<sub>3</sub>)<sub>2</sub> · 6 H<sub>2</sub>O with 0.1 M KNO<sub>3</sub> supporting electrolyte.

### 3.1.6 X-ray photoelectron spectroscopy (XPS)

Prior to XPS analysis, samples were dried inside the box, followed by rinsing with IPA and drying in air. The XPS measurements were performed with a Kratos Axis Ultra electron spectrometer, using monochromated Al K $\alpha$  radiation (1486.6 eV). Survey spectra were recorded at energy resolution of 1 eV, pass energy 160 eV and high-resolution spectra for individual elements recorded at 0.1 eV, pass energy 40 eV. The area interrogated was 0.3 mm  $\times$  0.7 mm. All spectra were calibrated to 284.4 eV C–C peak for graphite, and peak fitting was performed using CasaXPS v2.3.22. Voigt peaks of a Gaussian/Lorentzian product form with 30% Lorentzian mix factor (GL 30) was used as the line shape for the peak fitting, along with Shirley background. The C–C peak was fit with a GL30 peak shape modified with an asymmetric tail function A(0.5, 0.15, 0) in CasaXPS software.

### 3.1.7 Computational details

We performed geometry optimizations and Raman frequency calculations on FLG structures of varying intercalation stages with and without a fluorine-attached surface modifier. Each structure was treated as a slab, that is, a large vacuum of  $\approx 500$  Å was included to prevent interactions between adjacent unit cells. We performed the quantum calculations at the hybrid density functional theory (DFT) level, as implemented in the CRYSTAL17 code.[40, 41] CRYSTAL17 implements hybrid DFT using atom-centered Gaussian-type functions. These functions solve Hartree-Fock terms efficiently and enable quick computation of hybrid DFT density. Note that the Gaussian-type functions also permitted our large spacing between slabs which is different than codes using plane-waves as basis sets. Our calculations approximated the exchange-correlation with the Becke, 3-parameter, Lee-Yang-Parr (B3LYP)[42] functional. We included spin-polarization effects (unrestricted) and DFT-D3[43] corrections with Becke-Jonson damping[44] to account for dispersive interactions. We represented the orbitals of carbon, fluorine, and sodium with Gaussian basis sets with triple-zeta valence quality.[45] Self-consistent field (SCF) convergence was accelerated with the direct inversion of invariant subspace (DIIS),[46, 47] otherwise known as Pulay mixing, which constructs charge density from a linear combination of previous charge densities. The reciprocal space for all the structures was sampled by a  $\tau$ -centered Monkhorst-Pack scheme with a resolution of around  $2\pi \times 1/60$  Å<sup>-1</sup> ( $a.k_a = 40\text{-}60$ ,  $b.k_b = 40\text{-}60$ ,  $k_c = 1$ ). We initially optimized geometry with one set of convergence criteria and then used stricter criteria during frequency calculations. Vibrational modes are calculated using second derivatives of density, so they depend sensitively upon the potential energy surface and hence demand increased stringency. These stricter frequency calculation criteria included an SCF energy convergence criterion of  $2.72 \times 10^{-10}$  eV, an RMS force criterion of  $1.54 \times 10^{-3}$  eV Å<sup>-1</sup>, a max force criterion of  $2.31 \times 10^{-3}$  eV Å<sup>-1</sup>, an RMS displacement of  $6.35 \times 10^{-5}$  Å, a max displacement criterion of  $9.53 \times 10^{-5}$  Å and a between-geometry energy convergence criterion of  $2.72 \times 10^{-9}$  Å. We optimized both atomic

positions and unit cell parameters during frequency calculations.

### 3.2 Results and discussion

First, we utilized CV to characterize the Li<sup>+</sup> intercalation characteristics of F-FLG anodes. **Figure 3.3a** reveals that Li<sup>+</sup> (de)intercalation follows a well characterized staging mechanism displaying multiple peaks, and its behavior is similar to those reported in few and multi-layer graphene samples.[29–31] With the knowledge that the F-FLG is a suitable Li<sup>+</sup> intercalation host, we attempted Na<sup>+</sup> intercalation via CV at 1 mV s<sup>-1</sup>, as shown in **Figure 3.3b** in a solution of 0.1 M NaPF<sub>6</sub> dissolved in 1:1 PC-EC. All potentials were calibrated to the ferrocene redox couple unless stated otherwise. The first CV cycle revealed irreversible peaks between -1 to -2 V and beyond -2.5 V, likely associated with solid electrolyte interphase (SEI) formation processes. Further cycling in a shorter potential window reduces the current intensities at -1.25 V (**Figure A.4**), indicating that the resulting interphases are passivating in nature. Once the currents decreased by an order of magnitude, CV in an extended potential window did not reveal reversible intercalation signatures, despite what was reported previously in our simulations.[24] SEM and XPS characterization on the resulting interphase structures revealed a dense layer of inorganic species on the surface of F-FLG, primarily attributed to the formation of NaF (**Figure A.5**).

These observations imply that despite the calculations predicting thermodynamic stability of Na<sup>+</sup> intercalated graphene structures, the kinetics of the electrochemical intercalation process may be critical in achieving reversible intercalation. A similar observation was made for K<sup>+</sup> intercalation in FLG, wherein our group reported that a preformed Li-based SEI drastically improved K<sup>+</sup> intercalation kinetics.[31] Therefore, we hypothesized that the Na<sup>+</sup> intercalation may be impeded due to the properties of the SEI being formed on the F-FLG in Na-electrolyte. Subsequently, we explored Na<sup>+</sup> intercalation behavior in F-FLG samples with a preformed Li-based SEI.

For these measurements, we started with a F-FLG sample assembled in an open cell flooded with Li electrolyte. Li-based SEIs were formed by cycling the electrode in three different potential windows consecutively, as shown in **Figure A.6**. Subsequently, the Li-electrolyte was taken out, and the cell was rinsed 8 times with PC. We also soaked the cell in PC for 15 min to remove any residual salt from o-rings in the last two steps. Prior to cycling in NaPF<sub>6</sub> electrolyte, we cycled the electrode in 10 mM TkDAPF<sub>6</sub>, which lacks an alkali ion to intercalate, to rule out the presence of active Li<sup>+</sup> in the solution or in the SEI which could intercalate into FLG, as shown in **Figure A.7**. With these procedures, CVs in Na electrolyte, illustrated in **Figure 3.3c**, displayed two reversible but broad peaks (i) and (ii). These peaks, which were observed at a significantly different potential compared to Li<sup>+</sup> intercalation strongly suggest a reversible electrochemical process taking place. No such reversible peaks were observed when cycling pristine F-FLG samples in Na-electrolyte (**Figure A.8**). The baseline-corrected discharge capacity for F-FLG anode (**Figure 3.3c**), corresponding to peak (i) and (ii) was calculated to be 55 µC (between -1.75 and -0.75 V) and 72 µC (between -2.75 and -1.75 V) respectively. Repeat experiments on other F-FLG samples revealed that peak (i) is not always observable, and therefore, we consider the discharge capacity to be 72 µC, assuming that this value corresponds to reversible intercalation, as discussed below. For correlation to subsequent experiments, we have marked the potential regime (-1.75 to -3.0 V) associated with this reversible charge storage process with a red dashed box.

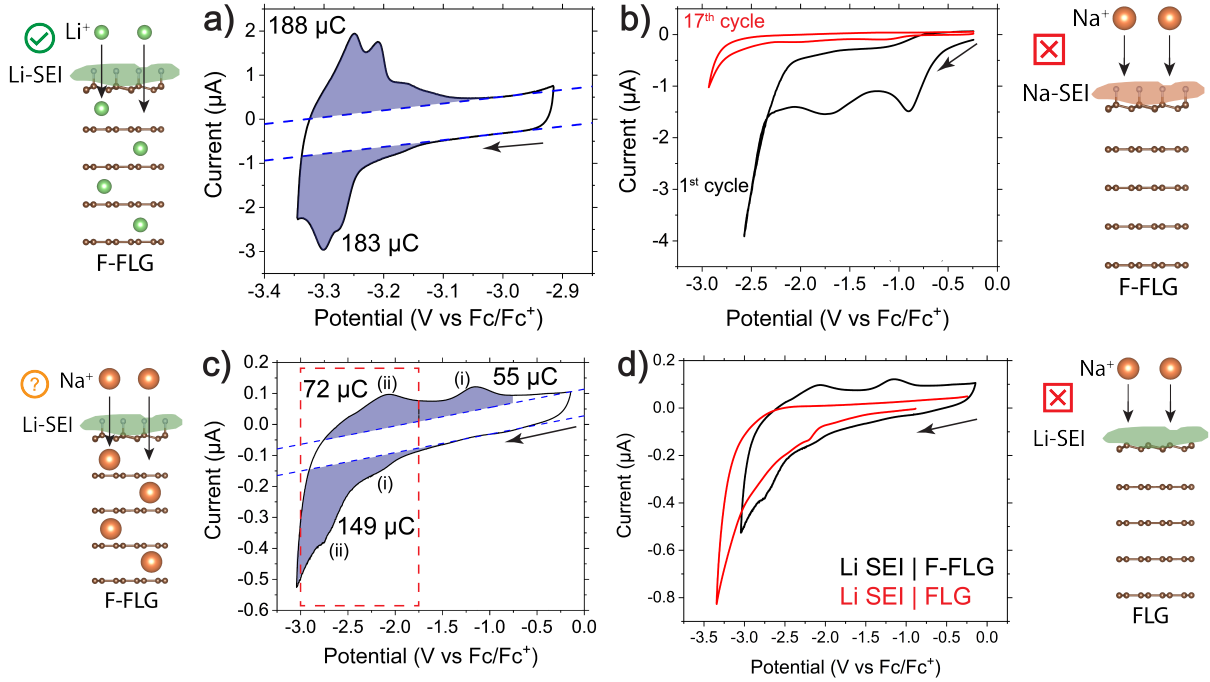


Figure 3.3: CV of F-FLG samples under different conditions, along with interpretations depicted by adjacent schemes. (a) Cycling F-FLG in 0.1 M LiBF<sub>4</sub> revealing clear staging peaks associated with Li<sup>+</sup> (de)intercalation. (b) Cycling F-FLG in 0.1 M NaPF<sub>6</sub> reveals no reversible peaks. (c) Cycling F-FLG with preformed Li-SEI (formed by CV, refer **Figure A.6**) in Na-electrolyte reveals reversible peaks, marked as i, ii. The red box highlights the potential regime associated with peak ii, which will be discussed later. (d) Comparison between F-FLG and FLG samples with preformed Li SEI, cycled in Na-electrolyte. All CVs at 1 mV s<sup>-1</sup>,  $\approx 7.1$  mm<sup>2</sup> electrode area.

The discharge capacity of Li<sup>+</sup> in this sample was observed to be 188 µC (**Figure 3.3a**),  $\approx 3$  times more than the Na<sup>+</sup> capacity. Assuming this charge capacity corresponds to LiC<sub>6</sub>,<sup>[31]</sup> the equivalent Na<sup>+</sup> stoichiometry is around NaC<sub>14</sub>. This Na-intercalated stoichiometry corresponds to a gravimetric capacity 159 mAh g<sup>-1</sup>. Repeat measurements on other F-FLG samples with galvanostatic cycling yielded discharge capacities of 150 and 50 µC in 0.1 M LiBF<sub>4</sub> and NaPF<sub>6</sub> respectively, shown in **Figure A.9**. The resulting equivalent stoichiometry is  $\approx$ NaC<sub>18</sub>, consistent with the CV charge capacity calculations. Therefore, reversible charge storage is confirmed to be taking place at stoichiometries far exceeding the previously reported value of NaC<sub>186</sub><sup>[21]</sup> in graphitic electrodes. The stoichiometry reported

in our work also exceeds the reported values of  $\text{NaC}_{64-96}$  for chemically intercalated  $\text{Na}^+$  in carbon.[48, 49] However, from this data it is difficult to discern if the charge storage follows a staging-type intercalation mechanisms or other processes such as adsorption (known to occur with  $\text{Na}^+$  charge storage in other carbon structures such as hard carbon).[50, 51]

We verified that these reversible peaks were not observable in nonfluorinated FLG anodes with a preformed Li-based SEI, as shown in **Figure 3.3d**. These observations indicate both fluorination and preformed Li-based SEIs are integral for reversible  $\text{Na}^+$  charge storage to take place. Interestingly, the use of fluorinated additives such as fluoroethylene carbonate in conjunction with  $\text{NaPF}_6$  salts have been reported to improve cycling performance and SEI characteristics with hard carbon anodes.[52, 53] These observations indicate the presence of kinetic barriers towards  $\text{Na}^+$  charge storage can be overcome with fluorinated interphases. While our CV and galvanostatic (dis)charge measurements indicate electrochemically reversible processes taking place, there is no direct evidence of this phenomenon being associated with  $\text{Na}^+$  intercalation. To first prove the participation of  $\text{Na}^+$  in this process, we utilized ion-sensitive SECM measurements.

Ion-sensitive SECM measurements performed in this study utilized Hg sphere-capped UME tips (HgSCs) positioned  $\approx 6 \mu\text{m}$  from F-FLG, subsequently referred as the substrate (**Figure A.8**).  $\text{Na}^+$  uptake and release from the substrate was tracked through stripping at the HgSC tip via SECM redox competition mode.[54–56] A recently developed chronoamperometric pulsing protocol[56, 57] was applied at the tip to track  $\text{Na}^+$  fluxes while preventing Hg oversaturation.[56] An ideal amalgamation/stripping response of  $\text{Na}^+$  with HgSCs is shown in **Figure 3.4a**, with the oversaturated response presented inset. Elaborating on this method, we first utilized tip CVs to locate amalgamation and stripping of  $\text{Na}^+$  at -1.8 V and -1.0 V vs Ag wire quasireference (QRE) (**Figure 3.4a** inset). Subsequently, we performed a double chronoamperometric measurement (consisting of 30 amalgamation and stripping pulses each of 0.05 s to prevent oversaturation) while varying

the substrate's potential in steps of 50 mV. The local concentration of  $\text{Na}^+$  is indirectly indicated by the average stripping charge, and fluxes are indicated by changes in the stripping charge at different substrate potentials. **Figure 3.4b** highlights the integrated region from the stripping pulses, which are averaged across the 30 pulses (**Figure A.11**).

Ion-sensitive SECM data in **Figure 3.4c** highlighted a clear uptake and release of  $\text{Na}^+$  at a potential window between -2 and -3.2 V. This reversible flux correlates well with the electrochemical process associated with peak (ii) in **Figure 3.3c**, confirming the involvement of  $\text{Na}^+$  in charge storage. Interestingly, we note that there is a minor deviation ( $\approx 0.02 \text{ nC}$ ) from the baseline charge values at -1.5 V to -1.0 V (**Figure 3.4c**), indicating a low flux of  $\text{Na}^+$  being consumed by the substrate. This electrochemical activity corresponds to peak (i) indicated in **Figure 3.3c**, highlighting its association with  $\text{Na}^+$ .

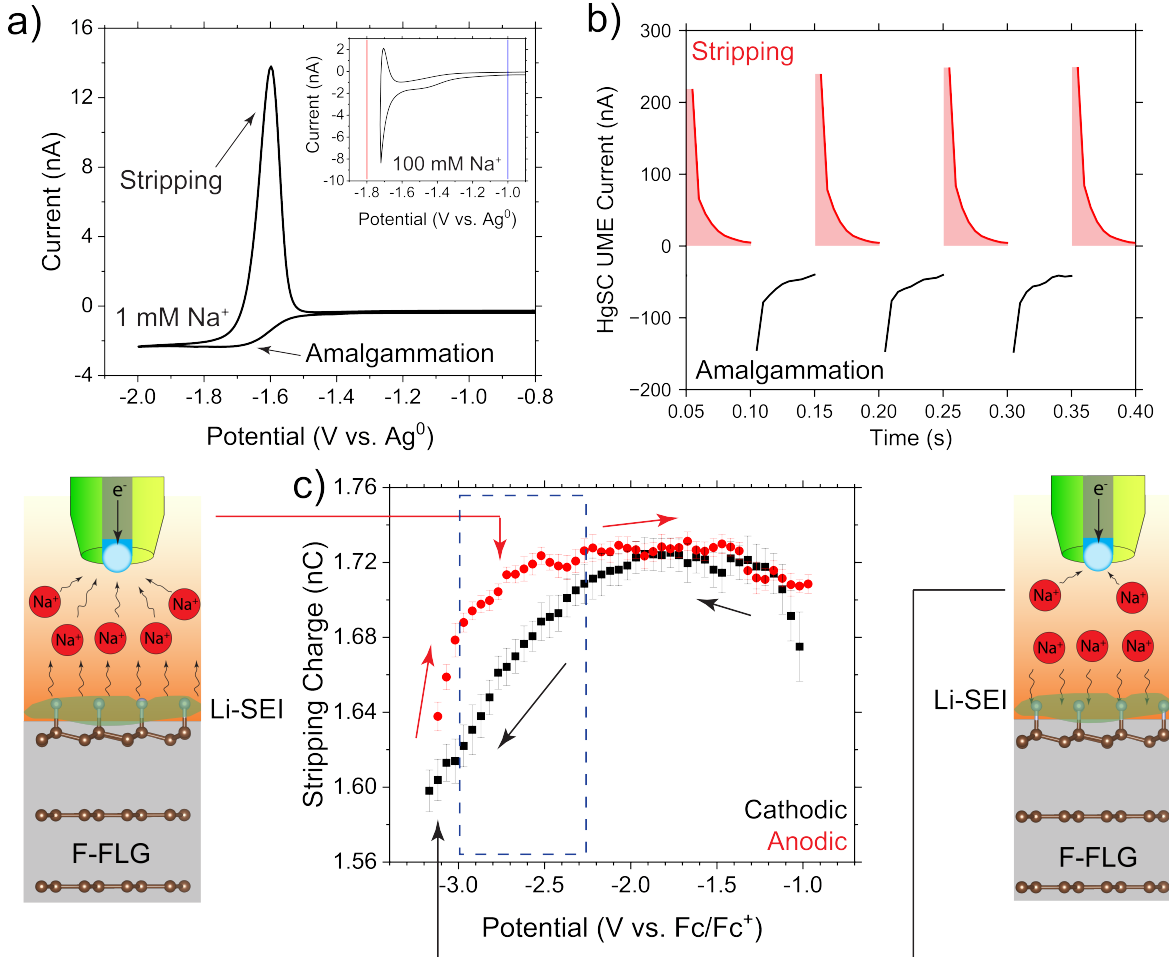


Figure 3.4: Ion-sensitive scanning electrochemical microscopy for tracking Na<sup>+</sup> fluxes. (a) Amalgamation and stripping behavior of HgSC in dilute 1 mM Na<sup>+</sup> concentrations, with inset revealing HgSC response at 100 mM Na<sup>+</sup> concentration. Identification of amalgamation (red line) and stripping potentials (blue line) for chronoamperometric measurement is shown in the inset Figure. (b) Initial chronoamperometric pulses at a fixed substrate potential illustrating calculation of stripping charge (shaded region), with full chronoamperometric data shown in **Figure A.11**. (c) Variation of Na<sup>+</sup> stripping charge from the HgSC as a function of potential applied at the F-FLG substrate. The schematics show how stripping charge decreases/increases depending on Na<sup>+</sup> being drawn in and out of F-FLG. The blue box highlights the potential regime associated with charge storage process, same as the red box in **Figure 3.3c**. All SECM measurements were performed with a F-FLG electrode with a preconditioned Li-based SEI in 0.1 M NaPF<sub>6</sub> in PC:EC. Fc/Fc<sup>+</sup> was used as an internal standard for the reference potential.

CV and SECM measurements suggest reversible Na<sup>+</sup> charge storage to be taking place in F-FLG, but a structurally-sensitive technique is required to discern between

intercalation and adsorption. Therefore, we resorted to in situ Raman spectroscopy which indicates structural distortion of the host based on the vibrational D and G modes of FLG.[31, 58] Experiments with Raman spectroscopy are challenging given that commercial devices (such as the EL-CELL[51]) typically does not allow solution rinsing, therefore, preforming a Li-based SEI on F-FLG followed by cycling in Na-electrolyte is considerably difficult. Additional difficulties arise in controlling potentials as the ELCel utilizes a two-electrode setup, making correlation to our three-electrode analytical experiments a challenge. Therefore, we constructed a sealed teflon cell in-house, equipped for performing three-electrode measurements with a bare PPyQRE reference and Pt counter electrode (**Figure A.12, A.13** shows schematics and pictures of the in situ cell respectively). This setup enabled the formation of a Li-based SEI, followed by subsequent cycling in Na electrolyte. Raman data shown in **Figure 3.5** was obtained from the back-side of the F-FLG electrode. This is a unique feature of our ultra-thin electrodes, which enable the Raman investigation without having to go directly through the electrolyte or the SEI. CVs from cycling the sealed Raman cell inside a glovebox was observed to be slightly different from those obtained outside (**Figure A.14**), likely due to some air and/or moisture intrusion. Nevertheless, the voltammograms in **Figure A.14** possessed an anodic peak between -2.7 to -2.0 V, matching the observations in **Figure 3.3c**. Subsequently, we analyzed the spectra collected in the experiment, after post processing to remove baselines and perform peak fits, using a Python script (details in **Figure A.15**).

The heat map in Figure 3.5a illustrates the evolution in Raman D and G bands of F-FLG during the cathodic sweep in CV. An increase in peak widths of the D and G peaks is clearly observed, starting from -1.7 V, (**Figure A.16**) which is an indicator of ion-intercalation processes.[51] However, we did not observe any change in the G peak position, contrary to what is reported during  $\text{Li}^+$  intercalation at FLG and  $\text{Na}^+$  intercalation in hard carbon.[31, 51] Therefore, to interpret the in situ Raman results, we turned to simulations of the D and G Raman modes, shown in **Figure 3.5b**. We observed that

complete intercalation of  $\text{Na}^+$  in fluorinated four-layer graphene does lead to the G peaks shifting to lower wavenumbers. This observation is in agreement with simulations in our previous work[31] with  $\text{Li}^+$  and  $\text{K}^+$  intercalation on FLG predicted a  $\approx 100 \text{ cm}^{-1}$  blueshift for the G peak, with experimental observations confirming this effect with a  $\approx 70 \text{ cm}^{-1}$  shift during the formation of stage 1 intercalated structures. Thus, we are aware that the extent of blueshift suggested by **Figure 3.5b** for the intercalated structures with high occupancy is possible. However, our voltammetry data in **Figure 3.3** highlighted that a Stage 0 intercalated structure ( $\text{NaC}_6$ ) was never attained, instead  $\text{NaC}_{14-18}$  stoichiometries ( $\approx 3$  times lesser  $\text{Na}^+$  content) were observed in F-FLG. Therefore, it is plausible that dilute intercalation structures (analogous to Stage 3) formed, whose Raman bands are presented in **Figure 3.5b**, and we could not verify if the predicted  $\approx 100 \text{ cm}^{-1}$  blueshift will take place owing to  $\text{NaC}_6$  type structures forming in F-FLG. These Raman peaks revealed no shift in the G peak position, rather additional peaks in the  $1500-1600 \text{ cm}^{-1}$  region were predicted, which will result in G peak broadening, consistent with our experimental data in **Figures 3.5a** and **3.5c**. The experimental data also shows the D peak slightly moving towards higher wavenumbers (**Figure A.17**), as observed in the simulation in **Figure 3.5b**. Additionally, the experimental observation of D peak broadening and some signal intensity in the  $1480-1520 \text{ cm}^{-1}$  region between -2.1 to -2.8 V, matched simulations of Raman peaks from a different Stage 3 structure (**Figure A.18**). SEI species do not show up in these in situ Raman experiments, as shown in **Figure A.19**. These correlations of our experiment with simulated structures provided strong evidence that a  $\text{Na}^+$  intercalation process is taking place in the F-FLG anode.

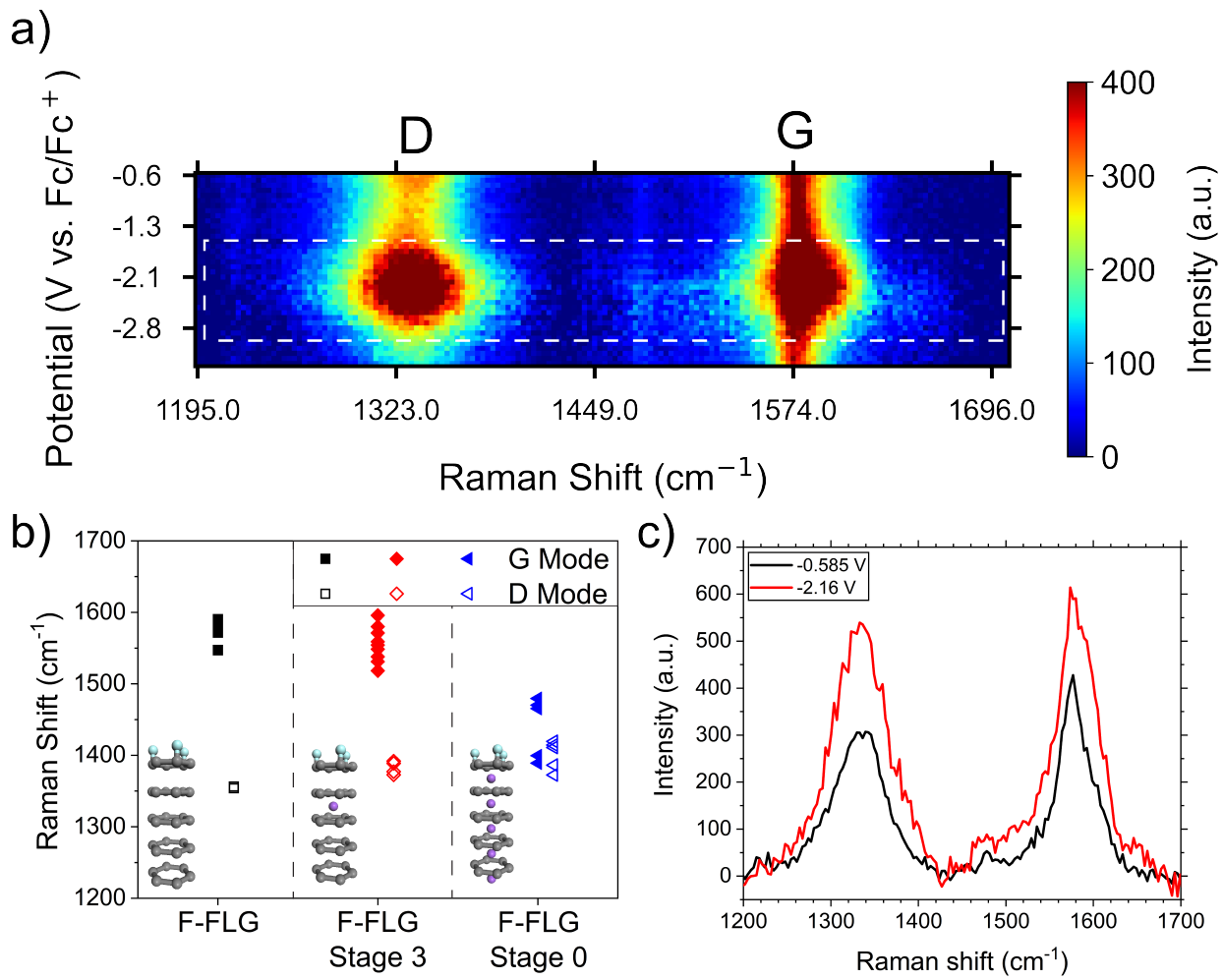


Figure 3.5: In situ Raman spectroscopic measurements of  $\text{Na}^+$  intercalation. (a) Heat map of Raman intensities illustrating changes in D and G peaks during CV in the cathodic sweep, with white box depicting potential regime associated with charge storage process. (b) Summary of vibrational modes in Raman for the different structures shown inset. (c) Raman spectra at the beginning of the CV (-0.585 V vs  $\text{Fc}/\text{Fc}^+$ ) and at -2.16 V vs  $\text{Fc}/\text{Fc}^+$ .

In situ Raman data in the anodic sweep (**Figure A.20a**) revealed a decrease in the G and D peak intensities, followed by a subsequent increase. While reasons behind this asymmetric behavior during cycling are unclear, we observed that the G peak position did not return to original values (**Figure A.20b**) over the course of the CV. This observation indicates that there are structural changes taking place in F-FLG during cycling in  $\text{Na}^+$  electrolyte. Additionally, in a separate control experiment, we observed significant loss of  $\text{Li}^+$  intercalation capacity after cycling an F-FLG electrode with preformed SEI in  $\text{Na}^+$

electrolyte (**Figure A.21**), indirectly adding evidence that the graphene structure changes during the  $\text{Na}^+$  intercalation. In summary, our measurements with CV, ion-sensitive SECM and in situ Raman spectroscopy provide collective evidence of  $\text{Na}^+$  intercalation taking place in F-FLG structures. These experimental observations therefore indicate that our earlier theoretical calculations have practical basis, and surface functionalization may enable  $\text{Na}^+$  intercalation by tailoring interactions between guest and host species. In addition, it has been reported previously that fluorination via  $\text{XeF}_2$  can expand the interlayer spacing of graphene layers,[59] which is something that we have observed through simulations (**Figure A.22**), albeit to a slight extent. Any expansion in interlayer spacing may influence  $\text{Na}^+$  intercalation, as illustrated in other work with Janus graphene structures.[60]

Finally, we utilized ex situ XPS and SEM to characterize the composition and morphology of the interphases formed on FLG and F-FLG with preformed Li-SEI. The F-FLG sample exhibits similar C 1 s intensities compared to FLG, but markedly different F 1 s and O 1 s signals after cycling in Na-electrolyte, as shown in **Figure 3.6a**. To understand the evolution of fluorinated phases in F-FLG, we performed peak fitting of the F 1 s signals on pristine and cycled samples, as shown in **Figures 3.6b** and **3.6c**. Peak fitting of the F 1 s signals indicates LiF formation after cycling at 684.7 eV, along with contributions from fluorinated carbon species at 687.8 eV. However, the peak at 687.1 eV likely comprises of contributions from B-F species present in the SEI, that have been observed previously on graphene anodes at binding energies slightly lesser than 687 eV.[56]

Comparing fluorinated species on cycled FLG and F-FLG anodes revealed that both SEIs comprised of LiF species; C-F and/or B-F maybe present in the FLG anodes (**Figure A.23**). The O 1 s spectra in Fig. S30 shows signals from  $\text{Li}_2\text{CO}_3$  (confirmed by C 1 s and Li 1 s spectra, **Figures A.25, A.26**), which was not observed in the SEI on FLG sample. However, given the ex situ nature of the measurement, it is plausible that the carbonates arose due to air exposure. The XPS also revealed the thin nature of the SEI,

with signals from underlying  $\text{SiO}_2$  visible (**Figure A.27**). While the true composition of the SEI interphases cannot be discerned from ex situ XPS, the differences in fluorinated content between the F-FLG and FLG samples are unambiguous. This observation ties well with a general trend of fluorinated interphases being beneficial for LIB and NIB anodes.[61, 62]

SEM micrographs in **Figures 3.6d, e** confirmed the thin nature of the SEIs formed, with underlying graphene being observable through the interphases on both FLG and F-FLG anodes. The F-FLG anode exhibits interphases composed of sub-micron particulates, whereas the FLG anode revealed well-defined, scattered, solid structures  $>1 \mu\text{m}$  in size. These particles maybe arising from artifacts given the ex situ nature of the measurement. In contrast to the thick SEI formed with  $\text{NaPF}_6$  on F-FLG with no preformed Li-based SEI (**Figure A.4**), both the Li-SEI modified FLG and F-FLG electrodes show no dense deposits. XPS shows little incorporation of Na (**Figure A.28**) inside the F-FLG interphase, likely due to the dissolution of Na-SEI components during rinsing, as reported in literature.[8, 63–65] Overall, the data in **Figure 3.6** shows that SEI is present in all surfaces that underwent cycling, whether fluorinated or not, as SEI formation takes place before intercalation. At present we cannot distinguish if there are domains with different SEI coverage and compositions. Despite these caveats, XPS and SEM data indicated that changes in the SEI composition likely played a role in achieving reversible  $\text{Na}^+$  intercalation on F-FLG.

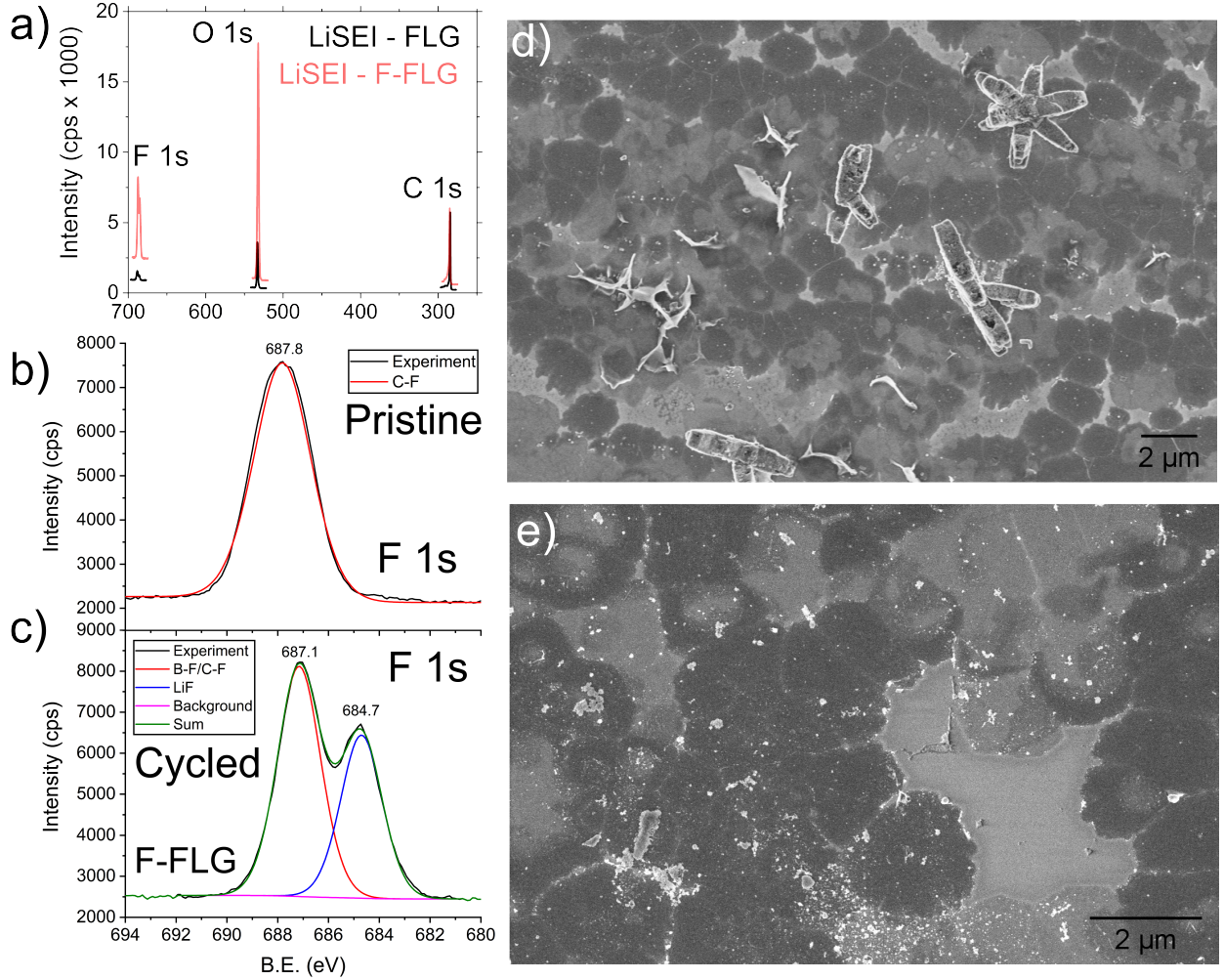


Figure 3.6: XPS and SEM characterization of SEIs formed on FLG and F-FLG. (a) Survey spectra showing the comparison of intensities from XPS C 1 s, O 1 s and F 1 s signals. Peak fitting of F 1 s spectra for (b) pristine and (c) cycled F-FLG samples. (d) and (e) SEM micrographs of Li-based SEI on FLG and F-FLG respectively.

### 3.3 Conclusions

Our measurements with F-FLG conclusively revealed the critical role that surface modification and subsequent interphase formation have in enabling reversible intercalation of  $\text{Na}^+$  in graphitic materials. Ion-sensitive SECM was able to confirm the participation of  $\text{Na}^+$  in charge storage, and in situ Raman measurements indicated a Stage-3 type intercalation structure forming during cycling. While simulations revealed  $\text{Na}^+$  intercalated four-layer fluorinated graphene structures were thermodynamically favorable, our electrochemical

experiments and in situ and ex situ characterization revealed that the interphase formed on F-FLG in Na electrolyte was not sufficient for  $\text{Na}^+$  intercalation in the graphitic host. Instead, a preformed Li-based SEI on F-FLG was required for attaining reversible intercalation. Since fluorination of FLG was necessary to observe  $\text{Na}^+$  intercalation, our results revealed the dual role that fluorination may exhibit towards this process, either for improving SEI properties for  $\text{Na}^+$  ion transfer and for stabilizing the intercalated structure. In summary, our approach using FLG electrodes shows promise as a platform for investigating intercalation processes for beyond Li-ion type systems. We also highlight surface modification as a potential strategy for enabling charge storage in thermodynamically unfavorable systems. These strategies may hold relevance in energy storage devices such as supercapacitors or batteries with thin film, nanostructured, or nanoparticle electrodes. Future work is required in the domain of materials engineering for evaluating the surface modifier approach in graphitic carbon materials with greater intercalation capacity for applications in technologically relevant devices.

### Bibliography for Chapter 3

- (1) Trahey, L. et al. *Proceedings of the National Academy of Sciences* **2020**, *117*, 12550–12557, DOI: [10.1073/pnas.1821672117](https://doi.org/10.1073/pnas.1821672117).
- (2) Xu, C.; Dai, Q.; Gaines, L.; Hu, M.; Tukker, A.; Steubing, B. *Communications Materials* **2020**, *1*, 1–10, DOI: [10.1038/s43246-020-00095-x](https://doi.org/10.1038/s43246-020-00095-x).
- (3) Weil, M.; Ziemann, S.; Peters, J. In *Behaviour of Lithium-Ion Batteries in Electric Vehicles: Battery Health, Performance, Safety, and Cost*, Pistoia, G., Liaw, B., Eds.; Springer International Publishing: Cham, 2018, pp 59–74, DOI: [10.1007/978-3-319-69950-9\\_3](https://doi.org/10.1007/978-3-319-69950-9_3).
- (4) Chayambuka, K.; Mulder, G.; Danilov, D. L.; Notten, P. H. L. *Advanced Energy Materials* **2020**, *10*, 2001310, DOI: [10.1002/aenm.202001310](https://doi.org/10.1002/aenm.202001310).
- (5) Mann, M. K.; Mayyas, A. T.; Steward, D. M. **2019**, DOI: <https://www.osti.gov/biblio/1529215>.
- (6) Hu, Y.-S.; Lu, Y. *ACS Energy Letters* **2019**, *4*, 2689–2690, DOI: [10.1021/acsenergylett.9b02190](https://doi.org/10.1021/acsenergylett.9b02190).
- (7) Kubota, K.; Dahbi, M.; Hosaka, T.; Kumakura, S.; Komaba, S. *The Chemical Record* **2018**, *18*, 459–479, DOI: [10.1002/tcr.201700057](https://doi.org/10.1002/tcr.201700057).

- (8) Yabuuchi, N.; Kubota, K.; Dahbi, M.; Komaba, S. *Chemical Reviews* **2014**, *114*, 11636–11682, DOI: [10.1021/cr500192f](https://doi.org/10.1021/cr500192f).
- (9) Abraham, K. M. *ACS Energy Letters* **2020**, *5*, 3544–3547, DOI: [10.1021/acsenergylett.0c02181](https://doi.org/10.1021/acsenergylett.0c02181).
- (10) *C&EN global enterprise*. **2022**, *100*, DOI: [10.1021/cen-10019-feature2](https://doi.org/10.1021/cen-10019-feature2).
- (11) Kubota, K.; Kumakura, S.; Yoda, Y.; Kuroki, K.; Komaba, S. *Advanced Energy Materials* **2018**, *8*, 1703415, DOI: [10.1002/aenm.201703415](https://doi.org/10.1002/aenm.201703415).
- (12) Patra, A.; Davis, J.; Pidaparthi, S.; Karigerasi, M. H.; Zahiri, B.; Kulkarni, A. A.; Caple, M. A.; Shoemaker, D. P.; Zuo, J. M.; Braun, P. V. *Proceedings of the National Academy of Sciences* **2021**, *118*, e2025044118, DOI: [10.1073/pnas.2025044118](https://doi.org/10.1073/pnas.2025044118).
- (13) Kundu, D.; Talaie, E.; Duffort, V.; Nazar, L. F. *Angewandte Chemie International Edition* **2015**, *54*, 3431–3448, DOI: [10.1002/anie.201410376](https://doi.org/10.1002/anie.201410376).
- (14) Komaba, S.; Murata, W.; Ishikawa, T.; Yabuuchi, N.; Ozeki, T.; Nakayama, T.; Ogata, A.; Gotoh, K.; Fujiwara, K. *Advanced Functional Materials* **2011**, *21*, 3859–3867, DOI: [10.1002/adfm.201100854](https://doi.org/10.1002/adfm.201100854).
- (15) Muñoz-Márquez, M. Á.; Saurel, D.; Gómez-Cámer, J. L.; Casas-Cabanas, M.; Castillo-Martínez, E.; Rojo, T. *Advanced Energy Materials* **2017**, *7*, 1700463, DOI: [10.1002/aenm.201700463](https://doi.org/10.1002/aenm.201700463).
- (16) Stevens, D. A.; Dahn, J. R. *Journal of The Electrochemical Society* **2000**, *147*, 1271, DOI: [10.1149/1.1393348](https://doi.org/10.1149/1.1393348).
- (17) Kamiyama, A.; Kubota, K.; Nakano, T.; Fujimura, S.; Shiraishi, S.; Tsukada, H.; Komaba, S. *ACS Applied Energy Materials* **2020**, *3*, 135–140, DOI: [10.1021/acsaem.9b01972](https://doi.org/10.1021/acsaem.9b01972).
- (18) Eldesoky, A.; Bauer, M.; Azam, S.; Zsoldos, E.; Song, W.; Weber, R.; Hy, S.; Johnson, M. B.; Metzger, M.; Dahn, J. R. *Journal of The Electrochemical Society* **2021**, *168*, 110543, DOI: [10.1149/1945-7111/ac39fc](https://doi.org/10.1149/1945-7111/ac39fc).
- (19) Zhao, C.; Lu, Y.; Yue, J.; Pan, D.; Qi, Y.; Hu, Y.-S.; Chen, L. *Journal of Energy Chemistry* **2018**, *27*, 1584–1596, DOI: [10.1016/j.jechem.2018.03.004](https://doi.org/10.1016/j.jechem.2018.03.004).
- (20) Zhao, Y.; Adair, K. R.; Sun, X. *Energy & Environmental Science* **2018**, *11*, 2673–2695, DOI: [10.1039/C8EE01373J](https://doi.org/10.1039/C8EE01373J).
- (21) Stevens, D. A.; Dahn, J. R. *Journal of The Electrochemical Society* **2001**, *148*, A803, DOI: [10.1149/1.1379565](https://doi.org/10.1149/1.1379565).
- (22) Dahn, J. R.; Zheng, T.; Liu, Y.; Xue, J. S. *Science* **1995**, *270*, 590–593, DOI: [10.1126/science.270.5236.590](https://doi.org/10.1126/science.270.5236.590).
- (23) Fong, R.; von Sacken, U.; Dahn, J. R. *Journal of The Electrochemical Society* **1990**, *137*, 2009, DOI: [10.1149/1.2086855](https://doi.org/10.1149/1.2086855).
- (24) Nijamudheen, A.; Sarbapalli, D.; Hui, J.; Rodríguez-López, J.; Mendoza-Cortes, J. L. *ACS Applied Materials & Interfaces* **2020**, *12*, 19393–19401, DOI: [10.1021/acsami.9b23105](https://doi.org/10.1021/acsami.9b23105).

- (25) Moriwake, H.; Kuwabara, A.; Fisher, C. A. J.; Ikuhara, Y. *RSC Advances* **2017**, *7*, 36550–36554, DOI: [10.1039/C7RA06777A](https://doi.org/10.1039/C7RA06777A).
- (26) Yoon, G.; Kim, H.; Park, I.; Kang, K. *Advanced Energy Materials* **2017**, *7*, 1601519, DOI: [10.1002/aenm.201601519](https://doi.org/10.1002/aenm.201601519).
- (27) Son, J.; Buzov, N.; Chen, S.; Sung, D.; Ryu, H.; Kwon, J.; Kim, S.; Namiki, S.; Xu, J.; Hong, S.; Watanabe, K.; Taniguchi, T.; King, W. P.; Lee, G.-H.; van der Zande, A. M. *Advanced Materials* **2019**, *31*, 1903424, DOI: [10.1002/adma.201903424](https://doi.org/10.1002/adma.201903424).
- (28) Son, J.; Kwon, J.; Kim, S.; Lv, Y.; Yu, J.; Lee, J.-Y.; Ryu, H.; Watanabe, K.; Taniguchi, T.; Garrido-Menacho, R., et al. *Nature Communications* **2018**, *9*, 1–9, DOI: [10.1038/s41467-018-06524-3](https://doi.org/10.1038/s41467-018-06524-3).
- (29) Hui, J.; Burgess, M.; Zhang, J.; Rodríguez-López, J. *ACS Nano* **2016**, *10*, 4248–4257, DOI: [10.1021/acsnano.5b07692](https://doi.org/10.1021/acsnano.5b07692).
- (30) Hui, J.; Nijamudheen, A.; Sarbapalli, D.; Xia, C.; Qu, Z.; Mendoza-Cortes, J. L.; Rodríguez-López, J. *Chemical Science* **2021**, *12*, 559–568, DOI: [10.1039/DOSC03226C](https://doi.org/10.1039/DOSC03226C).
- (31) Hui, J.; Schorr, N. B.; Pakhira, S.; Qu, Z.; Mendoza-Cortes, J. L.; Rodríguez-López, J. *Journal of the American Chemical Society* **2018**, *140*, 13599–13603, DOI: [10.1021/jacs.8b08907](https://doi.org/10.1021/jacs.8b08907).
- (32) Wood, J. D.; Doidge, G. P.; Carrion, E. A.; Koepke, J. C.; Kaitz, J. A.; Datye, I.; Behnam, A.; Hewaparakrama, J.; Aruin, B.; Chen, Y.; Dong, H.; Haasch, R. T.; Lyding, J. W.; Pop, E. *Nanotechnology* **2015**, *26*, 055302, DOI: [10.1088/0957-4484/26/5/055302](https://doi.org/10.1088/0957-4484/26/5/055302).
- (33) Nair, R. R.; Blake, P.; Grigorenko, A. N.; Novoselov, K. S.; Booth, T. J.; Stauber, T.; Peres, N. M. R.; Geim, A. K. *Science* **2008**, *320*, 1308–1308, DOI: [10.1126/science.1156965](https://doi.org/10.1126/science.1156965).
- (34) Robinson, J. T.; Burgess, J. S.; Junkermeier, C. E.; Badescu, S. C.; Reinecke, T. L.; Perkins, F. K.; Zalalutdinov, M. K.; Baldwin, J. W.; Culbertson, J. C.; Sheehan, P. E.; Snow, E. S. *Nano Letters* **2010**, *10*, 3001–3005, DOI: [10.1021/nl101437p](https://doi.org/10.1021/nl101437p).
- (35) Ghilane, J.; Hapiot, P.; Bard, A. J. *Analytical Chemistry* **2006**, *78*, 6868–6872, DOI: [10.1021/ac060818o](https://doi.org/10.1021/ac060818o).
- (36) Sarbapalli, D.; Mishra, A.; Rodríguez-López, J. *Analytical Chemistry* **2021**, *93*, 14048–14052, DOI: [10.1021/acs.analchem.1c03552](https://doi.org/10.1021/acs.analchem.1c03552).
- (37) Dou, X.; Hasa, I.; Saurel, D.; Vaalma, C.; Wu, L.; Buchholz, D.; Bresser, D.; Komaba, S.; Passerini, S. *Materials Today* **2019**, *23*, 87–104, DOI: [10.1016/j.mattod.2018.12.040](https://doi.org/10.1016/j.mattod.2018.12.040).
- (38) Barton, Z. J.; Rodríguez-López, J. *Analytical Chemistry* **2014**, *86*, 10660–10667, DOI: [10.1021/ac502517b](https://doi.org/10.1021/ac502517b).
- (39) Barton, Z. J.; Rodríguez-López, J. *Analytical Chemistry* **2017**, *89*, 2708–2715, DOI: [10.1021/acs.analchem.6b04093](https://doi.org/10.1021/acs.analchem.6b04093).

- (40) Dovesi, R.; Saunders, V.; Roetti, C.; Orlando, R.; Zicovich-Wilson, C.; Pascale, F.; Civalleri, B.; Doll, K.; Harrison, N.; Bush, I., et al. **2014**, DOI: <http://www.crystal.unito.it>.
- (41) Dovesi, R.; Erba, A.; Orlando, R.; Zicovich-Wilson, C. M.; Civalleri, B.; Maschio, L.; Rérat, M.; Casassa, S.; Baima, J.; Salustro, S.; Kirtman, B. *WIREs Computational Molecular Science* **2018**, *8*, e1360, DOI: [10.1002/wcms.1360](https://doi.org/10.1002/wcms.1360).
- (42) Vosko, S. H.; Wilk, L.; Nusair, M. *Canadian Journal of Physics* **1980**, *58*, 1200–1211, DOI: [10.1139/p80-159](https://doi.org/10.1139/p80-159).
- (43) Grimme, S.; Antony, J.; Ehrlich, S.; Krieg, H. *The Journal of Chemical Physics* **2010**, *132*, 154104, DOI: [10.1063/1.3382344](https://doi.org/10.1063/1.3382344).
- (44) Grimme, S.; Ehrlich, S.; Goerigk, L. *Journal of Computational Chemistry* **2011**, *32*, 1456–1465, DOI: [10.1002/jcc.21759](https://doi.org/10.1002/jcc.21759).
- (45) Peintinger, M. F.; Oliveira, D. V.; Bredow, T. *Journal of Computational Chemistry* **2013**, *34*, 451–459, DOI: [10.1002/jcc.23153](https://doi.org/10.1002/jcc.23153).
- (46) Pulay, P. *Chemical Physics Letters* **1980**, *73*, 393–398, DOI: [10.1016/0009-2614\(80\)80396-4](https://doi.org/10.1016/0009-2614(80)80396-4).
- (47) Pulay, P. *Journal of Computational Chemistry* **1982**, *3*, 556–560, DOI: [10.1002/jcc.540030413](https://doi.org/10.1002/jcc.540030413).
- (48) Metrot, A.; Guerard, D.; Billaud, D.; Herold, A. *Synthetic Metals* **1980**, *1*, 363–369, DOI: [10.1016/0379-6779\(80\)90071-5](https://doi.org/10.1016/0379-6779(80)90071-5).
- (49) Sleppy, W. C. *Inorganic Chemistry* **1966**, *5*, 2021–2023, DOI: [10.1021/ic50045a038](https://doi.org/10.1021/ic50045a038).
- (50) Saurel, D.; Orayech, B.; Xiao, B.; Carriazo, D.; Li, X.; Rojo, T. *Advanced Energy Materials* **2018**, *8*, 1703268, DOI: [10.1002/aenm.201703268](https://doi.org/10.1002/aenm.201703268).
- (51) Weaving, J. S.; Lim, A.; Millichamp, J.; Neville, T. P.; Ledwoch, D.; Kendrick, E.; McMillan, P. F.; Shearing, P. R.; Howard, C. A.; Brett, D. J. L. *ACS Applied Energy Materials* **2020**, *3*, 7474–7484, DOI: [10.1021/acsaem.0c00867](https://doi.org/10.1021/acsaem.0c00867).
- (52) Bouibes, A.; Takenaka, N.; Fujie, T.; Kubota, K.; Komaba, S.; Nagaoka, M. *ACS Applied Materials & Interfaces* **2018**, *10*, 28525–28532, DOI: [10.1021/acsami.8b07530](https://doi.org/10.1021/acsami.8b07530).
- (53) Dahbi, M.; Nakano, T.; Yabuuchi, N.; Fujimura, S.; Chihara, K.; Kubota, K.; Son, J.-Y.; Cui, Y.-T.; Oji, H.; Komaba, S. *ChemElectroChem* **2016**, *3*, 1856–1867, DOI: [10.1002/celc.201600365](https://doi.org/10.1002/celc.201600365).
- (54) Gossage, Z. T.; Hui, J.; Sarbapalli, D.; Rodríguez-López, J. *Analyst* **2020**, *145*, 2631–2638, DOI: [10.1039/C9AN02637A](https://doi.org/10.1039/C9AN02637A).
- (55) Gossage, Z. T.; Hui, J.; Zeng, Y.; Flores-Zuleta, H.; Rodríguez-López, J. *Chemical Science* **2019**, *10*, 10749–10754, DOI: [10.1039/C9SC03569A](https://doi.org/10.1039/C9SC03569A).
- (56) Zeng, Y.; Gossage, Z. T.; Sarbapalli, D.; Hui, J.; Rodríguez-López, J. *ChemElectroChem* **2022**, *9*, e202101445, DOI: [10.1002/celc.202101445](https://doi.org/10.1002/celc.202101445).

- (57) Mishra, A.; Sarbapalli, D.; Hossain, M. S.; Gossage, Z. T.; Li, Z.; Urban, A.; Rodríguez-López, J. **2022**, *169*, 086501, DOI: [10.1149/1945-7111/ac857e](https://doi.org/10.1149/1945-7111/ac857e).
- (58) Zou, J.; Sole, C.; Drewett, N. E.; Velický, M.; Hardwick, L. J. *The Journal of Physical Chemistry Letters* **2016**, *7*, 4291–4296, DOI: [10.1021/acs.jpclett.6b01886](https://doi.org/10.1021/acs.jpclett.6b01886).
- (59) Son, J.; Ryu, H.; Kwon, J.; Huang, S.; Yu, J.; Xu, J.; Watanabe, K.; Taniguchi, T.; Ji, E.; Lee, S.; Shin, Y.; Kim, J. H.; Kim, K.; van der Zande, A. M.; Lee, G.-H. *Nano Letters* **2021**, *21*, 891–898, DOI: [10.1021/acs.nanolett.0c03237](https://doi.org/10.1021/acs.nanolett.0c03237).
- (60) Sun, J.; Sadd, M.; Edengborg, P.; Grönbeck, H.; Thiesen, P. H.; Xia, Z.; Quintano, V.; Qiu, R.; Matic, A.; Palermo, V. *Science Advances* **2021**, *7*, eabf0812, DOI: [10.1126/sciadv.abf0812](https://doi.org/10.1126/sciadv.abf0812).
- (61) Wang, C.; Meng, Y. S.; Xu, K. *Journal of The Electrochemical Society* **2018**, *166*, A5184, DOI: [10.1149/2.0281903jes](https://doi.org/10.1149/2.0281903jes).
- (62) Nimkar, A.; Shpigel, N.; Malchik, F.; Bublil, S.; Fan, T.; Penki, T. R.; Tsubery, M. N.; Aurbach, D. *ACS Applied Materials & Interfaces* **2021**, *13*, 46478–46487, DOI: [10.1021/acsami.1c03844](https://doi.org/10.1021/acsami.1c03844).
- (63) Ma, L. A.; Naylor, A. J.; Nyholm, L.; Younesi, R. *Angewandte Chemie International Edition* **2021**, *60*, 4855–4863, DOI: [10.1002/anie.202013803](https://doi.org/10.1002/anie.202013803).
- (64) Dahbi, M.; Yabuuchi, N.; Kubota, K.; Tokiwa, K.; Komaba, S. *Physical Chemistry Chemical Physics* **2014**, *16*, 15007–15028, DOI: [10.1039/C4CP00826J](https://doi.org/10.1039/C4CP00826J).
- (65) Song, J.; Xiao, B.; Lin, Y.; Xu, K.; Li, X. *Advanced Energy Materials* **2018**, *8*, 1703082, DOI: [10.1002/aenm.201703082](https://doi.org/10.1002/aenm.201703082).

# Chapter 4

## Tracking Passivation and Cation Flux at Incipient Solid-Electrolyte Interphases on Multi-Layer Graphene using High Resolution Scanning Electrochemical Microscopy

*This work has been published. Citation:* Yunxiong Zeng, Zachary T. Gossage, **Dipobrato Sarbapalli**, Jingshu Hui and Joaquín Rodríguez-López. “Tracking Passivation and Cation Flux at Incipient Solid-Electrolyte Interphases on Multi-Layer Graphene using High Resolution Scanning Electrochemical Microscopy” *ChemElectroChem* **2021**, *9*, e202101445. DOI: [10.1002/celc.202101445](https://doi.org/10.1002/celc.202101445)

*Credit statement:* Y.Z. and Z.T.G. performed SECM measurements. D.S. collected XPS spectra. Y.Z. and D.S. fabricated substrates. D.S. analyzed the SECM data with Python. Z.T.G. and D.S. performed all supplementary measurements. Z.T.G., D.S. wrote the manuscript under supervision of J.R-L. All authors reviewed the manuscript.

As the Li-ion battery market expands, there are notable concerns over the future supply and demand of Li raw materials.<sup>[1, 2]</sup> Emerging alternative chemistries, including sodium-ion and potassium-ion batteries, are drawing attention due to their competitive operating voltage, higher abundance, and more even global distribution.<sup>[1–6]</sup> However, replacing  $\text{Li}^+$  with another alkali metal cation is non-trivial because intercalation-type batteries involve complex chemistries at both electrodes and at their resulting interphases.<sup>[3, 7–13]</sup> Further, the most common anode for LIBs, based on graphitic carbon, only forms low-concentration, intercalation compounds (GICs) with  $\text{Na}^+$ ,<sup>[11, 14]</sup> and likewise, shows poor cyclability in  $\text{K}^+$  electrolytes.<sup>[13, 15, 16]</sup> The formation of a stable solid-electrolyte interphase (SEI) on graphite and most other anodes is essential for long-term durability in LIBs,<sup>[12, 17, 18]</sup> and likely plays a similar role for  $\text{K}^+$  and  $\text{Na}^+$  systems.<sup>[3, 13, 19]</sup> Understanding the fundamental differences and driving chemistries underlying SEI

formation may provide key insight into achieving higher performance batteries based on these alternative alkali metals.[20, 21]

When graphitic electrodes are operated in commonly used organic carbonate solvents (e.g. propylene carbonate (PC), ethylene carbonate (EC), dimethyl carbonate (DMC)), the Li<sup>+</sup>-SEI consists of a nanoscale film with a compact inorganic inner layer, mainly containing LiF and Li<sub>2</sub>O, and a thicker organic outer layer, consisting of carbonates, semicarbonates, and polymers.[12, 18] The formation of a robust Li<sup>+</sup>-SEI passivates the electrode toward further reaction with the electrolyte and enables Li<sup>+</sup> flux to/from the electrode for up to a thousand cycles or more.[22] SEI formation also occurs during initial cycling with K<sup>+</sup>, though reports suggest incomplete SEI coverage and limited cycling on various graphitic electrodes.[13, 15, 16] Na<sup>+</sup>-SEI studies tend to focus on hard carbons due to the low concentration GICs formed with Na<sup>+</sup>.[3, 23–25] In one comparative study, the Na<sup>+</sup>-SEI was thinner, more heterogeneous, and predominantly inorganic compared to a Li<sup>+</sup>-SEI.[26] Aside, Na<sup>+</sup> can form GICs through solvent co-intercalation as well, with similar SEI formation processes often observed.[27]

Surface structure has a major impact on battery performance[28] leading to a growing interest in developing artificial SEIs.[29, 30] Indeed, our group showed major improvements in the rate of K<sup>+</sup> (de)intercalation through modifying a few layer graphene (FLG) interface with a preformed Li<sup>+</sup>-SEI.[13, 31] The role of the cation in formation of the SEI and its functionality appears to be significant, but has attracted very little attention. Thus, understanding the initial stages of SEI formation and its role in battery aging could lead to significant progress in improving SEI function. The identity of the cation may determine the extent and type of species formed on the surface, thus presenting differences in the charge transfer properties of the SEIs. Previous work indicates that charge transfer varies between the inner and outer SEI layers,[32] and that the SEI structures are electrolyte-dependent.[3, 30, 33] SEI structure and functionality are only recently being

revealed with emerging analytical tools that acquire information at operating batteries and electrodes.[18, 20, 34, 35]

Scanning probe methods (SPMs) provide unique opportunities for understanding interfacial processes at battery electrodes, where they access high spatial and temporal information.[18, 20, 36] In particular, scanning electrochemical microscopy (SECM) and related electrochemical SPM techniques provide a wealth of information regarding formation of the SEI.[20, 36–41] SECM provides a link between surface reactivity and passivation by the SEI,[42, 43] and can further provide insight on ion transfer[44–46] and gas formation.[20, 36, 41] Recently, groups have used redox mediators in SECM to map and evaluate passivation during Li<sup>+</sup>-SEI formation and stabilization on several materials.[41, 47–49] These studies revealed localized fluctuations at short (minutes) and long (days) times across the SEI surface. On the other hand, SECM has rarely been applied for evaluating the SEI in K<sup>+</sup> or Na<sup>+</sup> electrolytes.[43, 45] In this comparative study, we used a drybox SECM setup as well as multiple modes of SECM, to explore the impact of the electrolyte cation, M<sup>+</sup>, on charge transfer during SEI formation at a multi-layer graphene (MLG) electrode during its first stages of formation. These nm-thick MLG electrodes present an attractive proxy for comparison to graphite interfaces found in batteries: they have a heterogenous structure, allowing analysis on individual surface substructures; they are binder-free, preventing interferences from extraneous materials, and; are flat on the nanoscale, enabling quantitative SECM analysis.[28, 31, 42, 50] A 300 nm SECM probe allowed us to resolve lateral charge transfer via electrochemical imaging with unprecedented sub-micron resolution of surface features on MLG.

#### 4.1 Results and discussion

As seen in **Figure 4.1a**, voltammetry at a MLG electrode revealed two main SEI regions for Li<sup>+</sup>, K<sup>+</sup>, and Na<sup>+</sup> tetrafluoroborate (BF<sub>4</sub><sup>-</sup>) electrolytes at 0.1 M concentration. The two peaks at  $\approx$  -1.1 and -1.4 V were previously reported as electrode reactions with the

$\text{LiBF}_4$  electrolyte to form inorganic phases, including  $\text{LiF}$ .<sup>[51, 52]</sup> The large cathodic process at more negative potentials (< -2.5 V vs  $\text{Fc}^+/\text{Fc}$ ) involved solvent degradation reactions, and thus formation of organic components in the SEI.<sup>[52, 53]</sup> We note that the  $\text{K}^+$  electrolyte in **Figure 4.1a** displayed a lower solubility than the  $\text{Na}^+$  and  $\text{Li}^+$  electrolytes, thus likely causing differences in peak intensity.<sup>[10]</sup> We further verified this by using the more soluble potassium hexafluorophosphate,  $\text{KPF}_6$  electrolyte (provided in the Appendix B, **Figure B.1**). Overall, the voltammetry was in good agreement with previous studies<sup>[42]</sup> on SEI formation in  $\text{LiBF}_4$  and suggests that all three electrolytes undergo similar reactions with MLG even with a ferricinium/ferrocene ( $\text{Fc}^+/\text{Fc}$ ) redox couple present in solution.

To acquire a deeper understanding of the impact of alkali ion identity on SEI formation, we focused on SECM imaging using a 300 nm SECM probe and the ferricinium/ferrocene ( $\text{Fc}^+/\text{Fc}$ ) redox couple as charge transfer mediator as illustrated in **Figure 4.1b**. In this type of analysis, a low concentration of Fc is dissolved in the electrolyte in order to evaluate electron transfer at the MLG surface through transfer of charge between the probe and MLG via the mediator. The probe is first approached toward the  $\text{SiO}_2$  nearby the MLG substrate with the probe potential poised to oxidize Fc to  $\text{Fc}^+$  (**Figure B.2**). In bulk solution, the probe will measure a constant current ( $i_\infty$ ) from the steady-state diffusion of fresh Fc toward the probe, while simultaneously  $\text{Fc}^+$  diffuses away from the probe after oxidation. As the probe gets close to the MLG or  $\text{SiO}_2$  surface this constant current will either increase or decrease as the local availability of Fc changes and the produced  $\text{Fc}^+$  reaches the substrate electrode. Electrochemically active surfaces like pristine MLG can directly reduce the  $\text{Fc}^+$  back to Fc when applying a substrate potential negative of the standard potential of the  $\text{Fc}^+/\text{Fc}$  redox pair, or by shuttling charge away from the approach site on a large substrate electrode at open circuit potential (OCP). On such a non-passivated surface, this process leads to an increase in current, or positive feedback, at the SECM probe through a feedback loop.<sup>[54]</sup> On the other hand, if the  $\text{Fc}^+$  species does not interact with the substrate, as it occurs on the inert  $\text{SiO}_2$  surface, or as it could happen on a passivated electrode, it

results in negative feedback, i.e. lower probe currents.[55] For simplifying the analysis, the measured tip current, it, was normalized to the current far away from the substrate,  $i_t/i_\infty$ .[56] By tracking changes at the probe during raster we could reliably evaluate electron transfer and interphase formation across the MLG surface through feedback imaging (**Figure 4.1b**).[32, 57] For our first SECM measurements, we evaluated the in situ evolution of an MLG electrode within a 0.1 M LiBF<sub>4</sub> electrolyte. We focused on a  $\approx 30 \times 30 \mu\text{m}^2$  region of the MLG electrode; requiring approximately 5 minutes to collect each image.

Our measurements could effectively resolve small features (comparable to the probe size of 300 nm) and differences in feedback across the MLG. SEM imaging of the pristine MLG electrode revealed structural heterogeneity as shown in Figure 4.1c with distinct features varying in size on the order of  $1.7 \pm 0.6 \mu\text{m}$  (**Figure B.3,B.4**). AFM imaging (**Figure B.5**) of the same type of electrodes showed differences in thickness between these domains and the presence of cracking on the surface. Our initial SECM feedback image at OCP (**Figure 4.1d**) captured indications of the heterogeneities detected in AFM and SEM, indicating domains with heterogeneous electrochemical reactivity, some of which resembled the larger grains ( $> 1 \mu\text{m}$ ). Comparing the SECM feedback images and the structure of the electrode obtained by AFM and SEM, it is likely that our feedback imaging did not clearly resolve individual grains (with sizes  $< 1.5 \mu\text{m}$ ) or grain boundaries. Therefore, the observed heterogeneous reactivity may originate from differences in conductivity, spontaneous electrolyte precipitates at the MLG surface, holes exposing the SiO<sub>2</sub> surface (as observed via AFM), or polymer residues which occurred during transfer of the MLG electrode. However, these images provide a suitable reference point to evaluate the impact of SEI passivation on the reactivity of the MLG electrodes.

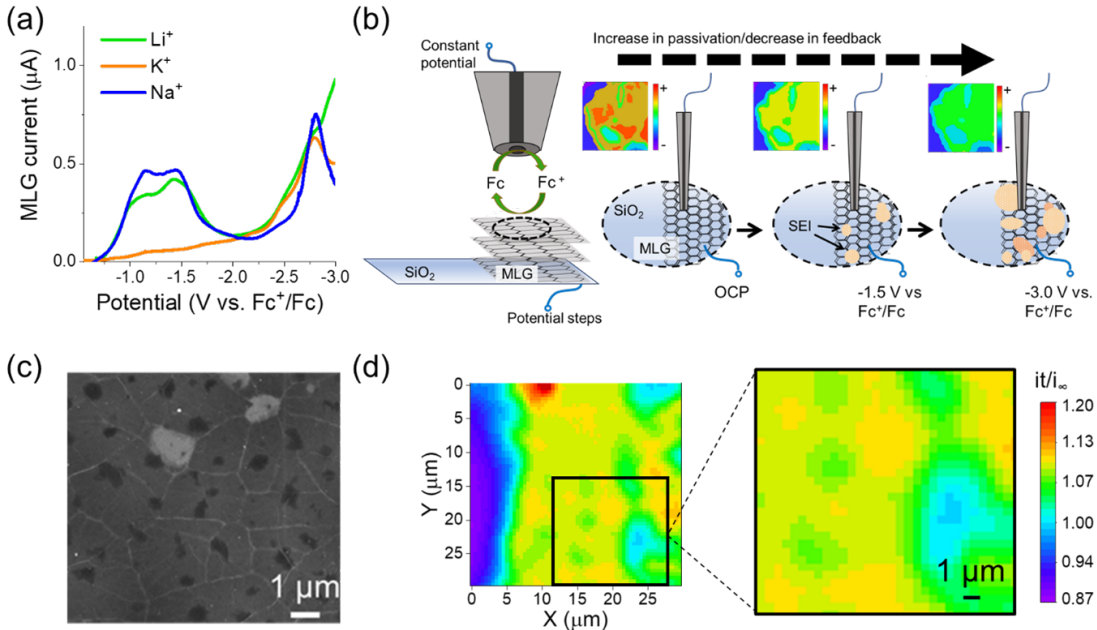


Figure 4.1: SEI reactions and mapping at a multi-layered graphene electrode. (a) Linear sweep voltammograms of SEI formation on MLG in 0.1 M LiBF<sub>4</sub>, 0.1 M NaBF<sub>4</sub>, and saturated KBF<sub>4</sub> in PC:EC. The sample was scanned at 0.2 mV/s. (b) Illustration of SECM feedback imaging procedure. (c) SEM image of an unused MLG electrode. (d) SECM feedback image of an MLG substrate in 0.1 M LiBF<sub>4</sub> at OCP before SEI formation. Image on right is rescaled for easier comparison with the SEM image in (c).

We then turned to analyzing the potential-dependent reactivity of the MLG electrode. We scanned the same  $\approx 30 \times 30 \mu\text{m}^2$  region while decreasing the MLG potential stepwise from -0.3 V to -2.9 V vs.  $\text{Fc}^+/\text{Fc}$ , and further while increasing the potential back to -0.3 V in a cyclic fashion (**Figure 4.2**). Feedback diminished above the MLG surface even after the first step to -0.8 V vs.  $\text{Fc}^+/\text{Fc}$  and continued as the MLG reached more negative potentials, indicating a fade in charge transfer rates. Using Python, we applied feedback theory and knowledge on the experimental parameters to extract electron transfer kinetics from regions of the SECM images (more information in the Experimental Procedures section, **Table 4.1**).<sup>[54, 56]</sup> We set an upper and lower limit on the kinetics to eliminate errors from holes, raised features, and artificial high/low kinetic values (**Figure B.6**). As seen in **Figure 4.2c**, the electron transfer rates,  $k_f$ , at -0.3 V vs  $\text{Fc}^+/\text{Fc}$  were on average 0.63  $\pm$  0.11 cm/s, in agreement with the various kinetics observed at other graphitic systems.<sup>[58]</sup>

59] As the substrate potential was made more negative, we observed a significant decrease in  $k_f$  consistent with the formation of an insulating SEI layer. However, stepping the MLG potential back to more positive potentials did not recover the original electron transfer rates up to -0.3 V vs.  $\text{Fc}^+/\text{Fc}$  (**Figure 4.2c** and **B.7**) in agreement with previous reports.[42]

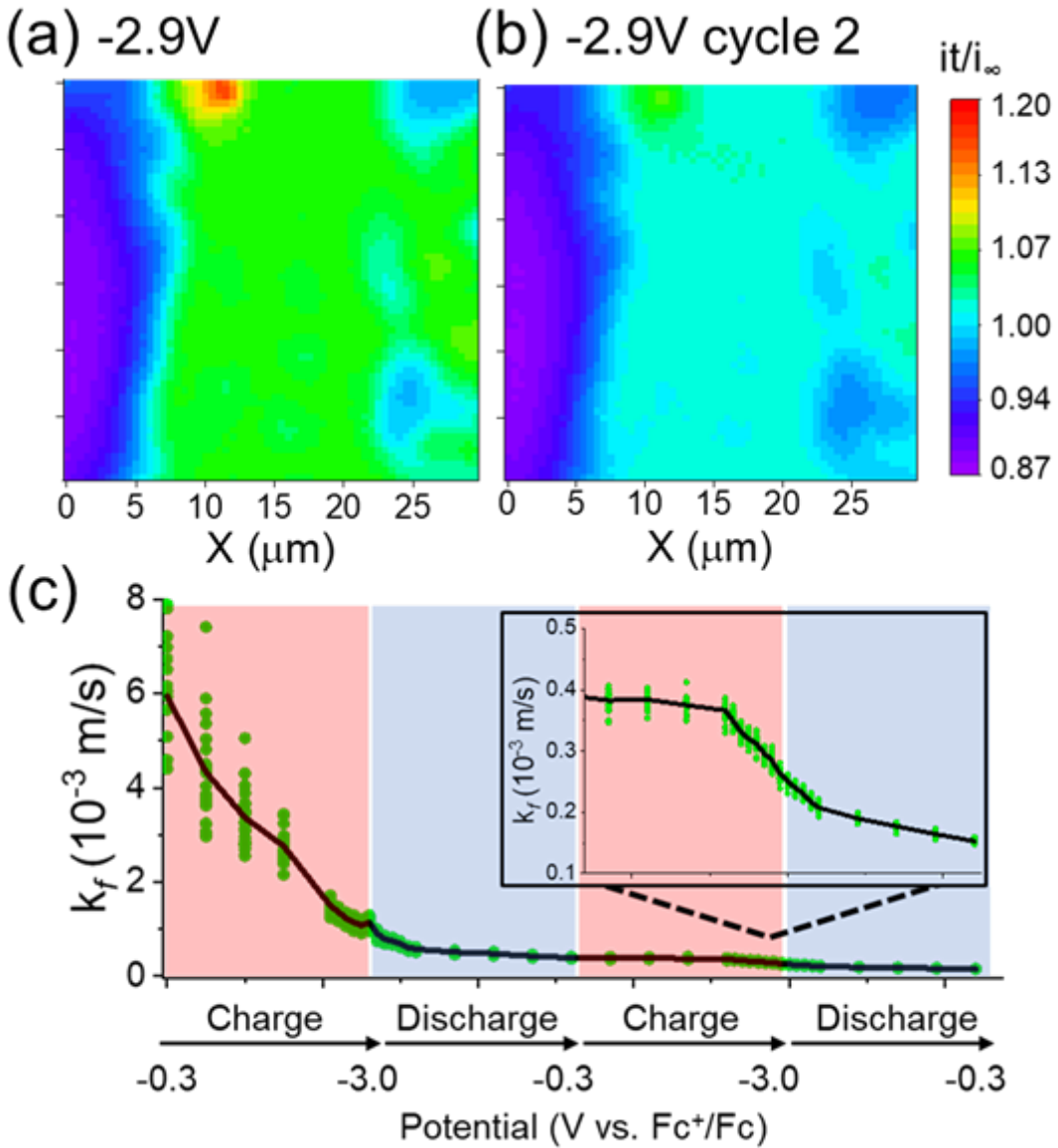


Figure 4.2: Mapping  $\text{Li}^+$ -SEI formation at an operating MLG electrode. SECM feedback images of MLG substrate in 0.1 M  $\text{LiBF}_4$  at -2.9 V vs.  $\text{Fc}^+/\text{Fc}$  at the end of the (a) first and (b) second cycle. (c) Change in electron transfer kinetics during the first and second cycle of SEI formation. The inset in (c) is the second cycle rescaled for clarity. The green points represent the distribution of feedback across the images from different locations. The black line represents feedback changes extracted from a single location.

The forming SEI structure could potentially decrease the feedback signal in different ways. One possibility is that a passivating layer blocks transport of the redox mediator, preventing its reactivity at the electrode surface. If the passivating layer is thin, homogeneous, and an ideal insulator, we would expect blocking of electron tunneling to be the main mechanism for the decrease in feedback, as it has been described for blocking self-assembled monolayers on electrodes.[60] In such a case, the feedback signal should show a strong dependence on the MLG electrode potential. In this case, we would expect the feedback signal to further decrease upon reversing the MLG electrode back toward more positive values as the overpotential for reduction of ferricenium would be lower. However, this was not clearly observed. **Figure 4.2c** shows that after the initial cathodic sweep, a subsequent anodic sweep maintained a similar level of feedback but still within the range of measurable kinetics (**Figure B.6**).

A second cathodic cycle showed a further passivation of the electrode when reaching potentials near -3 V (**Figure 4.2c**, inset), but still without reaching the behavior of an ideal insulator (i.e. negative feedback). These properties suggest that the surface of the MLG exhibits incomplete coverage by the SEI. On such an interface, there would be two contrasting outcomes: on the one hand, the presence of pinholes or uncovered regions on the electrode should display increasing electrode kinetics as the potential is made more negative (i.e. the overpotential for  $\text{Fc}^+$  reduction increases); on the other hand, the continuous formation of the SEI would lead to decreased feedback as some of these exposed regions are covered. The second cathodic scan (inset of **Figure 4.2c**) shows that between -0.5 and -1.8 V, the feedback signal is unchanging within the error represented by the averaged response across the electrode. While it is possible that the rate of surface passivation and the increase in kinetics due to pinholes cancel each other out in this potential region, we suspect that pinholes are not dominant in this case. Instead, the lowered feedback observed upon subsequent sweeps is likely dominated by mediator transport across a permeable SEI, as has been suggested before using rotating disk electrode techniques.[32]

As a suitable control for our measurements, the insulating region represented by the SiO<sub>2</sub> domain (**Figure 4.2a,b**, on left) remained unchanged across the images at all applied potentials, thus providing a reference point to rule out drifting in the tip-substrate distance or the tip response. Further, this suggested Fc was stable and did not undergo oxidation/decomposition at the forming SEIs. Though Fc<sup>+</sup>/Fc may have some unknown impact on the SEI, our measurement of the  $i_{tip}$  acts as an indicator of bulk Fc concentration, and this remained constant throughout our measurement above the inert SiO<sub>2</sub> surface. These high-resolution studies were in agreement with precedent work,[41, 42, 50] which revealed a passivating Li<sup>+</sup>-SEI across the MLG surface, despite differences in lateral resolution (i.e. 300 nm probe used here vs.  $\approx$ 10  $\mu$ m used elsewhere). Nevertheless, our imaging method characterized an evolution of the electrochemical properties of the MLG electrode in the LiBF<sub>4</sub> electrolyte during the initial formation cycles of the SEI that serves as a comparison for other systems.

For evaluating Na<sup>+</sup> and K<sup>+</sup> electrolyte systems, we used either 100 mM NaBF<sub>4</sub> or saturated KBF<sub>4</sub>, respectively. After positioning the SECM probe above a region of interest (**Figure B.8**), we again observed variation in electron transfer rates across the MLG at OCP during imaging (**Figure 4.3**). For evaluating the development of the Na<sup>+</sup> (**Figure 3a**) and K<sup>+</sup>-SEI (**Figure 4.3b**), we utilized smaller potential steps of 100 mV to gain greater insight into the overall passivation process. Again, we analyzed the kinetics from select regions using Python to process the  $k_f$  results. In both cases and unlike the case in Li<sup>+</sup> electrolyte, we observed a brief plateau before initiation of the passivation process (**Figure 4.3c**, more positive of  $\approx$  -1.25 V). Alike to the Li<sup>+</sup> electrolyte, both systems showed irreversible passivation suggesting a growing interphase structure (**Figure B.9,B.10**). Because passivation of the electrode occurred on all sites in the image, as in the case of Li<sup>+</sup>, we propose that the underlying graphene structure did not seem to impact the initially forming SEIs. Instead, there seems to be a stronger influence of the potential on the amount of passivation observed in these electrodes relative to that observed in LiBF<sub>4</sub>. Considering only the normalized

currents (**Figure B.11**) and extracted kinetics (**Figure B.12**), the  $\text{Na}^+$ -SEI showed the lowest kinetics after the first negative sweep. However, the  $\text{Na}^+$  and  $\text{K}^+$ -SEI were formed across longer time scales (approximately double compared with  $\text{Li}^+$ ) and the MLG samples used for the  $\text{Li}^+$  electrolyte showed slightly higher initial kinetics. For further analysis, we normalized based on the initial kinetics (**Figure 4.3c**), where the  $\text{Li}^+$ -SEI grew more quickly than the other SEI with the most significant change in passivation though none of the electrodes were passivated to the levels of pure negative feedback, i.e. an insulator. These differences in passivation may lead to distinct performance characteristics of the SEI in each electrolyte. Previous reports on FLG in  $\text{K}^+$  electrolytes have shown that the SEI tends to show a patchy structure (as revealed ex situ) compared with  $\text{Li}^+$ , likely the result of a less efficient passivation.[13]

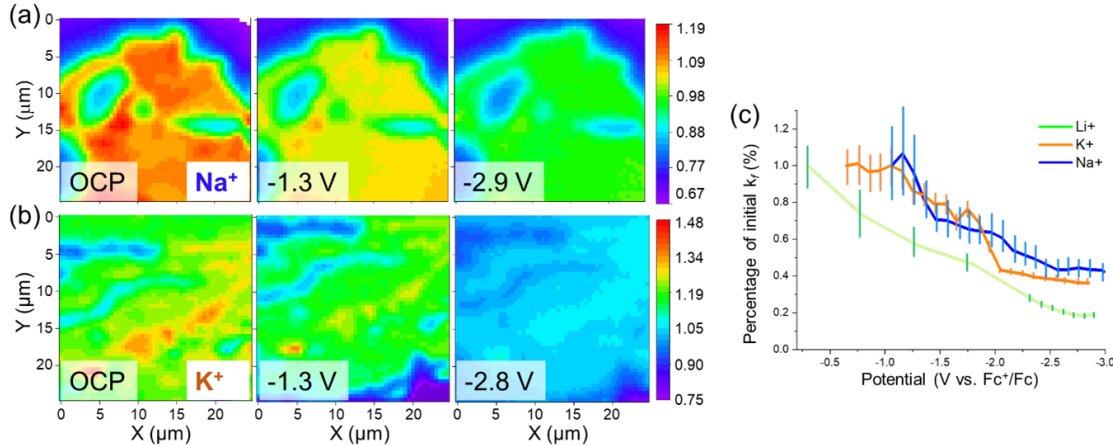


Figure 4.3: Mapping SEI formation in  $\text{Na}^+$  and  $\text{K}^+$  electrolytes. a) SECM feedback images of MLG in 0.1 M  $\text{NaBF}_4$  at (left) OCP, (middle) -1.3 V, and (right) -2.9 V vs.  $\text{Fc}^+/\text{Fc}$ . b) SECM feedback images of MLG in saturated  $\text{KBF}_4$  at (left) OCP (middle) -1.3 V, and (right) -2.8 V vs.  $\text{Fc}^+/\text{Fc}$ . c) Percent change in average extracted kinetic values with decreasing MLG potential. The lines represent standard deviation ( $n-1$ ) of the averaged response across the sample.

In an attempt to correlate passivation with ion uptake by each of the forming SEIs, we explored in situ measurements of ionic flux during SEI formation using Hg disc well (HgDW) probes with SECM (**Figure 4.4**).[61] Hg probes enable quantitative measurements

and mapping of ion flux at reactive electrodes through amalgamation and stripping reactions with the solution cations.[44–46, 50, 62] Voltammetry for each electrolyte showed a single forward amalgamation wave, where the metal cation was reduced and entered the Hg phase, then a stripping peak on the return sweep with the ions again returning to the electrolyte (**Figure B.13**). Although CVs can be used to directly evaluate ion concentrations, this type of measurement tends to cause probe failure when working with high metal ion concentrations due to saturation of the Hg amalgam phase.[61, 63] Thus we introduced a pulsing method (**Figure 4.4a**) between amalgamation and stripping potentials that better stabilized the Hg probe measurements toward the high concentration environments found in our electrolytes

As seen in **Figure 4.4a,b**, short pulses at amalgamation and stripping potentials on the Hg probe provided reliable measurements of metal ion consumption by the SEI at 0.1 M  $M^+$  electrolyte with a temporal resolution of 10 ms. With the probe positioned close to the MLG substrate, we pulsed the probe while stepping the applied potential at the MLG surface from  $\approx 0.2$  V to -3.0 V vs  $Fc^+/Fc$  in -100 mV increments. As illustrated in **Figure 4.4c**, the probe competes with the MLG substrate for alkali ions in the vicinity of the probe enabling detection of ion uptake processes.[44, 46] For each ion, we started with a pristine electrode in each case, and every measurement was conducted with the MLG potential held briefly (3-6 s) before stepping to the next condition. To avoid issues with the low  $K^+$  content, we instead used the more soluble  $KPF_6$  salt at 0.1 M concentration, otherwise we continued using  $LiBF_4$  and  $NaBF_4$ . Feedback measurements with  $KPF_6$  showed similar passivation to the  $KBF_4$  electrolyte (**Figure B.14**) and can produce similar SEI.[64] For all systems, we observed a decrease in the total amalgamation (**Figure 4.4c**) and stripping (**Figure B.15**) response during pulsing as ions were consumed in SEI reactions at the MLG surface. Since the amalgamation and stripping responses were similar with integrated charges showing  $\pm 1\%$  difference, we focused only on the amalgamation response to track ion uptake. For better comparison, we normalized the probe response to the measurements at OCP before SEI formation and report this as a percent change of the initial integrated

charge, i.e. % amalgamation. For all three systems (**Figure 4.4d**), we observed two main regions involving M<sup>+</sup>: (1) SEI reactions initiating at potentials positive of -1.5 V vs Fc<sup>+</sup>/Fc, and (2) SEI reactions at more negative potentials,  $\approx$  -2.0 V vs Fc<sup>+</sup>/Fc, concurrent with solvent breakdown. In region 1, we observed only a significant uptake of K<sup>+</sup> in comparison to Na<sup>+</sup> and Li<sup>+</sup>. However, changes in region 1 were small compared to those in region 2. As the potential was made more negative, Li<sup>+</sup> and Na<sup>+</sup> uptake increased while the response for K<sup>+</sup> reached a plateau even though the overall SEI formation time was very small ( $\approx$ 150 s). Overall, the ionic processes showed some correlation to the passivation processes revealed through SECM (**Figure 4.4e,f**) but further suggest the cation identity impacts initial and subsequent build-up of the SEI. At the most negative potentials, Li<sup>+</sup> was consumed more significantly than either Na<sup>+</sup> or K<sup>+</sup>, correlating to the higher passivation observed in SECM feedback results. This could be indicative behavior for a highly functional SEI, where simultaneous blocking of electron transfer takes place in addition to high cation incorporation into the SEI structure.

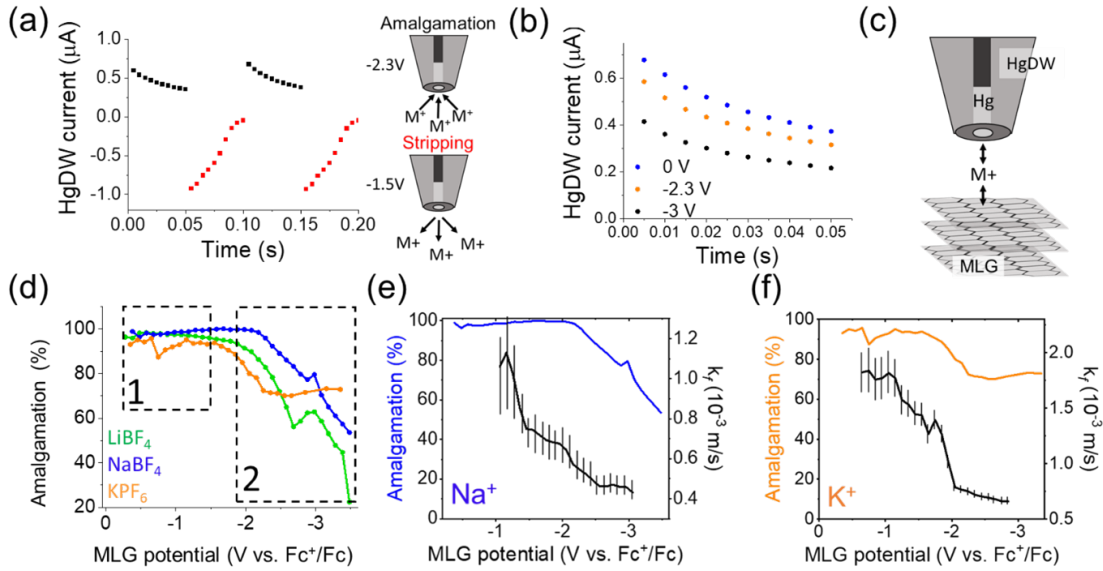


Figure 4.4: Mapping SEI formation in  $\text{Na}^+$  and  $\text{K}^+$  electrolytes. a) SECM feedback images of MLG in 0.1 M  $\text{NaBF}_4$  at (left) OCP, (middle) -1.3 V, and (right) -2.9 V vs.  $\text{Fc}^+/\text{Fc}$ . b) SECM feedback images of MLG in saturated  $\text{KBF}_4$  at (left) OCP (middle) -1.3 V, and (right) -2.8 V vs.  $\text{Fc}^+/\text{Fc}$ . c) Percent change in average extracted kinetic values with decreasing MLG potential. The lines represent standard deviation ( $n=1$ ) of the averaged response across the sample.

To correlate the evolution of chemical phases within the SEIs to the passivation and ion-uptake features observed via SECM, we used ex situ X-ray photoelectron spectroscopy (XPS). For this analysis, we focused on the SEI reactions that occurred on MLG at -1.4 V and -3.0 V vs.  $\text{Fc}^+/\text{Fc}$  within each electrolyte, as representative for region 1 and region 2 in **Figure 4.4d**. To form the SEI, we held the MLG at a constant potential for 2 hours (**Figure B.16**). After forming the SEI, we disassembled the cell and rinsed each sample with PC to remove the residual electrolyte. High resolution C 1s, O 1s, Li 1s, Na 1s, K 2p and survey spectra are presented in the Supplemental Section **Figures B.17-B.19**.

For both the  $\text{Li}^+$  and  $\text{K}^+$ -SEIs formed at -1.4 V (**Figure 4.5a**), the XPS results indicated an SEI composed of carbon-based species, with some formation of fluorinated phases. Most of the C 1s signal arises from the underlying MLG (**Figure B.19a,c**). In contrast, the  $\text{Na}^+$ -SEI appeared to be deficient of fluorinated species (**Figure 4.5a**) and

devoid of organic functional groups (**Figure B.19e**). We observed a notable shift in all three SEIs for samples held in region 2, at -3.0 V, as shown in **Figure 4.5a**. In this case, the Li<sup>+</sup>-SEI predominantly consisted of fluorinated species, which can be attributed to LiF, with lower relative area under the O 1s and C 1s peaks. The Na<sup>+</sup>-SEI also transitioned toward higher fluorinated content in its structure, though its XPS also indicated the significant formation of carboxylic species (**Figure B.19e, SB.19f**).[65] For the K<sup>+</sup>-SEI, the area under the F 1s peak decreased relative to the C 1s area, which indicated more extensive hydrocarbon/organic species content during build-up of the SEI.[66] This agrees with previous reports suggesting differences in the degradation mechanism of the K<sup>+</sup> electrolytes compared with Li<sup>+</sup> and Na<sup>+</sup>.[67]

Looking closer at the F 1s peaks,[68, 69] in **Figures 4.5b,c**, and in the valence band spectra (**Figure B.20**), the Li<sup>+</sup>-SEI was dominated by LiF at both formation potentials. For the K<sup>+</sup>-SEI, the KF peak remained overshadowed by P-F containing species (likely arising from KPF<sub>6</sub> crystals as shown in **Figure B.21** and **B.22**), suggesting poorer incorporation of K<sup>+</sup> in the SEI structure (also evident from decreasing K 2p peak intensities relative to the graphite C-C peak, **Figure B.19c,d**).[69–71] Unfortunately, we cannot rule out the changes in fluoride content in the K-SEI samples could be due to reactions between residual KPF<sub>6</sub> electrolyte with air. The F 1s spectra for the Na<sup>+</sup>-SEI revealed that NaF species did not form at -1.4 V, but instead become the major component of fluorinated species at -3.0 V. With all the three SEIs, we observed peaks attributable to B-F and P-F species. It is likely that the B-F species in the Li<sup>+</sup>-SEI are arising from SEI components since SEM micrographs (**Figure B.23,B.24**) revealed no presence of crystalline LiBF<sub>4</sub>. As noted by precedent work, both the electrolyte and the potential had a strong impact on the overall structure of the formed SEI.[53, 72]

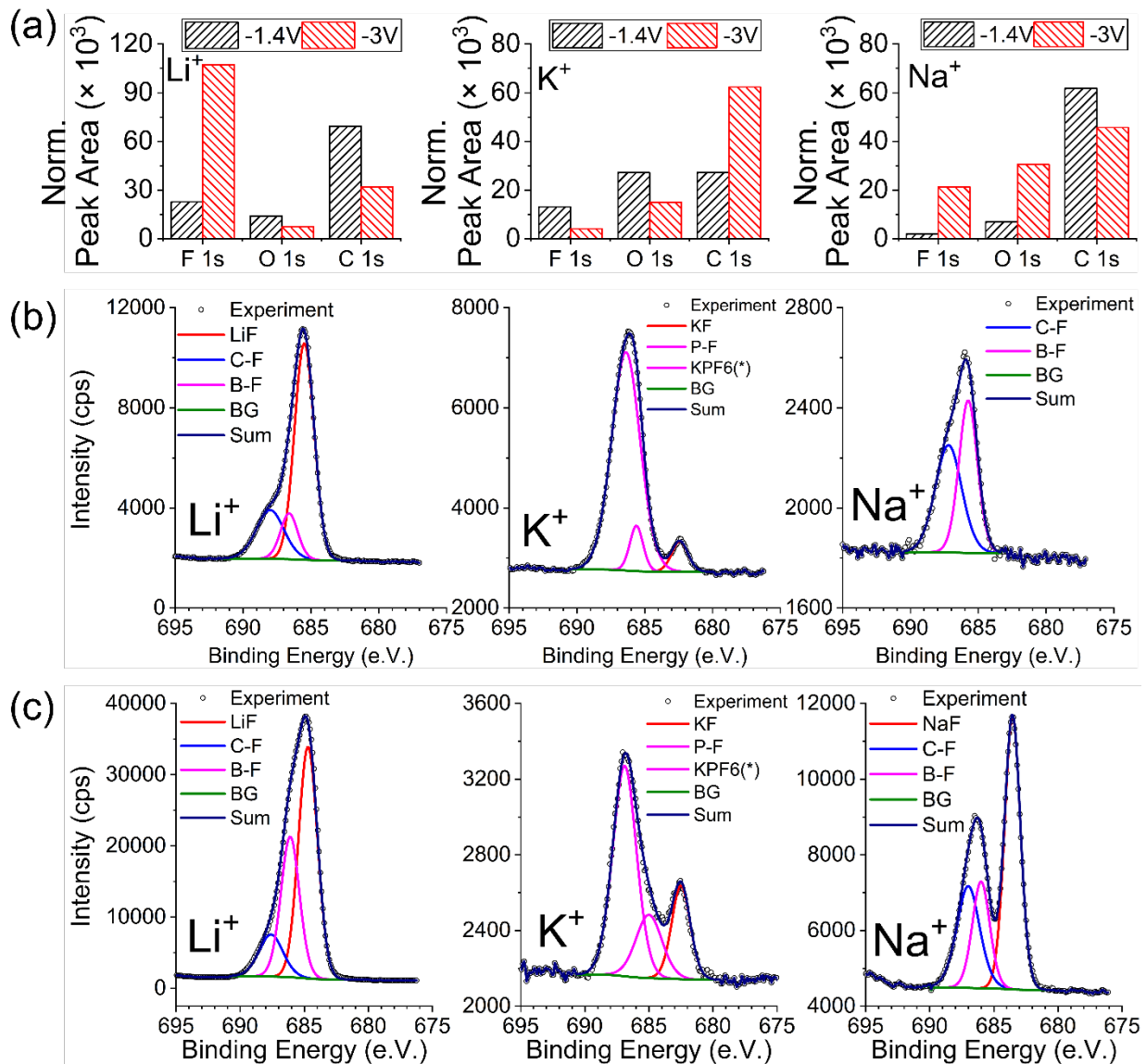


Figure 4.5: Mapping SEI formation in  $\text{Na}^+$  and  $\text{K}^+$  electrolytes. a) SECM feedback images of MLG in 0.1 M  $\text{NaBF}_4$  at (left) OCP, (middle) -1.3 V, and (right) -2.9 V vs.  $\text{Fc}^+/\text{Fc}$ . b) SECM feedback images of MLG in saturated  $\text{KBF}_4$  at (left) OCP (middle) -1.3 V, and (right) -2.8 V vs.  $\text{Fc}^+/\text{Fc}$ . c) Percent change in average extracted kinetic values with decreasing MLG potential. The lines represent standard deviation ( $n-1$ ) of the averaged response across the sample.

Correlating our XPS data with the SECM results suggests that LiF was the main passivating species for the  $\text{Li}^+$ -SEI. Given the widespread debate about its role in the SEI on graphitic anodes,[73] this correlation provides evidence that LiF is indeed responsible for the passivation of electron transfer at the electrode surface. Along similar lines, it appears

that passivation seen in  $\text{Na}^+$ -SEI is also arising due to  $\text{NaF}$  formation, whereas the  $\text{K}^+$ -SEI passivates due to organic species. Further, SECM ionic flux experiments in region 2 showed a significant flux of both  $\text{Li}^+$  and  $\text{Na}^+$ , which correlates well with the formation of  $\text{LiF}$  and  $\text{NaF}$ , unlike the case for KF which is not dominating in XPS and shows a limited flux in SECM. We acknowledge that sample rinsing and the ex-situ nature of XPS measurements will alter the composition of the SEI to some extent and therefore impact the XPS analysis.<sup>[70, 71]</sup> For example, dissolution of both inorganic and organic species during rinsing has been reported in Na-ion batteries,<sup>[74, 75]</sup> along with the formation of species such as carbonates due to air exposure.<sup>[70, 71]</sup> Therefore, we limit our analysis to a qualitative evolution of overall species (such as fluorinated phases and hydrocarbons) between SEIs formed -1.4 V and -3.0 V, (in **Figure 4.5a**). SEM results showed significant structural differences between the three SEI under voltammetric cycling (**Figure B.23**) and while formed at -3.0 V (**Figure B.24**). For SEIs formed at -3.0 V, the  $\text{Li}^+$ -SEI appeared to be the thinnest of the three samples (**Figure B.24**). On the other hand, the  $\text{Na}^+$  and  $\text{K}^+$ -SEIs were less passivating as per SECM feedback experiments, indicating that their greater organic content was accompanied with increased permeability to the  $\text{Fc}^+/\text{Fc}$  mediator. In comparison, the lesser proportion of metal fluorides in  $\text{Na}^+$  and  $\text{K}^+$  electrolytes suggests that the structures may not remain on the surface during initial SEI formation and therefore they do not as effectively passivate the electrode. This observation highlights the importance of inorganic fluorides in influencing the passivation and properties of the SEI.

## 4.2 Conclusions

In conclusion, our in situ SECM approach provided direct observation of the initial SEI formation and passivation processes within different alkali electrolytes. SECM feedback performed using a 300 nm Pt probe revealed a continual, irreversible loss of electrochemical reactivity which indicated passivation in each system as the MLG electrode potential was made more negative; the most rapid passivation was observed for the  $\text{Li}^+$  electrolyte. While

initially the small probe revealed detailed features across a heterogeneous pristine MLG surface, the kinetics of charge transfer became relatively homogenous after the SEI started to form, thereby indicating a lack of dependence of passivation on the underlying electrode structure. Ion-sensitive measurements designed to track the incorporation of the cation on the SEI further showed significant uptake for Li<sup>+</sup> and Na<sup>+</sup> and a lower intensity plateau within the K<sup>+</sup> electrolyte in a potential region more negative than -2 V vs. Fc<sup>+</sup>/Fc. No significant ion consumption was detected at potentials more positive. Overall, the trends observed during these ion measurements correlated well with XPS results, which suggested significant formation of metal fluorides in only the Li<sup>+</sup> and Na<sup>+</sup> electrolytes. Notably, the Li<sup>+</sup>-SEI showed significant passivation and metal fluoride content, and strong uptake of Li<sup>+</sup> during its formation. Altogether our results suggest that the metal fluorides are significant for functional SEI formation, though they do not seem to appreciably form in the K<sup>+</sup> electrolyte.

The components that make up the SEI are key to its functionality where they heavily impact ion and solvent transport to/from the electrode. The initial SEI layer likely has significant impact on SEI development and performance as the main contact with the electrode.[32] Understanding and improving this structure may lead to progressive growth of more functional Na<sup>+</sup> and K<sup>+</sup>-SEI and more extended cycling or improved rates.[13] Our results highlight the wide opportunities that SECM provides for understanding the correlations between electron and ion transfer processes at battery electrode surfaces.

### 4.3 Experimental section

#### 4.3.1 Materials

All chemicals were purchased from commercial sources and used without purification. Propylene carbonate (PC, anhydrous, 99.7%), ethylene carbonate (EC, anhydrous, 99%), lithium tetrafluoroborate (LiBF<sub>4</sub>, 98%), sodium tetrafluoroborate (NaBF<sub>4</sub>, 98%), potassium tetrafluoroborate (KBF<sub>4</sub>, 98%), ferrocene (C<sub>10</sub>H<sub>10</sub>Fe, 99%),

acetone (99.5%), isopropyl alcohol (IPA 99.5%), glacial acetic acid (99.5%) and ethylenediaminetetraacetic acid disodium salt dihydrate ( $\text{Na}_2\text{EDTA} \cdot 2\text{H}_2\text{O}$ , 99.0%) were all purchased from Sigma-Aldrich. 25  $\mu\text{m}$  thick copper foil was purchased from Alfa Aesar. Nano 950 K A4 PMMA and 495 K A2 PMMA were purchased from MicroChem. CE-100 copper etchant was purchased from Transene Company.  $\text{SiO}_2/\text{Si}$  wafer (3 inches, Boron-doped P-type Si wafer with 300 nm wet thermal oxide) was purchased from University Wafer. The deionized water (DI water,  $18.2\text{ M}\Omega$ ) was filtered using a Millipore system.

#### 4.3.2 Substrate preparation

Multilayer graphene (MLG) was synthesized by chemical vapor deposition (CVD) using methane and 25  $\mu\text{m}$  thick copper foil as catalyst according to previously reported CVD method.<sup>[13]</sup> In brief, the Cu foil was rinsed sequentially in acetone, water, glacial acetic acid, water, acetone, then IPA to remove surface contaminants. The Cu foil was then mounted in a CVD chamber at atmospheric pressure. With argon flowing at a 300 sccm rate, the quartz tube was heated to 940°C at 12°C/min. At this growth temperature, the flow ratio of  $\text{CH}_4:\text{H}_2$  was maintained at 1:3 for 5 min. After this step,  $\text{CH}_4$  was cut off and the furnace was cooled down to room temperature at a rate of 10°C/min under a 300 sccm flow of Ar and a 35 sccm flow of  $\text{H}_2$ . The MLG was transferred onto  $\text{SiO}_2/\text{Si}$  wafer through a wet transfer method. MLG substrates were characterized via optical microscopy (Zeiss Axio Lab.A1, Germany), scanning electron microscopy (SEM, Hitachi S-4800, Japan) and Raman spectroscopy (Nanophoton Laser Raman Microscope RAMAN-11, Japan). Energy dispersive x-ray spectroscopy (EDS) measurements were collected on a JEOL 6060 SEM.

#### 4.3.3 Bulk electrochemistry

All electrochemical experiments were conducted using a CHI 920D SECM from CH Instruments (Austin, TX) inside of a glovebox (MBraun, Stratham, NH) with mindful control of the oxygen ( $\leq 0.1$  ppm) and water levels ( $\leq 0.1$  ppm), respectively. MLG

substrates were assembled in an SECM cell as the working electrode. Pt and Ag wires were used as the counter and reference electrodes, respectively. For evaluating the Li<sup>+</sup>-SEI, we used an electrolyte composed of 0.1 M LiBF<sub>4</sub> and 5 mM ferrocene in a 50:50 (v/v) mixture of PC/EC. For the Na<sup>+</sup>-SEI, we prepared the same electrolyte, but replaced the LiBF<sub>4</sub> with 0.1 M NaBF<sub>4</sub>. For the K<sup>+</sup>-SEI, we again prepared the same electrolyte solution but replaced LiBF<sub>4</sub> with saturated KBF<sub>4</sub> and allowed precipitates to settle before transferring into the SECM cell. We focused on BF<sub>4</sub><sup>-</sup> electrolytes to minimize effects of our open electrochemical cell and potential moisture inside the glovebox.[76] All CVs were collected at a 0.2 mV/s scan rate starting from the open-circuit potential (OCP). All measured potentials were referenced to Fc<sup>+</sup>/Fc. After the experiments, the samples were removed from the glovebox. The samples were rinsed with deionized water and either isopropanol or acetonitrile then dried under ambient conditions before SEM and EDS measurements.

#### 4.3.4 SECM experiments

Fresh MLG substrates were assembled into an SECM cell, again with a Pt counter and Ag reference. First, the substrate was leveled using feedback current,  $i_t/i_\infty$ , with a Fc redox mediator at a Pt ultra-microelectrode (UME) with a 12.5  $\mu\text{m}$  electrode radius. Thereafter, the Pt UME was replaced with a 300 nm (electrode radius) SECM probe. The 300 nm probe was approached to fresh MLG samples within each electrolyte. Then feedback was collected while rastering the probe across a region of the MLG. First a feedback image was collected with the MLG at OCP, then the substrate potential was changed to 0 V vs. Fc<sup>+</sup>/Fc and decreased incrementally during each following SECM image. Each image was collected in approximately 5 minutes.

Electron transfer kinetics ( $k_f$ ) were extracted via the normalized tip current feedback images using the analytical expressions from Cornut and Lefrou.[56] Their analytical expression enables extraction of  $k_f$  with known parameters including the bulk tip current at infinite distance, tip electrode radius, ratio of the surrounding glass radius to the electrode

radius (tip RG), the mediator diffusion coefficient, and the tip-substrate distance determined through fitting of the approach curve (**Table 4.1**). A normalized parameter,  $\kappa$ , relates the rate constant to the measured currents based on the electrode radius and diffusion coefficient. A solver was written in Python and utilized to evaluate negative and positive feedback limits in our  $k_f$  distribution plots. Using parameters in **Table 4.1**, theoretical  $k_f$  vs. normalized current plots are presented in **Figure B.6**. We took the derivative of the plots and obtained practical limits for electron kinetics by taking a value corresponding to 10% of the maxima in the derivative, as shown in **Figure B.6**.

Table 4.1: Parameters used to compute  $k_f$  from normalized tip currents

	Li	K	Na
Steady state currents in bulk (A)	3.39E-10	2.42E-10	2.68E-10
Tip radius (nm)	300	300	300
Tip RG	10	10	10
Diff coefficient of Ferrocene (m <sup>2</sup> /s)	6.00E-10	6.00E-10	6.00E-10
Tip to sub distance (μm)	1.35	0.45	0.5

#### 4.3.5 Ion sensitive SECM

The HgDW probes were prepared according to previous reports.[46, 61] Briefly, Pt UMEs were sharpened and polished. Thereafter, they were etched while sonicating in a CaCl<sub>2</sub>/HCl solution by applying an AC waveform with a p-p voltage of 2.7 V. A graphite rod was used as the counter electrode. Each probe was etched for 10 s; then the probes were cleaned thoroughly with sonication. The probes were then immersed in a 10 mM solution of Hg(NO<sub>3</sub>)<sub>2</sub> with 0.1 M KNO<sub>3</sub> supporting electrolyte. A potential of 0 V vs Ag/AgCl was applied to deposit Hg and slightly overfill the etched well. Next, the probes were pressed carefully using a glass cover slip and transferred into the glovebox. The HgDW probes were positioned using approach curves and the mediator TMPD in 0.1 M of either LiBF<sub>4</sub>, NaBF<sub>4</sub>, or KPF<sub>6</sub>. The probe was pulsed back and forth between amalgamation and stripping potentials for 0.05 s each pulse while decreasing the potential of the MLG substrate in 100

mV increments. The amalgamation and stripping responses were further processed through integration and normalized based on the initial measurements at OCP.

#### 4.3.6 X-ray photoelectron spectroscopy

Prior to XPS analysis, SEI were formed on MLG samples using an LSV from open circuit to the potential of -1.4V or -3.0V vs.  $\text{Fc}^+/\text{Fc}$ , followed by a constant potential hold for 2 hours in 0.1 M of either  $\text{LiBF}_4$ ,  $\text{NaBF}_4$  or  $\text{KPF}_6$ . Thereafter, all samples were rinsed with PC. XPS samples at -3.0 V were transferred in a sealed container, whereas the -1.4 V samples were allowed to dry inside the glovebox for several days before transfer through air. The XPS measurements were performed with a Kratos Axis Ultra electron spectrometer, using monochromated  $\text{Al K}\alpha$  radiation (1486.6 eV). Survey spectra were recorded at energy resolution of 1 eV, pass energy 160 eV and high-resolution spectra for individual elements recorded at 0.1 eV, pass energy 40 eV. Area interrogated was 0.3 mm  $\times$  0.7 mm. All spectra were calibrated to 284.4 eV C-C peak for graphite, and deconvolution was performed using CasaXPS v2.3.22. Voigt peaks of a Gaussian/Lorentzian Product Form with 30% Lorentzian mix factor (GL 30, in some cases GL 10 in CasaXPS) was used as the line shape for the peak fitting, along with Shirley backgrounds.

### Bibliography for Chapter 4

- (1) Vaalma, C.; Buchholz, D.; Weil, M.; Passerini, S. *Nature Reviews Materials* **2018**, *3*, 1–11, DOI: [10.1038/natrevmats.2018.13](https://doi.org/10.1038/natrevmats.2018.13).
- (2) Larcher, D.; Tarascon, J.-M. *Nature Chemistry* **2015**, *7*, 19–29, DOI: [10.1038/nchem.2085](https://doi.org/10.1038/nchem.2085).
- (3) Song, J.; Xiao, B.; Lin, Y.; Xu, K.; Li, X. *Advanced Energy Materials* **2018**, *8*, 1703082, DOI: [10.1002/aenm.201703082](https://doi.org/10.1002/aenm.201703082).
- (4) Vaalma, C.; Buchholz, D.; Passerini, S. *Current Opinion in Electrochemistry* **2018**, *9*, 41–48, DOI: [10.1016/j.coelec.2018.03.031](https://doi.org/10.1016/j.coelec.2018.03.031).
- (5) Wu, X.; Leonard, D. P.; Ji, X. *Chemistry of Materials* **2017**, *29*, 5031–5042, DOI: [10.1021/acs.chemmater.7b01764](https://doi.org/10.1021/acs.chemmater.7b01764).
- (6) Hosaka, T.; Kubota, K.; Hameed, A. S.; Komaba, S. *Chemical Reviews* **2020**, *120*, 6358–6466, DOI: [10.1021/acs.chemrev.9b00463](https://doi.org/10.1021/acs.chemrev.9b00463).

- (7) Lenchuk, O.; Adelhelm, P.; Mollenhauer, D. *Physical Chemistry Chemical Physics* **2019**, *21*, 19378–19390, DOI: [10.1039/C9CP03453F](https://doi.org/10.1039/C9CP03453F).
- (8) Mogensen, R.; Brandell, D.; Younesi, R. *ACS Energy Letters* **2016**, *1*, 1173–1178, DOI: [10.1021/acsenergylett.6b00491](https://doi.org/10.1021/acsenergylett.6b00491).
- (9) Beard, K. W., *Linden's handbook of batteries*; McGraw-Hill Education: 2019.
- (10) Komaba, S.; Hasegawa, T.; Dahbi, M.; Kubota, K. *Electrochemistry Communications* **2015**, *60*, 172–175, DOI: [10.1016/j.elecom.2015.09.002](https://doi.org/10.1016/j.elecom.2015.09.002).
- (11) Ge, P.; Fouletier, M. *Solid State Ionics* **1988**, *28-30*, 1172–1175, DOI: [10.1016/0167-2738\(88\)90351-7](https://doi.org/10.1016/0167-2738(88)90351-7).
- (12) Peled, E.; Menkin, S. *Journal of The Electrochemical Society* **2017**, *164*, A1703, DOI: [10.1149/2.1441707jes](https://doi.org/10.1149/2.1441707jes).
- (13) Hui, J.; Schorr, N. B.; Pakhira, S.; Qu, Z.; Mendoza-Cortes, J. L.; Rodríguez-López, J. *Journal of the American Chemical Society* **2018**, *140*, 13599–13603, DOI: [10.1021/jacs.8b08907](https://doi.org/10.1021/jacs.8b08907).
- (14) Metrot, A.; Guerard, D.; Billaud, D.; Herold, A. *Synthetic Metals* **1980**, *1*, 363–369, DOI: [10.1016/0379-6779\(80\)90071-5](https://doi.org/10.1016/0379-6779(80)90071-5).
- (15) Xing, Z.; Qi, Y.; Jian, Z.; Ji, X. *ACS Applied Materials & Interfaces* **2017**, *9*, 4343–4351, DOI: [10.1021/acsami.6b06767](https://doi.org/10.1021/acsami.6b06767).
- (16) Luo, W.; Wan, J.; Ozdemir, B.; Bao, W.; Chen, Y.; Dai, J.; Lin, H.; Xu, Y.; Gu, F.; Barone, V.; Hu, L. *Nano Letters* **2015**, *15*, 7671–7677, DOI: [10.1021/acs.nanolett.5b03667](https://doi.org/10.1021/acs.nanolett.5b03667).
- (17) Markevich, E.; Salitra, G.; Aurbach, D. *ACS Energy Letters* **2017**, *2*, 1337–1345, DOI: [10.1021/acsenergylett.7b00163](https://doi.org/10.1021/acsenergylett.7b00163).
- (18) Tripathi, A. M.; Su, W.-N.; Hwang, B. J. *Chemical Society Reviews* **2018**, *47*, 736–851, DOI: [10.1039/C7CS00180K](https://doi.org/10.1039/C7CS00180K).
- (19) Zhang, J.; Cao, Z.; Zhou, L.; Liu, G.; Park, G.-T.; Cavallo, L.; Wang, L.; Alshareef, H. N.; Sun, Y.-K.; Ming, J. *ACS Energy Letters* **2020**, *5*, 2651–2661, DOI: [10.1021/acsenergylett.0c01401](https://doi.org/10.1021/acsenergylett.0c01401).
- (20) Hui, J.; Gossage, Z. T.; Sarbapalli, D.; Hernández-Burgos, K.; Rodríguez-López, J. *Analytical Chemistry* **2019**, *91*, 60–83, DOI: [10.1021/acs.analchem.8b05115](https://doi.org/10.1021/acs.analchem.8b05115).
- (21) Kubota, K.; Dahbi, M.; Hosaka, T.; Kumakura, S.; Komaba, S. *The Chemical Record* **2018**, *18*, 459–479, DOI: [10.1002/tcr.201700057](https://doi.org/10.1002/tcr.201700057).
- (22) Cano, Z. P.; Banham, D.; Ye, S.; Hintennach, A.; Lu, J.; Fowler, M.; Chen, Z. *Nature Energy* **2018**, *3*, 279–289, DOI: [10.1038/s41560-018-0108-1](https://doi.org/10.1038/s41560-018-0108-1).
- (23) Carboni, M.; Manzi, J.; Armstrong, A. R.; Billaud, J.; Brutti, S.; Younesi, R. *ChemElectroChem* **2019**, *6*, 1745–1753, DOI: [10.1002/celc.201801621](https://doi.org/10.1002/celc.201801621).
- (24) Dahbi, M.; Nakano, T.; Yabuuchi, N.; Fujimura, S.; Chihara, K.; Kubota, K.; Son, J.-Y.; Cui, Y.-T.; Oji, H.; Komaba, S. *ChemElectroChem* **2016**, *3*, 1856–1867, DOI: [10.1002/celc.201600365](https://doi.org/10.1002/celc.201600365).

- (25) Ponrouch, A.; Goñi, A.; Palacín, M. R. *Electrochemistry Communications* **2013**, *27*, 85–88, DOI: [10.1016/j.elecom.2012.10.038](https://doi.org/10.1016/j.elecom.2012.10.038).
- (26) Komaba, S.; Murata, W.; Ishikawa, T.; Yabuuchi, N.; Ozeki, T.; Nakayama, T.; Ogata, A.; Gotoh, K.; Fujiwara, K. *Advanced Functional Materials* **2011**, *21*, 3859–3867, DOI: [10.1002/adfm.201100854](https://doi.org/10.1002/adfm.201100854).
- (27) Cohn, A. P.; Share, K.; Carter, R.; Oakes, L.; Pint, C. L. *Nano Letters* **2016**, *16*, 543–548, DOI: [10.1021/acs.nanolett.5b04187](https://doi.org/10.1021/acs.nanolett.5b04187).
- (28) Nijamudheen, A.; Sarbapalli, D.; Hui, J.; Rodríguez-López, J.; Mendoza-Cortes, J. L. *ACS Applied Materials & Interfaces* **2020**, *12*, 19393–19401, DOI: [10.1021/acsami.9b23105](https://doi.org/10.1021/acsami.9b23105).
- (29) Wang, Y.; Liu, F.; Fan, G.; Qiu, X.; Liu, J.; Yan, Z.; Zhang, K.; Cheng, F.; Chen, J. *Journal of the American Chemical Society* **2021**, *143*, 2829–2837, DOI: [10.1021/jacs.0c12051](https://doi.org/10.1021/jacs.0c12051).
- (30) Liu, W.; Liu, P.; Mitlin, D. *Advanced Energy Materials* **2020**, *10*, 2002297, DOI: [10.1002/aenm.202002297](https://doi.org/10.1002/aenm.202002297).
- (31) Hui, J.; Nijamudheen, A.; Sarbapalli, D.; Xia, C.; Qu, Z.; Mendoza-Cortes, J. L.; Rodríguez-López, J. *Chemical Science* **2021**, *12*, 559–568, DOI: [10.1039/DOSC03226C](https://doi.org/10.1039/DOSC03226C).
- (32) Harris, K. C.; Tang, M. H. *The Journal of Physical Chemistry C* **2018**, *122*, 20632–20641, DOI: [10.1021/acs.jpcc.8b06564](https://doi.org/10.1021/acs.jpcc.8b06564).
- (33) Moshkovich, M.; Gofer, Y.; Aurbach, D. *Journal of The Electrochemical Society* **2001**, *148*, E155, DOI: [10.1149/1.1357316](https://doi.org/10.1149/1.1357316).
- (34) Huang, W.; Wang, H.; Boyle, D. T.; Li, Y.; Cui, Y. *ACS Energy Letters* **2020**, *5*, 1128–1135, DOI: [10.1021/acsenergylett.0c00194](https://doi.org/10.1021/acsenergylett.0c00194).
- (35) Boebinger, M. G.; Lewis, J. A.; Sandoval, S. E.; McDowell, M. T. *ACS Energy Letters* **2020**, *5*, 335–345, DOI: [10.1021/acsenergylett.9b02514](https://doi.org/10.1021/acsenergylett.9b02514).
- (36) Ventosa, E.; Schuhmann, W. *Physical Chemistry Chemical Physics* **2015**, *17*, 28441–28450, DOI: [10.1039/C5CP02268A](https://doi.org/10.1039/C5CP02268A).
- (37) Takahashi, Y.; Kumatani, A.; Munakata, H.; Inomata, H.; Ito, K.; Ino, K.; Shiku, H.; Unwin, P. R.; Korchev, Y. E.; Kanamura, K., et al. *Nature Communications* **2014**, *5*, 1–7, DOI: [10.1038/ncomms6450](https://doi.org/10.1038/ncomms6450).
- (38) Danis, L.; Gateman, S. M.; Kuss, C.; Schougaard, S. B.; Mauzeroll, J. *ChemElectroChem* **2017**, *4*, 6–19, DOI: [10.1002/celc.201600571](https://doi.org/10.1002/celc.201600571).
- (39) Kumatani, A.; Matsue, T. *Current Opinion in Electrochemistry* **2020**, *22*, 228–233, DOI: [10.1016/j.coelec.2020.07.010](https://doi.org/10.1016/j.coelec.2020.07.010).
- (40) Lipson, A. L.; Ginder, R. S.; Hersam, M. C. *Advanced Materials* **2011**, *23*, 5613–5617, DOI: [10.1002/adma.201103094](https://doi.org/10.1002/adma.201103094).
- (41) Bültner, H.; Peters, F.; Schwenzel, J.; Wittstock, G. *Angewandte Chemie International Edition* **2014**, *53*, 10531–10535, DOI: [10.1002/anie.201403935](https://doi.org/10.1002/anie.201403935).

- (42) Hui, J.; Burgess, M.; Zhang, J.; Rodríguez-López, J. *ACS Nano* **2016**, *10*, 4248–4257, DOI: [10.1021/acsnano.5b07692](https://doi.org/10.1021/acsnano.5b07692).
- (43) Zampardi, G.; La Mantia, F.; Schuhmann, W. *RSC Advances* **2015**, *5*, 31166–31171, DOI: [10.1039/C5RA02940F](https://doi.org/10.1039/C5RA02940F).
- (44) Barton, Z. J.; Rodríguez-López, J. *Analytical Chemistry* **2014**, *86*, 10660–10667, DOI: [10.1021/ac502517b](https://doi.org/10.1021/ac502517b).
- (45) Barton, Z. J.; Hui, J.; Schorr, N. B.; Rodríguez-López, J. *Electrochimica Acta* **2017**, *241*, 98–105, DOI: [10.1016/j.electacta.2017.04.105](https://doi.org/10.1016/j.electacta.2017.04.105).
- (46) Gossage, Z. T.; Hui, J.; Zeng, Y.; Flores-Zuleta, H.; Rodríguez-López, J. *Chem. Sci.* **2019**, *10*, 10749–10754, DOI: [10.1039/C9SC03569A](https://doi.org/10.1039/C9SC03569A).
- (47) Ventosa, E.; Wilde, P.; Zinn, A.-H.; Trautmann, M.; Ludwig, A.; Schuhmann, W. *Chemical Communications* **2016**, *52*, 6825–6828, DOI: [10.1039/C6CC02493A](https://doi.org/10.1039/C6CC02493A).
- (48) Bültner, H.; Schwager, P.; Fenske, D.; Wittstock, G. *Electrochimica Acta* **2016**, *199*, 366–379, DOI: [10.1016/j.electacta.2016.02.212](https://doi.org/10.1016/j.electacta.2016.02.212).
- (49) Dos Santos Sardinha, E.; Sternad, M.; R. Wilkening, H. M.; Wittstock, G. *ACS Applied Energy Materials* **2019**, *2*, 1388–1392, DOI: [10.1021/acsaem.8b01967](https://doi.org/10.1021/acsaem.8b01967).
- (50) Gossage, Z. T.; Hui, J.; Sarbapalli, D.; Rodríguez-López, J. *Analyst* **2020**, *145*, 2631–2638, DOI: [10.1039/C9AN02637A](https://doi.org/10.1039/C9AN02637A).
- (51) Oltean, V. A.; Philippe, B.; Renault, S.; Félix Duarte, R.; Rensmo, H.; Brandell, D. *Chemistry of Materials* **2016**, *28*, 8742–8751, DOI: [10.1021/acs.chemmater.6b04086](https://doi.org/10.1021/acs.chemmater.6b04086).
- (52) Kawaguchi, T.; Shimada, K.; Ichitsubo, T.; Yagi, S.; Matsubara, E. *Journal of Power Sources* **2014**, *271*, 431–436, DOI: [10.1016/j.jpowsour.2014.08.010](https://doi.org/10.1016/j.jpowsour.2014.08.010).
- (53) Cresce, A. v.; Russell, S. M.; Baker, D. R.; Gaskell, K. J.; Xu, K. *Nano Letters* **2014**, *14*, 1405–1412, DOI: [10.1021/nl404471v](https://doi.org/10.1021/nl404471v).
- (54) *Scanning Electrochemical Microscopy*; Bard A.J. and Mirkin, M., Ed.; CRC Press: 2022, DOI: [10.1201/9781003004592](https://doi.org/10.1201/9781003004592).
- (55) Sarbapalli, D.; Mishra, A.; Hatfield, K. O.; Gossage, Z. T.; Rodríguez-López, J. In *Batteries*; 2053–2563; IOP Publishing: 2021, 9–1 to 9–44, DOI: [10.1088/978-0-7503-2682-7ch9](https://doi.org/10.1088/978-0-7503-2682-7ch9).
- (56) Lefrou, C.; Cornut, R. *ChemPhysChem* **2010**, *11*, 547–556, DOI: [10.1002/cphc.200900600](https://doi.org/10.1002/cphc.200900600).
- (57) Tang, M.; Newman, J. *Journal of The Electrochemical Society* **2011**, *158*, A530, DOI: [10.1149/1.3567765](https://doi.org/10.1149/1.3567765).
- (58) Ritzert, N. L.; Rodríguez-López, J.; Tan, C.; Abruña, H. D. *Langmuir* **2013**, *29*, 1683–1694, DOI: [10.1021/la3042549](https://doi.org/10.1021/la3042549).
- (59) Yadav, A.; Wehrhold, M.; Neubert, T. J.; Iost, R. M.; Balasubramanian, K. *ACS Applied Nano Materials* **2020**, *3*, 11725–11735, DOI: [10.1021/acsanm.0c02171](https://doi.org/10.1021/acsanm.0c02171).

- (60) Kiani, A.; Alpuche-Aviles, M. A.; Eggers, P. K.; Jones, M.; Gooding, J. J.; Paddon-Row, M. N.; Bard, A. J. *Langmuir* **2008**, *24*, 2841–2849, DOI: [10.1021/la702811t](https://doi.org/10.1021/la702811t).
- (61) Barton, Z. J.; Rodríguez-López, J. *Analytical Chemistry* **2017**, *89*, 2716–2723, DOI: [10.1021/acs.analchem.6b04022](https://doi.org/10.1021/acs.analchem.6b04022).
- (62) Alpuche-Aviles, M. A.; Baur, J. E.; Wipf, D. O. *Analytical Chemistry* **2008**, *80*, 3612–3621, DOI: [10.1021/ac702568c](https://doi.org/10.1021/ac702568c).
- (63) Cogley, D. R.; Butler, J. N. *The Journal of Physical Chemistry* **1968**, *72*, 1017–1020, DOI: [10.1021/j100849a040](https://doi.org/10.1021/j100849a040).
- (64) Parimalam, B. S.; Lucht, B. L. *Journal of The Electrochemical Society* **2018**, *165*, A251, DOI: [10.1149/2.0901802jes](https://doi.org/10.1149/2.0901802jes).
- (65) Fondard, J.; Irisarri, E.; Courrèges, C.; Palacin, M. R.; Ponrouch, A.; Dedryvère, R. *Journal of The Electrochemical Society* **2020**, *167*, 070526, DOI: [10.1149/1945-7111/ab75fd](https://doi.org/10.1149/1945-7111/ab75fd).
- (66) Blyth, R.; Buqa, H.; Netzer, F.; Ramsey, M.; Besenhard, J.; Golob, P.; Winter, M. *Applied Surface Science* **2000**, *167*, 99–106, DOI: [10.1016/S0169-4332\(00\)00525-0](https://doi.org/10.1016/S0169-4332(00)00525-0).
- (67) Ells, A. W.; May, R.; Marbella, L. E. *ACS Applied Materials & Interfaces* **2021**, *13*, 53841–53849, DOI: [10.1021/acsami.1c15174](https://doi.org/10.1021/acsami.1c15174).
- (68) Murch, G.; Thorn, R. *Journal of Physics and Chemistry of Solids* **1980**, *41*, 785–791, DOI: [10.1016/0022-3697\(80\)90088-8](https://doi.org/10.1016/0022-3697(80)90088-8).
- (69) Eshetu, G. G.; Diemant, T.; Hekmatfar, M.; Grugueon, S.; Behm, R. J.; Laruelle, S.; Armand, M.; Passerini, S. *Nano Energy* **2019**, *55*, 327–340, DOI: [10.1016/j.nanoen.2018.10.040](https://doi.org/10.1016/j.nanoen.2018.10.040).
- (70) Edström, K.; Herstedt, M.; Abraham, D. P. *Journal of Power Sources* **2006**, *153*, 380–384, DOI: [10.1016/j.jpowsour.2005.05.062](https://doi.org/10.1016/j.jpowsour.2005.05.062).
- (71) Xiao, A.; Yang, L.; Lucht, B. L.; Kang, S.-H.; Abraham, D. P. *Journal of The Electrochemical Society* **2009**, *156*, A318, DOI: [10.1149/1.3078020](https://doi.org/10.1149/1.3078020).
- (72) An, S. J.; Li, J.; Daniel, C.; Mohanty, D.; Nagpure, S.; Wood, D. L. *Carbon* **2016**, *105*, 52–76, DOI: [10.1016/j.carbon.2016.04.008](https://doi.org/10.1016/j.carbon.2016.04.008).
- (73) Tan, J.; Matz, J.; Dong, P.; Shen, J.; Ye, M. *Advanced Energy Materials* **2021**, *11*, 2100046, DOI: [10.1002/aenm.202100046](https://doi.org/10.1002/aenm.202100046).
- (74) Ma, L. A.; Naylor, A. J.; Nyholm, L.; Younesi, R. *Angewandte Chemie International Edition* **2021**, *60*, 4855–4863, DOI: [10.1002/anie.202013803](https://doi.org/10.1002/anie.202013803).
- (75) Mandl, M.; Becherer, J.; Kramer, D.; Mönig, R.; Diemant, T.; Behm, R. J.; Hahn, M.; Böse, O.; Danzer, M. A. *Electrochimica Acta* **2020**, *354*, 136698, DOI: [10.1016/j.electacta.2020.136698](https://doi.org/10.1016/j.electacta.2020.136698).
- (76) Xu, K. *Chemical Reviews* **2004**, *104*, 4303–4418, DOI: [10.1021/cr030203g](https://doi.org/10.1021/cr030203g).

# Chapter 5

## A combined SECM and electrochemical AFM approach to probe interfacial processes affecting molecular reactivity at redox flow battery electrodes

*This work has been published. Citation:* Tylan S. Watkins\*, Dipobrato Sarbapalli\*, Michael J. Counihan\*, Andrew S. Danis, Jingjing Zhang, Lu Zhang, Kevin R. Zavadil, and Joaquín Rodríguez-López. “A combined SECM and electrochemical AFM approach to probe interfacial processes affecting molecular reactivity at redox flow battery electrodes” *J. Mater. Chem. A* **2020**, *8*, 15734–15745. DOI: [10.1039/D0TA00836B](https://doi.org/10.1039/D0TA00836B)

*Credit statement:* T.W. performed AFM and SIMS measurements under the direction of K.R.Z.; D.S. fabricated and characterized substrates, performed all SECM experiments, and converted images into kinetic maps via Matlab; A.S.D. performed macroelectrode experiments and fitting analysis; J.Z. synthesized molecules under the direction of L.Z. M.J.C designed experiments, compiled and analyzed data, created figures, and wrote the manuscript under the primary investigator J.R.-L.

Redox flow batteries (RFBs) are a promising technology for integrating renewable energy sources into the electrical grid at a large scale.[1, 2] In a RFB, soluble redox-active species (i.e. redoxmers) placed in a flow field engage in electron transfer (ET) reactions with current collectors, typically made out of carbon.[3] Graphitic carbons are one of the more cost-effective materials for redox flow battery electrodes, an essential aspect of scalability in these systems;[4, 5] therefore, we are motivated to understand the reactivity of the various features of graphitic electrodes towards redoxmers. Ideally, reactions with redoxmers only involve outer-sphere ET via electron tunneling to and from the electrode, observations of higher chemical and electrochemical complexity are pervasive in the field. These range from a strong sensitivity of ET kinetics to the presence of surface functional groups,[6] to the

---

\*denotes equal contribution

concentration of electrolyte and the redox active components,[7] and the charge-mediating properties of adsorbed redoxmer films,[8] and are further exacerbated by homogeneous reaction mechanisms.[9–11] Consequently, there is a pressing need to develop methodologies that address these complicating factors, especially in emerging technologies[12, 13] such as non-aqueous redox flow batteries (NRFBs). NRFBs maximize the potential of the synthetic organic toolbox for molecular design[10, 11] and device engineering[14–16] by utilizing organic solvents to access higher redox potential active species, thus increasing the battery’s energy density.[17] However, in comparison to aqueous technologies, NRFBs are incipient, and the interfacial reaction mechanisms underpinning the high redox potential redoxmers used in them remain largely unexplored. Understanding these mechanisms could provide additional insight to improve the efficiency of NRFBs[18–20] through identifying processes that hinder heterogeneous electron transfer (ET).

Film formation at the electrode/electrolyte interface is a common factor impacting ET since it results from several mechanisms, including precipitation driven by solute solubility,[21] interactions between electrolyte and redox components,[22] adsorption due to p–p stacking,[23, 24] or complex homogeneous mechanisms occurring in the diffusion layer.[25] These mechanisms depend on the chemistry of the catholyte or anolyte, the positive- and negative-side redox couples, respectively, that store charge in RFBs. For example, in a recent study of dialkoxybenzene (DAB) catholytes, it was observed that sterically protected molecules were able to cycle longer in RFBs than asymmetric, less-protected analogues.[26] The degradation of 2,3-dimethyl-1,4-dialkoxybenzene (also called C7) radical cations was proposed via a dimerization pathway where subsequent homogeneous reactions generated a dimer species (**Scheme 5.1**), which was argued as responsible for the decay of the coulombic efficiency over time.[26, 27] We postulate that in addition to deleterious homogeneous reactions, reactions occurring at the electrode surface also influence the battery lifetime in this system and other NRFBs. These heterogeneous processes may include assisting dimerization reactions, catalyzing catholyte or electrolyte

decomposition to form blocking films, or a combination of mechanisms (**Scheme 5.1**).

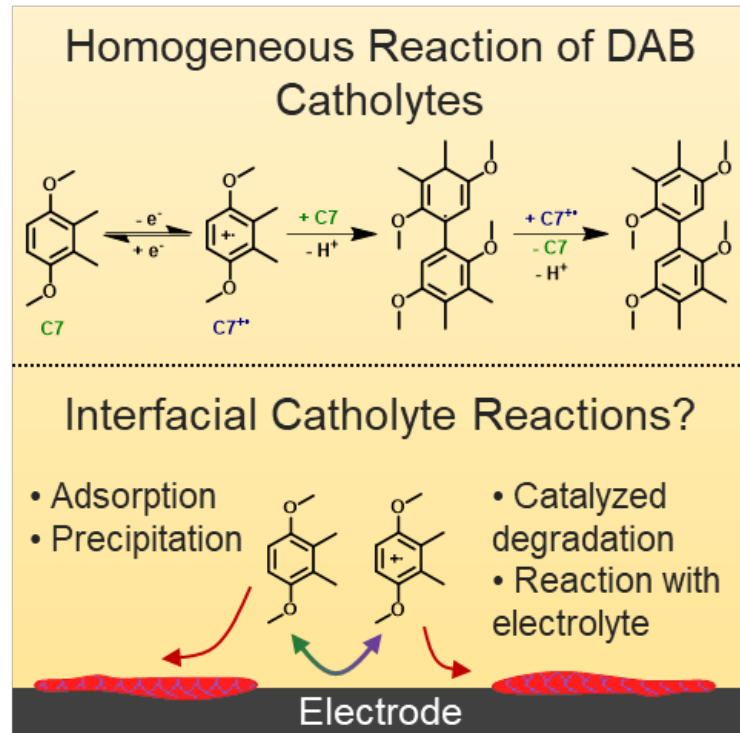


Figure 5.1: Decomposition of Dialkoxybenzene (DAB) Catholytes. (A) The dimerization of charged DAB molecules via homogeneous reaction as proposed in Ref. [27]. (B) The role of the electrode in interfacial degradation has not been thoroughly explored.

Herein, we establish a first step towards detecting changes in the ET rate constant for model DAB redoxmers as a function of electrode potential cycling history, electrode structure, and (preliminarily) electrolyte composition. We introduce scanning electrochemical microscopy (SECM) methodology to characterize spatiotemporally-resolved changes in the electron transfer (ET) behavior during electrode operation. In contrast to previous SECM studies of film and interphase formation on lithium-ion type systems, including those regarding cathodic or anodic solid electrolytes and those using DAB species as innocent mediators,[28–32] we are concerned with changes in the chemistry and electrochemistry of DAB redoxmers themselves at pristine carbon interfaces, as this is the relevant case for their use in RFBs. Complementing SECM, *in situ* atomic force microscopy (AFM) provides evidence about the formation of interfacial nanostructures that impact, and

ultimately control, the ET process. To unravel interfacial mechanisms in the DAB catholyte class, C1 (2,5-di-tert-butyl-1,4-bis(2-methoxyethoxy)benzene, also known as DBBB)[33] and C7 were compared due to their steric differences and proven cycling efficiencies (**Scheme 5.2**).[26, 27] Highly ordered pyrolytic graphite (HOPG) and single- and multilayer graphene (SLG, MLG) were used as model graphitic electrodes that enabled probing the reactivity of relevant surface structural motifs.[34–36] The complementarity of these two scanning probe techniques to diagnose electrode health in relation to mechanical and morphological changes at the interface will create new opportunities to understand what is (and what is not) consequential to cycle and/or shelf life in NRFB systems.

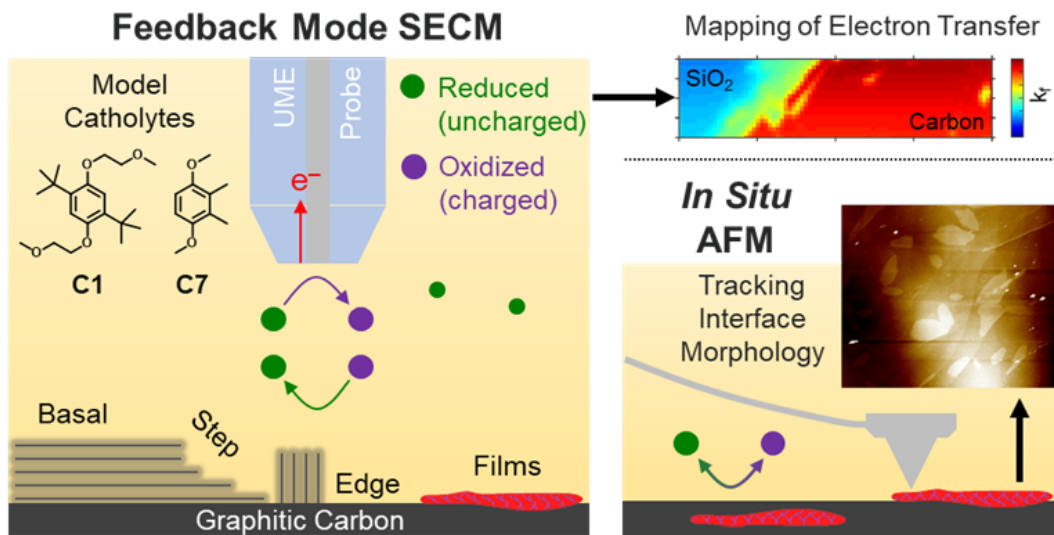


Figure 5.2: Interrogating Electrode Degradation during Catholyte Cycling. (Left, Top Right) SECM in the feedback mode was used to quantify changes in ET kinetics between different graphitic electrode structures and during cycling over time. (Bottom Right) In situ AFM was used to map morphological changes at the interface during catholyte cycling.

## 5.1 Materials and methods

### 5.1.1 Materials

All chemicals were purchased from commercial sources and used as received. Propylene carbonate (PC, anhydrous, 99.7%), lithium tetrafluoroborate ( $\text{LiBF}_4$ ,  $\geq 98\%$ ),

ferrocene (98%),  $\text{Li}_4\text{Ti}_5\text{O}_{12}$  (LTO, >99% Sigma Aldrich), and  $\text{LiFePO}_4$  (LFP, >97%) were purchased from Sigma-Aldrich. Lithium bis(tri-fluoromethanesulfonyl)imide (LiTFSI, 99.99%) was purchased from Ossila. Polyvinylidene fluoride (PVDF, high purity) was purchased from Solvay. Ketjen black (KB, <30 ppm metal impurity) was purchased from Alibaba. Propylene carbonate was used as the solvent here due to its low volatility in such a way that electrolyte and redoxmer concentrations during SECM and AFM testing were consistent over many hours of testing. C1 and C7 were synthesized via previously established procedures.[26, 27]

Multilayer graphene (MLG) was synthesized in house via chemical vapor deposition; details can be found in Appendix C(Section C.1.1). Single layer graphene (SLG) was purchased from GrollTex. Transfer of graphene onto  $\text{SiO}_2$ -coated Si wafers and characterization of samples by Raman, transmittance, and SEM can be found in the Appendix. Highly oriented pyrolytic graphite (HOPG, brand grade SPI-2, SPI) and solid slabs of flexible low density polyethylene (LDPE, 12"  $\times$  12"  $\times$  1/4" sheet, McMaster-Carr) were used for edge plane HOPG preparation, following previous work;[37] more details can also be found in Appendix C.

### 5.1.2 Scanning electrochemical microscopy

All SECM experiments were performed with CHI-920D scanning electrochemical microscope inside of an argon-filled glovebox ( $\text{O}_2 < 0.1 \text{ ppm}$ ,  $\text{H}_2\text{O} < 0.1 \text{ ppm}$ ) with substrates mounted in a custom Teflon cell. An ultramicroelectrode probe (UME) with a platinum wire electrode (radius of ca. 2  $\mu\text{m}$ ) sealed in patch clamp glass was brought within 2  $\mu\text{m}$  ( $L \approx 1$ ) of the substrate surface using the catholyte as a redox mediator. A 0.5 mm platinum wire and 1 mm silver wire were used as counter and quasi-reference electrode, respectively. All electrochemical potentials are reported as reference to the  $\text{Fc}/\text{Fc}^+$  couple in this electrolyte.

For redox imaging, the feedback mode of SECM was employed, in which the redox mediator was oxidized at the probe and re-reduced at the substrate electrode. This redox

recycling near the substrate electrode is known as positive feedback and leads to increased currents at the probe (**Scheme 5.2**). At a set probe-substrate distance, the current levels depend on the electron transfer rate of the carbon to the oxidized catholyte,[38] so differences in rates due to substrate heterogeneity will appear as higher or lower currents at the probe. Mass transfer limitations at the high current end (positive feedback, PF) and at the low current end (negative feedback, NF) provide an upper and lower bound for the rate constants that are measured; these bounds in all experimental results are indicated with green and red lines for PF and NF, respectively. All SECM images are presented as the probe current at each pixel,  $i$ , normalized to the probe current at semi-infinite distance from the substrate,  $i_\infty$ , i.e. in the bulk solution.

The nature of the electrode sample here is important in the calculation of kinetic rates. We used samples of single- or multilayer graphene (SLG and MLG) on SiO<sub>2</sub>-coated Si wafers, or HOPG sheets insulated in LDPE so that the sample exposed to solution was partially carbon (i.e., a conductor) and partially insulator (**Figure C.3**). This allows approach of the SECM probe to the insulator, leading to NF that does not depend on the kinetics of the mediator, so the exact distance from the substrate is known in each trial. A part of each SECM image always contained some insulator to ensure correct calibration of the probe-substrate distance for kinetic calculations.

Another important aspect of this sample geometry is the ability to perform open circuit (OCP) feedback measurements.[39–41] Since the probe electrode is orders of magnitude smaller than the substrate, only a fraction of substrate is impinged with charged catholyte during the imaging. When biased, electrons are forced through the circuit to reduce the DAB<sup>•+</sup>. However, at open circuit, an electron from a DAB or other species outside the probe range can be spontaneously transferred, conducted through the carbon, and given to a DAB<sup>•+</sup> at the substrate underneath the probe due to the potential difference between the two regions of the conductor, much like a bipolar electrode.[42] The kinetic rates calculated

from OCP feedback estimate the innate ability of the electrode to perform electron transfer, and these values are more indicative of changes compared to an external substrate bias generating a mass transfer-limited potential to reduce DAB<sup>•+</sup>. Thus, OCP imaging is more sensitive to changes in substrate behavior, as blocking films hinder not only the ability to re-reduce DAB<sup>•+</sup> underneath the probe but also the electrode's ability to transfer electrons everywhere in solution. OCP images only are shown here; the corresponding images biased at high overpotential can be found in Appendix C.

### 5.1.3 In situ atomic force microscopy

In situ AFM was conducted using a Bruker Dimension Fast Scan Microscope housed in an argon-filled glovebox ( $O_2 < 0.1$  ppm,  $H_2O < 0.1$  ppm). Imaging was conducted with ScanAsyst Fluid+ probes operated in Peak Force Tapping mode at a force setpoint between 200 and 600 pN, where variation is driven by differences in cantilever properties. Low force measurements are essential to minimize disruption of any surface films that form. HOPG crystals and graphene films were sealed with an O-ring in a bathtub style cell (430  $\mu L$  of electrolyte) equipped with  $Li_4Ti_5O_{12}$  (LTO)- and  $LiFePO_4$  (LFP)-coated Pt wires as counter and reference electrodes, respectively. Each active material in the counter and reference electrodes comprised 50 wt% of a composite with other constituents being 10 wt% PVDF and 40 wt% Ketjen black conductive carbon. LFP was pre-activated with cycling in the electrolyte prior to initiating the imaging experiments. HOPG crystals (grade ZYB, SPI supplies) were tape cleaved within the glove box just prior the imaging experiment.

### 5.1.4 Secondary ion mass spectrometry

SIMS analysis was performed on an IONTOF TOF.SIMS 5. system using a  $Bi_3^{2+}$  cluster to obtain both surface spectra and imaging. Images represent spatially correlated secondary ion emission determined by multivariate analysis of all spectra at all pixels.[43] The working electrodes were extracted from the cell, rinsed in dimethylcarbonate (anhydrous,

$\geq 99\%$ , Sigma-Aldrich), and allowed to dry in the glove box. Electrodes were transferred from glove box to SIMS spectrometer under Ar using a sealed transfer pod that prevents air exposure.

## 5.2 Results and discussion

We explored three NRFB components that may contribute to interfacial degradation: the chemical structure of the catholyte, the structure of the electrode, and the composition of the supporting electrolyte. Since molecule symmetry and sterics were shown to impact bulk behavior,[26, 27] we explored this aspect first by comparing the behaviors of C1 and C7 (**Scheme 5.2**).

### 5.2.1 Impact of catholyte chemical structure

**Figure 5.3** shows SECM images of MLG electrodes using C1 and C7 as the catholyte in 0.1 M LiBF<sub>4</sub>. The MLG electrodes presented a heterogeneous structure with a striped pattern displaying different number of graphitic layers (**Figure 5.3C**); the rate of electron transfer has been shown to be sensitive to the layer number,[44] so we used this structure to our advantage as it reveals changes in the heterogeneity of reactive sites at the MLG basal plane. Qualitatively comparing **Figure 5.3A** and **5.3B**, it is clear that C1 and C7 exhibit different degrees of reactive heterogeneity on MLG, as C1 reveals more of the underlying substrate structure than C7. However, MLG electrodes of identical structure were used for both catholytes, as shown by SEM, transmittance, and Raman characterization (**Figure 5.3C**, **C.1** and **C.2**). This suggests that C1 and C7 present differences in their electron transfer behavior at the interface. Thus, we turned to determining the distributions of rate constants for ET from the SECM feedback images.

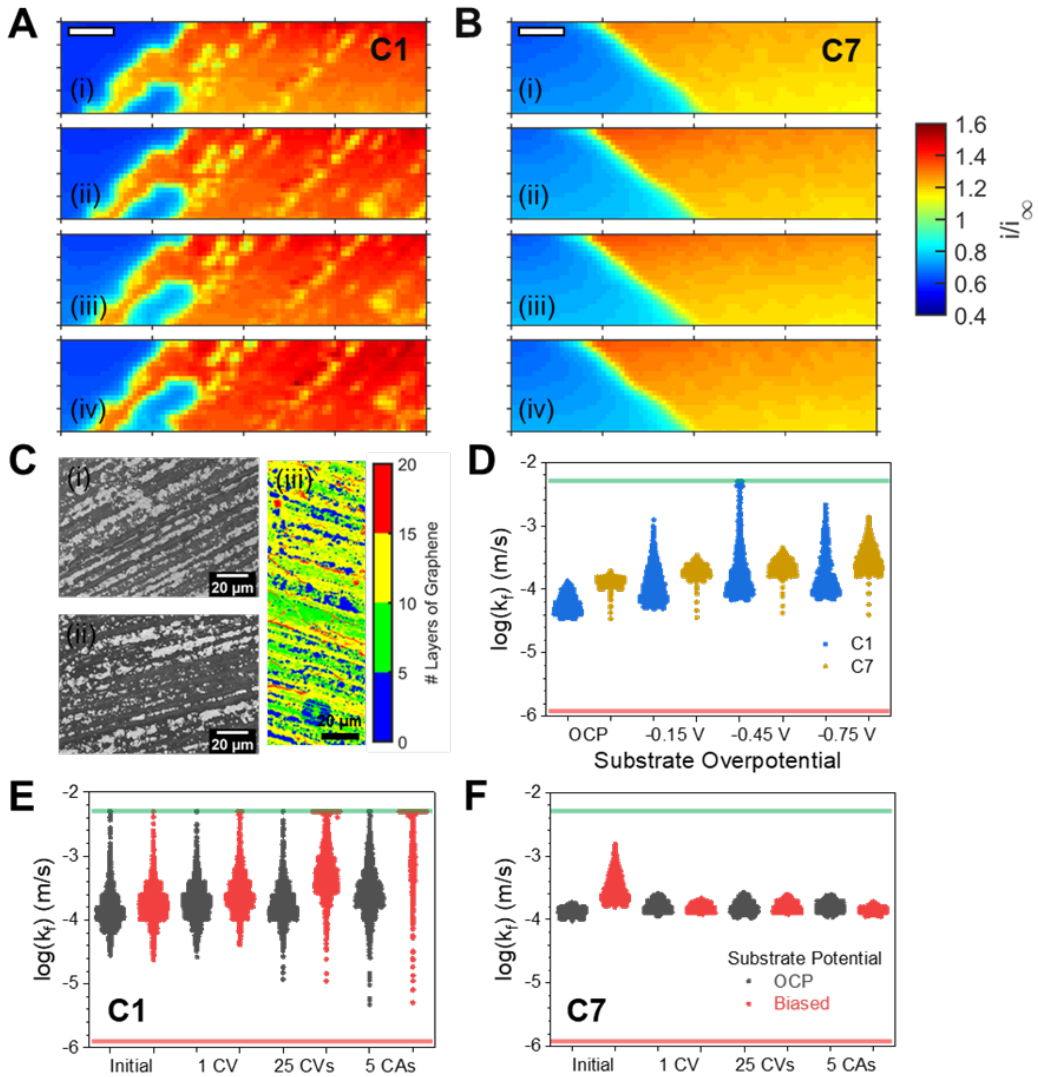


Figure 5.3: SECM of C1 and C7 on MLG Substrates. Normalized SECM images of an MLG electrode at open circuit with 5 mM (A) C1 and (B) C7 as catholyte mediator in LiBF<sub>4</sub> electrolyte; image scale bars are 20  $\mu\text{m}$ . Images were taken with the substrate electrode: (i) at the initial condition before substrate biasing, (ii) after 1 substrate CV, (iii) after 25 more substrate CVs, and (iv) after 5 sets of oxidative then reductive chronoamperograms (see Appendix C for more information). (C) SEM images of MLG substrates used for (i) C1 and (ii) C7 imaging. UV-VIS transmittance imaging (iii) reveals the graphitic layer number heterogeneity of these MLG electrodes. (D) Quantified kinetic values of C1 $^{\bullet+}$  (blue points) and C7 $^{\bullet+}$  (gold points) reduction at another MLG substrate as a function of substrate overpotential for the redox species. Points represent  $k_f$  values for a pixel over the substrate in SECM images, and the width of the distribution shows the relative population of pixels with that value. (E) Quantified kinetic values from C1 $^{\bullet+}$  reduction following the data in (A). (F) Quantified kinetic values from C7 $^{\bullet+}$  reduction following the data in (B). Green and red lines indicate the limits of quantification for positive and negative feedback, respectively, with our given electrode geometries.  $k_f$  values were quantified at substrate open circuit (gray points) and biasing the substrate (red points) at -0.2 V vs. Fc/Fc<sup>+</sup> which is ca. -0.75 V overpotential for the redox couples.

At a given tip-substrate distance, the kinetics of electron transfer in the feedback cycle determine the current at the tip: extremely fast kinetics give a totally mass transport-limited current known as positive feedback (PF), while extremely sluggish kinetics result in a lower limit known as negative feedback (i.e., NF, dominated by hindered mass transport). In contrast, ET limited by the chemistry or electrochemistry at the substrate will give mixed responses and currents in between these two limits. Rate constants in the range of  $10^{-6}$  to  $10^{-3}$  m/s can be confidently quantified using our probe geometry. Inspection of C7 rate constant plots versus overpotential applied at the substrate show that the forward rate constant for ET ( $k_f$ ) for reduction of tip-generated C7 $\bullet^+$  at the substrate does not approach the mass transport-limited value (green confidence interval) characteristic of positive feedback. At the overpotentials explored in **Figure 5.3D**, the rate constant for ET did not scale as predicted by the Butler–Volmer model with a commonly assumed value for  $\alpha \approx 0.5$ , as deduced from **Eqn. 5.1** and **5.2**:

$$k_f = k^0 e^{\frac{-\alpha F \eta}{RT}} \quad (5.1)$$

$$\ln k_f = \ln k^0 - \left( \frac{-\alpha F}{RT} \right) \eta \quad (5.2)$$

where  $k_f$  is the forward rate constant for reducing the oxidized molecule,  $k^0$  is the standard rate constant intrinsic to the redox couple,  $\alpha$  is the transfer coefficient,  $F$  is Faraday's constant,  $R$  is the gas constant,  $T$  is the temperature, and  $\eta$  is the applied overpotential, here defined as  $\eta = E - E^0$ , where  $E$  is the electrode potential and  $E^0$  is the standard redox potential of the molecule.

Analysis of the slopes (**Eqn 5.2**) using the median value for  $k_f$  in **Figure 5.3D** shows that the experimental values of  $\alpha$  are 0.028 and 0.017 respectively for C1 and C7. For a typical outer-sphere process, one would expect an  $\alpha$  of 0.5; at overpotentials past 0.15 V, this

would result in higher SECM currents closer to the positive feedback mass transport limit, as has been seen on debris-free graphitic electrodes.[45] For standard redox couples,  $\alpha$  in a range of 0.3 to 0.7 has been observed on graphene.[46] However, ET behavior can be variable depending of the number of layers of graphene.[47–49] On single layer graphene, SECM showed that redox mediators with finite kinetics ( $\text{Ru}(\text{NH}_3)_6^{3+}$ , hydroxymethylferrocene, etc.) display  $\alpha$  values of 0.1 and 0.9, well outside the expected range.[50] In our case, the exceptionally low  $\alpha$  values may extend beyond the attenuation of  $\alpha$  from the graphene surface alone. These trends might arise from the presence of a pinhole or porous film,[28, 51] the redox species being adsorbed to the electrode,[52] or the presence of a redox-active film mediating ET.[53] This suggests that in the case of C7, and to a lesser extent C1, kinetic control of the rate of ET originates from interfacial structures that are an interplay of the redox active molecule and the graphitic electrode.

Cyclic voltammetry of an MLG electrode cycled in C1 or C7 and tested in blank electrolyte after thorough rinsing showed evidence of a redox-active species remaining at the electrode (**Figure C.11, C.12, C.13** and **C.14**). While C1 displayed trace amounts of this residual species (which disappeared after cycling), C7 displayed a pronounced CV feature. The voltammetric profile for this feature did not display the typical characteristics of a surface-confined redox species (i.e. no peak-to-peak separation, and a Gaussian profile), but its resilience to rinsing and prolonged cycling, as well as the absence of C7 in solution (as probed through an independent Pt UME placed in the electrolyte) strongly suggest its association with the MLG surface. Multi-layer redox-active films often display diffusional limitations in their charge transfer, leading to similar voltammetric profiles even when surface bound.[54, 55] We hypothesize that if a redox-active film is controlling electron transfer rates, then the transfer properties would be determined by the reduced or oxidized population of the film.[56] At the probed potentials, all species based on the DAB core would be in the reduced state, and assuming a uniform surface coverage, a similar rate across the entire electrode regardless of overpotential is expected; this is consistent with **Figure 5.3D** and is

indeed observed in **Figure 5.3F**, where this effect is shown to be highly resilient to cycling. We cannot discard that, in addition to this potential redox-active film, contributions from pinholes in a surface film also play a role in controlling the rate of ET, as this would also give virtually potential-independent  $k_f$  values.[28, 51] Further support for the presence of a film can be obtained from the distribution of rate constants in **Figure 5.3E** and **5.3F**: C1 shows a wider distribution of kinetics, which speaks to the participation of the various surface features inherent to the MLG electrode on the ET process, while C7 is very consistent, suggesting a more homogeneous interface as would be expected for an abundant film covering the electrode.

Cycling the substrate with cyclic voltammetry (CV) perturbs the measured rates from the pristine condition, as seen by the  $k_f$  increase from “Initial” to “1 CV” in **Figure 5.3E** and **5.3F** and in the SECM images in **Figure 5.3A** and **5.3B**. This indicates that some initial thin film forms spontaneously (at least on the order of time of our experiments) and continuously across the electrode when assembled in the cell and solution is added. This initial film is perturbed only once electrochemistry is performed with this substrate electrode, leading to the observed changes in  $k_f$ . Further cycling, either through CV or alternating oxidative–reductive potential holds (chronoamperometry, CA) show very little rate drop, which suggests a self-limiting film mechanism if films are forming and controlling rates (**Figure 5.3E** and **5.3F**) as opposed to continued growth and passivation. Thus, to see how these films form and under what conditions, we turned to *in situ* AFM.

AFM of HOPG shows clear basal planes and step edges that are relatively clean before any electrochemistry is performed (**Figure 5.4A** and **5.4E**). When oxidizing either C1 or C7, virtually no debris or filming is seen (**Figure 5.4B** and **5.4F**). After reducing the radical cations, present in the diffusion layer after an oxidation step, surface products begin to form. In the case of C1 (**Figure 5.4C**), some particulate debris forms on step edges. In the case of C7 ((**Figure 5.4F**), small islands of film, nominally 0.5 nm thick (**Figure C.17**),

form on the basal plane and grow the longer the reducing potential is held until reaching the limiting sizes observed in **Figure 5.4G**.

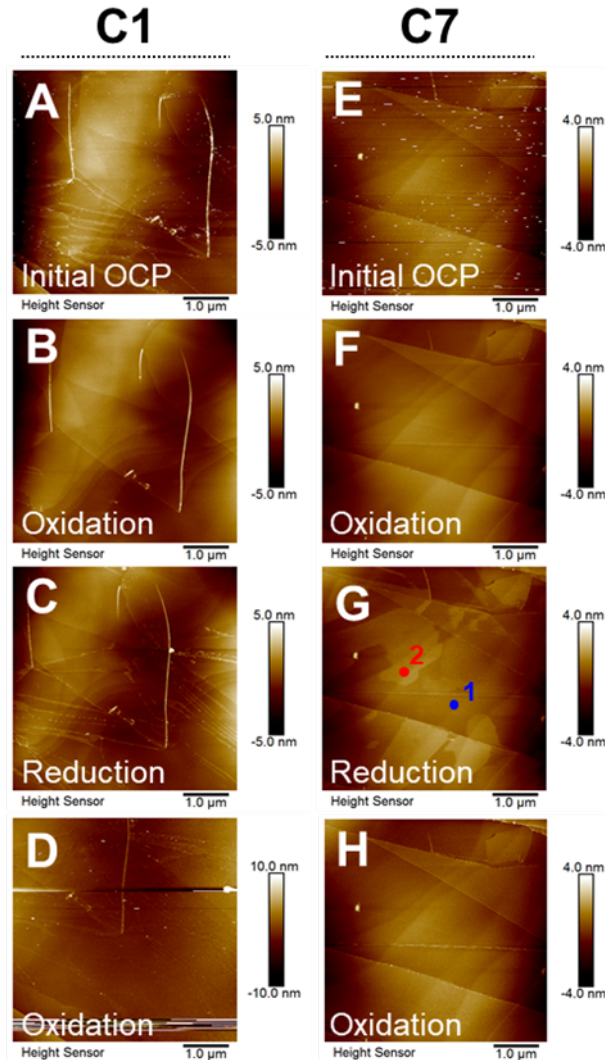


Figure 5.4: AFM Imaging of C1 and C7 on HOPG Electrodes. In situ AFM images of the HOPG surface: prior to any electrochemistry at open circuit (Initial OCP), during an anodic potential step (oxidation), during a cathodic potential step (reduction), and a subsequent oxidation step with 5 mM C1 (A-D) and C7 (E-H) catholytes in LiBF<sub>4</sub> electrolyte. Points 1 and 2 in (G) refer to relatively bare HOPG and island films, respectively, as discussed in the text.

To help identify the origin of these films, nanomechanical mapping was employed to determine film properties. Comparison of the maximum force required to remove the silicon nitride cantilever tip from the surface shows that the adhesive force for the film is 300

pN lower than the graphite basal plane (**Figure C.17**). Reduced tip-film adhesion relative to graphite could be a result of tip-induced removal of the outer weakly adherent molecular layer. We note that low adhesion forces are reported for polycyclic aromatic hydrocarbons (e.g. 55 pN for pyrene) on the graphite basal plane in aqueous media.<sup>[57]</sup> We also find that the films are more mechanically compliant as measured from cantilever retraction curves using a DMT-based analysis.<sup>[58]</sup> A map of effective elastic modulus (**Figure C.17**) yields a discernable, uniform decrease in magnitude for the filmed regions relative to the basal plane. A more mechanically compliant response is reasonable for  $\pi$ -stacked DAB molecules on the basal plane given the absence of extended lateral bonding of aromatic rings. We emphasize that this modulus comparison is qualitative as the limiting thickness of these films (0.5 nm) is below the typical extent of surface deformation ( $\approx$ 2 nm) required for quantitative measurements of elastic modulus. Together, these mechanical properties support the notion that an organically derived film builds on the basal planes of graphitic carbon during reductive conditions. Additionally, C1 does not show these basal plane deposits (**Figure 5.4C**), indicating that the chemistry of catholyte might determine the surface products. Indeed, as pointed out in **Scheme 5.1**, product analysis of bulk electrolysis of related DAB molecules have shown that dimerization processes are observed for sterically unhindered species.<sup>[26, 27]</sup> This is a process that potentially occurs in the diffusion layer at the vicinity of the MLG electrode, although it would likely lead to the formation of a chemically irreversible dimer that may precipitate or adsorb on the electrode surface.

Nonetheless, re-oxidation of the catholyte quickly refreshes the electrode surface, with most films and edge deposits disappearing in subsequent AFM images (**Figure 5.4D** and **5.4H**). The application of a potential bias may electrostatically desorb these films, but it is also possible that these potentials change the redox state of the films (i.e., neutral to positively charged) and thus increase their solubility. This result indicates that interfacial reactivity is mostly reversible and helps explain why little passivation is seen over the course of SECM experiments while cycling the electrodes. We note that the SECM experiments are

always performed under conditions where the oxidized products of C1 and C7 are generated above the MLG plane, so any mechanisms resulting from radical cation reactions would be operating during all experiments and the consequences apparent in all results. The adsorption of the reduced form of a redox couple inhibiting electron transfer to the oxidized form on carbon surfaces has been observed for cobalt phenanthroline complexes;<sup>[59]</sup> it is likely that a similar phenomenon with C7 or C7-based products is taking place here.

### 5.2.2 Impact of electrode structure

AFM images showed different surface structures at step edges and basal planes. To determine the impact of these electrode structures on catholyte reactivity, we “deconstructed” multilayer graphitic carbon to pure basal plane (SLG) and edge plane (HOPG edge) electrodes.

Extended cycling of C1 on SLG shows a distinct lowering of feedback current at substrate open circuit, corresponding to an order of magnitude drop in median  $k_f$  values (**Figure 5.5A** and **5.5B**). The distribution of  $k_f$  values also shrinks, suggesting a film has formed that controls the electron transfer rate as in the case of C7 on MLG (**Figure 5.3F**). **Figure 5.5B** and **5.5C** for C1 and C7 on SLG show a slight improvement in kinetics when biasing the electrode at -0.2 V vs. the case for OCP, consistent with the reversible reactivity of these filmed interfaces and the redox mediating role of the films. This result highlights the power of open circuit feedback imaging, where subtle changes in reactivity in biased imaging are exacerbated at open circuit due to the mechanism of electron shuttling.<sup>[38, 42]</sup>

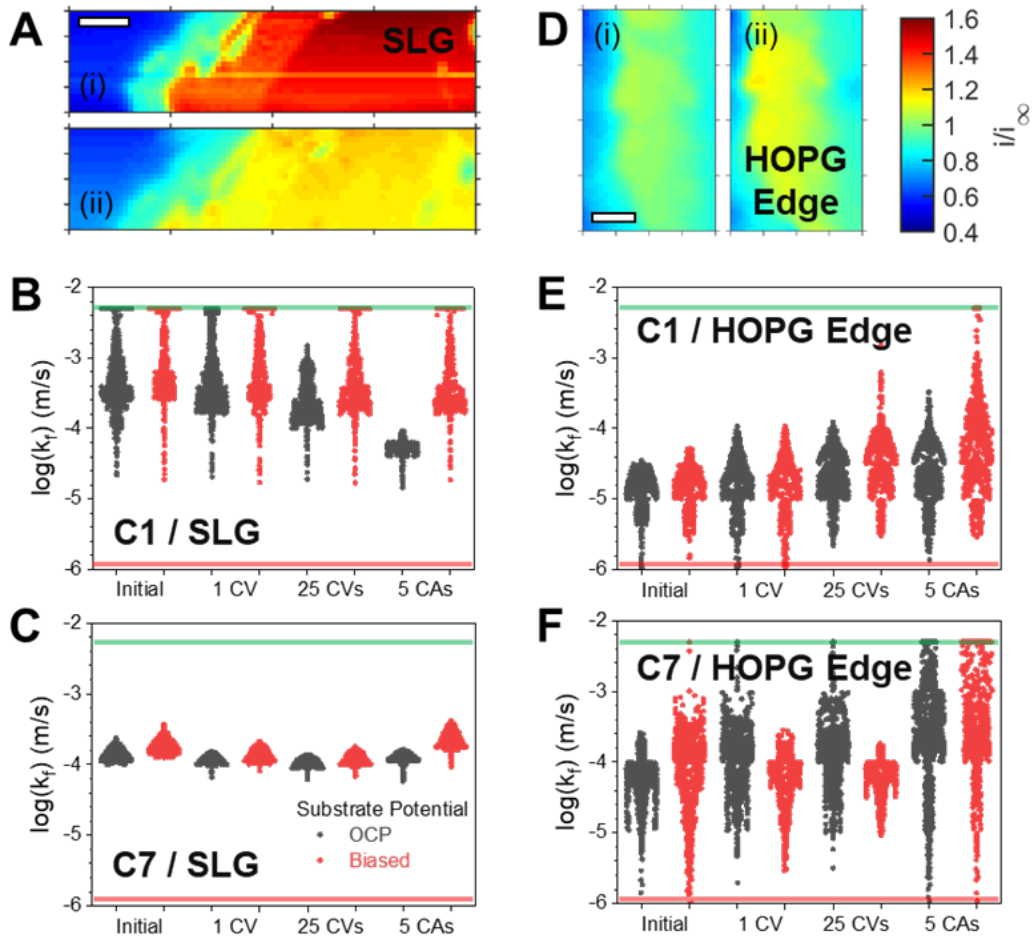


Figure 5.5: Comparison of SLG and HOPG Edge Electrodes. Normalized SECM images with 5 mM C1 catholyte mediator in LiBF<sub>4</sub> electrolyte on (A) SLG and (D) HOPG edge substrates at open circuit. Image scale bars are 20  $\mu\text{m}$ ; images were taken (i) at the initial condition before substrate biasing and (ii) after 26 substrate CVs and 5 CAs. Quantified kinetic values for C1<sup>•+</sup> reduction on (B) SLG and (E) HOPG edge electrodes at OCP (gray points) and biased at -0.2 V for SLG and 0.0 V for HOPG edge (red points). Quantified kinetic values for C7<sup>•+</sup> reduction on (C) SLG and (F) HOPG edge electrodes at OCP (gray points) and biased at -0.2 V for SLG and -0.3 V for HOPG edge (red points). Green and red lines indicate the limits of quantification for positive and negative feedback, respectively, with our given electrode geometries.

C7 kinetics on SLG decrease slightly with cumulative redox cycling, but not nearly as much as C1. The C7-SLG behavior is more similar to MLG, indicating that the C7-based film is more ubiquitous on basal planes than C1. We speculate a C1-based film requires the more reactive surface of SLG on SiO<sub>2</sub> to form, as the underlying support greatly influences

the electronic properties of SLG electrodes,[24] or through the natural corrugation of SLG surfaces.[46]

HOPG edge electrodes with the prismatic planes of HOPG exposed to solution show relatively slow kinetics and wide distributions with both catholytes (**Figure 5.5D-5.5F**). These attributes likely result from the uneven nature of the sample, which complicates the fitting procedure (**Figure C.5**). Nonetheless, no passivation is seen for C1 or C7 on HOPG edges; if anything, the feedback current actually increases over time. This indicates that little to no decomposition and byproduct accumulation takes place at step edges and is inconsequential for electron transfer. This is a surprising finding, since edges have higher surface energy compared to basal planes[60] and would be expected to affect more decomposition; HOPG step edges have been known to show increased redox mediator activity.[61] From this, we infer that the films discussed above form on basal planes aided by  $\pi-\pi$  interactions,[62–64] coming from the catholyte or catholyte-derived species, which is plausible given the structure of C1 and C7.

### 5.2.3 Impact of electrolyte composition

We next wanted to understand if these film-forming mechanisms are generalized across electrolytes given the testing conditions used here with C1 and C7 catholytes. Electrolyte effects may impact the solubility and adsorption properties of the radical cations and any newly formed species. In addition, different mechanisms at highly polarized electrodes could take place due to differences in the structure of the double layer. We compared LiBF<sub>4</sub> and LiTFSI electrolytes to determine if and how anions impact catholyte stability at the interface.

For C1 in LiTFSI, similar long-term trends are seen as with C1 on MLG with LiBF<sub>4</sub> electrolyte, where an initial increase in kinetics at OCP levels off after CV and CA cycles (**Figure 5.6A** and **5.6B**). However, no striations with different kinetic values are seen in the images, and the  $k_f$  distributions are smaller, indicating that a film is obscuring

the heterogeneity of the substrate seen in the case of C1-MLG-LiBF<sub>4</sub> (**Figure 5.3A**). Additionally, biasing the electrode at reducing potentials actually slightly decreases the kinetic values during imaging (**Figure 5.6B**). This may indicate that reduction of catholyte radical species in the presence of TFSI<sup>-</sup> causes active film formation that hinders electron transfer, though again the film dissipates after cycling (**Figure C.24**).

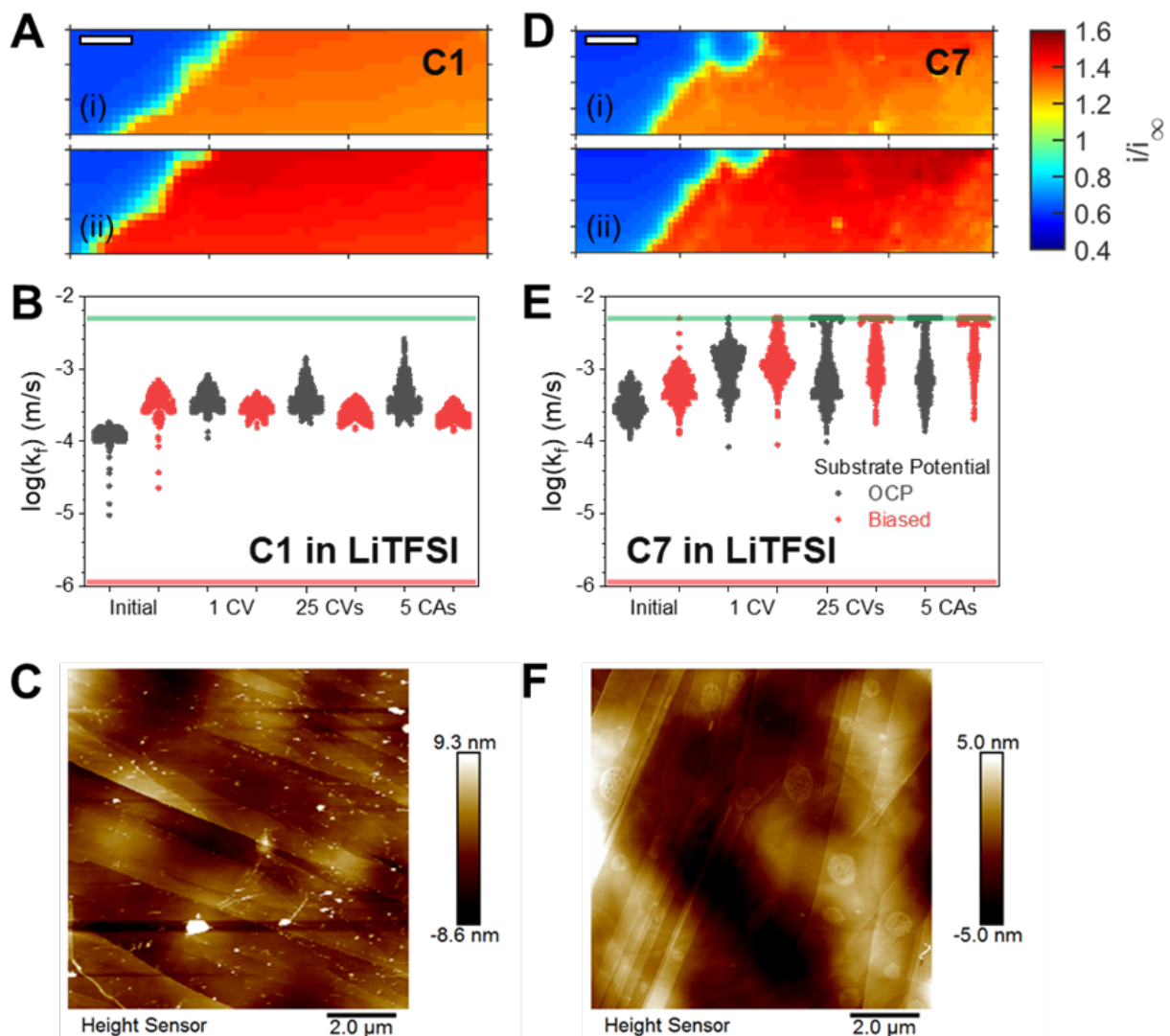


Figure 5.6: Comparing Behavior with LiTFSI Electrolyte. Normalized SECM images of MLG substrates at open circuit with 5 mM (A) C1 and (D) C7 catholyte mediators in 0.1 M LiTFSI electrolyte. Image scale bars are 20  $\mu\text{m}$ ; images were taken (i) at the initial condition before substrate biasing and (ii) after 26 substrate CVs and 5 CAs. Quantified kinetic values for (E)  $\text{C}1^{\bullet+}$  and (F)  $\text{C}7^{\bullet+}$  reduction at OCP (gray points) and biased (red points) at -0.5 V for C1 and -0.1 V for C7. Green and red lines indicate the limits of quantification for positive and negative feedback, respectively, with our given electrode geometries. In situ AFM images of HOPG electrodes with (C) C1 and (F) C7 catholytes in LiTFSI electrolyte following reductive holds to reduce oxidized catholyte.

An opposite trend is seen for C7-MLG-LiTFSI (Figure 5.6D and 5.6E), where striations now appear and kinetics are faster and more distributed compared to the LiBF<sub>4</sub> electrolyte (Figure 5.3B). Perhaps in LiTFSI, C7-based films are less stable or less favorable

to form and thus do not uniformly cover the electrode, exposing its heterogeneity. AFM images (**Figure 5.6F**) show that C7 cycling in LiTFSI still forms films on the basal plane, but the films are more porous than those in LiBF<sub>4</sub>. More porous films in conjunction with a return of substrate heterogeneity in SECM lends credence to one of our hypotheses about pinhole films controlling the kinetics of electron transfer in the C7 catholyte system. C1 in LiTFSI electrolyte shows substantially more debris forming than in LiBF<sub>4</sub>, though no films form like in the case of C7 (**Figure 5.6C**). This debris, if insulating, would act in much the same way as a pinhole film where electrode sites are blocked, thus limiting overall feedback. Overall, however, both LiBF<sub>4</sub> and LiTFSI seem to be compatible with both C1 and C7 catholytes, since no catastrophic irreversible passivation is seen on this scale of redox activity. LiTFSI has actually been shown to be an optimal (co-)salt for C1 as it enables better solubility and conductivity.<sup>[33]</sup>

Finally, to determine the chemical makeup of these surface decomposition products, we employed SIMS ex situ on HOPG samples cycled in C7 (**Figure 5.7**). While the composition of the filmed electrode is complex and no distinct organic polymeric species can be distinguished (e.g., the C7 dimer, **Scheme 5.1**), both inorganic and organic compounds were detected. The higher mass ions could indicate polymerization reactions involving the PC solvent with itself or between the solvent and the catholyte. An active role of the electrolyte is consistent with the formation of C–F and Li–F species indicating electrolyte decomposition is taking place. Since both the redox species and solvent contain C–O species, it is difficult to tell if solvent decomposition or catholyte decomposition originate the species detected at high m/z ratios (**Figure 5.7A**, inset).

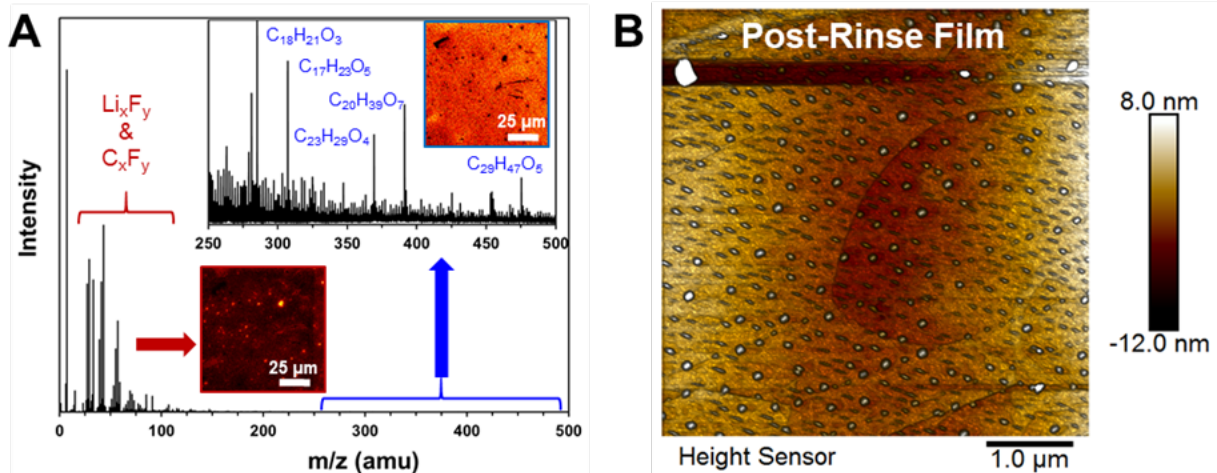


Figure 5.7: Post-Cycling SIMS Analysis of Decomposition Products. ToF-SIMS positive ion spectra and composition maps of an HOPG surface sample after cycling in a C7-LiBF<sub>4</sub>-PC electrolyte (monomer C<sub>10</sub>H<sub>14</sub>O<sub>2</sub>; dimer C<sub>20</sub>H<sub>14</sub>O<sub>2</sub>). Li<sub>x</sub>F<sub>y</sub> and C<sub>x</sub>F<sub>y</sub> species and larger organic species are prevalent as indicated by secondary ion generation in the low and high mass regions of the spectrum, respectively. Compositional maps (inset) show the organic components uniformly distributed across the surface with isolated regions of high inorganic content.

Additionally, these chemistries can be heterogeneous across the electrode, as shown in the mapping of inorganic vs. organic products on this sample (**Figure 5.7A**, inset images). It appears that small inorganic particulates are embedded in a more homogeneous organic film. It remains unclear how much of the generated surface products are retained after the careful rinsing procedure, but these preliminary experiments are a promising first step for understanding the chemical mechanisms underlying structural evolution of the interface. We are currently developing *in situ* spectroelectrochemical systems to identify specific product chemistries and directly correlate electrode structure (i.e., graphene layer number, defect density) with local electrochemical activity.<sup>[65]</sup>

### 5.3 Conclusions

We established a methodology using the advantages of both SECM and AFM to interrogate the impact of interfacial processes on electron transfer for a model catholyte in

NRFBs. SECM enabled the quantification of ET kinetics as well as the heterogeneity in electrode behavior, suggesting reactivity differences for similar dialkoxybenzene molecules C1 and C7. Inmost cases, but certainly at the basal plane of MLG and SLG, C1 and C7 failed to reach mass transfer limited reactivity at high overpotential for reduction of the corresponding radical cations, suggesting the formation of interfacial structures which controlled the reaction kinetics. AFM confirmed the formation of surface films with distinct mechanical properties; these films formed conditionally on electrodes and were correlated to the reactive changes observed in SECM experiments. Voltammetric analysis revealed that these films are redoxactive, although their kinetic stability towards desorption on the MLG surface differs, with that formed with C7 being more persistent. SIMS analysis on these films showed they contain both organic and inorganic components, suggesting the participation of the supporting electrolyte in the film formation process, although the mechanisms of formation seem complex. We further observed that electron transfer on the edge plane was relatively insensitive to the formation of these surface products, while monolayer graphene exhibited more pronounced decreases in reactivity as the electrode was cycled. These rate-limiting films seem to affect primarily the basal plane of graphitic carbons, a likely indication of  $\pi-\pi$  interactions, thus suggesting new directions in the fabrication or treatment of electrodes with better resilience against these unwanted processes. Altogether, this integrated methodology opens new opportunities in the characterization of redox processes for RFBs, including aqueous and non-aqueous systems, where interfacial processes associated with adsorption and film formation may become dominating at high active concentrations.

## Bibliography for Chapter 5

- (1) Yang, Z.; Zhang, J.; Kintner-Meyer, M. C. W.; Lu, X.; Choi, D.; Lemmon, J. P.; Liu, J. *Chemical Reviews* **2011**, *111*, 3577–3613, DOI: [10.1021/cr100290v](https://doi.org/10.1021/cr100290v).
- (2) Zhen, Y.; Zhang, C.; Yuan, J.; Zhao, Y.; Li, Y. *Journal of Power Sources* **2020**, *445*, 227331, DOI: [10.1016/j.jpowsour.2019.227331](https://doi.org/10.1016/j.jpowsour.2019.227331).
- (3) Weber, A. Z.; Mench, M. M.; Meyers, J. P.; Ross, P. N.; Gostick, J. T.; Liu, Q. *Journal of applied electrochemistry* **2011**, *41*, 1137–1164, DOI: [10.1007/s10800-011-0348-2](https://doi.org/10.1007/s10800-011-0348-2).

- (4) Chakrabarti, M.; Brandon, N.; Hajimolana, S.; Tariq, F.; Yufit, V.; Hashim, M.; Hussain, M.; Low, C.; Aravind, P. *Journal of Power Sources* **2014**, *253*, 150–166, DOI: [10.1016/j.jpowsour.2013.12.038](https://doi.org/10.1016/j.jpowsour.2013.12.038).
- (5) Ha, S.; Gallagher, K. G. *Journal of Power Sources* **2015**, *296*, 122–132, DOI: [10.1016/j.jpowsour.2015.07.004](https://doi.org/10.1016/j.jpowsour.2015.07.004).
- (6) Kim, K. J.; Park, M.-S.; Kim, Y.-J.; Kim, J. H.; Dou, S. X.; Skyllas-Kazacos, M. *Journal of Materials Chemistry A* **2015**, *3*, 16913–16933, DOI: [10.1039/C5TA02613J](https://doi.org/10.1039/C5TA02613J).
- (7) Roznyatovskaya, N.; Noack, J.; Pinkwart, K.; Tübke, J. *Current Opinion in Electrochemistry* **2020**, *19*, 42–48, DOI: [10.1016/j.coelec.2019.10.003](https://doi.org/10.1016/j.coelec.2019.10.003).
- (8) Burgess, M.; Hernández-Burgos, K.; Schuh, J. K.; Davila, J.; Montoto, E. C.; Ewoldt, R. H.; Rodríguez-López, J. *Journal of the American Chemical Society* **2018**, *140*, 2093–2104, DOI: [10.1021/jacs.7b08353](https://doi.org/10.1021/jacs.7b08353).
- (9) Goulet, M.-A.; Tong, L.; Pollack, D. A.; Tabor, D. P.; Odom, S. A.; Aspuru-Guzik, A.; Kwan, E. E.; Gordon, R. G.; Aziz, M. J. *Journal of the American Chemical Society* **2019**, *141*, 8014–8019, DOI: [10.1021/jacs.8b13295](https://doi.org/10.1021/jacs.8b13295).
- (10) Sevov, C. S.; Hickey, D. P.; Cook, M. E.; Robinson, S. G.; Barnett, S.; Minteer, S. D.; Sigman, M. S.; Sanford, M. S. *Journal of the American Chemical Society* **2017**, *139*, 2924–2927, DOI: [10.1021/jacs.7b00147](https://doi.org/10.1021/jacs.7b00147).
- (11) Yan, Y.; Robinson, S. G.; Sigman, M. S.; Sanford, M. S. *Journal of the American Chemical Society* **2019**, *141*, 15301–15306, DOI: [10.1021/jacs.9b07345](https://doi.org/10.1021/jacs.9b07345).
- (12) Ding, Y.; Zhang, C.; Zhang, L.; Zhou, Y.; Yu, G. *Chem* **2019**, *5*, 1964–1987, DOI: [10.1016/j.chempr.2019.05.010](https://doi.org/10.1016/j.chempr.2019.05.010).
- (13) Luo, J.; Hu, B.; Hu, M.; Zhao, Y.; Liu, T. L. *ACS Energy Letters* **2019**, *4*, 2220–2240, DOI: [10.1021/acsenergylett.9b01332](https://doi.org/10.1021/acsenergylett.9b01332).
- (14) Burgess, M.; Moore, J. S.; Rodríguez-López, J. *Accounts of Chemical Research* **2016**, *49*, 2649–2657, DOI: [10.1021/acs.accounts.6b00341](https://doi.org/10.1021/acs.accounts.6b00341).
- (15) Baran, M. J.; Braten, M. N.; Montoto, E. C.; Gossage, Z. T.; Ma, L.; Chénard, E.; Moore, J. S.; Rodríguez-López, J.; Helms, B. A. *Chemistry of Materials* **2018**, *30*, 3861–3866, DOI: [10.1021/acs.chemmater.8b01318](https://doi.org/10.1021/acs.chemmater.8b01318).
- (16) Zhu, Y. G.; Du, Y.; Jia, C.; Zhou, M.; Fan, L.; Wang, X.; Wang, Q. *Journal of the American Chemical Society* **2017**, *139*, 6286–6289, DOI: [10.1021/jacs.7b01146](https://doi.org/10.1021/jacs.7b01146).
- (17) Wei, X.; Xu, W.; Vijayakumar, M.; Cosimescu, L.; Liu, T.; Sprenkle, V.; Wang, W. *Advanced Materials* **2014**, *26*, 7649–7653, DOI: [10.1002/adma.201403746](https://doi.org/10.1002/adma.201403746).
- (18) Bamgbopa, M. O.; Shao-Horn, Y.; Almheiri, S. *Journal of Materials Chemistry A* **2017**, *5*, 13457–13468, DOI: [10.1039/C7TA02022H](https://doi.org/10.1039/C7TA02022H).
- (19) Shin, S.-H.; Yun, S.-H.; Moon, S.-H. *RSC Advances* **2013**, *3*, 9095–9116, DOI: [10.1039/C3RA00115F](https://doi.org/10.1039/C3RA00115F).
- (20) Carino, E. V.; Newman, D. J.; Connell, J. G.; Kim, C.; Brushett, F. R. *Langmuir* **2017**, *33*, 11911–11918, DOI: [10.1021/acs.langmuir.7b02243](https://doi.org/10.1021/acs.langmuir.7b02243).

- (21) Wedege, K.; Dražević, E.; Konya, D.; Bentien, A. *Scientific Reports* **2016**, *6*, 1–13, DOI: [10.1038/srep39101](https://doi.org/10.1038/srep39101).
- (22) Wei, X.; Xu, W.; Huang, J.; Zhang, L.; Walter, E.; Lawrence, C.; Vijayakumar, M.; Henderson, W. A.; Liu, T.; Cosimescu, L.; Li, B.; Sprenkle, V.; Wang, W. *Angewandte Chemie International Edition* **2015**, *54*, 8684–8687, DOI: [10.1002/anie.201501443](https://doi.org/10.1002/anie.201501443).
- (23) Mann, J. A.; Rodríguez-López, J.; Abruña, H. D.; Dichtel, W. R. *Journal of the American Chemical Society* **2011**, *133*, 17614–17617, DOI: [10.1021/ja208239v](https://doi.org/10.1021/ja208239v).
- (24) Hui, J.; Pakhira, S.; Bhargava, R.; Barton, Z. J.; Zhou, X.; Chinderle, A. J.; Mendoza-Cortes, J. L.; Rodríguez-López, J. *ACS Nano* **2018**, *12*, 2980–2990, DOI: [10.1021/acsnano.8b00702](https://doi.org/10.1021/acsnano.8b00702).
- (25) Kowalski, J. A.; Su, L.; Milshtein, J. D.; Brushett, F. R. *Current Opinion in Chemical Engineering* **2016**, *13*, 45–52, DOI: [10.1016/j.coche.2016.08.002](https://doi.org/10.1016/j.coche.2016.08.002).
- (26) Huang, J.; Pan, B.; Duan, W.; Wei, X.; Assary, R. S.; Su, L.; Brushett, F. R.; Cheng, L.; Liao, C.; Ferrandon, M. S., et al. *Scientific Reports* **2016**, *6*, 1–9, DOI: [10.1038/srep32102](https://doi.org/10.1038/srep32102).
- (27) Huang, J.; Su, L.; Kowalski, J. A.; Barton, J. L.; Ferrandon, M.; Burrell, A. K.; Brushett, F. R.; Zhang, L. *Journal of Materials Chemistry A* **2015**, *3*, 14971–14976, DOI: [10.1039/C5TA02380G](https://doi.org/10.1039/C5TA02380G).
- (28) Bültner, H.; Peters, F.; Schwenzel, J.; Wittstock, G. *Angewandte Chemie International Edition* **2014**, *53*, 10531–10535, DOI: [10.1002/anie.201403935](https://doi.org/10.1002/anie.201403935).
- (29) Bültner, H.; Sternad, M.; dos Santos Sardinha, E.; Witt, J.; Dosche, C.; Wilkening, M.; Wittstock, G. *Journal of The Electrochemical Society* **2015**, *163*, A504, DOI: [10.1149/2.0731603jes](https://doi.org/10.1149/2.0731603jes).
- (30) Bültner, H.; Schwager, P.; Fenske, D.; Wittstock, G. *Electrochimica Acta* **2016**, *199*, 366–379, DOI: [10.1016/j.electacta.2016.02.212](https://doi.org/10.1016/j.electacta.2016.02.212).
- (31) Zampardi, G.; Trocoli, R.; Schuhmann, W.; La Mantia, F. *Physical Chemistry Chemical Physics* **2017**, *19*, 28381–28387, DOI: [10.1039/C7CP05453J](https://doi.org/10.1039/C7CP05453J).
- (32) Zampardi, G.; La Mantia, F.; Schuhmann, W. *RSC Advances* **2015**, *5*, 31166–31171, DOI: [10.1039/C5RA02940F](https://doi.org/10.1039/C5RA02940F).
- (33) Su, L.; Ferrandon, M.; Kowalski, J. A.; Vaughey, J. T.; Brushett, F. R. *Journal of The Electrochemical Society* **2014**, *161*, A1905, DOI: [10.1149/2.0811412jes](https://doi.org/10.1149/2.0811412jes).
- (34) Unwin, P. R.; Güell, A. G.; Zhang, G. *Accounts of Chemical Research* **2016**, *49*, 2041–2048, DOI: [10.1021/acs.accounts.6b00301](https://doi.org/10.1021/acs.accounts.6b00301).
- (35) Banks, C. E.; Davies, T. J.; Wildgoose, G. G.; Compton, R. G. *Chemical Communications* **2005**, 829–841, DOI: [10.1039/B413177K](https://doi.org/10.1039/B413177K).
- (36) Banks, C. E.; Compton, R. G. *Analyst* **2006**, *131*, 15–21, DOI: [10.1039/B512688F](https://doi.org/10.1039/B512688F).
- (37) Gossage, Z. T.; Hui, J.; Zeng, Y.; Flores-Zuleta, H.; Rodríguez-López, J. *Chemical Science* **2019**, *10*, 10749–10754, DOI: [10.1039/C9SC03569A](https://doi.org/10.1039/C9SC03569A).

- (38) Lefrou, C.; Cornut, R. *ChemPhysChem* **2010**, *11*, 547–556, DOI: [10.1002/cphc.200900600](https://doi.org/10.1002/cphc.200900600).
- (39) Xiong, H.; Guo, J.; Amemiya, S. *Analytical Chemistry* **2007**, *79*, 2735–2744, DOI: [10.1021/ac062089i](https://doi.org/10.1021/ac062089i).
- (40) Xiong, H.; Kim, J.; Kim, E.; Amemiya, S. *Journal of Electroanalytical Chemistry* **2009**, *629*, 78–86, DOI: [10.1016/j.jelechem.2009.01.034](https://doi.org/10.1016/j.jelechem.2009.01.034).
- (41) Bültner, H.; Peters, F.; Schwenzel, J.; Wittstock, G. *ECS Transactions* **2015**, *66*, 69, DOI: [10.1149/06609.0069ecst](https://doi.org/10.1149/06609.0069ecst).
- (42) Oleinick, A. I.; Battistel, D.; Daniele, S.; Svir, I.; Amatore, C. *Analytical Chemistry* **2011**, *83*, 4887–4893, DOI: [10.1021/ac2006075](https://doi.org/10.1021/ac2006075).
- (43) Ohlhausen, J.; Zavadil, K. *Journal of Vacuum Science & Technology A: Vacuum, Surfaces, and Films* **2006**, *24*, 1172–1178, DOI: [10.1116/1.2188412](https://doi.org/10.1116/1.2188412).
- (44) Güell, A. G.; Ebejer, N.; Snowden, M. E.; Macpherson, J. V.; Unwin, P. R. *Journal of the American Chemical Society* **2012**, *134*, 7258–7261, DOI: [10.1021/ja3014902](https://doi.org/10.1021/ja3014902).
- (45) Amemiya, S.; Chen, R.; Nioradze, N.; Kim, J. *Accounts of Chemical Research* **2016**, *49*, 2007–2014, DOI: [10.1021/acs.accounts.6b00323](https://doi.org/10.1021/acs.accounts.6b00323).
- (46) Li, W.; Tan, C.; Lowe, M. A.; Abruña, H. D.; Ralph, D. C. *ACS Nano* **2011**, *5*, 2264–2270, DOI: [10.1021/nn103537q](https://doi.org/10.1021/nn103537q).
- (47) Valota, A. T.; Kinloch, I. A.; Novoselov, K. S.; Casiraghi, C.; Eckmann, A.; Hill, E. W.; Dryfe, R. A. W. *ACS Nano* **2011**, *5*, 8809–8815, DOI: [10.1021/nn202878f](https://doi.org/10.1021/nn202878f).
- (48) Valota, A. T.; Toth, P. S.; Kim, Y.-J.; Hong, B. H.; Kinloch, I. A.; Novoselov, K. S.; Hill, E. W.; Dryfe, R. A. *Electrochimica Acta* **2013**, *110*, 9–15, DOI: [10.1016/j.electacta.2013.03.187](https://doi.org/10.1016/j.electacta.2013.03.187).
- (49) Velický, M.; Bradley, D. F.; Cooper, A. J.; Hill, E. W.; Kinloch, I. A.; Mishchenko, A.; Novoselov, K. S.; Patten, H. V.; Toth, P. S.; Valota, A. T.; Worrall, S. D.; Dryfe, R. A. W. *ACS Nano* **2014**, *8*, 10089–10100, DOI: [10.1021/nn504298r](https://doi.org/10.1021/nn504298r).
- (50) Ritzert, N. L.; Rodríguez-López, J.; Tan, C.; Abruña, H. D. *Langmuir* **2013**, *29*, 1683–1694, DOI: [10.1021/la3042549](https://doi.org/10.1021/la3042549).
- (51) Kiani, A.; Alpuche-Aviles, M. A.; Eggers, P. K.; Jones, M.; Gooding, J. J.; Paddon-Row, M. N.; Bard, A. J. *Langmuir* **2008**, *24*, 2841–2849, DOI: [10.1021/la702811t](https://doi.org/10.1021/la702811t).
- (52) Guidelli, R.; Compton, R. G.; Feliu, J. M.; Gileadi, E.; Lipkowski, J.; Schmickler, W.; Trasatti, S. *Pure and Applied Chemistry* **2014**, *86*, 259–262, DOI: [10.1515/pac-2014-5025](https://doi.org/10.1515/pac-2014-5025).
- (53) Tsionsky, M.; Bard, A. J.; Dini, D.; Decker, F. *Chemistry of Materials* **1998**, *10*, 2120–2126, DOI: [10.1021/cm970795h](https://doi.org/10.1021/cm970795h).
- (54) Ikeda, T.; Leidner, C.; Murray, R. W. *Journal of Electroanalytical Chemistry and Interfacial Electrochemistry* **1982**, *138*, 343–365, DOI: [10.1016/0022-0728\(82\)85087-0](https://doi.org/10.1016/0022-0728(82)85087-0).

- (55) Lyons, M. E., *Electroactive Polymer Electrochemistry*; Springer Science & Business Media: 1994.
- (56) Schmehl, R. H.; Murray, R. W. *Journal of Electroanalytical Chemistry and Interfacial Electrochemistry* **1983**, *152*, 97–109, DOI: [10.1016/S0022-0728\(83\)80036-9](https://doi.org/10.1016/S0022-0728(83)80036-9).
- (57) Zhang, Y.; Liu, C.; Shi, W.; Wang, Z.; Dai, L.; Zhang, X. *Langmuir* **2007**, *23*, 7911–7915, DOI: [10.1021/la700876d](https://doi.org/10.1021/la700876d).
- (58) Derjaguin, B.; Muller, V.; Toporov, Y. *Progress in Surface Science* **1994**, *45*, 131–143, DOI: [10.1016/0079-6816\(94\)90044-2](https://doi.org/10.1016/0079-6816(94)90044-2).
- (59) Chen, R.; Najarian, A. M.; Kurapati, N.; Balla, R. J.; Oleinick, A.; Svir, I.; Amatore, C.; McCreery, R. L.; Amemiya, S. *Analytical Chemistry* **2018**, *90*, 11115–11123, DOI: [10.1021/acs.analchem.8b03023](https://doi.org/10.1021/acs.analchem.8b03023).
- (60) Abrahamson, J. *Carbon* **1973**, *11*, 337–362, DOI: [10.1016/0008-6223\(73\)90075-4](https://doi.org/10.1016/0008-6223(73)90075-4).
- (61) Güell, A. G.; Cuharuc, A. S.; Kim, Y.-R.; Zhang, G.; Tan, S.-y.; Ebejer, N.; Unwin, P. R. *ACS Nano* **2015**, *9*, 3558–3571, DOI: [10.1021/acsnano.5b00550](https://doi.org/10.1021/acsnano.5b00550).
- (62) Kurapati, N.; Pathirathna, P.; Chen, R.; Amemiya, S. *Analytical Chemistry* **2018**, *90*, 13632–13639, DOI: [10.1021/acs.analchem.8b03883](https://doi.org/10.1021/acs.analchem.8b03883).
- (63) Zhang, G.; Kirkman, P. M.; Patel, A. N.; Cuharuc, A. S.; McKelvey, K.; Unwin, P. R. *Journal of the American Chemical Society* **2014**, *136*, 11444–11451, DOI: [10.1021/ja505266d](https://doi.org/10.1021/ja505266d).
- (64) Xu, J.; Chen, Q.; Swain, G. M. *Analytical Chemistry* **1998**, *70*, 3146–3154, DOI: [10.1021/ac9800661](https://doi.org/10.1021/ac9800661).
- (65) Schorr, N. B.; Jiang, A. G.; Rodríguez-López, J. *Analytical Chemistry* **2018**, *90*, 7848–7854, DOI: [10.1021/acs.analchem.8b00730](https://doi.org/10.1021/acs.analchem.8b00730).

# Chapter 6

## An SECM-based spot analysis for redoxmer-electrode kinetics: identifying redox asymmetries on model graphitic carbon interfaces

*This work is conditionally accepted for publication. Citation: Raghuram Gaddam\*, Dipobrato Sarbapalli\*, Jason Howard, Larry A. Curtiss, Rajeev S. Assary, Joaquín Rodríguez-López. “An SECM-based spot analysis for redoxmer-electrode kinetics: identifying redox asymmetries on model graphitic carbon interfaces” *Chem. Asian J.* **2022***

*Credit statement:* D.S., R.G. and J.R-L. conceptualized the study. R.G. performed all SECM experiments. D.S. fabricated, characterized samples and assisted in some electrochemical experiments. D.S. analyzed all data, prepared figures and wrote the manuscript with assistance from R.G. and J.R-L. J.H. performed simulations under the guidance of L.A.C. and R.S.A. All authors reviewed the manuscript.

Non-aqueous redox flow batteries (NRFBs) are an upcoming candidate for grid level energy storage applications. These batteries store energy by using redoxmers, i.e. redox-active molecules, oligomers or polymers in solution.<sup>[1–6]</sup> (Dis)charge processes are carried out between current collector electrodes and these redoxmers, via heterogeneous electron transfer (ET) reactions, with graphitic carbon being an inexpensive option for electrode materials.<sup>[7, 8]</sup> Out of various forms of RFBs, non-aqueous systems are attracting increased attention due to higher operating potentials in non-aqueous media and the ability to develop engineered redoxmers with high intrinsic redox potentials.<sup>[1]</sup> Nonetheless, while significant improvements have been achieved on the solubility, redox potential, and stability of these redoxmers,<sup>[9–12]</sup> there is a knowledge gap in characterizing and predicting their behavior at electrodes. Therefore, tools that evidence potential non-idealities for ET

---

\*denotes equal contribution

reactions are highly desirable.

Ideally, redoxmers should engage in outer-sphere electron transfer (ET) reactions i.e. bypassing specific interactions with the electrode materials that could lead to kinetic deviations from those ideally predicted by electron transfer theories (e.g. Marcus-Hush and others).[13] However, in reality, there is the possibility that interfacial processes dramatically modify the observed kinetics.[14] For instance, with increasing concentrations of redoxmers used in RFBs one could suspect that adsorption or deposition of the redoxmer on the electrode, i.e. as a function of state of charge, could play a role in modifying the electrochemical interface, and therefore ET dynamics.[13, 15–17] Additionally, lesser differences in hydrophobicity between electrodes and non-aqueous solvents creates favorable conditions for adsorption and could lead to significantly different interfacial structures.[18–22] These interfacial interactions may also differ based on different types of electrode materials used, such as when comparing graphitic carbons and metal electrodes.

While the homogeneous degradation pathways can be explored with electrochemical (such as cyclic voltammetry[23] or generation-collection measurements[24]) and chemical (such as electron paramagnetic resonance spectroscopy) characterization methods,[23] it is difficult to explore interfacial processes that affect ET kinetics within RFBs using macroscopic electrochemical techniques. Typical transient electrochemical measurements with macrodisks and ultramicroelectrodes (UME) have been utilized to quantify parameters of relevance to RFBs such as diffusion coefficients, state of charge, and standard heterogeneous electron transfer rate constants ( $k^0$ ) in redoxmers.[4, 5, 25, 26] However, these approaches may be insensitive towards more subtle interfacial processes that could cause deviations at higher rates of ET than can be measured with them. Here we posit that a first step towards identifying nonidealities is to quantify the heterogeneous rate constant ( $k_f$  or  $k_b$ ) for ET as a function of applied potentials. This data allows for comparison to ET kinetic models such as Butler-Volmer, and subsequent quantification of the transfer

coefficient  $\alpha$  and  $k^0$  using Eq. 6.1 and 6.2. While the Butler-Volmer model is empirical, it is a powerful predictor of ideal ET behavior, with most molecules exhibiting  $\alpha \approx 0.5$ .[13] For instance, a deviation of  $\alpha$  from 0.5 to low values of  $\approx 0.01$ - $0.02$  was observed in a previous study, which was attributed to the presence of porous insulating and/or redox-active films forming on the electrode-electrolyte interface and confirmed via in situ AFM.[14]

$$k_f = k^0 \exp [-\alpha f (E - E^0)] \quad (6.1)$$

$$k_b = k^0 \exp [(1 - \alpha) f (E - E^0)] \quad (6.2)$$

Considering a prototypical redox reaction,  $O + e^- \rightleftharpoons R$ , the variables in Eq. 6.1 and 6.2 are defined as follows.[13]  $k_f$  is the heterogeneous rate constant for the forward reaction from  $O \rightarrow R$ .  $k_b$  is the heterogeneous rate constant for the reverse reaction from  $R \rightarrow O$ .  $k^0$  is the standard heterogeneous rate constant for the redox reaction between O and R.  $\alpha$  is the transfer coefficient.  $E^0$  is the formal potential for the redox couple O & R. For a redox couple with Nernstian kinetics,  $E_{1/2} = E^0$ ;  $E_{1/2}$  being the half-wave potential obtained from ultramicroelectrode (UME) voltammetry.[13]

In this paper, we report an SECM-based point measurement (henceforth referred to as “spot analysis”) to understand ET kinetics between redoxmers and carbon electrodes. Specifically, this point measurement focuses on quantifying ET kinetics as a function of  $E - E^0$  for enabling quantification of  $\alpha$  and  $k^0$  with Eq. 6.1 and 6.2. First, we develop COMSOL finite element models to present theoretical results from the procedure. Subsequently, we test this method with ferrocene (Fc) and hydroxymethylferrocene (FcMeOH), which are presumed to possess fast ET kinetics.[13, 27] This work focuses on investigating how the pairings of these two redoxmer systems in their corresponding two states of charge, four distinct graphitic materials (multi-layer graphene (MLG), highly ordered pyrolytic graphite

(HOPG), glassy carbon (GC) and graphite films) and Pt, two solvents (water and propylene carbonate) and various concentrations (0.1 mM to 100 mM) lead to measurable differences in the electrochemical properties of interfaces that are relevant to flow batteries. While similar measurements can be obtained with SECM feedback theory[28] by employing probe approach curves at discrete substrate potentials,[26] here we specifically focus on a method that can rapidly identify non-idealities in the kinetics vs. potential profiles for electrodes/redoxmer pairs. By solving for the electrode kinetics at constant SECM tip-substrate distance, we overcome difficulties in fitting of approach curves.[29, 30] This allows us to promptly obtain electrode kinetic profiles which are useful to identify interfacial dynamics that may be limiting in the operation of redox-flow batteries.

## 6.1 Experimental methods

### 6.1.1 Chemicals and materials

All materials were purchased commercially and used as received unless otherwise mentioned. Propylene carbonate (PC, 99.7%, anhydrous), tetrabutylammonium hexafluorophosphate (TBAPF<sub>6</sub>, 99%), potassium nitrate (KNO<sub>3</sub>, ACS grade, 99+%), hydroxymethylferrocene (FcMeOH, 97%), and ferrocenium hexafluorophosphate (Fc<sup>+</sup>PF<sub>6</sub><sup>-</sup>, 97%) were purchased from Sigma. Ferrocene (Fc, 98%, Sigma) was recrystallized twice out of hexane. DI water was obtained from a Millipore ultrapure system. Grade 1 HOPG and GC were purchased from SPI supplies. Cu (99.99%) and Ni (99%) foil were purchased from Alfa Aesar. 3 mm GC macro-disc electrodes were purchased from BASi. Cu etchant (CE-100) and Ni etchant (TFB) was procured from Transene Company Inc. Si/SiO<sub>2</sub> wafers were purchased from University Wafer.

### 6.1.2 CVD growth of MLG and graphite

Multi-layer graphene (MLG) was grown in a manner similar to our previous studies.[14, 31–33] In brief, Cu foil was cleaned in acetic acid to remove surface oxides.

CVD growth was performed for 5 minutes under 30 sccm H<sub>2</sub> and 10 sccm CH<sub>4</sub> gas flow, at atmospheric pressure. Resulting MLG was transferred using poly-bisphenol A carbonate as a sacrificial polymer, as reported earlier.[14, 34] The layer number distribution of MLG is presented in **Figure D.1**, as characterized with optical transmittance at 561 nm.

CVD growth of graphite was obtained with the same recipe, with Ni foil being used as the catalyst. Graphite films were transferred without using any sacrificial polymers. Ni was etched, and the films were rinsed four times by floating them on DI water, followed by two hours in EDTA, and four rinses on DI water, same as MLG films. Both MLG and graphite films were transferred on SiO<sub>2</sub>/Si wafer.

### 6.1.3 Electrochemical measurements

SECM measurements were performed with a CHI 920D bipotentiostat maintained in an Ar-atmosphere glovebox (O<sub>2</sub> < 0.1 ppm, H<sub>2</sub>O < 0.1 ppm). Measurements in aqueous media were performed with another instrument of the same make and model exposed to the environment. Pt wire (0.5 mm) was used as a counter electrode. For all measurements with Fc or FcMeOH in PC, we used Ag wire or a polypyrrole[35, 36] quasi-reference electrode (PPyQRE). The use of Fc and FcMeOH redoxmers enables us to approximate the theoretical  $E - E^0$  with the experimentally accessible  $E - E_{1/2}$ , with  $E_{1/2}$  measured from voltammetry at the SECM tip. In our study, we use the notation of  $E - E^0$  for describing applied potentials. For measurements with Fc<sup>+</sup>PF<sub>6</sub><sup>-</sup>, a graphite rod (99.9995%, Alfa Aesar) was used as a quasi-reference electrode.

All SECM substrate electrodes were assembled in an open teflon cell, with a 3 mm o-ring isolating the substrate electrode. SECM tips utilized Pt ultramicroelectrodes (UME)  $\approx$  2  $\mu$ m in diameter (PT005103, Pt Wollaston wire, Goodfellow). SECM on CVD graphite films was performed with a 25  $\mu$ m diameter Pt (Goodfellow) UME, owing to the heterogeneity in film thickness. All SECM spot analysis measurements were performed with  $\approx$  1 mM redoxmer in 0.1 M supporting electrolyte concentrations unless otherwise

mentioned. Tip positioning was performed with probe approach curves (**Figure D.2**). For ease, we report relevant parameters used in our measurements and data analysis in **Table D.1**. Diffusion coefficients reported in this table were obtained with UME measurements (**Figure D.3**).<sup>[37]</sup>

Three or five spot measurements were performed for each redoxmer-electrode pairing at random locations on the substrate, by going from  $|E_{sub} - E^0| >> 0$  to  $|E_{sub} - E^0| = 0$ . Between each measurement, a bulk concentration resetting step was implemented, wherein, we perform a 30-min i-t curve at the substrate at potentials to convert any species electrogenerated by the substrate. Before all spot analysis measurements, we performed cyclic voltammetry and steady state i-t curves at the UME tip to estimate the  $E_{1/2}$  of the redoxmer and for obtaining  $i_\infty$ , the tip current in the bulk of the solution. Negative feedback approach curves were performed on an insulating glass substrate to estimate the RG (ratio of glass to electrode radii) for the tip, **Figure D.2**.

#### 6.1.4 Materials characterization

Atomic force microscopy (AFM) was performed using a Park Instruments NX10 AFM operated in tapping mode. Profilometry measurements were made using a Keyence VK-X1000 laser scanning confocal microscope. Raman spectra were collected using a Nanophoton Raman 11 confocal microscope. Optical transmittance was collected with a Leica SP8 confocal microscope.

#### 6.1.5 Computational methods

First principles quantum chemistry simulations were carried out with the Qchem code.<sup>[38]</sup> The calculations were performed with the PBE exchange and correlation functional,<sup>[39]</sup> Van der Waals corrections were treated with the D2 method of Grimme,<sup>[40]</sup> and the calculations utilized the 6-31G\* Pople basis set. The convergence criteria for the self-consistent cycles was  $10^{-6}$  Hartrees and the convergence criteria for structural relaxation

was  $3 \times 10^{-6}$  atomic units of force. To model the carbon surface a large hexagonal cluster of single layer “graphene” with hydrogen terminations was generated. A picture of the cluster used to model the carbon surface is shown in **Figure D.4**. To investigate the effects of solvents on the binding of the molecules to the surface the PCM (Polarizable continuum model)[41] and COSMO[42] solvent models were used as implemented in Qchem. The binding energies were calculated with the following equation (**Eq. 6.3**).

$$E_{bind} = E_{ms} - (E_s + E_m) \quad (6.3)$$

Where  $E_{ms}$  is the total energy of the molecule on the surface,  $E_s$  is the energy of the isolated surface, and  $E_m$  is the energy of the isolated molecule. Two solvents were considered: water and propylene carbonate. Dielectric constants of 80.4 and 64.9, respectively, were used.

## 6.2 Results and discussion

First, we used COMSOL simulations to explore the ability of the spot analysis approach to extract Butler-Volmer kinetic parameters  $\alpha$  and  $k^0$ . The COMSOL geometry chosen uses a 2D-axisymmetric finite element model, with UME diameter,  $a = 1 \mu\text{m}$ , and geometrical factor,  $RG = 10$ , which was close to typical experimental values between 8 and 15. Normalized tip substrate distance,  $L$  ( $d/a$ , where  $d$  is the distance between tip and substrate) = 1, as illustrated in **Figure 6.1a** and **6.1b**. Simulations were performed under the transport for diluted species module, with species R in solution, R being oxidized to O at the tip ( $k^0 = 1 \times 10^{-1} \text{ m/s}$  and  $E^0 = 0 \text{ V}$ ), and the reverse process occurring at the substrate. Flux boundaries are shown in **Figure 6.1b**, and their corresponding Butler-Volmer expressions, are presented in **Figure 6.1c** (refer **Eq. 6.1** and **6.2**). A semi-infinite boundary condition is placed on the solution boundaries, with concentration fixed to initial bulk concentrations of O (0 mM) and R (1 mM). A detailed list of parameters used in the simulations is presented

**Table D.2.**

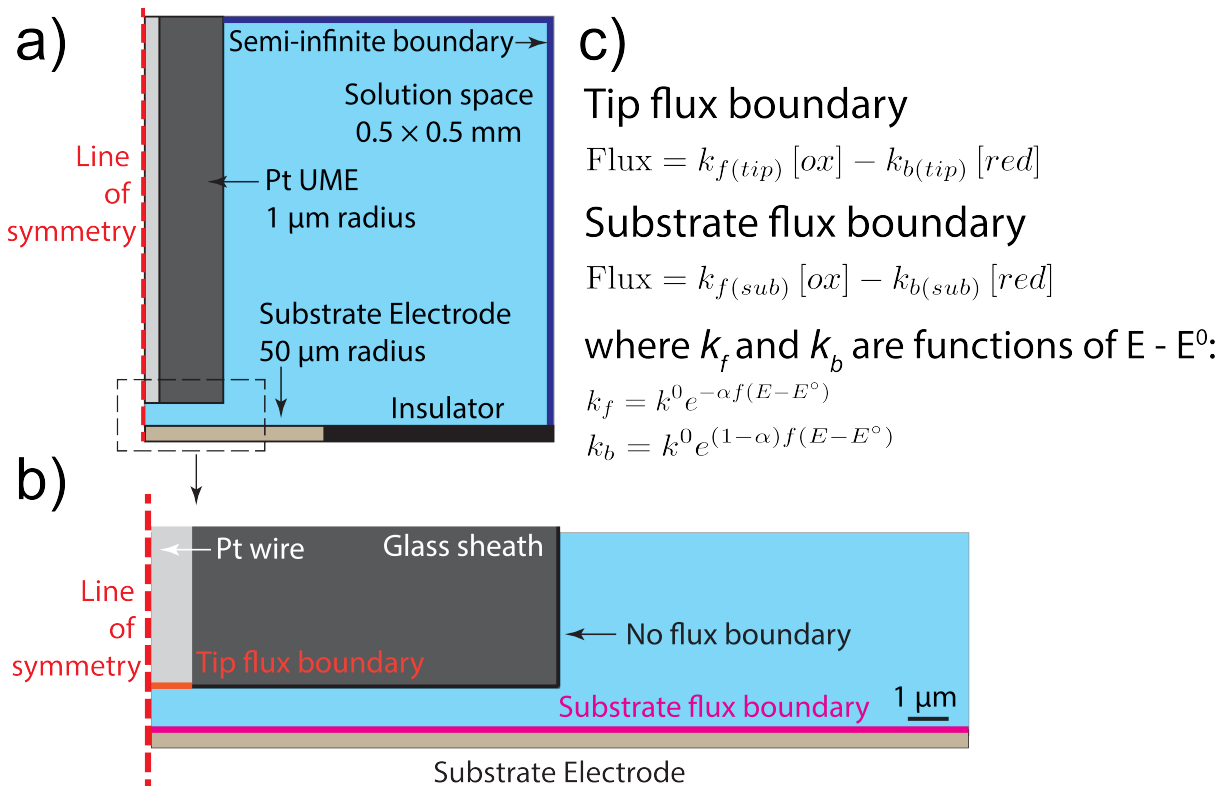


Figure 6.1: COMSOL finite element model description. a) General schematic of the model showing components, b) Scaled schematic illustrating specific boundary conditions with corresponding flux equations in c).

A general measurement scheme is illustrated in **Figure 6.2a**, with the tip being held at a constant potential for oxidation of  $\text{R} \longrightarrow \text{O}$  under mass-transfer limited conditions ( $|E_{\text{tip}} - E^0| = 0.2 \text{ V}$ ) and the substrate running chronoamperometric steps at different potentials (**Figure 6.2b**) for reduction of  $\text{O} \longrightarrow \text{R}$ . The duration of each chronoamperometric step was 12 s, and the tip currents (**Figure 6.2c**) for the first 10 s of each step were neglected in the subsequent analysis to allow for steady-state current measurements. The tip currents were normalized with respect to the steady-state current values in bulk solution, averaged, and plotted as a function of  $E_{\text{sub}} - E^0$ , in **Figure 6.2d**. These values are overlaid with practical positive and negative feedback limits, as obtained from **Figure D.5**. Finally, we utilized a Python script to convert these values into the

heterogeneous ET rate constant,  $k_f$ , utilizing expressions from Cornut and Lefrou.[43] The resulting relationship between  $\log k_f$  and  $E_{sub} - E^0$  (**Figure 6.2e**) was utilized to extract Butler-Volmer kinetic parameters,  $\alpha$  and  $k^0$  using **Eq. 6.1**. Identifying a linear region for the fitting process introduces a practical complication. To this end, we delineated two boundaries that help us define the region on which linearity is expected. In the first case we used the upper bound for the positive feedback at the values in which the currents approach mass transfer limitation (**Figure D.5**). The lower bound was set by analyzing the substrate response to rule out redox competition influence on the data, i.e. the condition at which the substrate is also oxidizing the redox mediator ( $R \longrightarrow O$ ). This redox competition occurs when  $E_{sub} - E^0$  approaches 0 V and above (**Figure D.6**). **Figure 6.2f** illustrates the ratio of charge passed by the substrate to that of the tip as a function of  $E_{sub} - E^0$ . Initially, when  $E_{sub} - E^0$  is -0.7 V, the negative value arises due to the substrate and tip performing opposing redox processes. Subsequently, as the substrate competes with the tip for the same redox process, the charge ratio starts to move toward positive values as visible at  $E_{sub} - E^0 > -0.2$  V. For consistent data analysis, the lower potential limit for the linear fit measurements is set to the value corresponding to a charge ratio of -0.5 as depicted by the dashed lines in **Figure 6.2f**. The linear fit to extract  $\alpha$  and  $k^0$  as per **Eq. 6.1** is then performed in the green bounded region in **Figure 6.2e**.

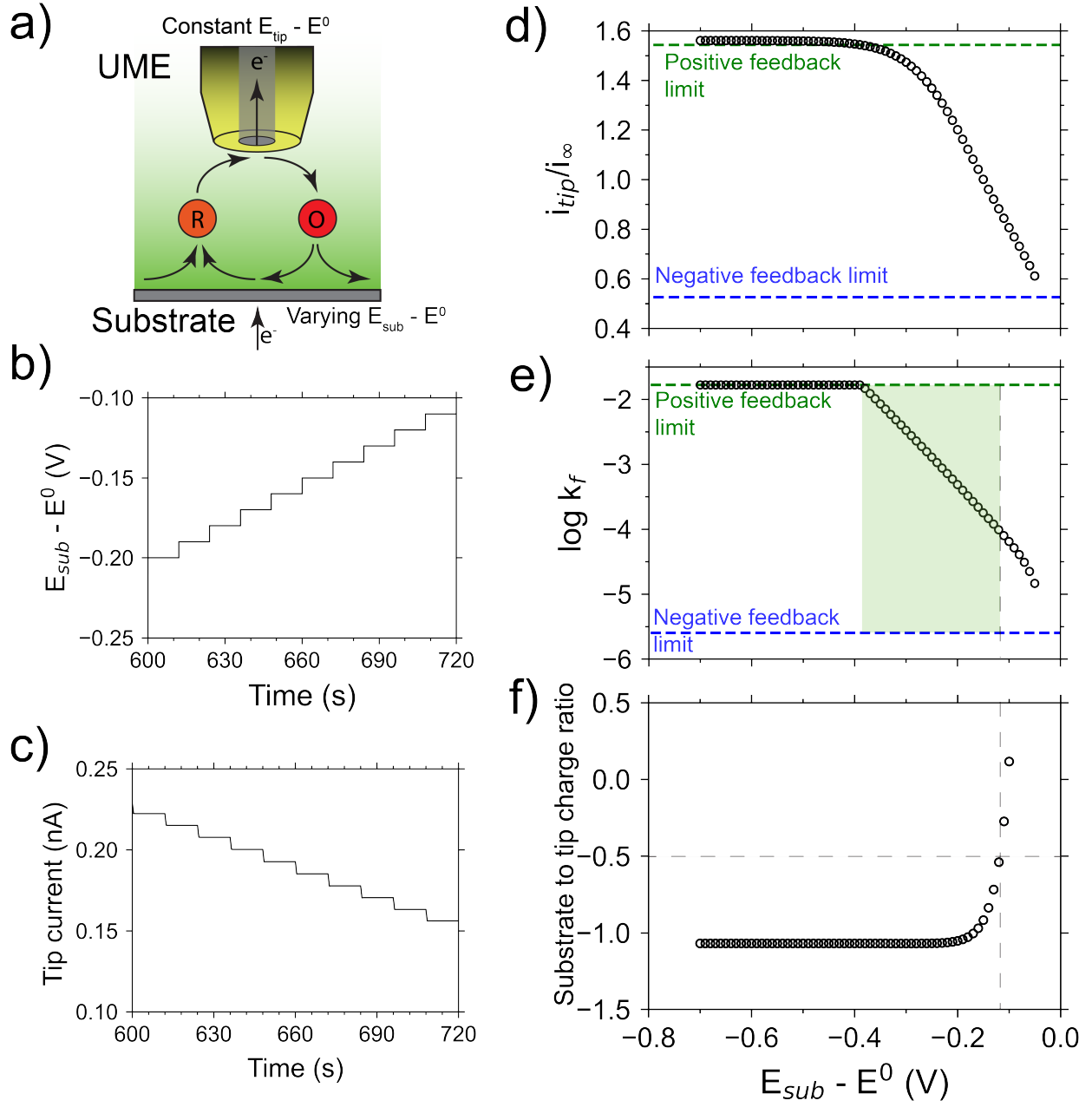


Figure 6.2: Experiment details and data analysis procedures. a) Schematic of the spot analysis measurement, where tip initiates feedback measurements through oxidation of R. b) Portion of the substrate potential steps utilized in the COMSOL simulations (full range shown in **Figure D.7**), with corresponding tip currents in c). d) Data illustrating the variation in normalized tip currents vs.  $E_{sub} - E^0$ . e) Conversion of normalized tip currents to  $k_f$  (for the reaction of O  $\longrightarrow$  R at the substrate, refer **Eq. 6.1**). Linear fits for fitting **Eq. 6.1** taken from the green shaded region. f) Use of substrate to tip charge ratio to determine the lower limit for linear fit in e). Data in these plots correspond to input  $k^0 = 1 \times 10^{-5}$  m/s and  $\alpha = 0.5$  at the substrate used in COMSOL simulation.

Using our COMSOL model, we investigated two use cases for our spot analysis method. In the first case, we set  $\alpha$  to 0.5, and investigated the COMSOL results as a function of changing  $k^0$  between  $10^{-3}$  and  $10^{-7}$  m/s at the substrate. In the second case, we fix  $k^0$  to  $10^{-4}$  m/s and vary  $\alpha$  between 0.3 to 0.7 at the substrate. Results from these two cases are shown in **Figure 6.3a** and **6.3b** respectively.

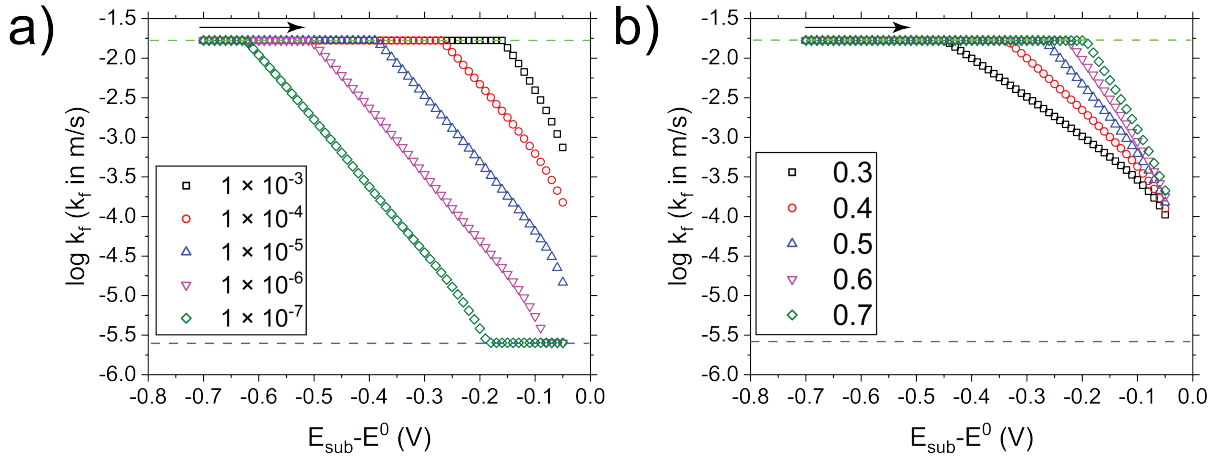


Figure 6.3: COMSOL simulation results from a) varying  $k^0$  and b)  $\alpha$ , with positive and negative feedback limits designated by the dashed lines. Arrows indicate scan direction for potentials applied at the substrate.

Using the COMSOL simulation results as shown in **Figure 6.3**,  $k^0$  and  $\alpha$  were extracted through linear fits of Eq. 6.1. The data used for fitting was bound by positive feedback mass-transfer limited kinetics and redox competition from the substrate, as described previously. A full example of the analysis is presented in **Figure D.8**, with  $k^0$  and  $\alpha$  estimates presented in **Table 6.1** and **6.2** (for data from **Figure 6.3a** and **6.3b** respectively).

Error percentages in estimating  $k^0$  and  $\alpha$  are observed to be mostly within 10%. This agreement of simulations to the input  $k^0$  and  $\alpha$  is because the spot analysis method uses steady-state currents from a pure kinetic regime, with minimal interference from mass-transfer or redox competition, which are common challenges faced during similar

analyses such as Tafel approximations in CV, LSV and RDE measurements.[44–46] Steady state currents are ensured owing to the 10 s quiet time given before current measurements, therefore ensuring preceding measurements are not influencing the measured tip currents. However, major errors were observed in the estimates for substrate  $k^0 = 1 \times 10^{-3}$  m/s and  $\alpha = 0.5$  (**Table 6.1**), thus setting the measurement limit for our approach using the a, L, and d values simulated and used experimentally (**Figure D.9**). In summary, our analysis using COMSOL simulations illustrates that the spot analysis approach estimates  $k^0$  and  $\alpha$  to a reasonable accuracy while avoiding the pitfalls associated with redox competition.

Table 6.1: COMSOL simulation results with  $k^0$  varied in simulations ( $\alpha = 0.5$  for all cases)

Input $k^0$ (m/s)	Butler Volmer parameter	Result	Error, %
$1 \times 10^{-3}$	$k^0$ (m/s)	$3.16 \times 10^{-4}$	68.4
$1 \times 10^{-3}$		0.65	29.5
$1 \times 10^{-4}$	$k^0$ (m/s)	$1.03 \times 10^{-4}$	3.1
$1 \times 10^{-4}$		0.49	2.3
$1 \times 10^{-5}$	$k^0$ (m/s)	$1.01 \times 10^{-5}$	1.3
$1 \times 10^{-5}$		0.50	0.9
$1 \times 10^{-6}$	$k^0$ (m/s)	$1.00 \times 10^{-6}$	0.2
$1 \times 10^{-6}$		0.50	0.4
$1 \times 10^{-7}$	$k^0$ (m/s)	$0.92 \times 10^{-7}$	8.0
$1 \times 10^{-7}$		0.5	0.6

Table 6.2: COMSOL simulation results with  $\alpha$  varied in simulations ( $k^0 = 1 \times 10^{-4}$  m/s for all cases)

Input $k^0$ (m/s)	Butler Volmer parameter	Result	Error, %
$1 \times 10^{-3}$	$k^0$ (m/s)	$1.03 \times 10^{-4}$	2.8
	$\alpha$	0.29	2.0
$1 \times 10^{-4}$	$k^0$ (m/s)	$1.02 \times 10^{-4}$	2.2
	$\alpha$	0.39	1.9
$1 \times 10^{-5}$	$k^0$ (m/s)	$1.03 \times 10^{-4}$	2.3
	$\alpha$	0.49	1.3
$1 \times 10^{-6}$	$k^0$ (m/s)	$0.95 \times 10^{-5}$	5.4
	$\alpha$	0.59	0.8
$1 \times 10^{-7}$	$k^0$ (m/s)	$0.92 \times 10^{-5}$	8.5
	$\alpha$	0.69	1.1

With the results from our simulations firmly asserting the validity of the spot analysis approach, we now explored the application of this method in practical experiments. Keeping in mind that the overarching goal is to apply this method for characterizing redoxmers and practically relevant electrode materials, we chose ferrocene (Fc) and hydroxymethylferrocene (FcMeOH) as model redoxmers in a solution with 0.1 M TBAPF<sub>6</sub> in propylene carbonate (PC). FcMeOH was chosen because it is soluble in aqueous and non-aqueous media, and therefore was used to evaluate the solvent effects on ET behavior.[21] The use of PC as a solvent enabled us to perform studies without concerns of solvent evaporation, which would lead to changes in UME currents, thus confounding our quantitative analysis.

First, a comparison of the ET kinetics between Pt and multi-layer graphene (MLG) samples towards FcMeOH was performed. Our experiments involved placing the tip close to the substrate using positive feedback approach curves (**Figure D.2**) using FcMeOH in solution. Once placed, spot analysis measurements were performed in accordance with the protocol described in **Figure 6.2** at five random locations. The dependence of  $k_f$  with  $E - E^0$  at one spot is shown in **Figure 6.4a**, for a sputtered Pt metal substrate, with the

shaded region representing standard deviation from the five measurements. Analysis of the substrate to tip charge ratio reveals no data in a kinetically limited regime (**Figure D.10**), displaying a response that is similar to that simulated with COMSOL corresponding to  $k^0$  values of  $10^{-3}$  m/s and  $\alpha$  of 0.5. This result reveals that the  $k^0$  for FcMeOH reduction in non-aqueous media is greater than  $10^{-3}$  m/s, which is 1-2 orders of magnitude faster than those reported using CV and RDE measurements with Pt and GC electrodes, respectively, in non-aqueous media.<sup>[47, 48]</sup> Additionally, the agreement between the experimental result and COMSOL simulations also highlights no systemic errors in our measurements when applied to practice.

Upon switching to an MLG electrode as substrate (**Figure 6.4b**), there is a clear change in redox behavior, with the experimental result revealing significantly slower kinetics than on Pt. This result indicates that unaccounted interfacial phenomena influence ET behavior of FcMeOH reduction on MLG electrodes. Because both experiments on Pt and MLG used PC as solvent, there is no influence of the solution viscosity influencing ET behavior<sup>[21]</sup> in the concentration regime tested. To discard that this is a unique effect of FcMeOH, we also performed spot analysis measurements of Fc in 0.1 M TBAPF<sub>6</sub>/PC electrolyte with MLG substrates, which also revealed the same response as in **Figure 6.4b**, while Pt substrate once more revealed faster kinetics (shown later in **Figure 6.5**). Interestingly, a linear fit on the spot analysis curve for **Figure 6.4b** reveals an  $\alpha$  value of  $\approx 0.3$ , as shown in **Figure D.11**. These  $\alpha$  values have been reported for Fc redox in carbonate-based non-aqueous solvents through Koutecky-Levich analysis using rotating disk electrode measurements.<sup>[47]</sup> Other studies report similar values for Fc redox in CHCl<sub>3</sub><sup>[49]</sup> and polyelectrolytes.<sup>[50]</sup> Similarly, SECM approach curve measurements revealed mass-transfer limited kinetics at low  $E - E^0$  values for FcMeOH in aqueous media, whereas sluggish ET was observed in non-aqueous acetonitrile solvent.<sup>[26]</sup> Therefore, the findings with Fc redox from the spot analysis measurement are consistent with literature in nonaqueous electrolytes.

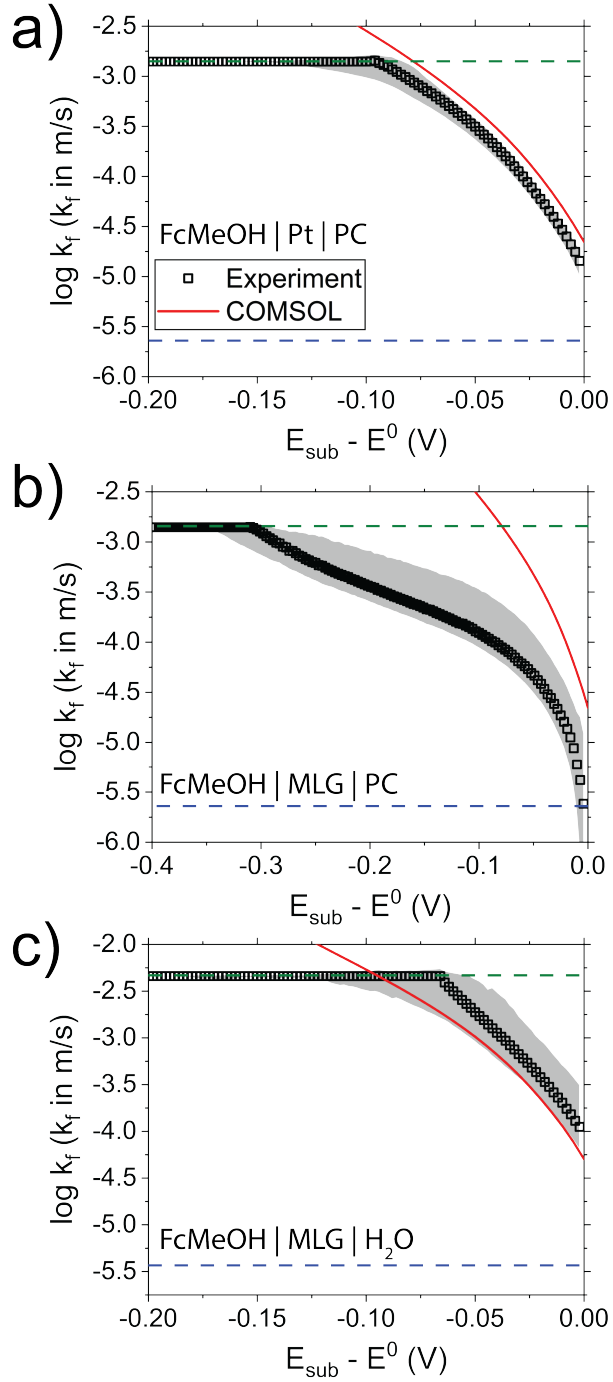


Figure 6.4: Experimental results on different electrode and solvent conditions. Spot analysis of a) FcMeOH in PC on sputtered Pt electrodes, b) FcMeOH in PC on MLG electrodes, c) FcMeOH in  $H_2O$  on MLG electrodes. Gray regions depict standard deviation across five measured spots. All experimental parameters are reported in Table D.1. Red line indicates COMSOL simulation with  $k^0$  of  $10^{-3}$  m/s,  $\alpha$  of 0.5, L = 1.

Additionally, we performed a third control measurement, this time utilizing

FcMeOH dissolved in aqueous 0.1 M KNO<sub>3</sub> solution and MLG as substrate. This data is shown in **Figure 6.4c**, which now revealed a similar behavior to that over Pt in **Figure 6.4a**, and consistent with the COMSOL predictions of our measurement limitation near  $k^0$  of 10<sup>-3</sup> m/s,  $\alpha$  of 0.5. Apart from solution effects, this experiment also rules out electrode properties such as tears, fabrication residues, or limited conductivity influencing the ET behavior observed in **Figure 6.4b**. In summary, **Figure 6.4** clearly points to a slowing down of ET during the reduction of FcMeOH<sup>+</sup> in PC with MLG electrodes.

To further clarify our observations and discard the influence of day-to-day variability in electrode or solution preparation procedures, we performed SECM feedback imaging and spot analysis on a substrate with four distinct areas in a single sample: i) insulating SiO<sub>2</sub>, ii) MLG, iii) sputtered Pt, and iv) MLG on Pt, as shown in **Figure 6.5a**. SECM feedback images were taken at two different  $E_{sub} - E^0$  values of -0.1 V and -0.2 V, as shown in **Figure 6.5b** using Fc in PC solution. The feedback images revealed uniform reactivity over Pt electrodes, with mass-transfer limited ET kinetics clearly attained at  $E_{sub} - E^0$  of -0.2 V. The MLG areas are observed to be less reactive than the Pt electrode, both on the feedback images and by spot analysis measurements, as shown in **Figures 6.5c** and **6.5d**, thus confirming the contrasting behavior observed in **Figure 6.4**. It is noteworthy that feedback images, which display the normalized SECM feedback current as scale, did not immediately reveal the stark kinetic differences observed in the spot analysis. Thus, we believe that the spot analysis helps amplify kinetic differences that might go unnoticed in typical feedback imaging experiments. Nonetheless, feedback over the MLG areas did show heterogeneity in ET kinetics, and a comparison with the optical micrograph reveals that the areas with lower reactivity arise from the optically clearer regions of MLG. Raman measurements on our MLG samples (**Figure D.12**) reveal that these regions on MLG are comprised primarily of single-layer (SLG) or bi-layer graphene (BLG). In general, the reactivity of these thinner regions was observed to be lower compared to thicker areas irrespective of whether the underlying material was SiO<sub>2</sub> or Pt metal. It should be noted

that other SECM and scanning electrochemical cell microscopy (SECCM) measurements over graphene of various layer numbers have found a decrease in the rate of electron transfer as the layer number decreases.[51, 52] A feedback image acquired at the unbiased electrode, i.e. at the open circuit potential (OCP), taken after the biased feedback measurements revealed decreased reactivity over these SLG/BLG areas, compared to the original OCP image (**Figure D.13**). This observation indicated that the phenomenon causing the decrease in ET kinetics may be influenced by the application of electrode bias to reduce  $\text{Fc}^+$  to  $\text{Fc}$ , and/or has a time dependence associated with it (the time difference between the two images was  $\approx 2\text{h}$ ).

The reduction in SECM feedback while applying reducing potentials to generate  $\text{Fc}$  near the substrate over a prolonged time period may prompt the hypothesis that the decreased ET is occurring due to molecular adsorption of ferrocene on carbon electrodes. Such an adsorption event will lead to ET being mediated through the adsorbed species, which consequently may lead to a deviation from  $k_f$  values estimated from applied electrode potential using [Eq. 6.1](#) and [6.2](#).[16] Such adsorption events are well-reported in literature,[16, 53–55] where ferrocenylmethyltrimethylammonium ( $\text{FcTMA}^+$ ), hydroxymethylferrocene ( $\text{FcMeOH}$ ), and ferrocenecarboxylic acid ( $\text{FcCOOH}$ ) have been found to adsorb on HOPG surfaces in the uncharged state in aqueous media. However, there is significant discussion about the role that each member of the redox pair has towards the surface.[16, 53] Other studies with  $\text{FcMeOH}$  on SLG electrodes have reported an irreversible adsorption event taking place in aqueous media,[54] consistent with the fact that the SLG/BLG regions on our MLG substrate exhibit low ET (**Figure 6.5b**).

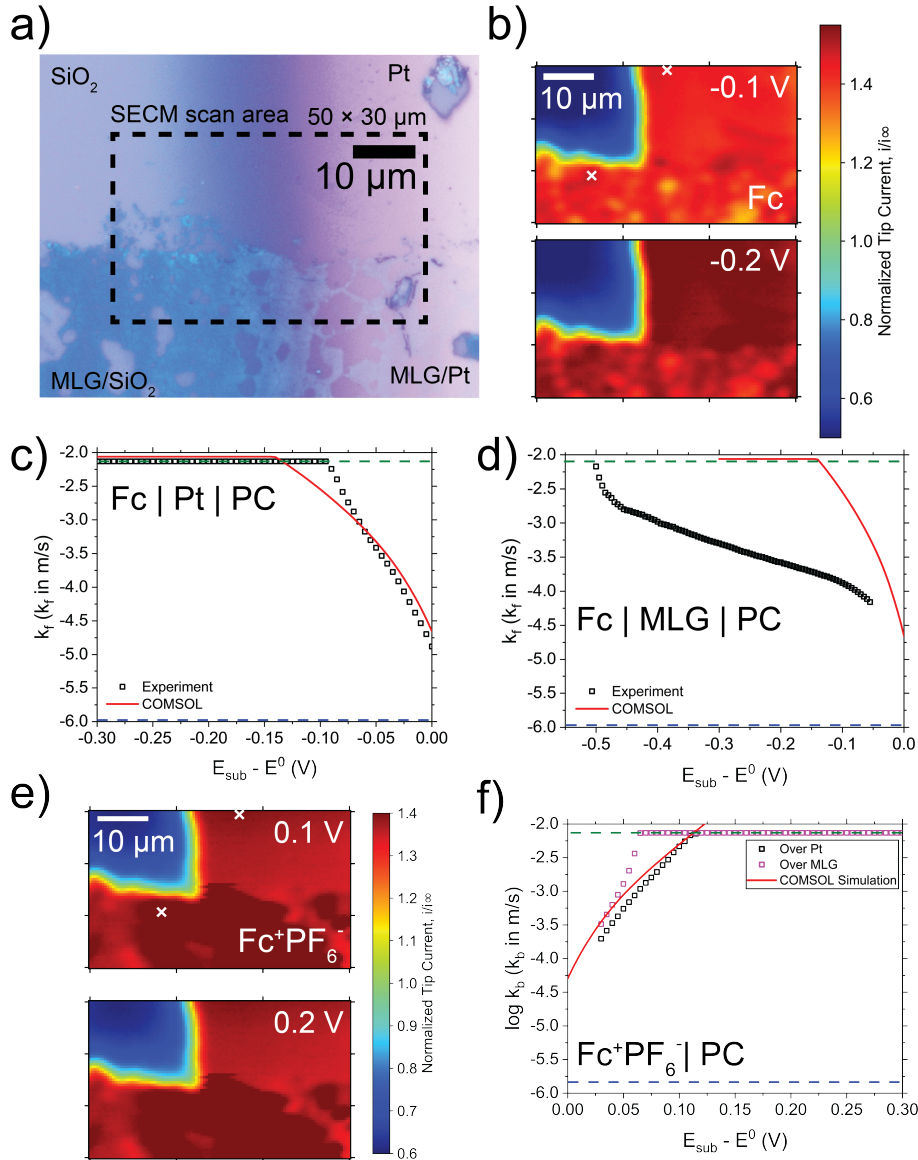


Figure 6.5: SECM feedback measurements on MLG and Pt electrodes. a) Optical micrograph of the substrate, depicting the SECM scan area and b) SECM feedback images at  $E_{\text{sub}} - E^0$  of  $-0.1 \text{ V}$  and  $-0.2 \text{ V}$  respectively. c) and d) spot analysis over Pt and MLG areas respectively (locations marked with white crosses in b). e) SECM feedback images, and f) spot analysis over MLG and Pt with locations marked with white crosses in e). Feedback images were obtained at increment distance of  $0.5 \mu\text{m}$  and increment time of  $0.05\text{s}$ . COMSOL simulations were performed with  $k^0$  of  $10^{-3} \text{ m/s}$ ,  $\alpha$  of  $0.5$ ,  $L = 1$ .

Investigating further on the basis that Fc adsorption also occurs in non-aqueous media in the uncharged state, we performed SECM experiments with  $\text{Fc}^+\text{PF}_6^-$  in solution on the same sample as that in **Figure 6.5a**, on its MLG surface. In this case, oxidation of

tip-generated Fc takes place at the substrate. SECM feedback imaging and spot analysis measurements presented in **Figures 6.5e** and **6.5f** respectively, revealed significantly faster ET behavior during Fc oxidation at the substrate, suggesting even faster kinetics than on Pt. This is in contrast to the kinetically limited  $\text{Fc}^+$  or  $\text{FcMeOH}^+$  reduction when starting from Fc or FcMeOH redoxmers in solution. Thus, if adsorption takes place, it would likely depend strongly on the initial composition of the electrolyte, with Fc or FcMeOH at the interface presumably affecting the MLG more profoundly. However, to the best of our knowledge, there is no report of Fc (or its derivatives) adsorption in non-aqueous media on carbon electrodes, only with an early study from Bard and co-workers reporting FcMeOH adsorption on Pt electrodes in DMSO solvent.<sup>[21]</sup>

To investigate whether the solvent is affecting Fc adsorption by altering the binding energy on carbon electrodes, Q-Chem simulations on a graphene cluster model was used. The Fc had its structure relaxed to an optimal adsorption configuration in vacuum while incorporating the effects of the solvent through either the PCM or COSMO model. The geometry utilized in this study is similar to the low energy adsorption configuration for Fc at the graphene surface found by Nigar et al.<sup>[56]</sup> An image of the Fc molecule at the surface of the graphene cluster model is shown in **Figure D.14**. Effects of the solvent on the binding energy of the molecule were then inspected. The computed binding energy of Fc in the neutral state with the graphene cluster without solvent is -0.61 eV. Using a periodic calculation in VASP with the PBE functional and D2 Van der Waals correction, Nigar et al., calculated a similar value of -0.45 eV.<sup>[56]</sup> The binding energies of Fc on the graphene cluster in propylene carbonate and water are -0.57 eV using PCM, while for COSMO they were both -0.55 eV. This lack of solvent effect on the binding energy in the computations suggests that the dramatic effect the solvent has on charge transfer in **Figure 6.4b** and **6.4c** is not related to a change in binding energy caused by the different solvents. However, it is also possible that the solvent is affecting some other parameter that is important for charge transfer, for example, the reorganization energy of Fc.

In addition to the possibility of redoxmer adsorption, asymmetric limiting currents during oxidation and reduction of ferrocene derivatives (such as  $\text{FcTMA}^+$ ) have been reported through nanogap SECM measurements.[57, 58] This observation was attributed to contamination present on HOPG carbon electrodes used in the study, with Pt electrode materials exhibiting no asymmetric behavior.[59] Other nanogap SECM measurements revealed asymmetry in redox behavior arising out of polymer residues on CVD grown graphene.[60] However, it has also been highlighted that there may be confounding factors in nanogap measurements, arising for example, from adsorption of  $\text{FcTMA}^+$  species on glass and carbon electrodes.[61] A critical factor in contamination is also the presence of TOC carbon in aqueous media, with ppb level TOC observed to impact ET behavior.[58] Such purity can be implemented by a series of filtration steps,[58] which were not adopted in this study. However, sluggish ET behavior for  $\text{FcMeOH}^+$  reduction in aqueous media was not observed in our measurements (**Figure 6.4c**). In summary, our experiments and computational simulations suggest the asymmetric behavior with Fc redox on MLG substrates are not fully explicable by the two known non-idealities associated with Fc and its derivatives: adsorption and contamination.

To rule out the asymmetric behavior of Fc and  $\text{FcMeOH}$  redox originating due to the use of MLG electrodes, we also explored HOPG and GC as bulk carbon electrode materials for performing spot analysis measurements. HOPG materials can be cleaved prior to imaging, resulting in a relatively clean basal plane carbon surface for measurements. AFM image of the HOPG substrate is shown in **Figure 6.6a**, revealing basal planes with lengths between 1-2  $\mu\text{m}$ . This implies that the areas interrogated during spot analysis comprise primarily basal planes. Spot analysis of  $\text{FcMeOH}^+$  reduction at the substrate is shown in **Figure 6.6b**, and the ET behavior is observed to be very similar to **Figure 6.4b** and **6.5d**. Additionally, the use of  $\text{Fc}^+\text{PF}_6^-$  as a redoxmer (**Figure 6.6c**) revealed faster ET kinetics agreeing with results from MLG electrodes in **Figure 6.5f**. On the other hand, GC is a bulk carbon material with a different microstructure consisting of disordered graphitic

planes with dimensions  $< 100 \text{ \AA}$ , as compared to HOPG.[62] Irrespectively, the Raman 2D/G spectral map in **Figure 6.6d** revealed a chemically homogeneous surface, distinct from HOPG (Raman spectra of HOPG in **Figure D.15**). Yet, spot analysis revealed the same low reactivity with FcMeOH in solution (**Figure 6.6e**) and faster ET kinetics with  $\text{Fc}^+\text{PF}_6^-$  in solution (**Figure 6.6f**).

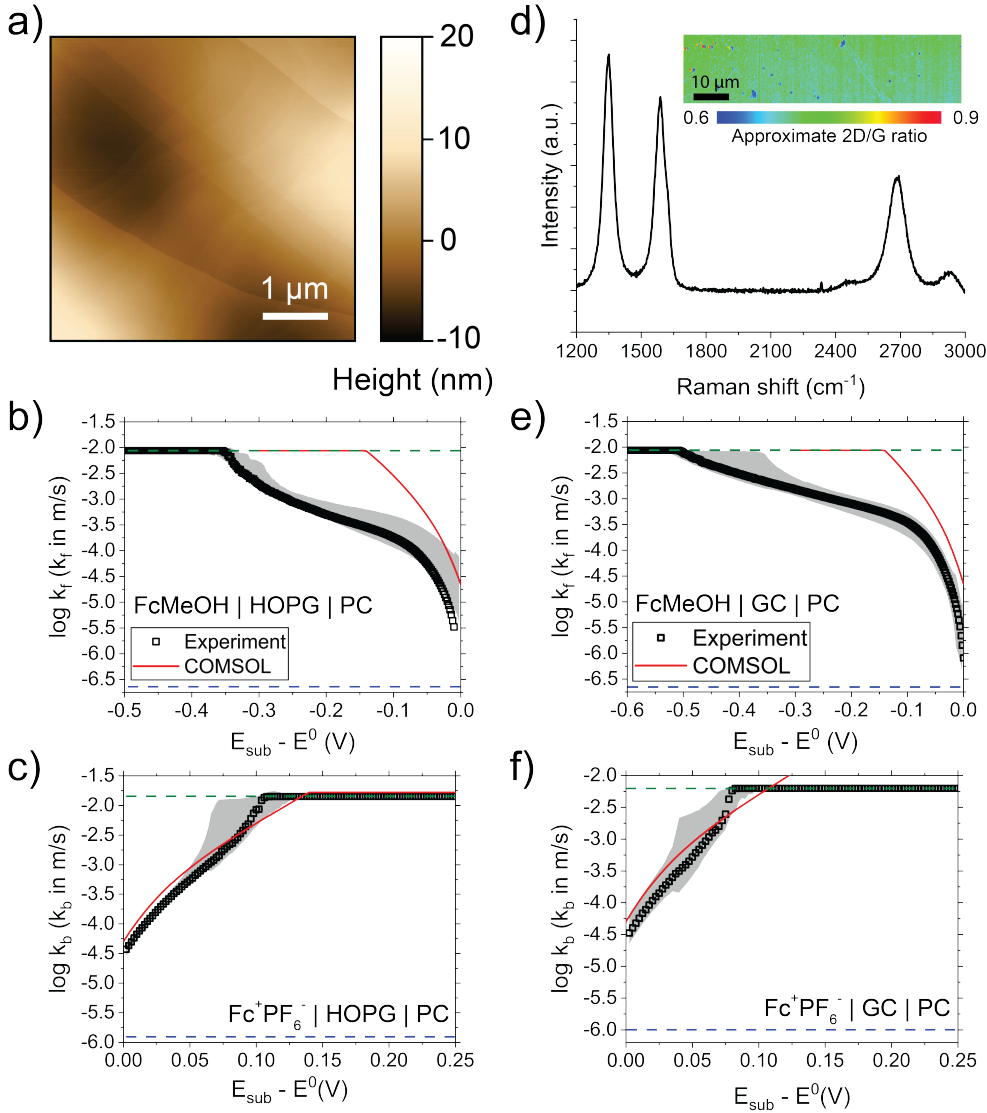


Figure 6.6: Spot analysis measurements on Grade 1 HOPG and GC electrodes. a) AFM image of HOPG, and spot analysis measurements with b)  $\text{FcMeOH}$  and c)  $\text{Fc}^+\text{PF}_6^-$  in solution. d) Raman spectra of GC, with spectral map inset, and spot analysis measurements with e)  $\text{FcMeOH}$  and f)  $\text{Fc}^+\text{PF}_6^-$  in solution. Gray areas represent standard deviation across five measurements. COMSOL simulations were performed with  $k^0$  of  $10^{-3} \text{ m/s}$ ,  $\alpha$  of 0.5,  $L = 1$ .

The similarity in the ET behavior of Fc and FcMeOH on HOPG, GC and MLG electrodes rules out two important factors: i) during MLG transfer, a sacrificial polymer is used, which potentially leaves behind residues upon its removal in organic solvents.[63] While polybisphenol A carbonate utilized for MLG transfer is known to leave the least amount of residues,[63] it is clear that its residues are not contributing to the lower rates of ET observed in **Figures 6.4b** and **6.5d**. This is made even more certain with the use of freshly cleaved HOPG electrodes (**Figures 6.6a-6.6c**), although  $\approx$ 10 mins air exposure was unavoidable owing to cell assembly and transfer inside the glovebox. Brief periods of air exposure are well known to contaminate HOPG surfaces, which consequently can affect the ET behavior reported.[58] In addition, the MLG electrode's conductivity or related factors like the presence of tears and holes is not a limiting factor either, since bulk HOPG and GC electrodes do not have such features.

In an effort to obtain direct experimental evidence of molecular adsorption, we performed scan rate dependence CV measurements of Fc and  $\text{Fc}^+\text{PF}_6^-$  with a 3 mm GC macrodisk (**Figure D.16, D.17**). Contrary to the literature on CVs of Fc (and its derivatives) obtained with HOPG and Pt electrodes,[21, 53, 61] the voltammograms were easily fit to a semi-infinite diffusion limited redox process, without the need for considering adsorption. Therefore, the bulk measurements did not reveal any obvious Fc adsorption. After the CV measurements, we soaked the GC electrode in PC, followed by CVs in 0.1 M TBAPF<sub>6</sub>/PC blank electrolyte, which revealed no redox peaks (**Figure D.18**). This result indicates that no irreversible adsorption of Fc or  $\text{Fc}^+\text{PF}_6^-$  takes place on GC electrodes. We also performed measurements with macrodisk MLG (**Figure D.19**) with similar results to those obtained with GC. These experiments are inherently challenging in non-aqueous media owing to the high ohmic losses observable ( $\approx$ 700 - 3000  $\Omega$ ) in our measurements, which consequently leads to distorted CVs (**Figure D.20**). Furthermore, the deviation of  $\alpha$  from 0.5 is hard to observe in bulk measurements as well, with simulated macro-disc CVs revealing very little changes with varying  $\alpha$  (**Figure D.21**). It should also be noted that

fast reversible adsorption processes are difficult to distinguish from diffusion-limited redox reactions in CV measurements.[53, 64] While our bulk CV experiments did not provide any evidence of adsorption, the analysis highlights the advantages of using spot analysis measurements to characterize deviations from ideal ET behavior at the electrode-electrolyte interface.

Lastly, to correlate these observations on model carbon electrodes towards more practical, bulk materials relevant in RFBs, we utilized CVD-grown graphite films as a substrate electrode. Topography of the material is presented in **Figure 6.7a** which reveals heterogeneity in layer numbers, with maximum thickness being  $\approx 1 \mu\text{m}$ . Optical micrograph (**Figure 6.7b**) and Raman spectral maps (**Figure 6.7c**) show complete coverage with graphitic structures ranging from bulk graphite (evidenced by the characteristic asymmetric 2D peak[65]) to graphene (**Figure 6.7d**). Spot analysis with FcMeOH in solution and a readily available 25  $\mu\text{m}$  diameter UME tip revealed kinetically limited ET for FcMeOH $^+$  reduction, (**Figure 6.7e**) consistent with our observations from MLG, HOPG and GC electrodes. These experiments therefore suggest that the carbon electrode structure (i.e. variations in edge planes/basal planes, graphite domain size, etc.) has no or little effect on the factors impacting ET behavior of Fc $^+$  reduction at the substrate. Furthermore, a spot analysis experiment with FcMeOH $^+$ Pf $_6^-$  in solution (obtained through bulk electrolysis) revealed fast ET behavior (**Figure D.22**), similar to behavior of Fc $^+$ Pf $_6^-$  on MLG, HOPG and GC.

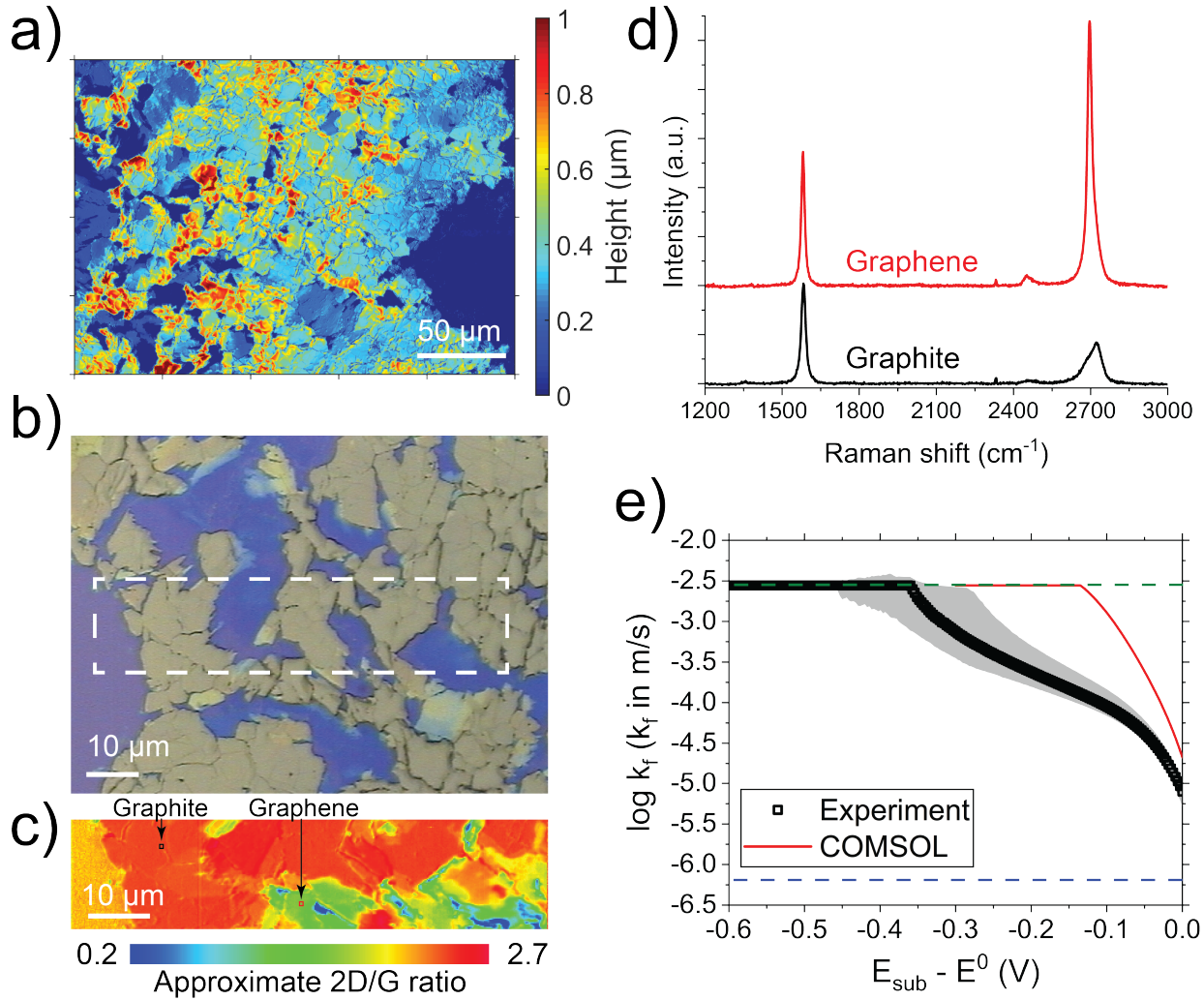


Figure 6.7: CVD graphite characterization and spot analysis with FcMeOH in solution. a) Height topography of the graphitic carbons revealing bulk graphite structures  $\approx 1 \mu\text{m}$  in thickness. b) Optical micrograph with Raman 2D/G map (without baseline correction) of the area within the white dashed box in c) reveals distinct graphite and graphene domains. d) Baseline corrected Raman spectra from  $1 \times 1 \mu\text{m}$  areas of graphite and graphene in c). e) Spot analysis measurements revealing kinetically limited ET, as observed with MLG, HOPG and GC electrodes. COMSOL simulations were performed with  $k^0$  of  $10^{-3} \text{ m/s}$ ,  $\alpha$  of 0.5,  $L = 0.5$ .

With the idea that the decrease in ET kinetics is arising out of adsorption, we performed spot analysis measurements with these graphite electrode materials at different redoxmer concentrations. Thus far we have analyzed the behavior of Fc (and FcMeOH) at  $\approx 1 \text{ mM}$  concentration. According to adsorption theories such as the Langmuir isotherm,[13,

[16] it is plausible to expect that the equilibrium concentration of the redoxmer has an effect on reversible adsorption. Thus, we investigated the ET behavior at a concentration tenfold lower, 0.1 mM (which is around the lowest limit we could investigate practically given the capacitance of 25  $\mu\text{m}$  diameter UMEs), as well as 100-fold higher, up to 100 mM.

Our measurements reveal sluggish ET kinetics across all concentrations between 0.1 mM to 100 mM for  $\text{Fc}^+$  reduction (**Figure 6.8a-6.8c**, i.e. Fc originally in solution) at the substrate electrode, consistent again with our previous measurements. Although no clear trends were evident for  $\alpha$ , the  $k_f$  values corresponding to  $E_{\text{sub}} - E^0 = 0 \text{ V}$  increase almost by two orders of magnitude as concentration increases. This factor cannot be accounted for by the minor changes in viscosity ( $\approx 10\%$ , based on experimental literature[66]) and diffusion coefficient of Fc in the concentration regime evaluated. This observation is indicative of the fact that the  $k^0$  for Fc maybe increasing with concentration. This observation would go against the idea that adsorption is occurring and decreasing ET kinetics. The behavior of  $\text{Fc}^+\text{PF}_6^-$  in the spot analysis experiments is consistent with the fast ET as described previously for all cases, even at the highest tested concentration of 100 mM (**Figure 6.8d-6.8f**). The  $k_b$  values corresponding to  $E_{\text{sub}} - E^0 = 0 \text{ V}$  match well with  $k_f$  values obtained similar concentrations Fc in solution, adding more strength that our measurements are capturing the correct ET behavior. As a final note, these measurements of ET behavior at high concentrations are impossible in macroscopic electrochemical techniques such as CVs, with the large currents involved leading to severe ohmic losses (**Figure D.23**), thus demonstrating a clear advantage of the spot analysis over conventional techniques (e.g. CV, RDE) to elucidate kinetic complications of redoxmers.

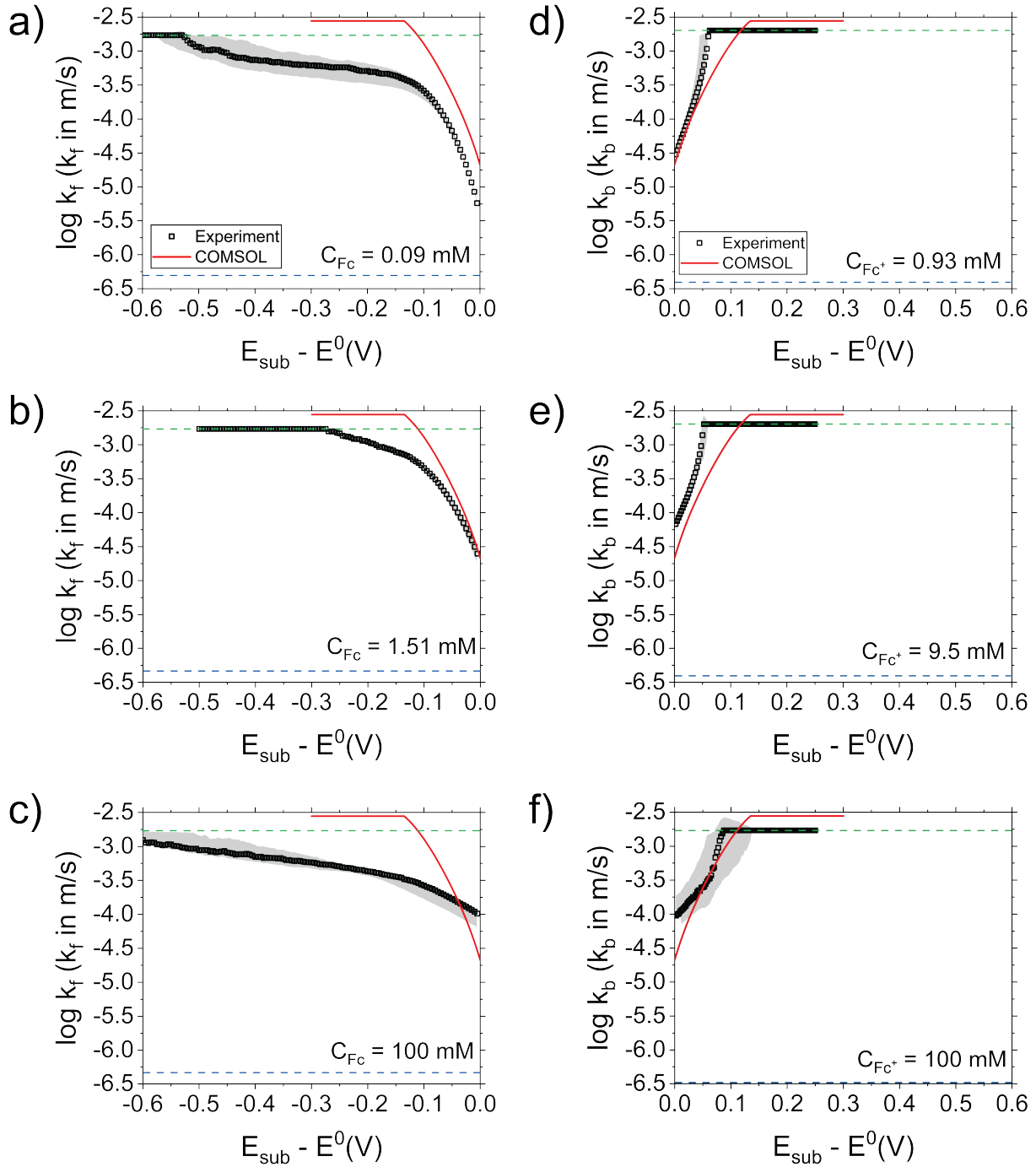


Figure 6.8: Effect of redox mediator concentration on the spot analysis measurements on graphite electrodes. a) – c) measurements performed with varying concentrations of  $\text{Fc}$ . d) – f) measurements performed with varying concentrations of  $\text{Fc}^+\text{PF}_6^-$ . The electrolyte solution was 0.1 M TBAPF<sub>6</sub> in PC for all cases. COMSOL simulations were performed with  $k^0$  of  $10^{-3}$  m/s,  $\alpha$  of 0.5,  $L = 1$ .

### 6.3 Conclusions

In summary, we presented an SECM-based spot analysis protocol to interrogate ET kinetics between a redoxmer and any substrate electrode. COMSOL simulations revealed that the method can estimate ET kinetic parameters of  $k^0$  and  $\alpha$  described in the Butler-Volmer model for charge transfer. The data obtained through the method enables a clear delineation of the electrochemical regime influenced solely by ET kinetics, which increases the accuracy of the method. When applied to redoxmers comprising of Fc and FcMeOH, the method was sensitive enough to detect ET kinetics deviating from the expected Butler-Volmer behavior for each member of the redox pair. Specifically, significantly lower rate constants were measured for  $\text{Fc}^+$  reduction to Fc compared to oxidation of Fc to  $\text{Fc}^+$  at the same  $E - E^0$  over various carbon electrodes ranging from MLG, HOPG, GC and graphite films. This asymmetry was in stark contrast to the behavior of these redox pairs over Pt or in aqueous media, highlighting the critical value that this type of spot analysis tool might bring to redox-flow battery research.

Analysis of our data with literature on ferrocene redox suggested that differential adsorption of Fc derivatives could be the source of the observed kinetic asymmetric behavior. This could be the case through a reversible adsorption step associated with ferrocene redox in non-aqueous solvents which is not captured in bulk measurements but is manifesting in the SECM spot analysis measurements. However, we were unable to identify clear signatures of such adsorption events. For example, GC and MLG electrodes, which otherwise displayed the asymmetry in the SECM spot analysis, revealed macroscopic CVs that could be well fit to a simple semi-infinite linear diffusion model without adsorption using a digital simulator. Similarly, we were unable to observe a clear progression of the spot analysis measured ET behavior as a function of Fc concentration (ranging from  $\approx 0.1$  mM up to 100 mM). DFT simulations did not suggest that solvent contributes to significant differences in the binding energy of Fc on to a graphitic surface, which contrasts to the clear differences

in kinetics observed when comparing MLG in aqueous electrolyte vs PC. Furthermore, control experiments in aqueous electrolyte, and with several types of samples obtained through different procedures indicated that adventitious and ambient contamination of electrodes appear to be an unlikely reason for the observed asymmetric behavior. This leads us to conclude that the PC solvent influences ET behavior of redoxmers in ways that are not accounted for in our current exploration of these graphitic electrochemical interfaces. While the exact reason for the asymmetric behavior remains an open question, this study highlights a robust pathway to investigate ET behavior at flow battery interfaces without resorting to bulk measurements such as CV, which is unsuitable for use at high concentrations of redoxmers in solution, and is also insensitive to such interfacial processes. The method presented here can be used to assess such non-idealities in a variety of redoxmer/electrode/solvent systems with quantitative evaluation of kinetics to decide if these will have an impact on flow-battery performance.

## Bibliography for Chapter 6

- (1) Trahey, L. et al. *Proceedings of the National Academy of Sciences* **2020**, *117*, 12550–12557, DOI: [10.1073/pnas.1821672117](https://doi.org/10.1073/pnas.1821672117).
- (2) Park, M.; Ryu, J.; Wang, W.; Cho, J. *Nature Reviews Materials* **2016**, *2*, 1–18, DOI: [10.1038/natrevmats.2016.80](https://doi.org/10.1038/natrevmats.2016.80).
- (3) Nguyen, T.; Savinell, R. F. *The Electrochemical Society Interface* **2010**, *19*, 54, DOI: [10.1149/2.F05103if](https://doi.org/10.1149/2.F05103if).
- (4) Baran, M. J.; Braten, M. N.; Montoto, E. C.; Gossage, Z. T.; Ma, L.; Chénard, E.; Moore, J. S.; Rodríguez-López, J.; Helms, B. A. *Chemistry of Materials* **2018**, *30*, 3861–3866, DOI: [10.1021/acs.chemmater.8b01318](https://doi.org/10.1021/acs.chemmater.8b01318).
- (5) Montoto, E. C.; Nagarjuna, G.; Moore, J. S.; Rodríguez-López, J. *Journal of The Electrochemical Society* **2017**, *164*, A1688, DOI: [10.1149/2.1511707jes](https://doi.org/10.1149/2.1511707jes).
- (6) Montoto, E. C.; Nagarjuna, G.; Hui, J.; Burgess, M.; Sekerak, N. M.; Hernández-Burgos, K.; Wei, T.-S.; Kneer, M.; Grolman, J.; Cheng, K. J.; Lewis, J. A.; Moore, J. S.; Rodríguez-López, J. *Journal of the American Chemical Society* **2016**, *138*, 13230–13237, DOI: [10.1021/jacs.6b06365](https://doi.org/10.1021/jacs.6b06365).
- (7) Wong, A. A.; Aziz, M. J. *Journal of The Electrochemical Society* **2020**, *167*, 110542, DOI: [10.1149/1945-7111/aba54d](https://doi.org/10.1149/1945-7111/aba54d).

- (8) Forner-Cuenca, A.; Brushett, F. R. *Current Opinion in Electrochemistry* **2019**, *18*, 113–122, DOI: [10.1016/j.coelec.2019.11.002](https://doi.org/10.1016/j.coelec.2019.11.002).
- (9) Robinson, S. G.; Yan, Y.; Hendriks, K. H.; Sanford, M. S.; Sigman, M. S. *Journal of the American Chemical Society* **2019**, *141*, 10171–10176, DOI: [10.1021/jacs.9b04270](https://doi.org/10.1021/jacs.9b04270).
- (10) Zhang, J.; Shkrob, I. A.; Assary, R. S.; Tung, S. o.; Silcox, B.; Curtiss, L. A.; Thompson, L.; Zhang, L. *The Journal of Physical Chemistry C* **2017**, *121*, 23347–23358, DOI: [10.1021/acs.jpcc.7b08281](https://doi.org/10.1021/acs.jpcc.7b08281).
- (11) Sevov, C. S.; Hickey, D. P.; Cook, M. E.; Robinson, S. G.; Barnett, S.; Minteer, S. D.; Sigman, M. S.; Sanford, M. S. *Journal of the American Chemical Society* **2017**, *139*, 2924–2927, DOI: [10.1021/jacs.7b00147](https://doi.org/10.1021/jacs.7b00147).
- (12) Sevov, C. S.; Hendriks, K. H.; Sanford, M. S. *The Journal of Physical Chemistry C* **2017**, *121*, 24376–24380, DOI: [10.1021/acs.jpcc.7b06247](https://doi.org/10.1021/acs.jpcc.7b06247).
- (13) Bard, A.; Faulkner, L., *Electrochemical Methods*, 2nd; John Wiley & Sons, New York: 2001.
- (14) Watkins, T. S.; Sarbapalli, D.; Counihan, M. J.; Danis, A. S.; Zhang, J.; Zhang, L.; Zavadil, K. R.; Rodríguez-López, J. *Journal of Materials Chemistry A* **2020**, *8*, 15734–15745, DOI: [10.1039/DOTA00836B](https://doi.org/10.1039/DOTA00836B).
- (15) Burgess, M.; Hernández-Burgos, K.; Schuh, J. K.; Davila, J.; Montoto, E. C.; Ewoldt, R. H.; Rodríguez-López, J. *Journal of the American Chemical Society* **2018**, *140*, 2093–2104, DOI: [10.1021/jacs.7b08353](https://doi.org/10.1021/jacs.7b08353).
- (16) Cuharuc, A. S.; Zhang, G.; Unwin, P. R. *Physical Chemistry Chemical Physics* **2016**, *18*, 4966–4977, DOI: [10.1039/C5CP06325F](https://doi.org/10.1039/C5CP06325F).
- (17) Mann, J. A.; Rodríguez-López, J.; Abruña, H. D.; Dichtel, W. R. *Journal of the American Chemical Society* **2011**, *133*, 17614–17617, DOI: [10.1021/ja208239v](https://doi.org/10.1021/ja208239v).
- (18) Howard, J. D.; Assary, R. S.; Curtiss, L. A. *The Journal of Physical Chemistry C* **2020**, *124*, 2799–2805, DOI: [10.1021/acs.jpcc.9b10403](https://doi.org/10.1021/acs.jpcc.9b10403).
- (19) Peng, Q.; Liu, H.; Ye, S. *Journal of Electroanalytical Chemistry* **2017**, *800*, Special Issue in honor of Masatoshi Osawa, 134–143, DOI: [10.1016/j.jelechem.2016.09.006](https://doi.org/10.1016/j.jelechem.2016.09.006).
- (20) Humphreys, E. K.; Casford, M. T. L.; Allan, P. K.; Grey, C. P.; Clarke, S. M. *The Journal of Physical Chemistry C* **2017**, *121*, 20567–20575, DOI: [10.1021/acs.jpcc.7b04731](https://doi.org/10.1021/acs.jpcc.7b04731).
- (21) Miao, W.; Ding, Z.; Bard, A. J. *The Journal of Physical Chemistry B* **2002**, *106*, 1392–1398, DOI: [10.1021/jp013451u](https://doi.org/10.1021/jp013451u).
- (22) Conway, B. *Electrochimica Acta* **1995**, *40*, 1501–1512, DOI: [10.1016/0013-4686\(95\)00031-9](https://doi.org/10.1016/0013-4686(95)00031-9).
- (23) Li, M.; Odom, S. A.; Pancoast, A. R.; Robertson, L. A.; Vaid, T. P.; Agarwal, G.; Doan, H. A.; Wang, Y.; Suduwella, T. M.; Bheemireddy, S. R.; Ewoldt, R. H.; Assary, R. S.; Zhang, L.; Sigman, M. S.; Minteer, S. D. *ACS Energy Letters* **2021**, *6*, 3932–3943, DOI: [10.1021/acsenergylett.1c01675](https://doi.org/10.1021/acsenergylett.1c01675).

- (24) Pence, M. A.; Rodríguez, O.; Lukhanin, N. G.; Schroeder, C. M.; Rodríguez-López, J. *ACS Measurement Science Au* **0000**, 0, null, DOI: [10.1021/acsmeasuresciau.2c00054](https://doi.org/10.1021/acsmeasuresciau.2c00054).
- (25) Nagarjuna, G.; Hui, J.; Cheng, K. J.; Lichtenstein, T.; Shen, M.; Moore, J. S.; Rodríguez-López, J. *Journal of the American Chemical Society* **2014**, 136, 16309–16316, DOI: [10.1021/ja508482e](https://doi.org/10.1021/ja508482e).
- (26) Ritzert, N. L.; Rodríguez-López, J.; Tan, C.; Abruña, H. D. *Langmuir* **2013**, 29, 1683–1694, DOI: [10.1021/la3042549](https://doi.org/10.1021/la3042549).
- (27) Wang, Y.; Velmurugan, J.; Mirkin, M. V. *Israel Journal of Chemistry* **2010**, 50, 291–305, DOI: [10.1002/ijch.201000026](https://doi.org/10.1002/ijch.201000026).
- (28) Bard, A. J.; Mirkin, M. V.; Unwin, P. R.; Wipf, D. O. *The Journal of Physical Chemistry* **1992**, 96, 1861–1868, DOI: [10.1021/j100183a064](https://doi.org/10.1021/j100183a064).
- (29) Skaanvik, S. A.; Stephens, L. I.; Gateman, S. M.; Geissler, M.; Mauzeroll, J. *Analytical Chemistry* **2022**, 94, 13852–13859, DOI: [10.1021/acs.analchem.2c02498](https://doi.org/10.1021/acs.analchem.2c02498).
- (30) Leslie, N.; Mena-Morcillo, E.; Morel, A.; Mauzeroll, J. *Analytical Chemistry* **2022**, 94, 15315–15323, DOI: [10.1021/acs.analchem.2c02681](https://doi.org/10.1021/acs.analchem.2c02681).
- (31) Gossage, Z. T.; Hui, J.; Sarbapalli, D.; Rodríguez-López, J. *Analyst* **2020**, 145, 2631–2638, DOI: [10.1039/C9AN02637A](https://doi.org/10.1039/C9AN02637A).
- (32) Hui, J.; Nijamudheen, A.; Sarbapalli, D.; Xia, C.; Qu, Z.; Mendoza-Cortes, J. L.; Rodríguez-López, J. *Chemical Science* **2021**, 12, 559–568, DOI: [10.1039/DOSC03226C](https://doi.org/10.1039/DOSC03226C).
- (33) Zeng, Y.; Gossage, Z. T.; Sarbapalli, D.; Hui, J.; Rodríguez-López, J. *ChemElectroChem* **2022**, 9, e202101445, DOI: [10.1002/celc.202101445](https://doi.org/10.1002/celc.202101445).
- (34) Sarbapalli, D.; Lin, Y.-H.; Stafford, S.; Son, J.; Mishra, A.; Hui, J.; Nijamudheen, A.; Romo, A. I. B.; Gossage, Z. T.; van der Zande, A. M.; Mendoza-Cortes, J. L.; Rodríguez-López, J. *Journal of The Electrochemical Society* **2022**, 169, 106522, DOI: [10.1149/1945-7111/ac9c33](https://doi.org/10.1149/1945-7111/ac9c33).
- (35) Ghilane, J.; Hapiot, P.; Bard, A. J. *Analytical Chemistry* **2006**, 78, 6868–6872, DOI: [10.1021/ac060818o](https://doi.org/10.1021/ac060818o).
- (36) Sarbapalli, D.; Mishra, A.; Rodríguez-López, J. *Analytical Chemistry* **2021**, 93, 14048–14052, DOI: [10.1021/acs.analchem.1c03552](https://doi.org/10.1021/acs.analchem.1c03552).
- (37) Denuault, G.; Mirkin, M. V.; Bard, A. J. *Journal of Electroanalytical Chemistry and Interfacial Electrochemistry* **1991**, 308, 27–38, DOI: [10.1016/0022-0728\(91\)85056-U](https://doi.org/10.1016/0022-0728(91)85056-U).
- (38) Shao, Y. et al. *Molecular Physics* **2015**, 113, 184–215, DOI: [10.1080/00268976.2014.952696](https://doi.org/10.1080/00268976.2014.952696).
- (39) Perdew, J. P.; Burke, K.; Ernzerhof, M. *Phys. Rev. Lett.* **1996**, 77, 3865–3868, DOI: [10.1103/PhysRevLett.77.3865](https://doi.org/10.1103/PhysRevLett.77.3865).
- (40) Grimme, S. *Journal of Computational Chemistry* **2006**, 27, 1787–1799, DOI: [10.1002/jcc.20495](https://doi.org/10.1002/jcc.20495).

- (41) Tomasi, J.; Mennucci, B.; Cammi, R. *Chemical Reviews* **2005**, *105*, 2999–3094, DOI: [10.1021/cr9904009](https://doi.org/10.1021/cr9904009).
- (42) Klamt, A.; Schüürmann, G. *Journal of the Chemical Society, Perkin Transactions 2* **1993**, 799–805, DOI: [10.1039/P29930000799](https://doi.org/10.1039/P29930000799).
- (43) Lefrou, C.; Cornut, R. *ChemPhysChem* **2010**, *11*, 547–556, DOI: [10.1002/cphc.200900600](https://doi.org/10.1002/cphc.200900600).
- (44) Anantharaj, S.; Noda, S.; Driess, M.; Menezes, P. W. *ACS Energy Letters* **2021**, *6*, 1607–1611, DOI: [10.1021/acsenergylett.1c00608](https://doi.org/10.1021/acsenergylett.1c00608).
- (45) Li, D.; Lin, C.; Batchelor-McAuley, C.; Chen, L.; Compton, R. G. *Journal of Electroanalytical Chemistry* **2018**, *826*, 117–124, DOI: [10.1016/j.jelechem.2018.08.018](https://doi.org/10.1016/j.jelechem.2018.08.018).
- (46) Wang, H.; Sayed, S. Y.; Luber, E. J.; Olsen, B. C.; Shirurkar, S. M.; Venkatakrishnan, S.; Tefashe, U. M.; Farquhar, A. K.; Smotkin, E. S.; McCreery, R. L.; Buriak, J. M. *ACS Nano* **2020**, *14*, 2575–2584, DOI: [10.1021/acsnano.0c01281](https://doi.org/10.1021/acsnano.0c01281).
- (47) Laoire, C. O.; Plichta, E.; Hendrickson, M.; Mukerjee, S.; Abraham, K. *Electrochimica Acta* **2009**, *54*, 6560–6564, DOI: [10.1016/j.electacta.2009.06.041](https://doi.org/10.1016/j.electacta.2009.06.041).
- (48) Kadish, K. M.; Ding, J. Q.; Malinski, T. *Analytical Chemistry* **1984**, *56*, 1741–1744, DOI: [10.1021/ac00273a051](https://doi.org/10.1021/ac00273a051).
- (49) Pournaghi-Azar, M.; Ojani, R. *Electrochimica Acta* **1994**, *39*, 953–955, DOI: [10.1016/0013-4686\(94\)85111-5](https://doi.org/10.1016/0013-4686(94)85111-5).
- (50) Zhou, H.; Dong, S. *Electrochimica Acta* **1997**, *42*, 1801–1807, DOI: [10.1016/S0013-4686\(96\)00380-5](https://doi.org/10.1016/S0013-4686(96)00380-5).
- (51) Schorr, N. B.; Jiang, A. G.; Rodríguez-López, J. *Analytical Chemistry* **2018**, *90*, 7848–7854, DOI: [10.1021/acs.analchem.8b00730](https://doi.org/10.1021/acs.analchem.8b00730).
- (52) Güell, A. G.; Cuharuc, A. S.; Kim, Y.-R.; Zhang, G.; Tan, S.-y.; Ebejer, N.; Unwin, P. R. *ACS Nano* **2015**, *9*, 3558–3571, DOI: [10.1021/acsnano.5b00550](https://doi.org/10.1021/acsnano.5b00550).
- (53) Kurapati, N.; Pathirathna, P.; Ziegler, C. J.; Amemiya, S. *ChemElectroChem* **2019**, *6*, 5651–5660, DOI: [10.1002/celc.201901664](https://doi.org/10.1002/celc.201901664).
- (54) Li, W.; Tan, C.; Lowe, M. A.; Abruña, H. D.; Ralph, D. C. *ACS Nano* **2011**, *5*, 2264–2270, DOI: [10.1021/nn103537q](https://doi.org/10.1021/nn103537q).
- (55) Bond, A. M.; McLennan, E. A.; Stojanovic, R. S.; Thomas, F. G. *Analytical Chemistry* **1987**, *59*, 2853–2860, DOI: [10.1021/ac00151a007](https://doi.org/10.1021/ac00151a007).
- (56) Nigar, S.; Wang, H.; Imtiaz, M.; Yu, J.; Zhou, Z. *Applied Surface Science* **2019**, *481*, 1466–1473, DOI: [10.1016/j.apsusc.2019.03.222](https://doi.org/10.1016/j.apsusc.2019.03.222).
- (57) Chen, R.; Balla, R. J.; Li, Z.; Liu, H.; Amemiya, S. *Analytical Chemistry* **2016**, *88*, 8323–8331, DOI: [10.1021/acs.analchem.6b02273](https://doi.org/10.1021/acs.analchem.6b02273).
- (58) Nioradze, N.; Chen, R.; Kurapati, N.; Khvataeva-Domanov, A.; Mabic, S.; Amemiya, S. *Analytical Chemistry* **2015**, *87*, 4836–4843, DOI: [10.1021/acs.analchem.5b00213](https://doi.org/10.1021/acs.analchem.5b00213).

- (59) Nioradze, N.; Kim, J.; Amemiya, S. *Analytical Chemistry* **2011**, *83*, 828–835, DOI: [10.1021/ac102352v](https://doi.org/10.1021/ac102352v).
- (60) Chen, R.; Nioradze, N.; Santhosh, P.; Li, Z.; Surwade, S. P.; Shenoy, G. J.; Parobek, D. G.; Kim, M. A.; Liu, H.; Amemiya, S. *Angewandte Chemie International Edition* **2015**, *54*, 15134–15137, DOI: [10.1002/anie.201507005](https://doi.org/10.1002/anie.201507005).
- (61) Tan, S.-y.; Zhang, J.; Bond, A. M.; Macpherson, J. V.; Unwin, P. R. *Analytical Chemistry* **2016**, *88*, 3272–3280, DOI: [10.1021/acs.analchem.5b04715](https://doi.org/10.1021/acs.analchem.5b04715).
- (62) McCreery, R. L. *Chemical Reviews* **2008**, *108*, 2646–2687, DOI: [10.1021/cr068076m](https://doi.org/10.1021/cr068076m).
- (63) Wood, J. D.; Doidge, G. P.; Carrion, E. A.; Koepke, J. C.; Kaitz, J. A.; Datye, I.; Behnam, A.; Hewaparakrama, J.; Aruin, B.; Chen, Y.; Dong, H.; Haasch, R. T.; Lyding, J. W.; Pop, E. *Nanotechnology* **2015**, *26*, 055302, DOI: [10.1088/0957-4484/26/5/055302](https://doi.org/10.1088/0957-4484/26/5/055302).
- (64) Oleinick, A.; Svir, I.; Amatore, C. *Journal of Solid State Electrochemistry* **2020**, *24*, 2023–2025, DOI: [10.1007/s10008-020-04553-x](https://doi.org/10.1007/s10008-020-04553-x).
- (65) Ferrari, A. C. *Solid State Communications* **2007**, *143*, Exploring graphene, 47–57, DOI: [10.1016/j.ssc.2007.03.052](https://doi.org/10.1016/j.ssc.2007.03.052).
- (66) Tyunina, E.; Afanas'ev, V.; Chekunova, M. *Journal of solution chemistry* **2012**, *41*, 307–317, DOI: [10.1007/s10953-012-9793-8](https://doi.org/10.1007/s10953-012-9793-8).

# Chapter 7

## Reactivity of redoxmers on sp<sup>3</sup> carbon electrodes: Hydrogenated graphene and boron-doped diamond

*Note: This work is part of a manuscript in preparation, in collaboration with Dr. Jason Howard, Dr. Larry A. Curtiss and Dr. Rajeev S. Assary.*

Redox flow batteries (RFBs) are a promising technology for large-scale storage of energy[1–5] owing to their decoupled power and capacity characteristics[1, 4], enabling scalability. In RFBs, energy storage occurs between redox couples of molecules, which are stored in separate tanks and (dis)charged in a reactor separated by a membrane. Non-aqueous RFBs (NRFBs) offer additional advantages, such as accessing the higher potential window of organic solvents and the ability to engineer tailored redox-active organic molecules, oligomers, and polymers (henceforth referred to as redoxmers) for high energy density.[1, 6–9] The fundamental process behind charge storage is the heterogeneous electron transfer (ET) reaction between current collector electrodes (typically carbon[5, 10]) and redoxmers in solution. While the electrochemistry of carbon structures such as graphite have been well studied in aqueous media through a variety of macroscopic and microscopic techniques, little knowledge exists on non-aqueous ET behavior between graphitic carbon and redoxmers in non-aqueous media.

The behavior of graphite structures in aqueous media may not necessarily extend to non-aqueous solvents, and there is plenty of indirect evidence in the literature for the same. For example, the exposure of freshly cleaved highly-ordered pyrolytic graphite (HOPG) towards non-aqueous solvents such as acetonitrile (MeCN), methanol, acetone,

among others, increased the peak splitting of  $\text{Fe}(\text{CN})_6^{3-}/\text{Fe}(\text{CN})_6^{4-}$  from  $\approx 100$  mV to  $\approx 700\text{-}800$  mV, indicating a severe deterioration in heterogeneous ET kinetics.[11, 12] No such passivation was observed with electrodes such as Pt, Au, and other carbon electrodes such as glassy carbon (GC),[11] therefore indicating that the observation arises out of interaction of MeCN with the HOPG basal plane. Interestingly, the well-known adsorption of anthraquinone-2,6-disulfonate (AQDS) on carbon electrodes[13] such as HOPG[14] was found to be limited over MeCN-exposed HOPG, indicating that adventitious defects from the MeCN exposure blocked adsorption sites. Similar effects of adventitious organic contamination arising from polishing in organic solvents blocking AQDS and ferrocene dimethanol adsorption has been reported on GC and edge plane pyrolytic graphite electrodes.[15, 16] Presence of acetone in ppb amounts has also been observed influence nanoparticle impact measurements.[17] Likewise, ambient organic impurities have been shown to decrease the surface conductivity of HOPG electrodes, as characterized by AFM measurements.[18] Our own measurements have revealed asymmetric ET kinetics with ferrocene-based redoxmers only in the case of non-aqueous propylene carbonate solvents and not aqueous solutions (refer **Chapter 6**).

In order to advance the performance of NRFBs, a fundamental understanding of how the solution molecules interact with the electrode surface must be developed. Previous studies involving both experiment and computational calculations have utilized single and multi-layer graphene (MLG) as model electrodes to understand the interaction of redox-active molecules and solvents with a carbon surface[19, 20]. These studies revealed that many candidate redoxmers and non-aqueous solvents such as acetonitrile and ethylene carbonate exhibit a strong thermodynamic binding energy on graphene basal planes with defects.[20] Additionally, it was revealed that passivating defect sites with species such as hydrogen could reduce the binding energy. Concurrently, experiments using scanning electrochemical microscopy (SECM) and atomic force microscopy (AFM) revealed film formation and passivation of electron-transfer (ET) kinetics occurring on basal plane

graphene with dialkoxybenzene redoxmers.[19] However, edge planes of graphite did not exhibit passivation. These observations provide motivation to understand the interplay of carbon electrode surface structure on ET behavior in non-aqueous media.

In this chapter, we used single-layer graphene (SLG) as a substrate in SECM experiments to examine ET kinetics of the basal plane of graphite in non-aqueous media with ferrocene (Fc) and 2,3-dimethyl-1,4-dialkoxybenzene (C7) redoxmers. Photolithography was employed to expose areas of the SLG to plasma for modifying the SLG structure. We used these substrates to our advantage of using an electrochemical scanning probe technique like SECM to provide insights into molecular reactivity between modified and un-modified regions of the SLG within a single experiment. For functionalization, we resorted to hydrogenation given that it does add foreign elements to the substrate yet is known to reduce binding energies between redoxmers and SLG.[20] Defects on SLG were created by exposure to Ar-plasma as a suitable comparison to the H-SLG substrates. Bulk sp<sup>3</sup> carbon in the form of boron-doped diamond (BDD) was also utilized for SECM measurements. BDD electrodes are known for their low background currents, wide solvent windows and have also been shown to be less prone to fouling in biological systems.[21]

## 7.1 Methods and materials

### 7.1.1 Materials

Propylene carbonate (PC, anhydrous, 99.7%), tetrabutylammonium hexafluorophosphate (TBAPF<sub>6</sub>, 99%), ferrocene (Fc, 98%) were purchased from Sigma-Aldrich. Fc was recrystallized twice over hexane. C7[22] was synthesized via previously established procedures. Single layer graphene (SLG) was purchased from GrollTex and transferred on SiO<sub>2</sub>/Si wafers using polybisphenol-A carbonate in a wet-transfer method as described in our previous work.[19, 23] Boron-doped diamond (BDD) was purchased from Fraunhofer USA CMW.

### 7.1.2 Microfabrication

SLG substrates were modified to have select areas hydrogenated, leading to H-SLG and SLG regions on a single substrate using photolithography. AZ5214E photoresist was used in the positive mode for device fabrication, with AZ917 MIF developer utilized for developing UV exposed areas. The complete lithography process is illustrated in **Figure 7.1**.

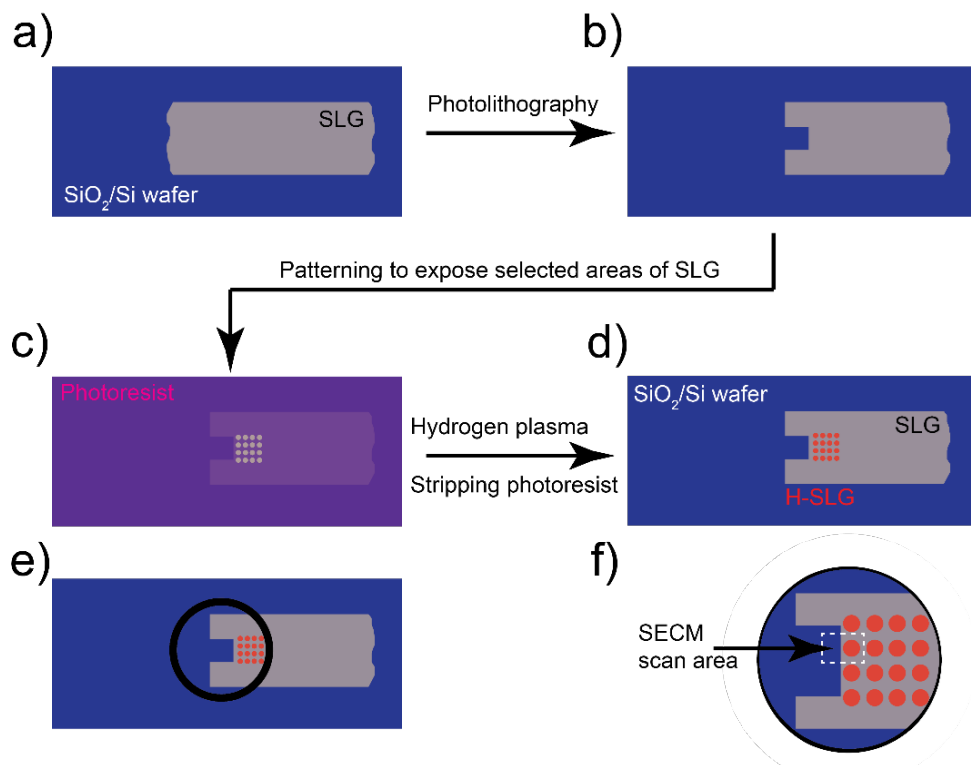


Figure 7.1: Schematics illustrating microfabrication procedure for selective hydrogenation of SLG. Photolithography was employed on a a) wet transferred SLG on  $\text{SiO}_2$  wafer, b) photolithography to introduce a defined rectangular  $\text{SiO}_2$  indent for SECM imaging. c) Photolithography to expose an array of circles 25  $\mu\text{m}$  diameter, 50  $\mu\text{m}$  center to center distance near the indent. d) Resulting substrate is exposed to hydrogen plasma to obtain H-SLG and SLG areas in a single substrate. e) Area isolated by SECM cell (black ring), and f) SECM scan area (white dashed lines) encompassing SLG and H-SLG areas depicted.

Two reactive plasma sources, namely Ar plasma and Ar/H<sub>2</sub> plasma were utilized to obtain H-SLG and defective SLG (henceforth referred as Ar-SLG). Ar/H<sub>2</sub> plasma functionalization was performed with a Tergeo plasma cleaner operating in a remote plasma

mode (plasma ignited upstream enabling a gentle surface functionalization). Recipe used 10 W power, 5 sccm Ar/H<sub>2</sub> flow (5% H<sub>2</sub>, 95% Ar gas mixture). Two exposure durations were used: 4.5 and 2 mins. This recipe was based on previous studies with H-SLG obtained with the same instrument.[24, 25] Ar plasma exposure was carried out on a Oxford Freon ICP RIE instrument, with parameters: 20 mtorr pressure, 10 W power, 5 sccm Ar flow, and 3 sec exposure. XPS and Raman characterization of H-SLG and Ar-SLG is shown in **Figure 7.2**. The XPS indicates pristine SLG graphene with little/no functional groups. H-SLG shows a characteristic upshift in binding energies, consistent with literature on H-functionalization of graphene[24, 26]. Ar-SLG reveals the presence of functional groups around 285 and 286 eV, indicating presence of C-H and C-OH species, which are also consistent with Ar-plasma induced defects on SLG.[27, 28]

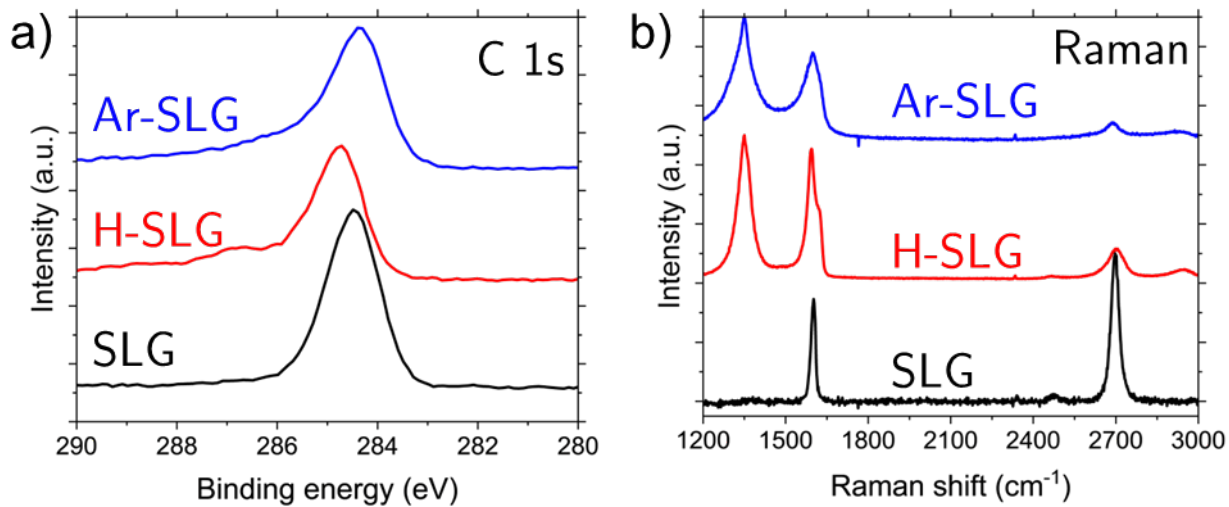


Figure 7.2: Characterization of functionalized SLG substrates. a) XPS C 1s and b) Raman spectra for SLG, H-SLG and Ar-SLG

### 7.1.3 Scanning electrochemical microscopy

SECM measurements were performed with a CHI-920D scanning electrochemical microscope with a wollaston wire ultramicroelectrode (UME) probe of 1 μm radius. A 0.5 mm dia Pt and 1 mm dia Ag wire were used as counter and reference electrodes. Experiments were performed in a MBraun Ar-filled glovebox (O<sub>2</sub>, H<sub>2</sub>O < 0.1 ppm). Potentials reported in

experimental data are vs. the half wave potential of the mediator examined, and described as overpotential or  $E_{sub} - E^0$ . A 3  $\mu\text{m}$  diameter Pt UME was used to examine ET kinetics in the case of BDD owing to the intrinsic roughness associated with the substrate.

SECM feedback imaging was used to extract information on electron transfer between SLG substrates and redox molecules of interest. Positive feedback currents above SLG was used in conjunction with analytical expressions derived by Cornut and Lefrou[24] to quantify heterogeneous ET rate constants. We also applied a recently developed spot-analysis protocol to characterize the ET rate constants  $k_f$  as a function of  $E_{sub} - E^0$  (also referred to as overpotential) applied to the substrate (see Chapter 6).

#### 7.1.4 Materials characterization

Profilometry measurements were made using a Keyence VK-X1000 laser scanning confocal microscope. Raman spectra were collected using a Nanophoton Raman 11 confocal microscope with 532 nm green laser. XPS measurements were performed with a Kratos Axis Ultra electron spectrometer, using monochromated Al K $\alpha$  radiation (1486.6 eV). XPS spectra were calibrated to the O 1s peak for SiO<sub>2</sub> at 532.8 eV.[29]

## 7.2 Results and discussion

Our first measurement involved using ferrocene to obtain a baseline understanding of how outer-sphere redox mediators[30, 31] behave on these substrates. **Figure 7.3a** shows Raman D/G maps of the SLG substrate used, with **Figure 7.3b** illustrating distinct SLG and H-SLG areas. We performed SECM feedback experiments with increasing substrate overpotential from -0.15 to -0.450 V (**Figure 7.3c**). The SECM feedback experiments revealed higher normalized feedback currents  $i/i_\infty$  over the H-SLG areas, indicating that greater ET kinetics compared to SLG areas. To probe further into the differences in ET kinetics, we resolved to spot measurements with SECM, illustrated in **Figure 7.3d**. This analysis correlated the heterogeneous electron transfer kinetics  $k_f$  to applied

overpotential, following which we used Buttler-Volmer (BV) kinetic theory to extract the transfer coefficient,  $\alpha$  ([Chapter 6](#)). It is observed that behavior is close to those predicted by COMSOL simulations using Buttler Volmer parameters of  $k^0 = 1 \times 10^{-3} \text{ m/s}$ , and  $\alpha$  of 0.5 ([Figure 6.3](#)). However, ET kinetics between Fc and SLG were observed to be kinetically limited, consistent with our previous observations with other carbon electrodes in [Chapter 6](#).

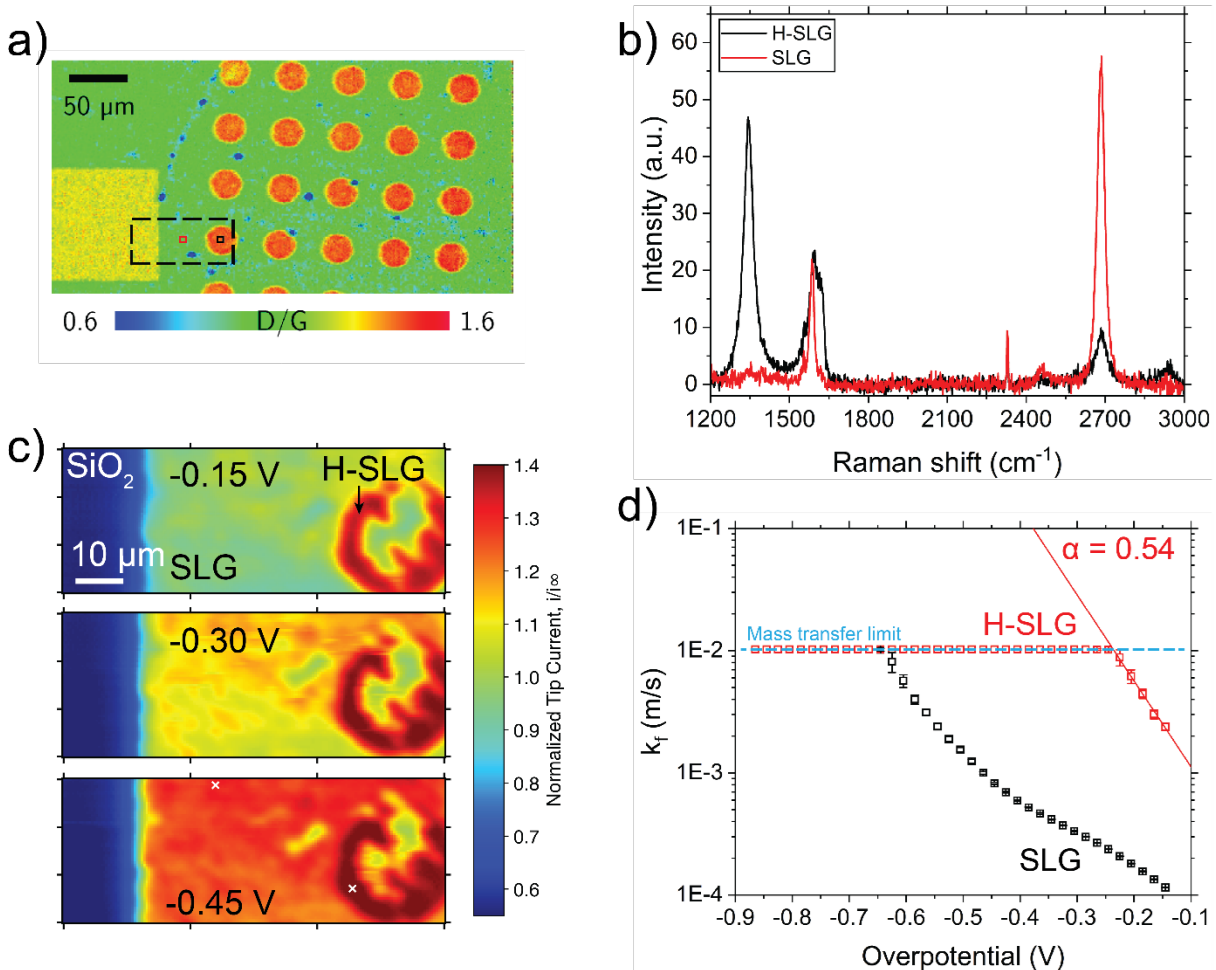


Figure 7.3: Raman characterization and reactivity of ferrocene characterized by SECM on microfabricated SLG substrates. a) Raman D/G map (without baseline correction) of the microfabricated sample with baseline corrected Raman spectra from  $10 \times 10 \mu\text{m}$  spots over H-SLG (black) and SLG (red) presented in b). c) SECM mapping in the region denoted by dashed box in a) at substrate overpotentials of  $-0.15 \text{ V}$ ,  $-0.30 \text{ V}$  and  $-0.45 \text{ V}$ . d) ET kinetics studied as a function of substrate overpotential, with cyan dashed line indicating positive feedback mass-transfer limit from the SECM experiment. The spot location over SLG and H-SLG for the measurements are highlighted by white crosses in c).

Therefore, the observation of fast kinetics over H-SLG now provides evidence that the kinetic limitations can be overcome by changing the electrode structure. Since our previous experiments did not reveal any obvious sign of the redox-active species adsorbing, our findings now raise the possibility that the kinetic limitations maybe arising out of adsorption the inactive components in the solution, as described in literature on the passivation of carbon electrode surfaces by organic solvents.

The same substrate was used for investigating the ET behavior between SLG/H-SLG and C7, as shown in **Figure 7.4a** and **7.4b**. Interestingly, our OCP kinetics were observed to be close to MT limits, however, the kinetics decreased drastically upon the application of a substrate bias. This observation was consistent with our previously published results on the C7 redoxmer, with film formation being proven to occur during the reduction of  $\text{C7}^{\bullet+}$  at the substrate.[19] However, the SECM feedback over the H-SLG areas were greater than the SLG areas, similar to what was observed for during experiments with Fc. Spot analysis confirms the greater ET kinetics over H-SLG, with a 3-fold increase observable at low overpotentials, compared to SLG. However, the dependence of  $k_f$  with applied overpotentials deviate from predictions from Butler-Volmer model, with  $\alpha < 0.3$ .

A comparison of ET kinetics before and after cycling C7 with the substrate is presented in **Figure 7.4c** and **7.4d**. In these measurements, we utilize the open circuit feedback[32, 33] as a means to discern passivation induced by filming, without influence of substrate bias.[19] We see a considerable loss in  $k_f$  at -0.15 V, compared to those at OCP over SLG before cycling, as is evident from the feedback images in **Figure 7.4a**. This drastic loss is largely mitigated over H-SLG areas.  $k_f$  at OCP decreases drastically before and after cycling, which is known to be arising from film formation. However, we see no such decrease in OCP kinetics after cycling over the H-SLG area, possibly indicating changes to the mechanisms limiting ET kinetics. However, this observation still does not explain the sluggish ET behavior over the wide range of applied potentials for C7, therefore indicating

additional factors at play behind the poor ET kinetics observed for C7.

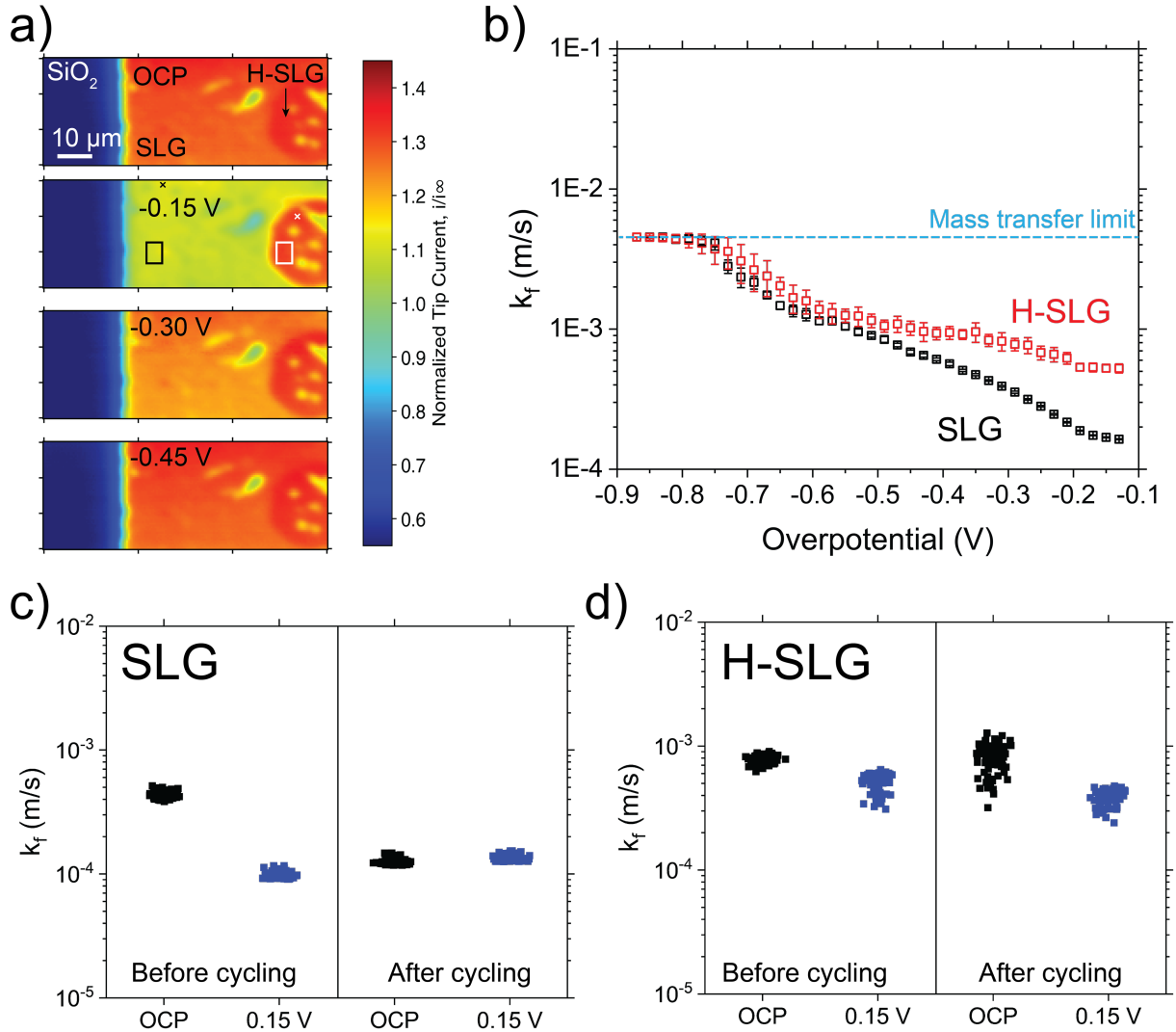


Figure 7.4: Reactivity of C7 over SLG and H-SLG as characterized by SECM. a) SECM mapping of electrochemical reactivity at open circuit and at substrate overpotentials of -0.15 V, -0.30 V and -0.45 V. b) SECM spot analysis as indicated by white and black crosses at -0.15 V in a). c) and d) Distribution of rate constants from SLG and H-SLG areas ( $\approx 27 \mu\text{m}^2$ ) denoted by white and black rectangles at -0.15V in a), before and after cycling C7 with the substrate.

Motivated by this observation of H-SLG enhancing ET kinetics, we examined SLG substrates functionalized with a lesser exposure duration to Ar/H<sub>2</sub> plasma, as shown in **Figure 7.5a**. Raman spectroscopy illustrates the presence of sharp G peaks, with little

change in peak width compared to the SLG spectra (**Figure 7.5**). Along with the presence of the 2D peak, this indicates a low degree of H-functionalized defects on the substrate.[27, 34, 35] While SECM feedback imaging and spot analysis once again revealed kinetically limited behavior over SLG consistent with **Figure 7.3**, enhanced reactivity was observed over H-SLG areas. However, spot analysis in **Figure 7.5d** reveals little difference in reactivity when comparing H-SLG and SLG with the reactivity observed over SLG in **Figure 7.3c**.  $\alpha$  measured over SLG and H-SLG in **Figure 7.5d** is  $\approx 0.15$ , reinforcing the kinetically limited behavior is taking place. This result also serves as an indication that the presence of photoresist or polycarbonate residues involved in the preparation of SLG samples are not kinetically limiting in the SECM measurements reported here. Therefore, the limited functionalization does not increase reactivity of Fc, with the spot analysis providing clearer support of this fact than the SECM feedback images in **Figure 7.5c**.

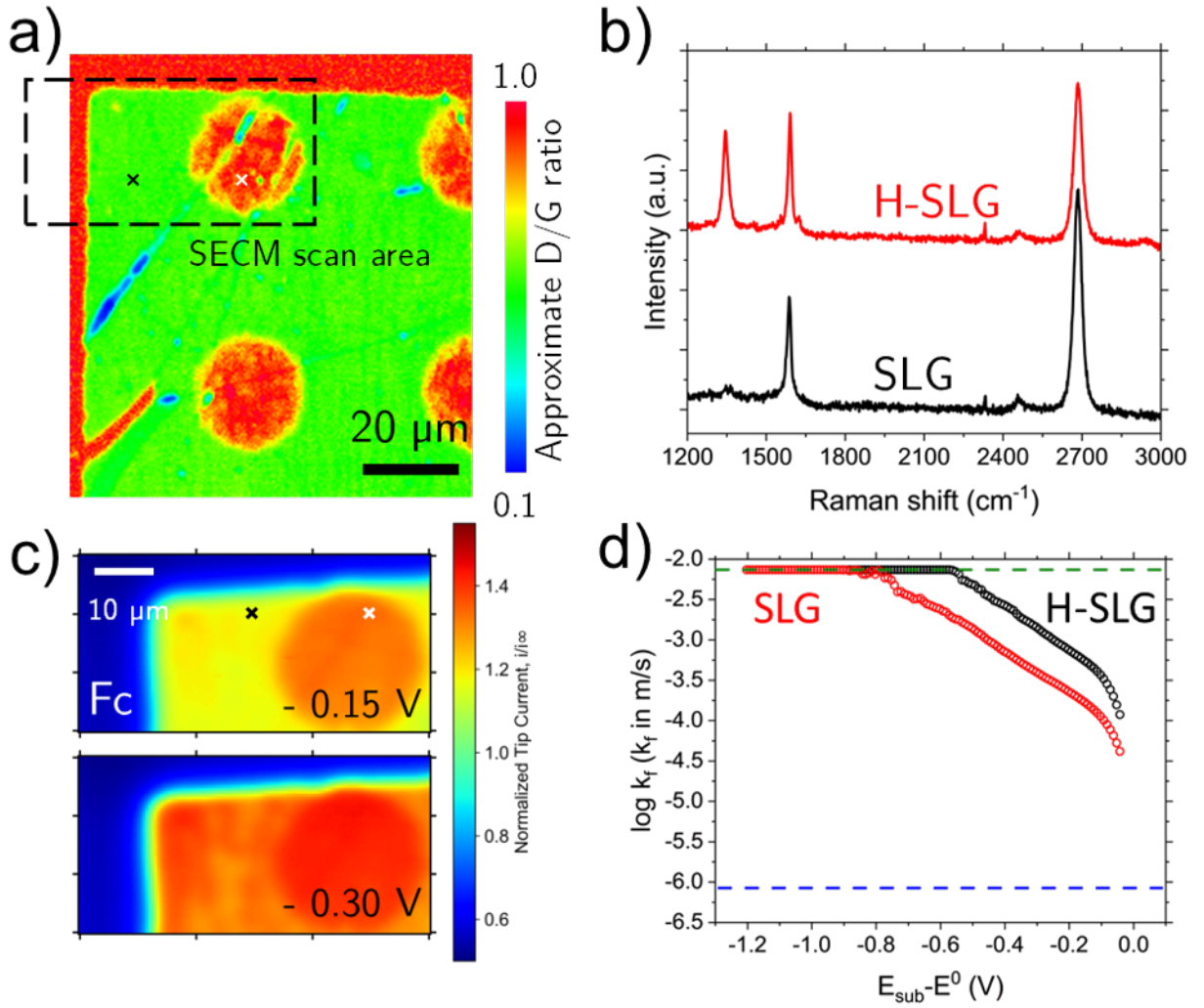


Figure 7.5: Reactivity of Fc over H-SLG obtained by lower duration of plasma exposure. a) Raman D/G map illustrating SECM scan area, b) spectra from  $2 \times 2 \mu\text{m}$  areas indicated by black and white crosses in a) characterizing SLG and H-SLG areas respectively. c) SECM feedback imaging at two different overpotentials, d) spot analysis carried out at spots marked with black and white crosses in c). Dashed lines in d) indicate MT limits.

The observation of increased ET kinetics over functionalized SLG has been reported in literature, with hydroxymethyl ferrocene reactivity over Ar-induced defects increasing, compared to pristine SLG areas.[27] This study reported that the standard heterogeneous electron transfer rate constant,  $k^0$ , increases as a function of defect density owing to an enhancement in density of states (DOS) in defective SLG, however, after a certain degree, it decreases rapidly owing to decreased conductivity of the electrode. Our

observations match qualitatively to some extent, with Fc reactivity behavior following expected Butler Volmer kinetics at high degree of functionalization (**Figure 7.3d**), with lower  $\alpha$  values being observed at lower Ar/H<sub>2</sub> plasma exposure durations (**Figure 7.5d**). However, we do not report  $k^0$  values, given the limitations associated with mass-transfer in such SECM measurements (**Chapter 6**). More importantly, the prior SECM study estimated  $k^0$  from  $k_f$  values, with the assumption that  $\alpha$  is 0.5, which clearly is not the case in non-aqueous solutions containing Fc mediators. Our results indicate that the functionalization affects the dependence of  $k_f$  as a function of  $E_{sub} - E^0$ , while it may be affecting  $k^0$ , it cannot be conclusively estimated from SECM measurements alone. If anything, these results again bring into question the role of defects in carbon electrodes on heterogeneous electron transfer reactions. Even if we assume that the defects increase reactivity via enhancing the DOS for SLG, the observations of kinetically limited behavior for Fc over bulk electrodes such as MLG, GC, HOPG and graphite (**Chapter 6**) goes unexplained.

Investigating further, we focused our attention on the effect of Ar-plasma induced defects on the reactivity of Fc and C7. The microfabricated Ar-SLG samples exhibit a slightly higher defect density (**Figures 7.6a, 7.6b**) as compared to the sample in **Figure 7.5a**.[34, 35] While Fc reveals higher reactivity over the Ar-SLG areas (**Figure 7.6c**), C7 reactivity over the Ar-SLG area is diminished compared to the pristine SLG surfaces. This observation again highlights the fact that the increased DOS does not necessarily imply greater heterogeneous electron-transfer rate constants. Rather, it is becoming increasingly likely that these deviations from expectations stem from interface-related effects. Therefore, we propose the following hypothesis: Fc reactivity over H-SLG is enhanced due to the mitigation of subtle interface effects associated between Fc and sp<sup>2</sup> graphitic carbons, which are sensitive to the presence of sp<sup>3</sup> hybridized carbon. On the other hand, C7 reactivity is always kinetically limited with limited sensitivity to the presence of sp<sup>3</sup> carbon, with the behavior being governed due to the interphase structures it forms during redox reactions, as

characterized earlier.[19]

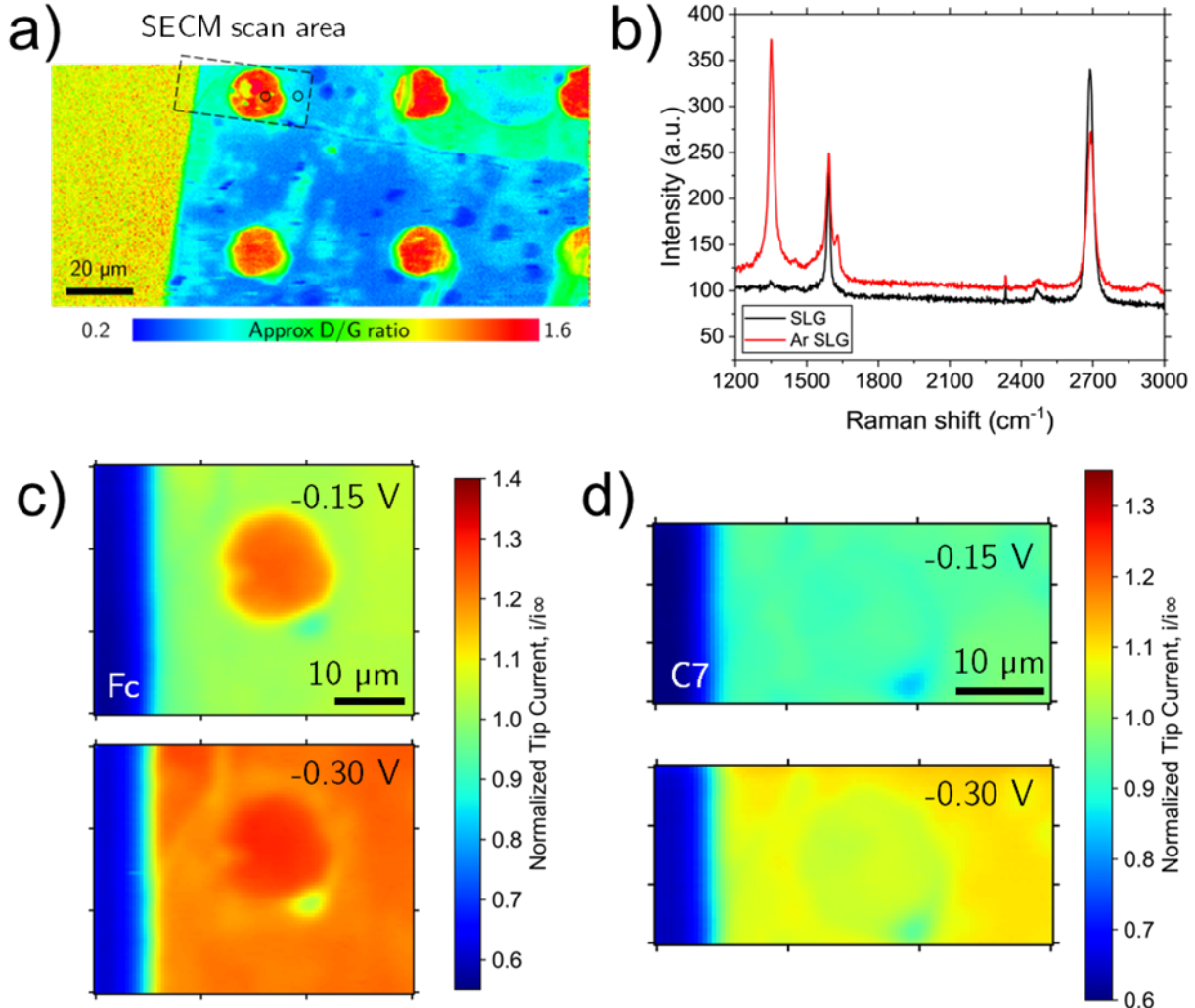


Figure 7.6: Reactivity of Fc and C7 over defects induced by Ar-plasma. a) Raman D/G map illustrating SECM scan area, b) spectra from  $2 \times 2 \mu\text{m}$  areas indicated by circles in a). characterizing SLG and SLG areas with defects with SECM feedback imaging with c) Fc and d) C7 at  $-0.15 \text{ V}$  and  $-0.30 \text{ V}$  respectively.

As a final attempt in strengthening the hypothesis, we turned to a bulk  $\text{sp}^3$  carbon sample – BDD. Optical images and resulting profilometry shown in **Figure 7.7a** and **7.7b** revealed a substrate with grain sizes  $< 1\text{-}2 \mu\text{m}$ , and surface heights fluctuating on the order of  $0.5 \mu\text{m}$ . Raman spectrum of a  $5 \mu\text{m}$  line along the length of BDD surface (**Figure 7.7c**) indicated presence of  $\text{sp}^2$  carbon at  $1520 \text{ cm}^{-1}$ .[36] The peak at

$1215\text{ cm}^{-1}$  indicates significant boron doping to ensure conductivity.[36–38] Spot analysis of Fc reveals fast kinetics, similar to those observed over H-SLG in **Figure 7.3d**. This observation reinforces our hypothesis that bulk  $\text{sp}^3$  conducting carbons is able to mitigate kinetic limitations associated with the reduction of  $\text{Fc}^+$  to Fc (i.e. electrolyte solution had Fc at the beginning). On the other hand, the C7 reactivity was kinetically limited (**Figure 7.7d**), consistent with measurements in **Figure 7.4b**.

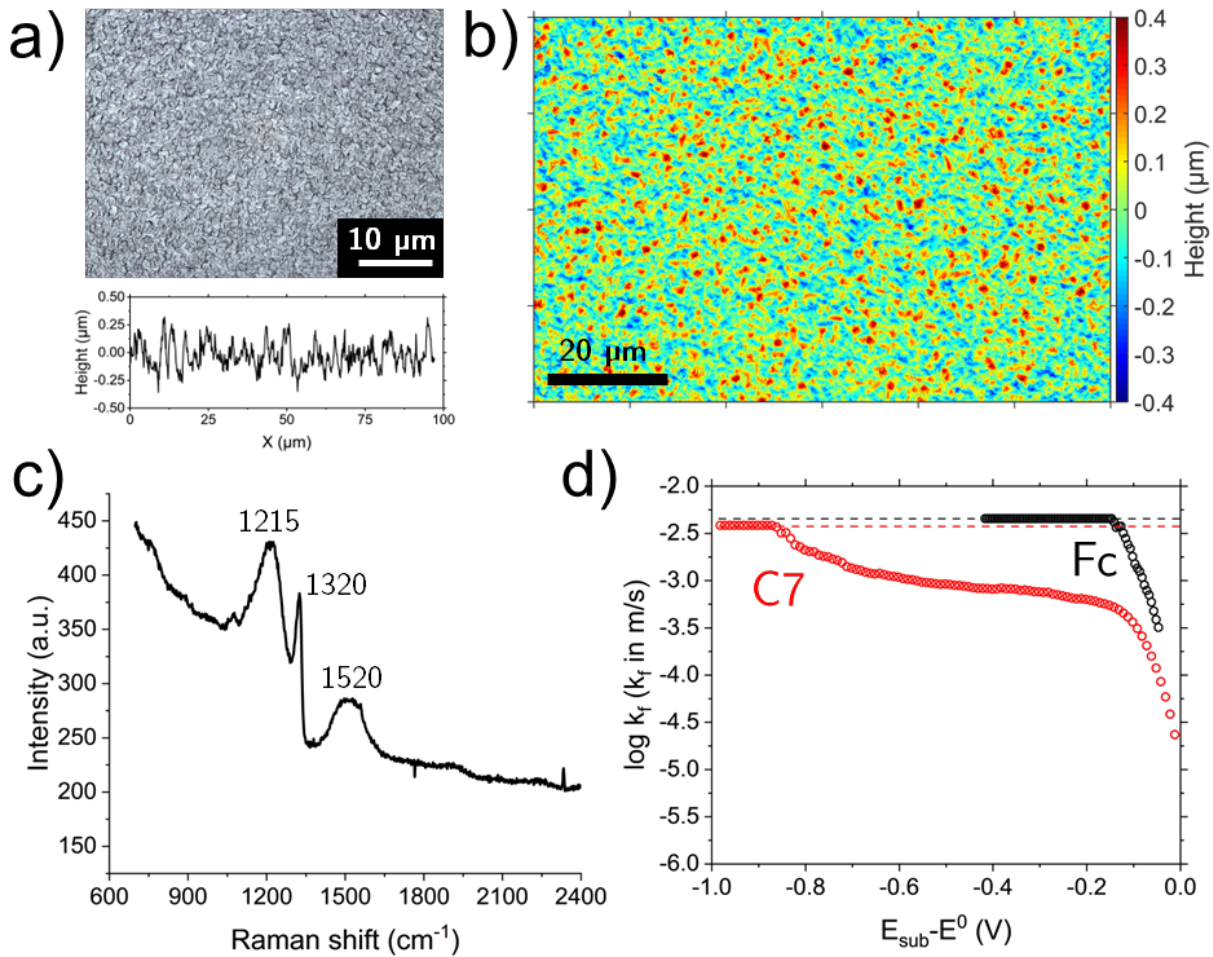


Figure 7.7: Characterization and reactivity of Fc and C7 over BDD electrodes. a) Optical micrograph and b) profilometry of the sample. c) Raman spectra of BDD with 532 nm excitation wavelength. d) Spot analysis of Fc and C7 over BDD. Dashed lines in d) indicate MT limits.

### 7.3 Conclusions

This study focused on the role of the carbon electrode structure, specifically  $sp^2$  vs.  $sp^3$  hybridization by utilizing substrates with defects induced by exposure to Ar/H<sub>2</sub> and Ar plasma. ET kinetics were quantified by SECM feedback imaging and spot analysis measurements on the same substrates, with Fc and C7 mediators. SECM measurements with Fc mediators revealed kinetically limited behavior over SLG areas, consistent with previous measurements on other multi-layer graphene and bulk carbon electrodes. However, the kinetics consistent with Butler-Volmer charge-transfer theory was observed over H-SLG areas. This observation was lost on H-SLG areas obtained with a lesser exposure time to reactive plasma. Slower kinetics were also observed on defective SLG obtained from Ar plasma exposure. These observations indicated that the kinetically limited behavior could be arising out of defects affecting DOS of SLG or subtle interface effects. Measurements with C7, on the other hand, revealed sluggish behavior on both H-SLG and SLG areas, although ET kinetics were enhanced at low overpotentials. This observation, coupled with the fact that kinetically limited behavior has been observed with Fc on bulk carbon electrodes indicated that the effect originates from uncharacterized behavior at the electrode-electrolyte interface. Indeed, upon performing measurements on a bulk BDD electrode, Fc kinetics were observed to be fast and following trends explained by Butler-Volmer kinetics, whereas as C7 reactivity remained sluggish, owing to interphase structures that form during C7 cycling. This study reinforces the fact that heterogeneous ET kinetics of carbon electrodes in non-aqueous media are influenced by electrode-electrolyte interface effects. A possible solution to overcome kinetic limitations arising from these effects appear to be changing the electrode structure from  $sp^2$  to  $sp^3$  hybridization.

### Bibliography for Chapter 7

- (1) Trahey, L. et al. *Proceedings of the National Academy of Sciences* **2020**, *117*, 12550–12557, DOI: [10.1073/pnas.1821672117](https://doi.org/10.1073/pnas.1821672117).

- (2) Skyllas-Kazacos, M.; Menictas, C.; Lim, T. In *Electricity Transmission, Distribution and Storage Systems*, Melhem, Z., Ed.; Woodhead Publishing Series in Energy; Woodhead Publishing: 2013, pp 398–441, DOI: [10.1533/9780857097378.3.398](https://doi.org/10.1533/9780857097378.3.398).
- (3) Alotto, P.; Guarneri, M.; Moro, F. *Renewable and Sustainable Energy Reviews* **2014**, *29*, 325–335, DOI: [10.1016/j.rser.2013.08.001](https://doi.org/10.1016/j.rser.2013.08.001).
- (4) Nguyen, T.; Savinell, R. F. *The Electrochemical Society Interface* **2010**, *19*, 54, DOI: [10.1149/2.F06103if](https://doi.org/10.1149/2.F06103if).
- (5) Noack, J.; Roznyatovskaya, N.; Herr, T.; Fischer, P. *Angewandte Chemie International Edition* **2015**, *54*, 9776–9809, DOI: [10.1002/anie.201410823](https://doi.org/10.1002/anie.201410823).
- (6) Wang, W.; Sprenkle, V. *Nature Chemistry* **2016**, *8*, 204–206, DOI: [10.1038/nchem.2466](https://doi.org/10.1038/nchem.2466).
- (7) Rhodes, Z.; Cabrera-Pardo, J. R.; Li, M.; Minteer, S. D. *Israel Journal of Chemistry* **2021**, *61*, 101–112, DOI: [10.1002/ijch.202000049](https://doi.org/10.1002/ijch.202000049).
- (8) Montoto, E. C.; Nagarjuna, G.; Hui, J.; Burgess, M.; Sekerak, N. M.; Hernández-Burgos, K.; Wei, T.-S.; Kneer, M.; Grolman, J.; Cheng, K. J.; Lewis, J. A.; Moore, J. S.; Rodríguez-López, J. *Journal of the American Chemical Society* **2016**, *138*, 13230–13237, DOI: [10.1021/jacs.6b06365](https://doi.org/10.1021/jacs.6b06365).
- (9) Baran, M. J.; Braten, M. N.; Montoto, E. C.; Gossage, Z. T.; Ma, L.; Chénard, E.; Moore, J. S.; Rodríguez-López, J.; Helms, B. A. *Chemistry of Materials* **2018**, *30*, 3861–3866, DOI: [10.1021/acs.chemmater.8b01318](https://doi.org/10.1021/acs.chemmater.8b01318).
- (10) Chakrabarti, M.; Brandon, N.; Hajimolana, S.; Tariq, F.; Yufit, V.; Hashim, M.; Hussain, M.; Low, C.; Aravind, P. *Journal of Power Sources* **2014**, *253*, 150–166, DOI: [10.1016/j.jpowsour.2013.12.038](https://doi.org/10.1016/j.jpowsour.2013.12.038).
- (11) Liu, Y.; Freund, M. S. *Langmuir* **2000**, *16*, 283–286, DOI: [10.1021/la991044s](https://doi.org/10.1021/la991044s).
- (12) Xiong, L.; Batchelor-McAuley, C.; Ward, K. R.; Downing, C.; Hartshorne, R. S.; Lawrence, N. S.; Compton, R. G. *Journal of Electroanalytical Chemistry* **2011**, *661*, 144–149, DOI: [10.1016/j.jelechem.2011.07.028](https://doi.org/10.1016/j.jelechem.2011.07.028).
- (13) McCreery, R. L. *Chemical Reviews* **2008**, *108*, 2646–2687, DOI: [10.1021/cr068076m](https://doi.org/10.1021/cr068076m).
- (14) Zhang, G.; Kirkman, P. M.; Patel, A. N.; Cuharuc, A. S.; McKelvey, K.; Unwin, P. R. *Journal of the American Chemical Society* **2014**, *136*, 11444–11451, DOI: [10.1021/ja505266d](https://doi.org/10.1021/ja505266d).
- (15) Batchelor-McAuley, C.; Gonçalves, L. M.; Xiong, L.; Barros, A. A.; Compton, R. G. *Chemical Communications* **2010**, *46*, 9037–9039, DOI: [10.1039/C0CC03961F](https://doi.org/10.1039/C0CC03961F).
- (16) Ranganathan, S.; Kuo, T.-C.; McCreery, R. L. *Analytical Chemistry* **1999**, *71*, 3574–3580, DOI: [10.1021/ac981386n](https://doi.org/10.1021/ac981386n).
- (17) Kätelhön, E.; Cheng, W.; Batchelor-McAuley, C.; Tschulik, K.; Compton, R. G. *ChemElectroChem* **2014**, *1*, 1057–1062, DOI: [10.1002/celc.201402014](https://doi.org/10.1002/celc.201402014).
- (18) Patel, A. N.; Collignon, M. G.; O'Connell, M. A.; Hung, W. O. Y.; McKelvey, K.; Macpherson, J. V.; Unwin, P. R. *Journal of the American Chemical Society* **2012**, *134*, 20117–20130, DOI: [10.1021/ja308615h](https://doi.org/10.1021/ja308615h).

- (19) Watkins, T. S.; Sarbapalli, D.; Counihan, M. J.; Danis, A. S.; Zhang, J.; Zhang, L.; Zavadil, K. R.; Rodríguez-López, J. *Journal of Materials Chemistry A* **2020**, *8*, 15734–15745, DOI: [10.1039/DOTA00836B](https://doi.org/10.1039/DOTA00836B).
- (20) Howard, J. D.; Assary, R. S.; Curtiss, L. A. *The Journal of Physical Chemistry C* **2020**, *124*, 2799–2805, DOI: [10.1021/acs.jpcc.9b10403](https://doi.org/10.1021/acs.jpcc.9b10403).
- (21) Cobb, S. J.; Ayres, Z. J.; Macpherson, J. V. *Annual Review of Analytical Chemistry* **2018**, *11*, 463–484, DOI: [10.1146/annurev-anchem-061417-010107](https://doi.org/10.1146/annurev-anchem-061417-010107).
- (22) Huang, J.; Pan, B.; Duan, W.; Wei, X.; Assary, R. S.; Su, L.; Brushett, F. R.; Cheng, L.; Liao, C.; Ferrandon, M. S., et al. *Scientific Reports* **2016**, *6*, 1–9, DOI: [10.1038/srep32102](https://doi.org/10.1038/srep32102).
- (23) Sarbapalli, D.; Lin, Y.-H.; Stafford, S.; Son, J.; Mishra, A.; Hui, J.; Nijamudheen, A.; Romo, A. I. B.; Gossage, Z. T.; van der Zande, A. M.; Mendoza-Cortes, J. L.; Rodríguez-López, J. *Journal of The Electrochemical Society* **2022**, *169*, 106522, DOI: [10.1149/1945-7111/ac9c33](https://doi.org/10.1149/1945-7111/ac9c33).
- (24) Son, J.; Buzov, N.; Chen, S.; Sung, D.; Ryu, H.; Kwon, J.; Kim, S.; Namiki, S.; Xu, J.; Hong, S.; Watanabe, K.; Taniguchi, T.; King, W. P.; Lee, G.-H.; van der Zande, A. M. *Advanced Materials* **2019**, *31*, 1903424, DOI: [10.1002/adma.201903424](https://doi.org/10.1002/adma.201903424).
- (25) Ryu, H.; Kim, D.-H.; Kwon, J.; Park, S. K.; Lee, W.; Seo, H.; Watanabe, K.; Taniguchi, T.; Kim, S.; van der Zande, A. M.; Son, J.; Lee, G.-H. *Advanced Electronic Materials* **2022**, *8*, 2101370, DOI: [10.1002/aem.202101370](https://doi.org/10.1002/aem.202101370).
- (26) Pumera, M.; Wong, C. H. A. *Chemical Society Reviews* **2013**, *42*, 5987–5995, DOI: [10.1039/C3CS60132C](https://doi.org/10.1039/C3CS60132C).
- (27) Zhong, J.-H.; Zhang, J.; Jin, X.; Liu, J.-Y.; Li, Q.; Li, M.-H.; Cai, W.; Wu, D.-Y.; Zhan, D.; Ren, B. *Journal of the American Chemical Society* **2014**, *136*, 16609–16617, DOI: [10.1021/ja508965w](https://doi.org/10.1021/ja508965w).
- (28) Chen, J.; Shi, T.; Cai, T.; Xu, T.; Sun, L.; Wu, X.; Yu, D. *Applied Physics Letters* **2013**, *102*, 103107, DOI: [10.1063/1.4795292](https://doi.org/10.1063/1.4795292).
- (29) Jensen, D. S.; Kanyal, S. S.; Madaan, N.; Vail, M. A.; Dadson, A. E.; Engelhard, M. H.; Linford, M. R. *Surface Science Spectra* **2013**, *20*, 36–42, DOI: [10.1116/11.20121101](https://doi.org/10.1116/11.20121101).
- (30) Bard, A.; Faulkner, L., *Electrochemical Methods*, 2nd; John Wiley & Sons, New York: 2001.
- (31) Bard, A. J. *Journal of the American Chemical Society* **2010**, *132*, 7559–7567, DOI: [10.1021/ja101578m](https://doi.org/10.1021/ja101578m).
- (32) Xiong, H.; Guo, J.; Amemiya, S. *Analytical Chemistry* **2007**, *79*, 2735–2744, DOI: [10.1021/ac062089i](https://doi.org/10.1021/ac062089i).
- (33) Ghilane, J.; Hauquier, F.; Fabre, B.; Hapiot, P. *Analytical Chemistry* **2006**, *78*, 6019–6025, DOI: [10.1021/ac060058h](https://doi.org/10.1021/ac060058h).
- (34) Dresselhaus, M.; Jorio, A.; Saito, R. *Annual Reviews of Condensed Matter Physics* **2010**, *1*, 89–108, DOI: [10.1146/annurev-conmatphys-070909-103919](https://doi.org/10.1146/annurev-conmatphys-070909-103919).

- (35) Ferrari, A. C.; Basko, D. M. *Nature Nanotechnology* **2013**, *8*, 235–246, DOI: [10.1038/nnano.2013.46](https://doi.org/10.1038/nnano.2013.46).
- (36) Macpherson, J. V. *Physical Chemistry Chemical Physics* **2015**, *17*, 2935–2949, DOI: [10.1039/C4CP04022H](https://doi.org/10.1039/C4CP04022H).
- (37) Mortet, V.; Taylor, A.; Vlčková Živcová, Z.; Machon, D.; Frank, O.; Hubík, P.; Tremouilles, D.; Kavan, L. *Diamond and Related Materials* **2018**, *88*, 163–166, DOI: [10.1016/j.diamond.2018.07.013](https://doi.org/10.1016/j.diamond.2018.07.013).
- (38) Mortet, V.; Vlčková Živcová, Z.; Taylor, A.; Frank, O.; Hubík, P.; Trémouilles, D.; Jomard, F.; Barjon, J.; Kavan, L. *Carbon* **2017**, *115*, 279–284, DOI: [10.1016/j.carbon.2017.01.022](https://doi.org/10.1016/j.carbon.2017.01.022).

# Appendix A

## Supplementary Information for Chapter 3

### A.1 Synthesis and characterization of tetrakis(decyl)ammonium hexafluorophosphate $[\text{N}(\text{C}_{10}\text{H}_{21})_4](\text{PF}_6)$

Tetra(decyl)ammonium bromide (98% of purity) was purchased from Tokyo Chemical Company, ammonium hexafluorophosphate was purchased from Sigma-Aldrich and Ethanol (analytical grade) from Merck.  $\text{NH}_4\text{PF}_6$  (5 g, 30 mmol) was added to a hot ethanol solution containing 10 g, 15 mmol of  $[\text{N}(\text{C}_{10}\text{H}_{21})_4]\text{Br}$ . The mixture was stirred and concentrated by evaporation of the ethanol. A flaky crystalline precipitate was formed and was filtered under vacuum. The precipitate was washed 3 times with cold ethanol and subsequently washed 3 times with ethyl ether. The solid was redissolved in hot ethanol and recrystallized again repeating the procedure previously described. Yield 9.16 g, 90%.  $^{19}\text{F-NMR}$ : -72 ppm. X-ray fluorescence analysis on the precipitate did not reveal any impurities from Ag and Br species.

### A.2 Pt padding on Si wafer

The padding on Si wafer (**Figure A.1**) was performed with a sputter coater employing a Pt target. A 1 mm square glass coverslip was pressed on Si wafer, and sputtering performed using a Denton Desk V sputter coater. Setpoint pressure on the coater was  $6 \times 10^{-5}$  torr, sputtering current was set to 12 mA, sputter duration to 240 s. Sputtering took place at  $\approx 4 \times 10^{-4}$  torr. The resulting Pt film thickness from the sputtering process was  $\approx 15$

nm as measured by AFM in **Figure A.2**. All cycling was performed by isolating F-FLG samples over exposed Si/SiO<sub>2</sub> with a 3 mm diameter Teflon cell equipped with chemically resistant viton o-rings.

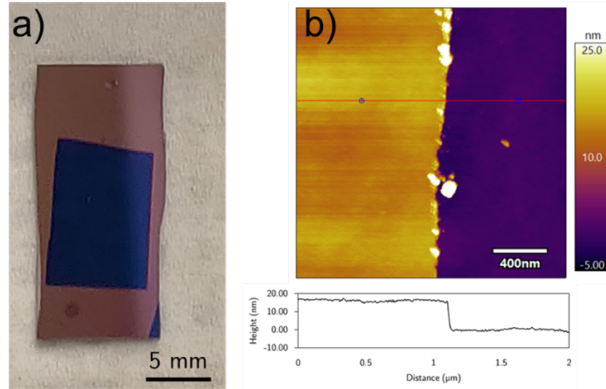


Figure A.1: Pt padded Si wafer and its thickness profile. a) Photograph of resulting wafer, b) AFM height profile of the Pt pad, illustrating  $\approx 15$  nm thickness of Pt film.

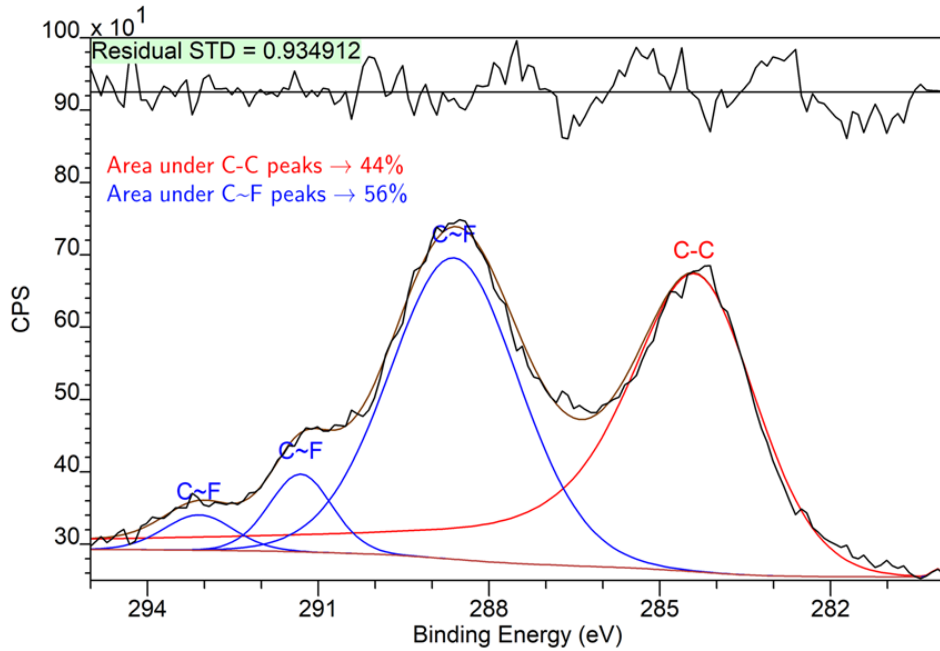


Figure A.2: XPS C 1s spectra of fluorinated SLG reveals  $\approx 56\%$  contribution of C-F species. Note CF<sub>x</sub> species can lead to XPS peaks in the range of 288-293 eV.[1] Y-axis units are presented in counts per second (CPS).

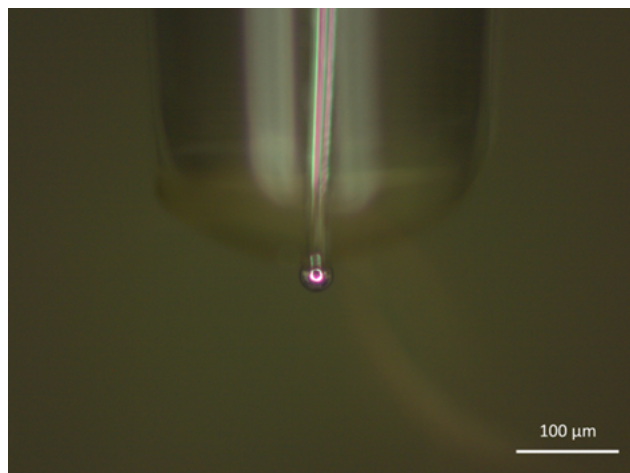


Figure A.3: Optical micrograph of HgSC UME used in ion-sensitive SECM measurements.

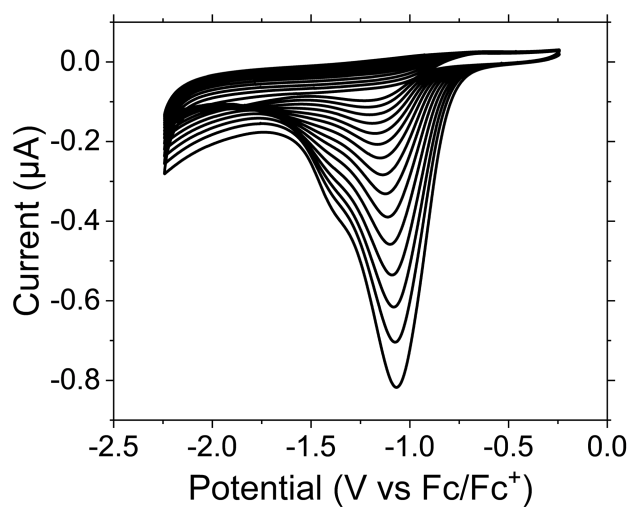


Figure A.4: CV cycles 2-16 of F-FLG in Na-electrolyte.

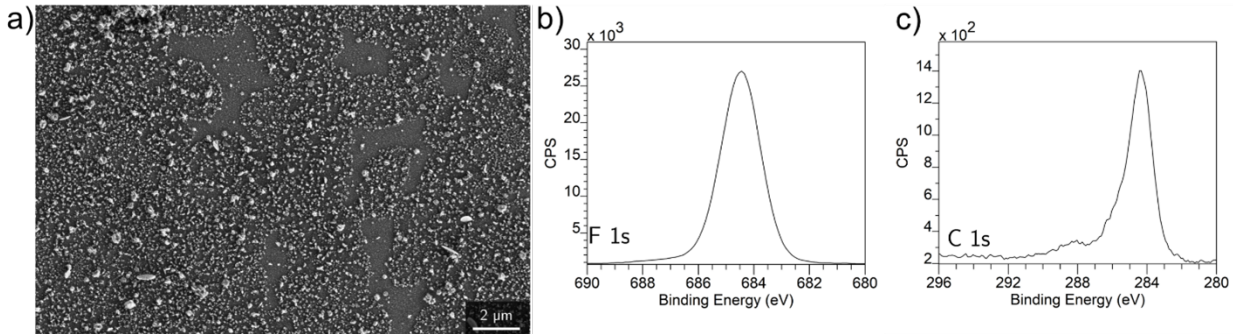


Figure A.5: SEM and XPS characterization of Na-SEI formed on F-FLG upon cycling in 0.1 M  $\text{NaPF}_6$ . a) SEM micrograph shows dense deposits throughout, with underlying graphene not visible. b) and c) XPS F 1s and C 1s characterization reveals presence of NaF species ( $\approx 684.5$  eV[2]) and little organic character other than C-C peak contribution from FLG. Note, peak at 288 eV could be attributed to C-F bonds (Figure A.2).

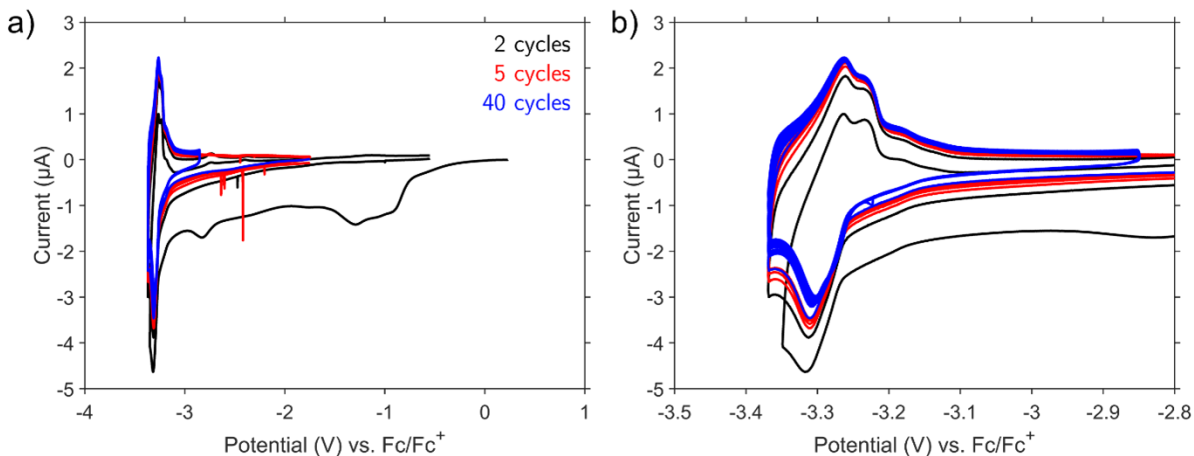


Figure A.6: CV cycling protocol form Li-based SEI on a FLG/F-FLG. a) Sample was cycled in black, red, blue traces consecutively, with Li-intercalation potential window illustrated in b). Electrolyte: 0.1 M  $\text{LiBF}_4$  in PC/EC; Scan rate 1 mV/s.

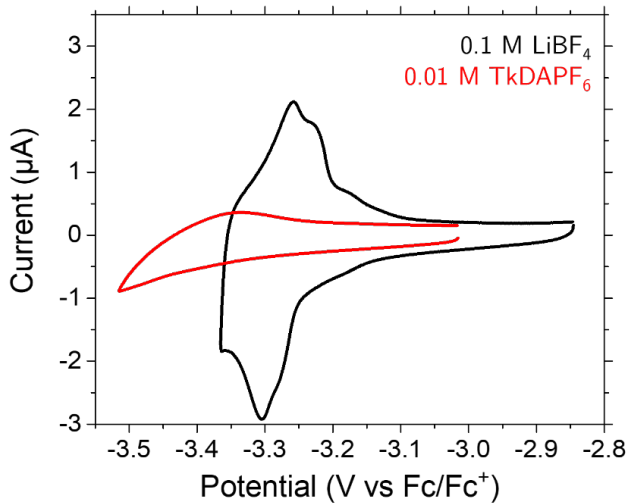


Figure A.7: CVs of F-FLG in 0.01 M  $\text{TkDAPF}_6$  after performing Li-SEI and rinsing out 0.1 M  $\text{LiBF}_4$ . No reversible peaks are observed, implying no intercalation active  $\text{Li}^+$  present in solution. Scan rate 1 mV/s for both measurements.

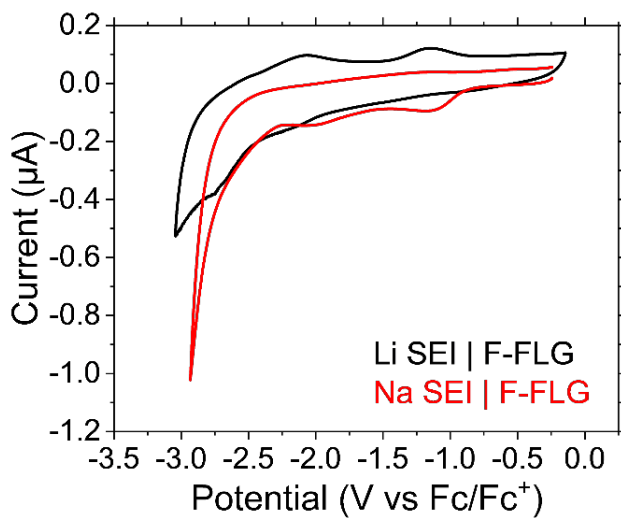


Figure A.8: Cycling F-FLG in Na-electrolyte with preformed Li-based SEI and native Na-based SEI. Reversible anodic peaks are not observed when cycling F-FLG in Na-electrolyte, in the absence of the preformed Li-based SEI.

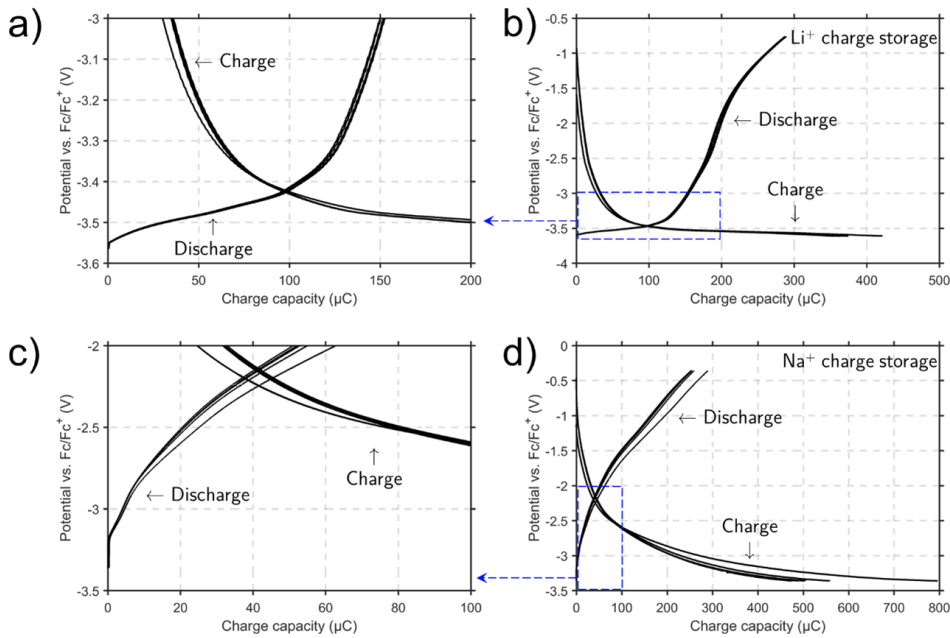


Figure A.9: Galvanostatic cycling of F-FLG samples. a) and b) illustrate 5 cycles in 0.1 M  $\text{LiBF}_4$  across the reduced and full potential window respectively. Discharge capacity is observed to be  $\approx 150 \mu\text{C}$  from the reduced potential window. (Dis)charge was performed at a constant current of 0.44  $\mu\text{A}$ . c) and d) same as a) and b) apart from the fact that cycling was done in F-FLG with preformed Li-SEI in 0.1 M  $\text{NaPF}_6$  (28 cycles performed). Discharge capacity was observed to be  $\approx 50 \mu\text{C}$ , and (dis)charge was performed at a constant current of 0.2  $\mu\text{A}$ . Note galvanostatic measurements performed after preforming SEI and cycling in Na-electrolyte with CV.

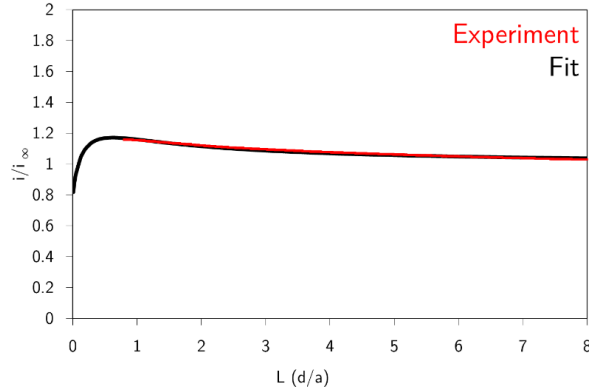


Figure A.10: Approach curve revealing partial positive feedback with HgSC UME, indicating distance from substrate  $L = 0.5$ . Given tip radius of 12.5  $\mu\text{m}$ , distance between tip and substrate is  $\approx 6 \mu\text{m}$ .

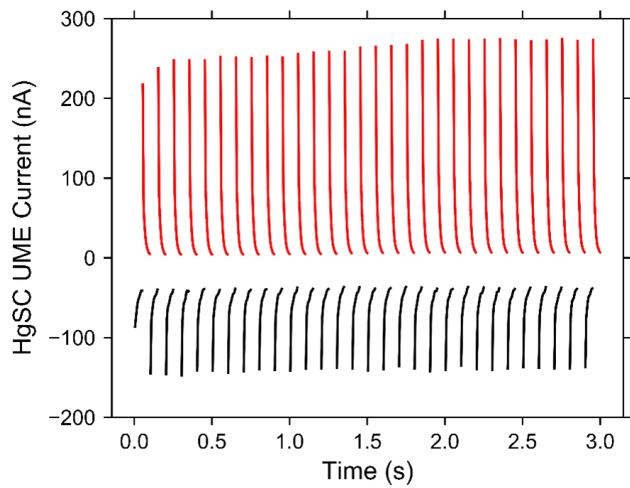


Figure A.11: Thirty amalgamation and stripping pulses recorded at the HgSC tip at a fixed substrate potential during ion-sensitive SECM measurements.

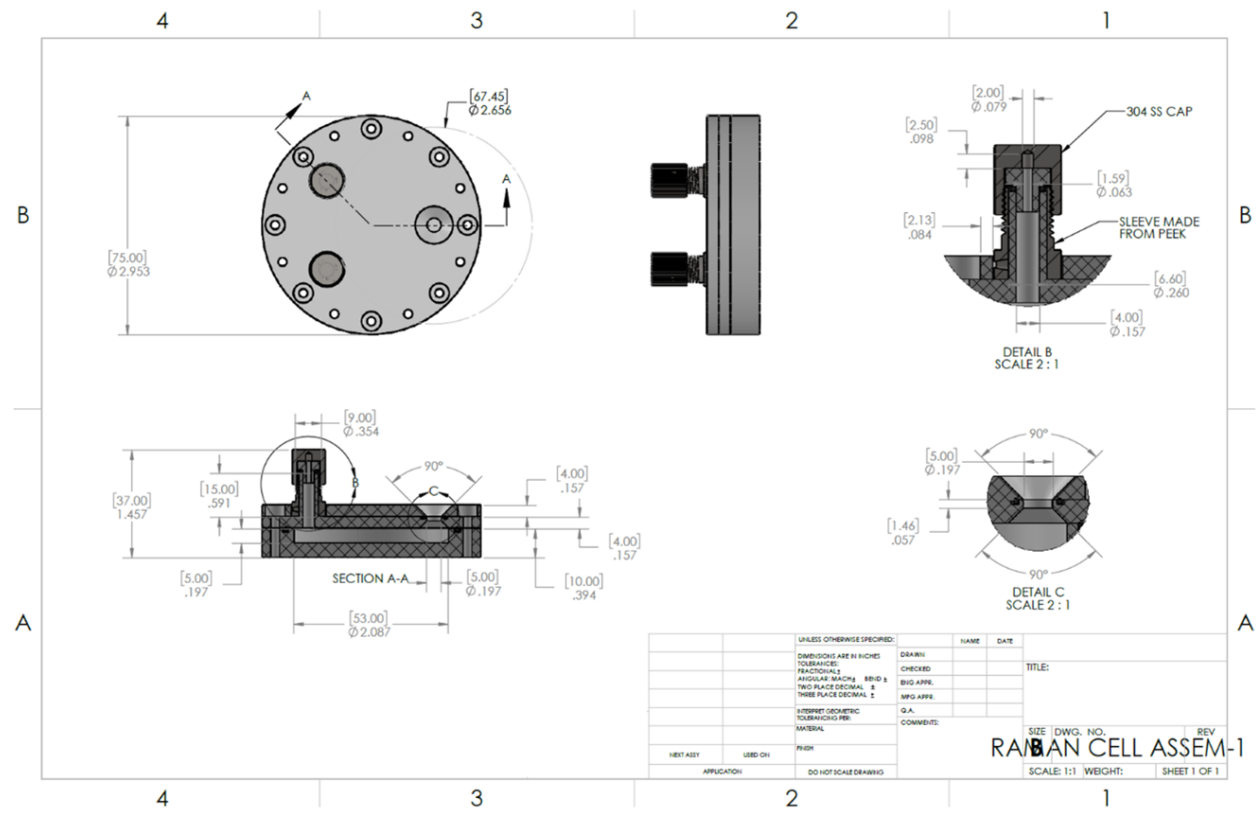


Figure A.12: CAD schematics of the in-house cell used for in situ Raman measurements.

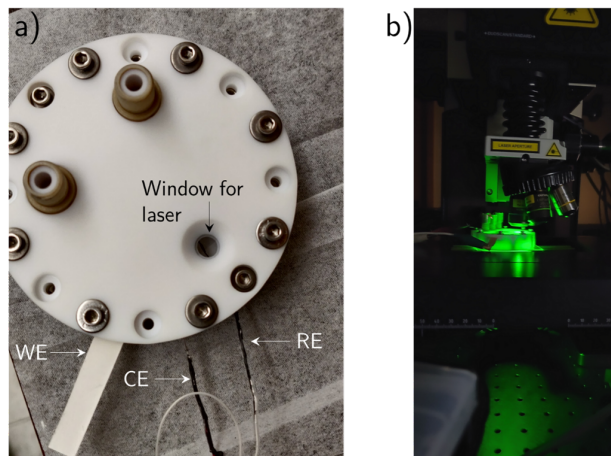


Figure A.13: Pictures of the in situ Raman cell illustrating a) electrode and viewing port layout and b) an in situ measurement.

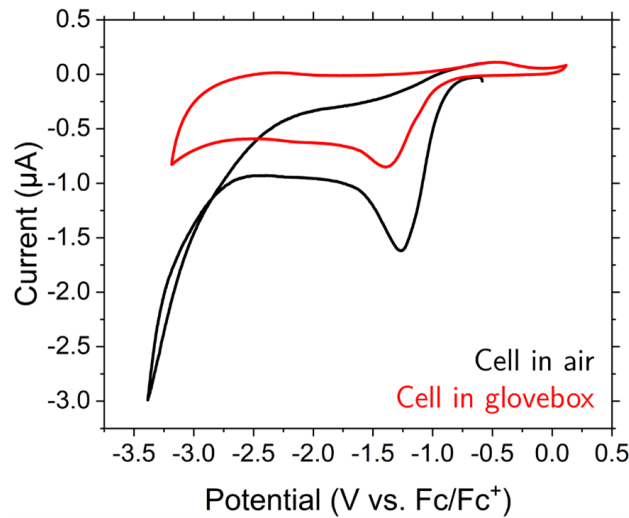


Figure A.14: CV from cycling F-FLG in Na electrolyte, within the sealed in situ Raman cell in air (black) and inside a glovebox (red). Scan rate was 2.5 mV/s. Li-SEI was formed on the F-FLG prior to cycling in Na-electrolyte. Peak at -1.2 V in the cathodic sweep is likely some modification to the SEI as evidenced from the lack of a peak in the anodic sweep. Peak potential of -1.2 V also corresponds to the Na-SEI peak seen in [Figure 3.3b](#).

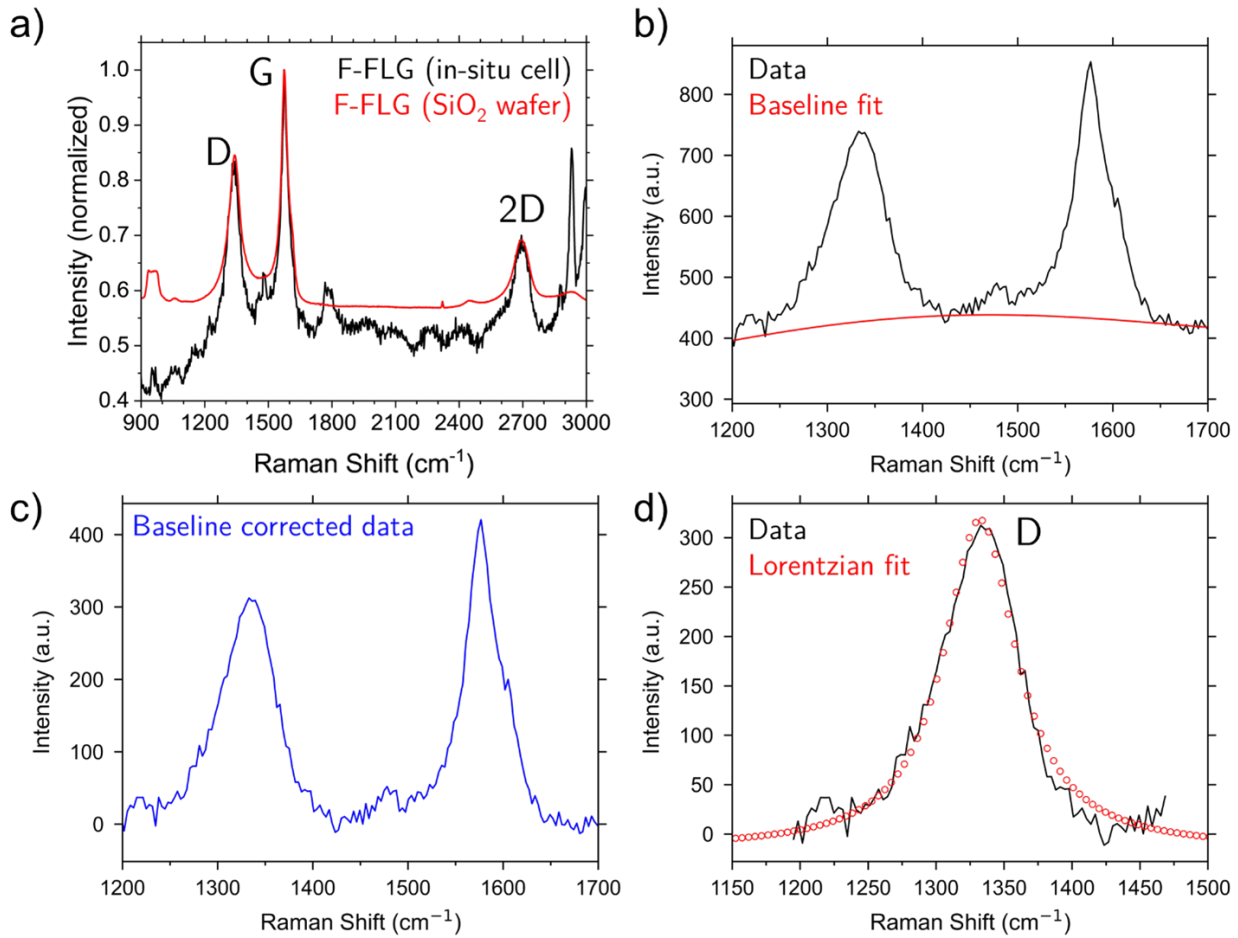


Figure A.15: Python processing of Raman spectra using `rampy.py`.<sup>[3]</sup> a) Comparison of spectra from F-FLG in contact with Na-electrolyte solution against F-FLG in air on  $\text{SiO}_2$  wafer. Note broad response from solution in  $2500 - 2630 \text{ cm}^{-1}$  region owing to which 2D peak fitting was not performed. b) Spline baseline is fit to the Raman spectra, and c) resulting subtracted spectra. d) Example of peak fitting the D peak in Raman spectra using `lmfit.py`. A Lorentzian peak function was utilized to extract peak position of the D and G peaks.

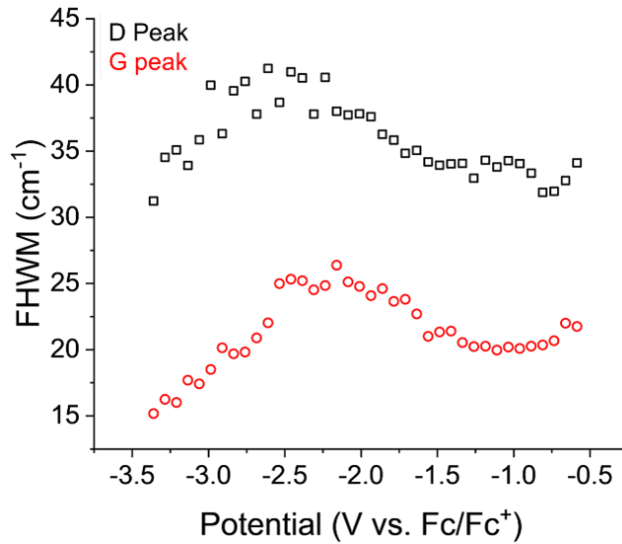


Figure A.16: Variation in FHMW for the D and G peaks in the Raman data corresponding to **Figure 3.5a** in the main script.

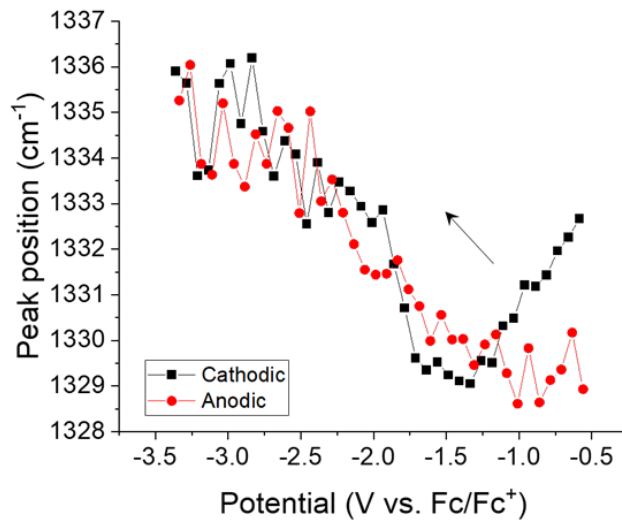


Figure A.17: Changes in the D peak position during in situ Raman experiment in **Figure 3.5a**.

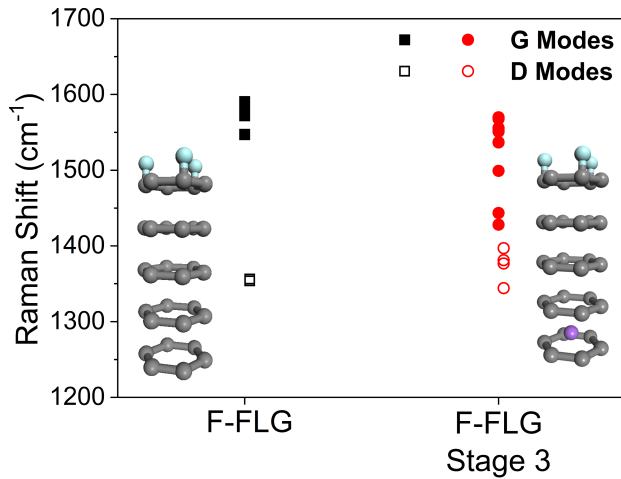


Figure A.18: Predicted G and D band positions for another Stage 3 structure compared to non-intercalated F-FLG.

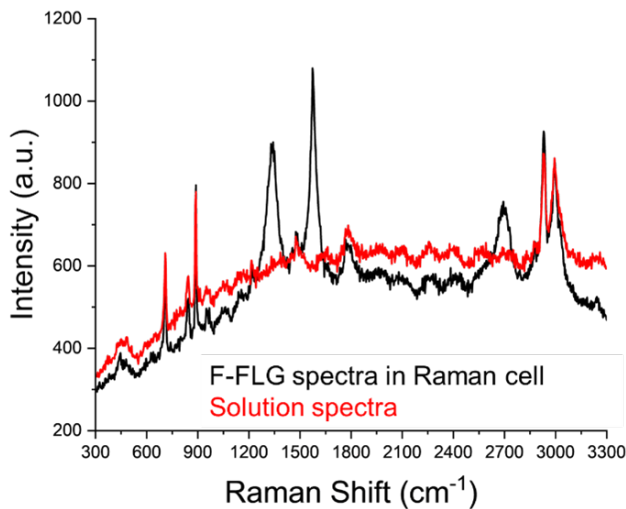


Figure A.19: Comparison of Raman spectra from F-FLG in raman cell to that of solution reveals no peaks that could be assigned to SEI species.

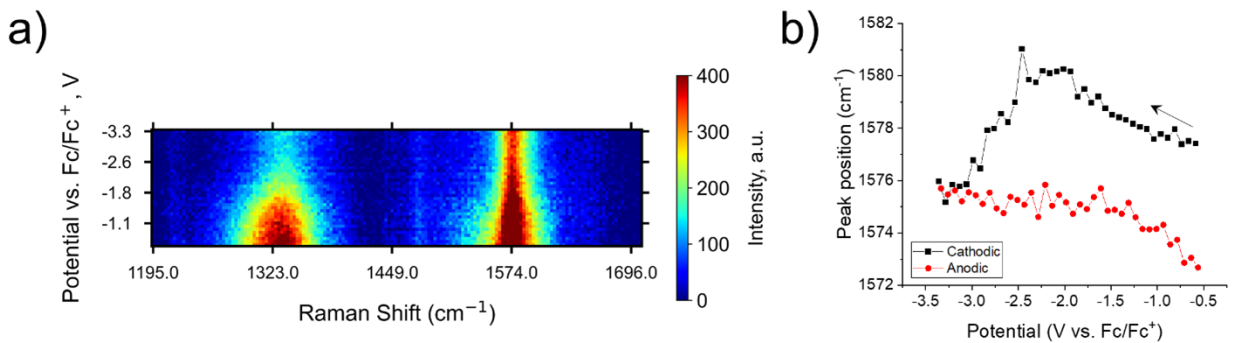


Figure A.20: Additional results from in situ Raman spectroscopy. a) Heat map of the Raman spectra in the anodic sweep. b) Variation of G peak position during the in situ measurement.

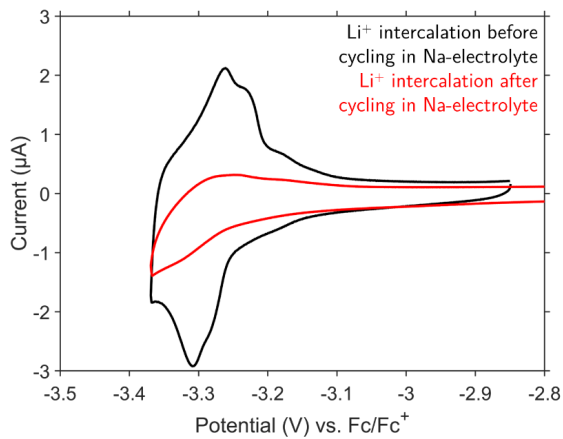


Figure A.21:  $\text{Li}^+$  intercalation signatures characterized via cyclic voltammetry in a F-FLG sample with preformed Li-SEI, before and after cycling in Na-electrolyte. Drastically diminished  $\text{Li}^+$  intercalation capacity is observed after cycling in Na-electrolyte, indicating structural changes in F-FLG.

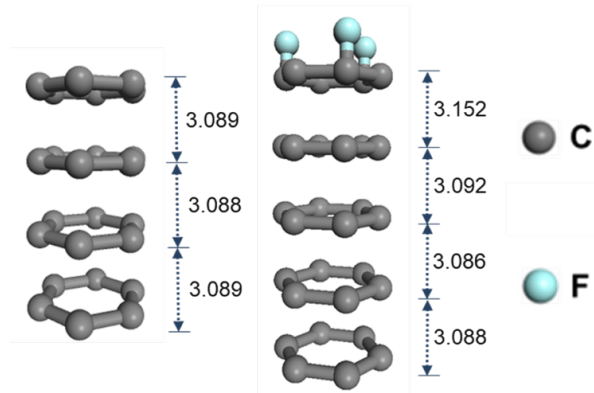


Figure A.22: Computationally calculated inter-layer distances in FLG and F-FLG structures.

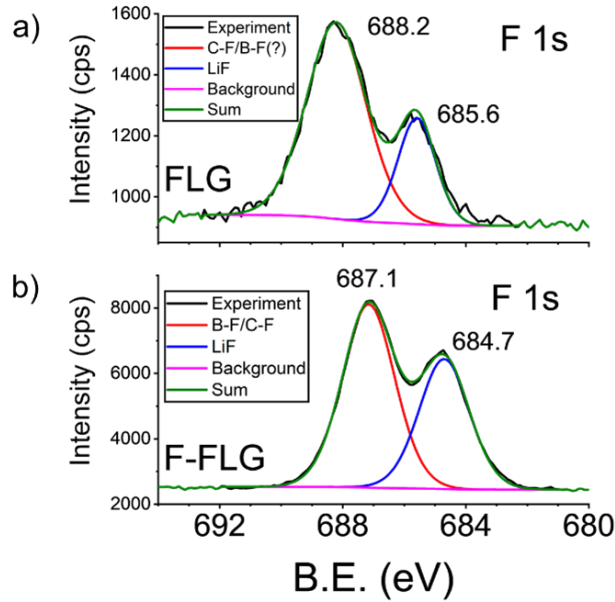


Figure A.23: F 1s XPS spectra comparing fluorinated species in cycled a) FLG and b) F-FLG samples. FLG anode displays contributions from C-F and LiF species, although there is evidence of a 1 eV calibration error in binding energies when compared to the F-FLG anode. Given that C-F species are detected in low amounts in C 1s spectra (Figure A.25), it is likely that the binding energies were unable to be calibrated with the C-C peak as reference. Nevertheless, relative ratios between two peaks are similar across both F-FLG and FLG samples, with intensity being the major difference in the two samples.

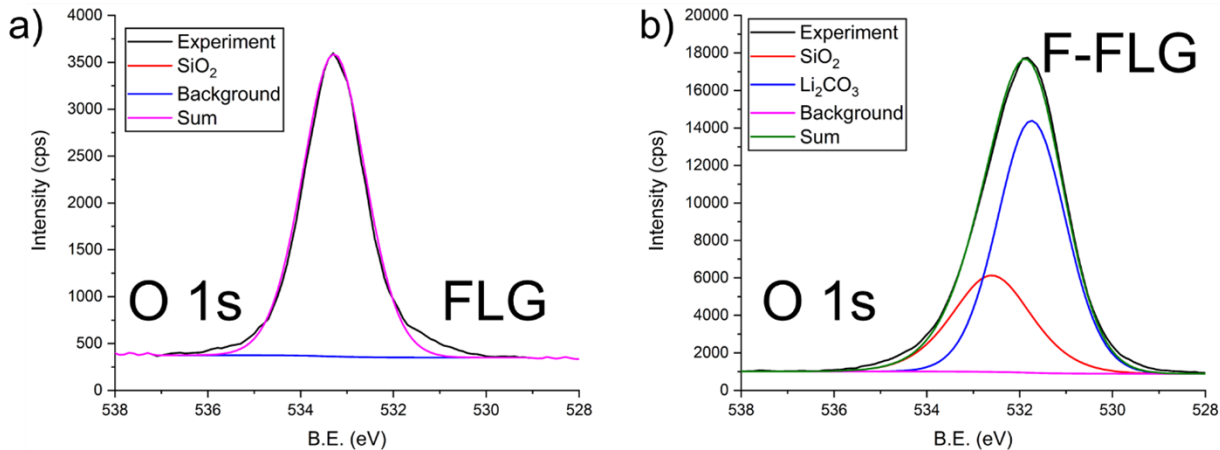


Figure A.24: O 1s XPS spectra of a) FLG and b) F-FLG electrodes with preformed Li-SEI after cycling in Na electrolyte.  $\text{Li}_2\text{CO}_3$  is observed at binding energies around 531.8 eV.[4]

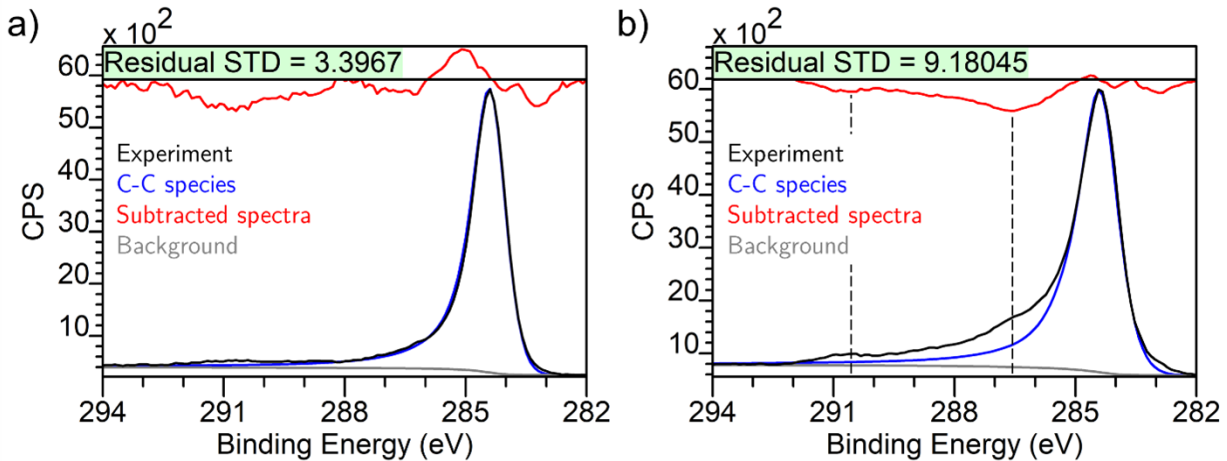


Figure A.25: XPS C 1s spectra from a) FLG and b) F-FLG sample with preformed Li-SEI after cycling in Na-electrolyte. Both spectra were fitted with an asymmetric peak (blue trace) for highlighting C-C carbon. Therefore, subtracted spectra (red) now reveals functional groups on carbon. Trace organic functional groups and C-F groups are evident in a) whereas the F-FLG SEI in b) reveals carbonates and/or fluorocarbons (290.5 eV) and -OH organic groups such as esters and alcohols (286.5 eV).<sup>[5]</sup>

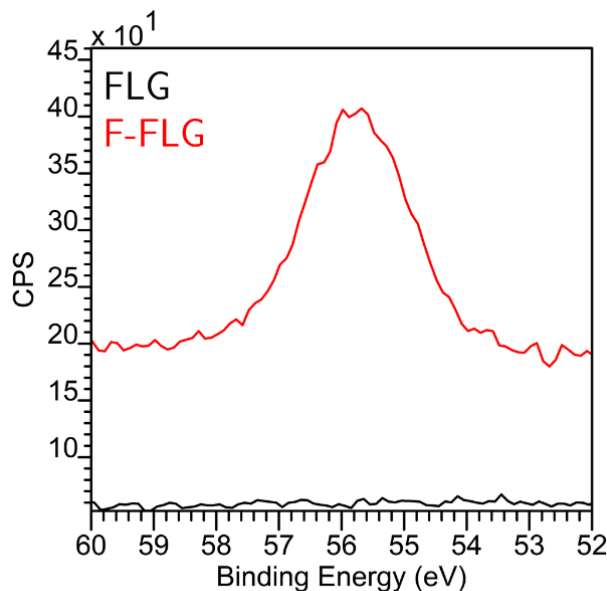


Figure A.26: High resolution XPS spectra of Li 1s for the FLG and F-FLG samples with preformed Li-SEI and cycled in NaPF6. Peak centered at  $\approx 55.6$  eV for Li 1s corresponds to Li<sub>2</sub>CO<sub>3</sub>.<sup>[6]</sup>

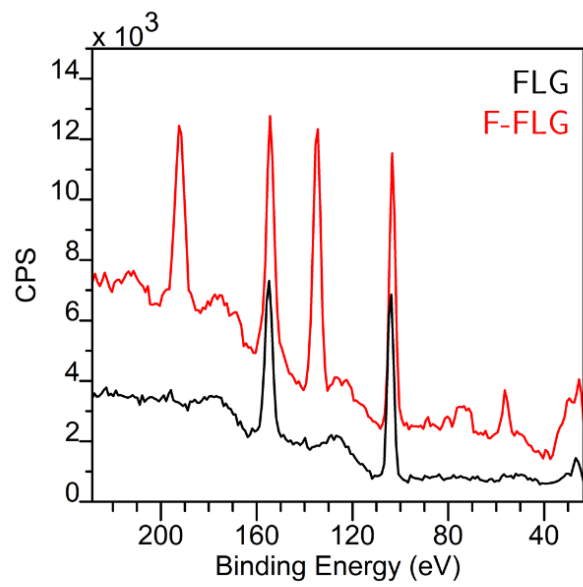


Figure A.27: Si peaks observable in both FLG and F-FLG interphases (Si 2s at  $\approx$ 153 eV and Si 2p at  $\approx$ 100 eV).

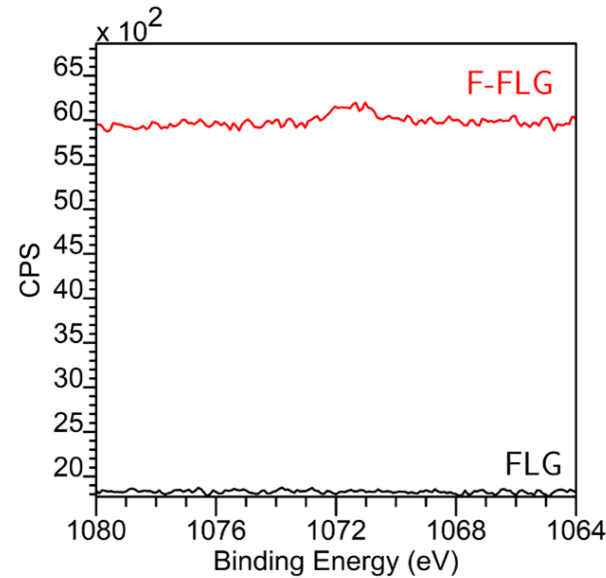


Figure A.28: Na 1s XPS spectra arising from FLG and F-FLG interphases revealing no major incorporation of Na species in the interphases, possibly an artifact from rinsing.

## References

- (1) Wang, B.; Wang, J.; Zhu, J. *ACS Nano* **2014**, *8*, 1862–1870, DOI: [10.1021/nn406333f](https://doi.org/10.1021/nn406333f).
- (2) Fondard, J.; Irisarri, E.; Courrèges, C.; Palacin, M. R.; Ponrouch, A.; Dedryvère, R. *Journal of The Electrochemical Society* **2020**, *167*, 070526, DOI: [10.1149/1945-7111/ab75fd](https://doi.org/10.1149/1945-7111/ab75fd).
- (3) Le Losq, C. *Zenodo* **2018**, DOI: [10.5281/zenodo.1168730](https://doi.org/10.5281/zenodo.1168730).
- (4) Shchukarev, A.; Korolkov, D. *Central European Journal of Chemistry* **2004**, *2*, 347–362, DOI: [10.2478/BF02475578](https://doi.org/10.2478/BF02475578).
- (5) Blyth, R.; Buqa, H.; Netzer, F.; Ramsey, M.; Besenhard, J.; Golob, P.; Winter, M. *Applied Surface Science* **2000**, *167*, 99–106, DOI: [10.1016/S0169-4332\(00\)00525-0](https://doi.org/10.1016/S0169-4332(00)00525-0).
- (6) Jiang, F.; Ma, L.; Sun, J.; Guo, L.; Peng, Z.; Cui, Z.; Li, Y.; Guo, X.; Zhang, T. *ACS Applied Materials & Interfaces* **2021**, *13*, 14321–14326, DOI: [10.1021/acsami.1c01770](https://doi.org/10.1021/acsami.1c01770).

## Appendix B

### Supplementary Information for Chapter 4

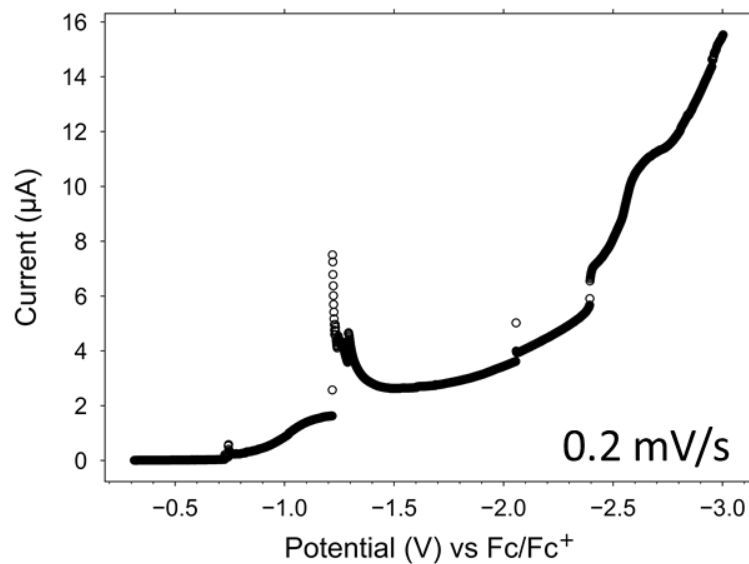


Figure B.1: LSV of MLG in 0.1 M  $\text{KPF}_6$  at  $0.2 \text{ mV/s}$ .

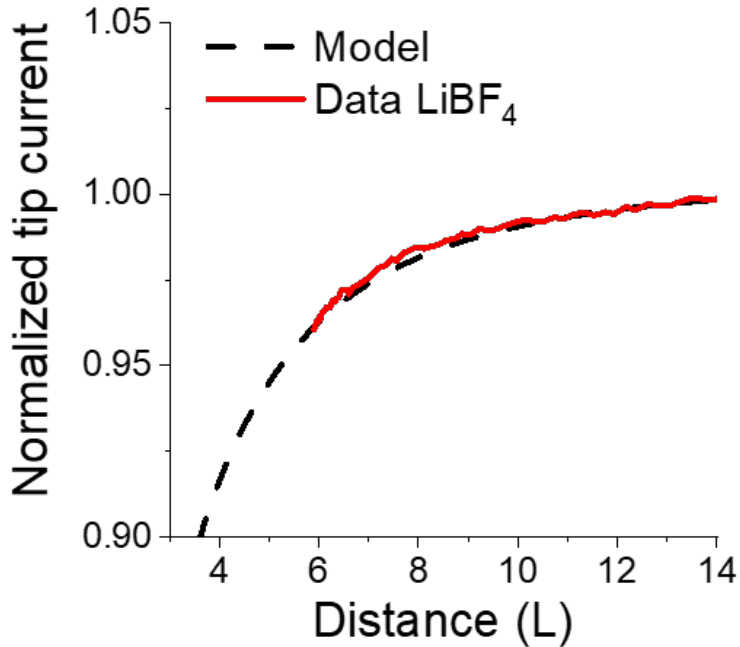


Figure B.2: Approach and fitting for the 300 nm SECM probe to a bare Si/SiO<sub>2</sub> surface on the same chip on which MLG was transferred; measurement performed using 5 mM ferrocene mediator before Li<sup>+</sup>-SEI imaging.

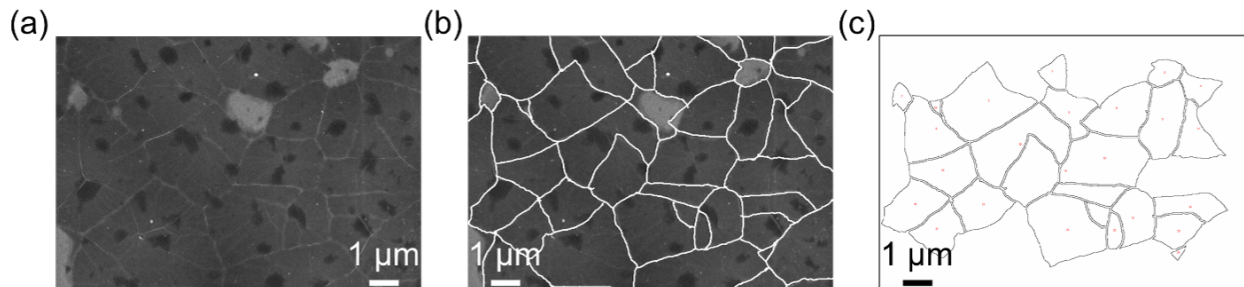


Figure B.3: Grain size analysis. (a) SEM micrograph of MLG showing faint outlines of grains, (b) Marking grain boundaries manually, (c) ImageJ analysis revealing grain outlines used for analysis (grains on the edge of the micrograph were not counted).

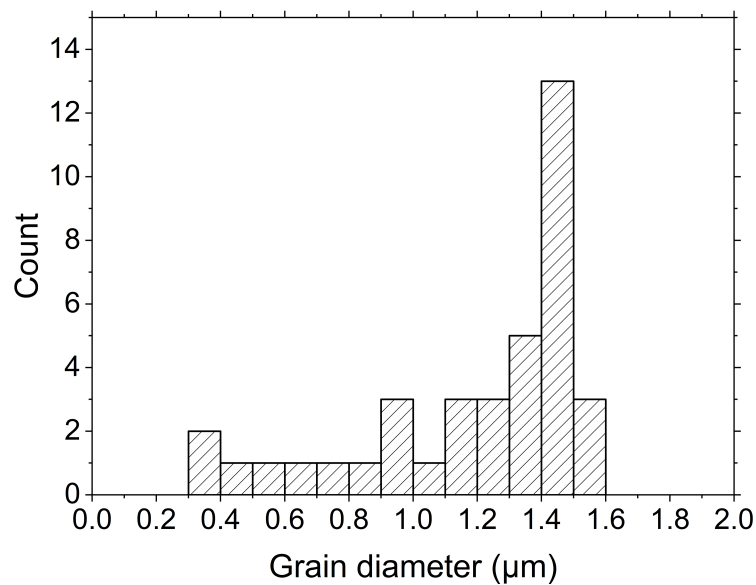


Figure B.4: Histogram of feature sizes observed on MLG.

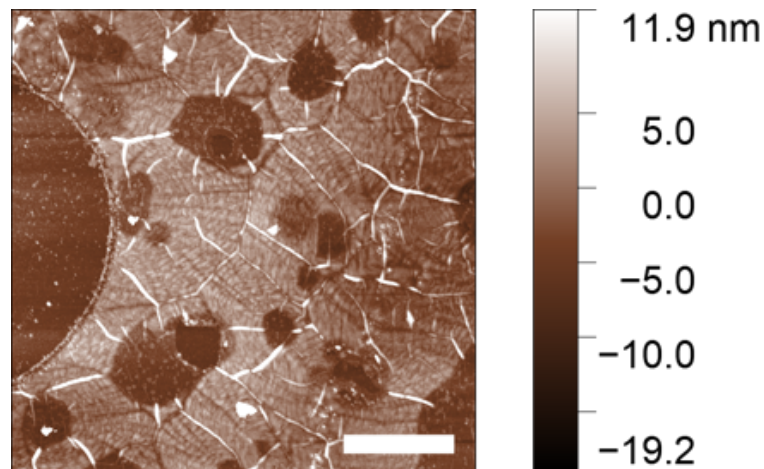


Figure B.5: AFM image of unused MLG sample. Scalebar is 2  $\mu\text{m}$ .

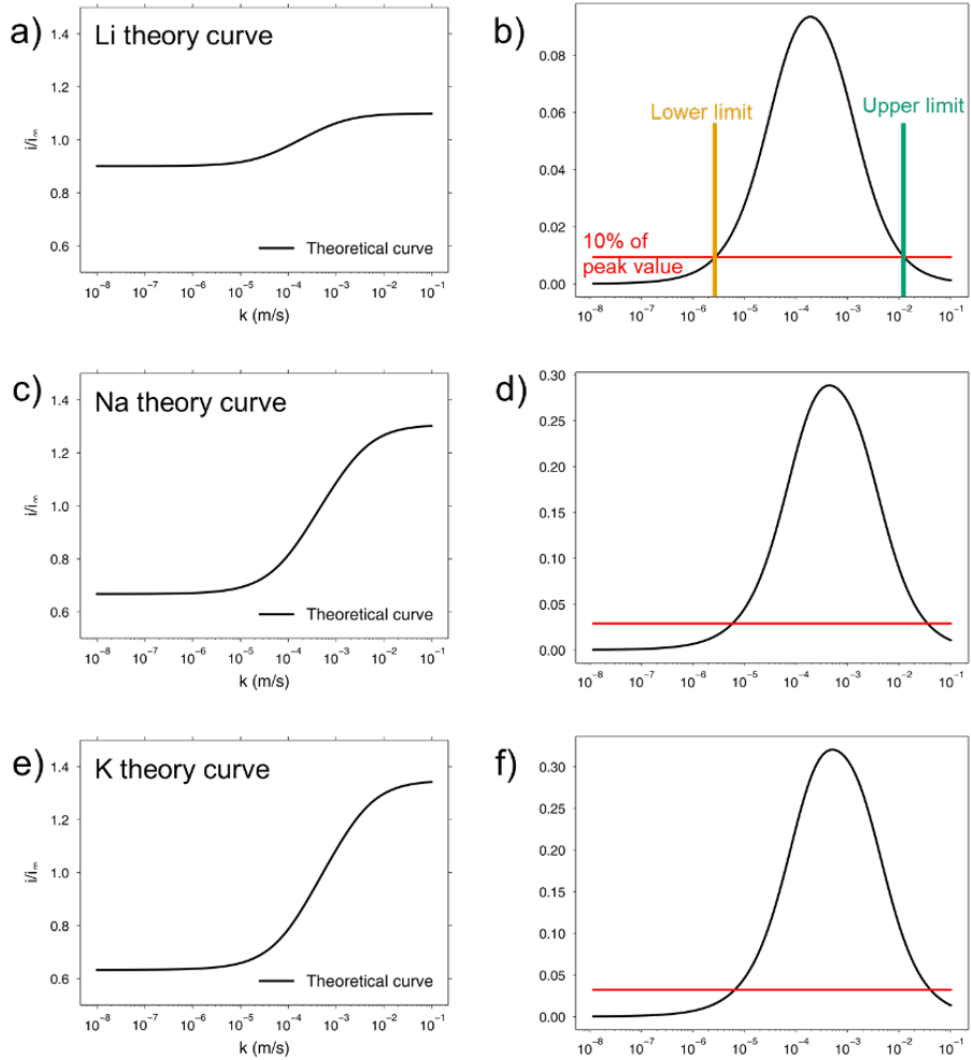


Figure B.6: Theoretical curves for extracting kinetics of electron transfer using the feedback mode under the experimental conditions found in each electrolyte. Curves for (a) Li, (c) Na, and (e) K and corresponding derivate curves for (b) Li, (d) Na and (f) K. Practical limits for  $k_f$  values are obtained from the derivative plots, as shown in (b).

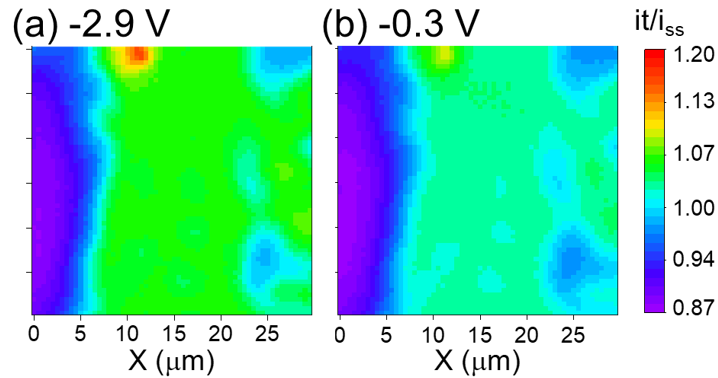


Figure B.7: SECM imaging during further formation of the  $\text{Li}^+$ -SEI. (a) SECM image at  $-2.9 \text{ V}$  vs.  $\text{Fc}^+/\text{Fc}$  during the first sweep to low potentials. (b) SECM image at the end of the first cycle at  $-0.3 \text{ V}$ .

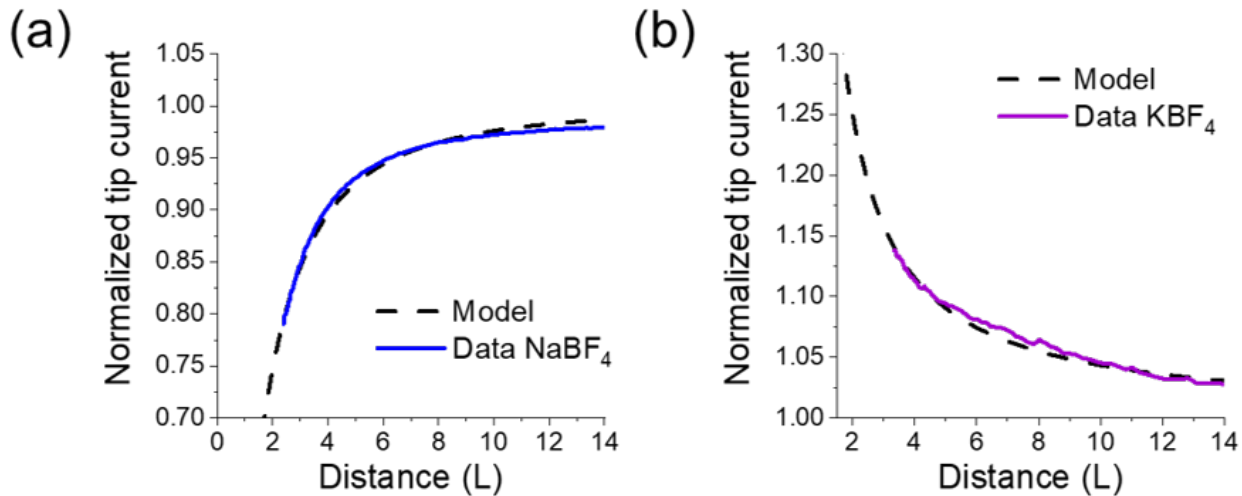


Figure B.8: Approach curves and fittings before  $\text{Na}^+$  and  $\text{K}^+$ -SEI imaging experiments showing feedback at the  $(0,0)$  coordinate in **Figure 4.3a,b** in the manuscript. (a) Approach and fitting for the 300 nm SECM probe before  $\text{Na}^+$ -SEI imaging. (b) Approach and fitting for the 300 nm SECM probe before  $\text{K}^+$ -SEI imaging. Notice that consistent with the images in **Figure 4.3**, the  $(0,0)$  pixel displays negative feedback for  $\text{Na}^+$ , in contrast to the positive feedback observed for  $\text{K}^+$ .

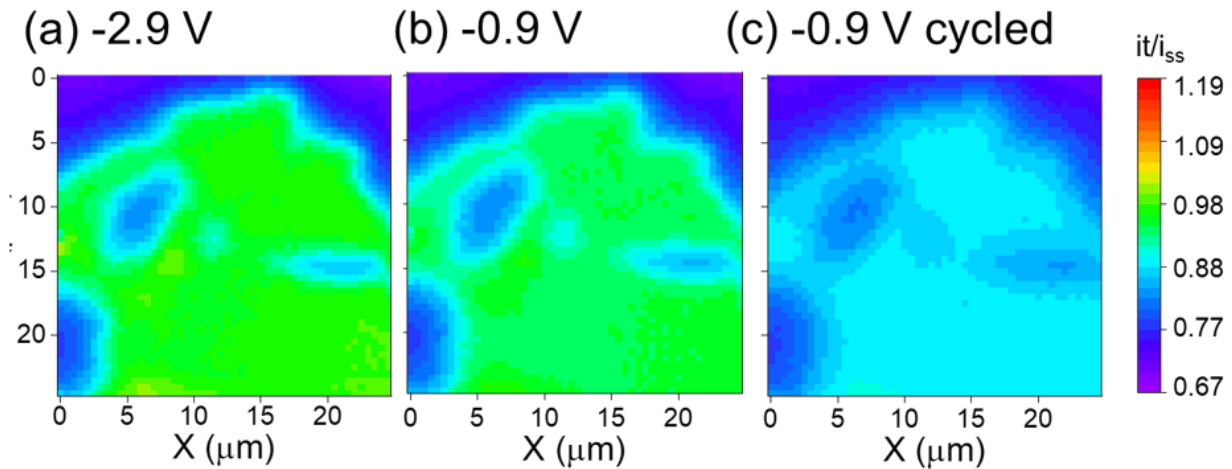


Figure B.9: SECM imaging during further formation of the  $\text{Na}^+$ -SEI. (a) SECM image at  $-2.9 \text{ V}$  vs.  $\text{Fc}^+/\text{Fc}$  during the first sweep to low potentials. SECM images at (b) the end of the first cycle at  $-0.9 \text{ V}$  and (c) after more cycling.

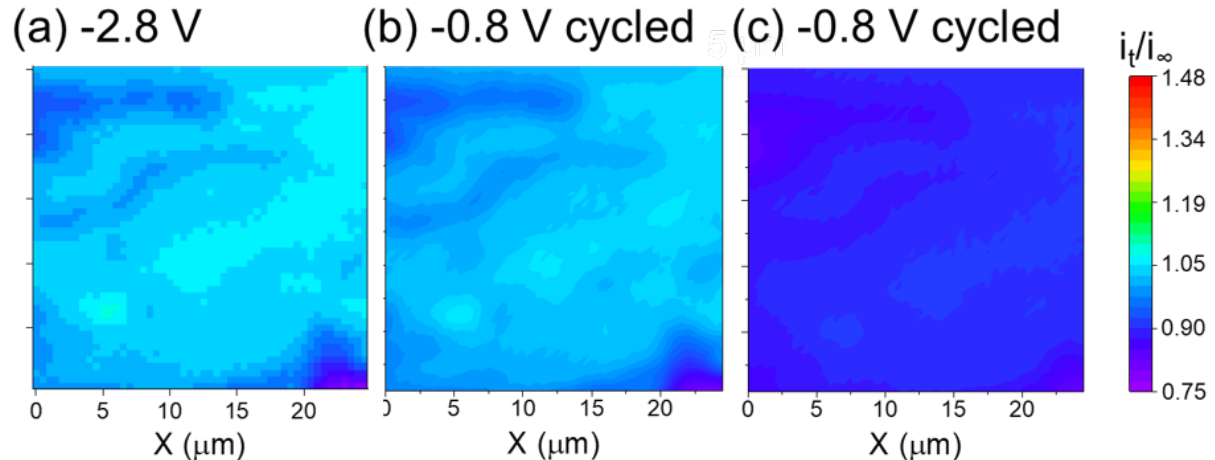


Figure B.10: SECM imaging during further formation of the  $\text{K}^+$ -SEI. (a) SECM image at  $-2.9 \text{ V}$  vs.  $\text{Fc}^+/\text{Fc}$  during the first sweep to low potentials. SECM images at (b) the end of the first cycle at  $-0.8 \text{ V}$  and (c) after more cycling.

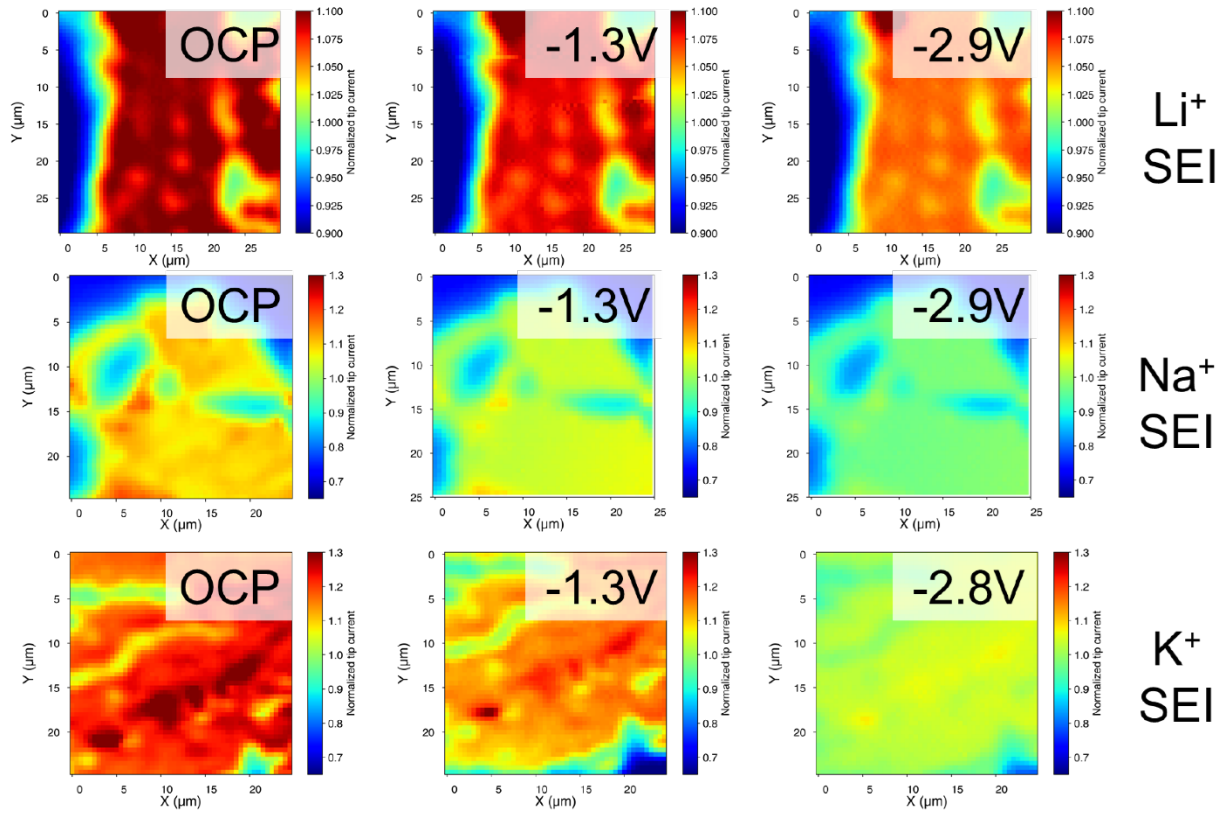


Figure B.11: SECM normalized feedback response of ferrocene from different SEIs, with the substrates held at different potentials, indicated in the figure.

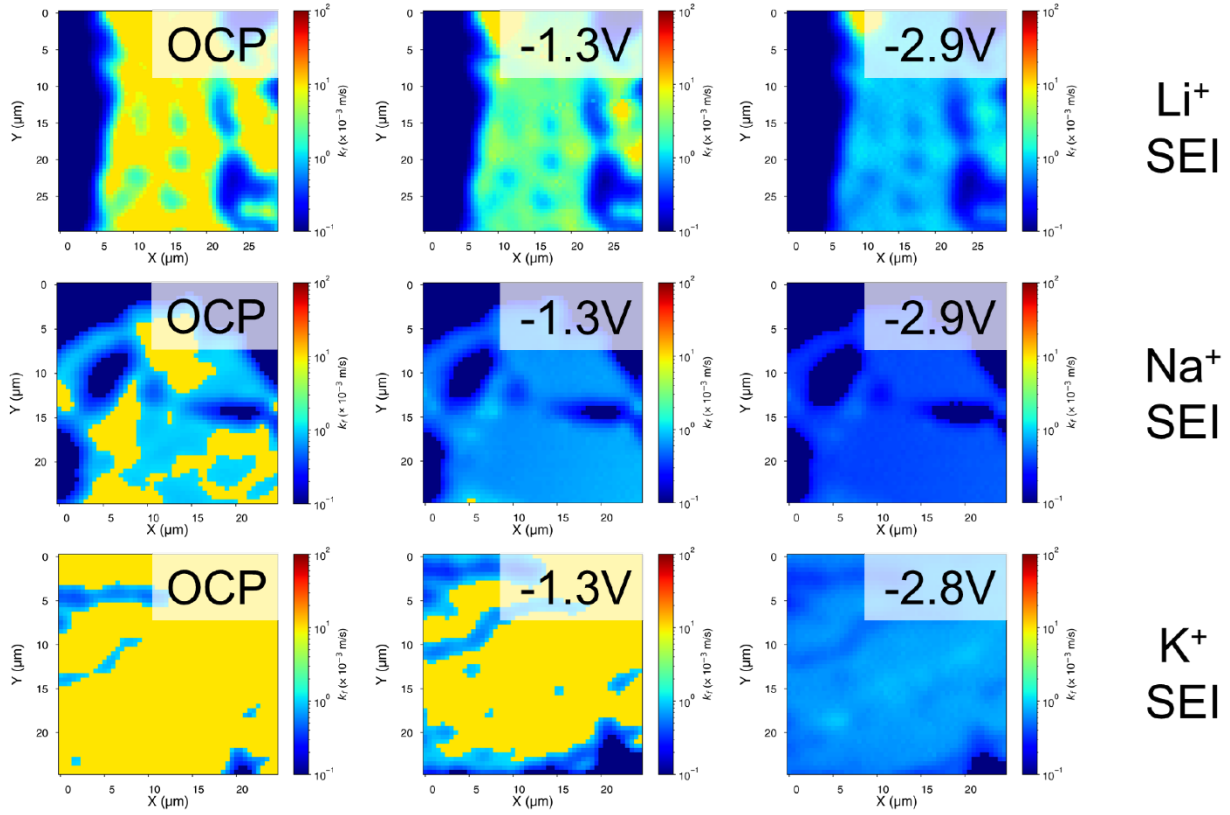


Figure B.12: Maps of electron transfer kinetics between the MLG substrates and ferrocene, estimated using normalized feedback currents from the data in [Figure B.11](#).

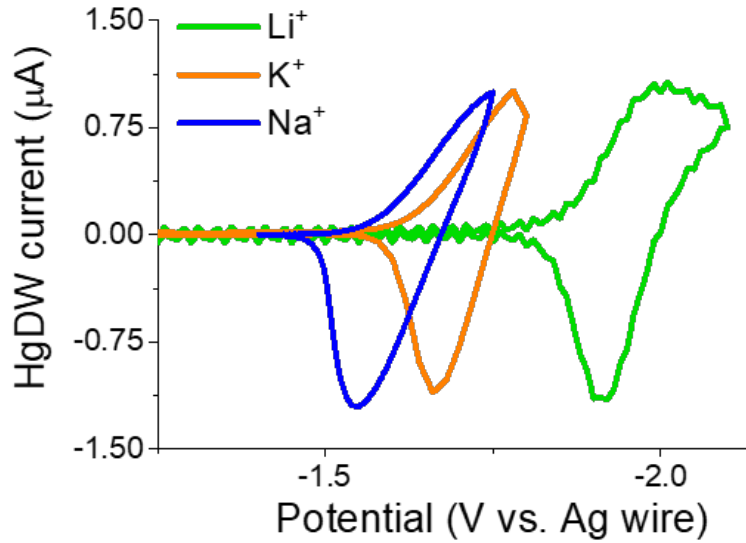


Figure B.13: Cyclic voltammetry using a HgDW probe in either  $\text{LiBF}_4$ ,  $\text{KBF}_4$ , or  $\text{NaBF}_4$  electrolytes. Here, the reference potentials are versus a quasi-reference and not adjusted.

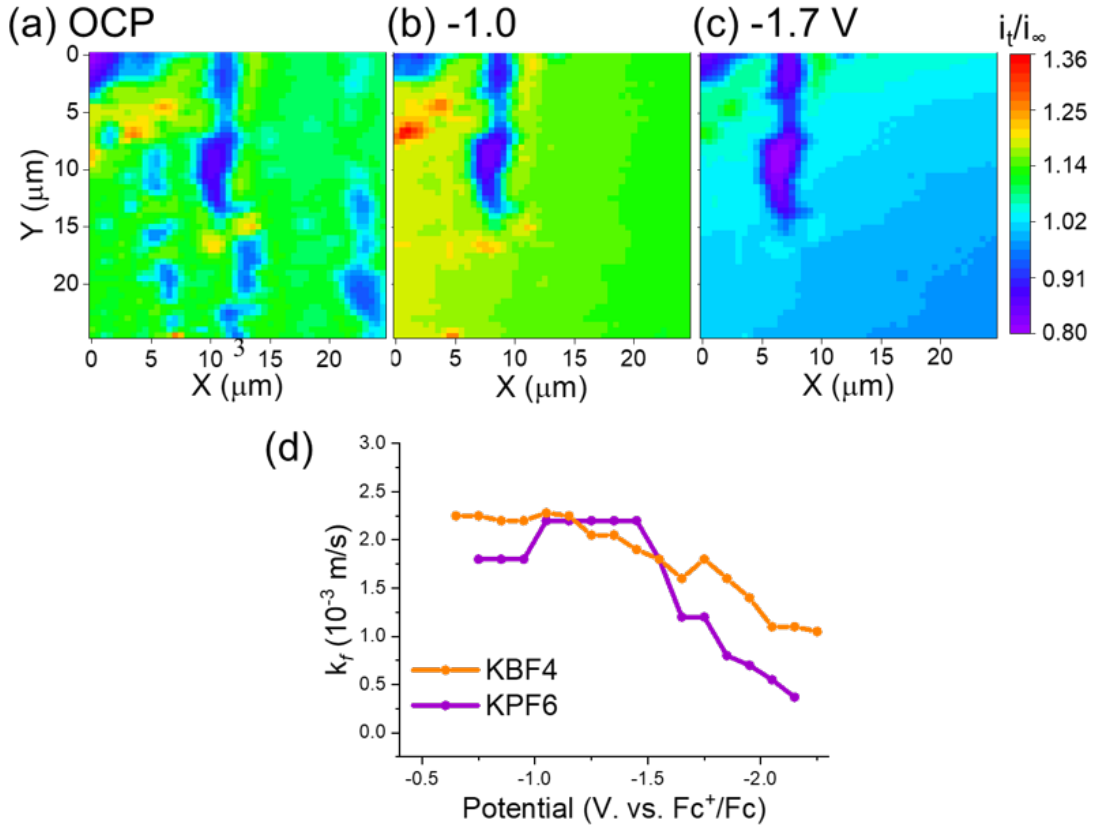


Figure B.14: SECM imaging during SEI formation in 0.1 M KPF<sub>6</sub>. SECM feedback images at (a) OCP, (b) -1.0 V and (c) -1.7 V vs. Fc<sup>+</sup>/Fc during the first sweep to low potentials. SECM images. (d) Comparison of extracted kinetics for KBF<sub>4</sub> and KPF<sub>6</sub> images.

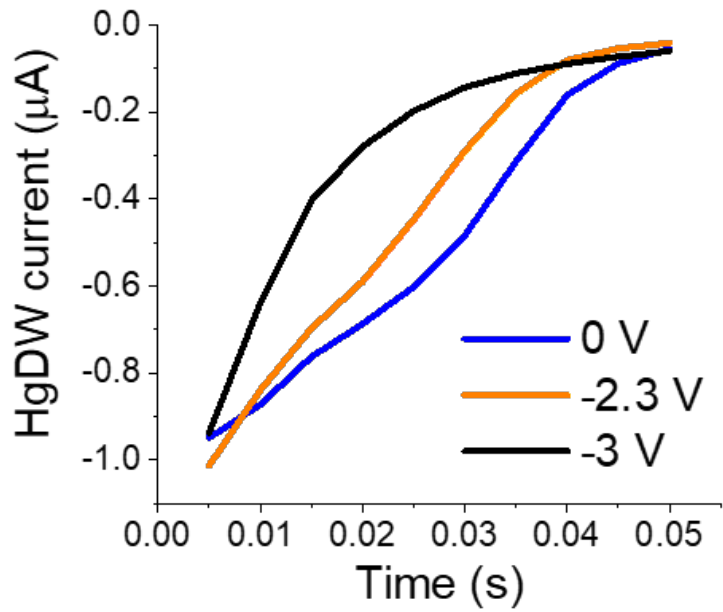


Figure B.15: Stripping pulses at a HgDW probe in 0.1 M  $\text{NaBF}_4$  near a reactive MLG substrate.

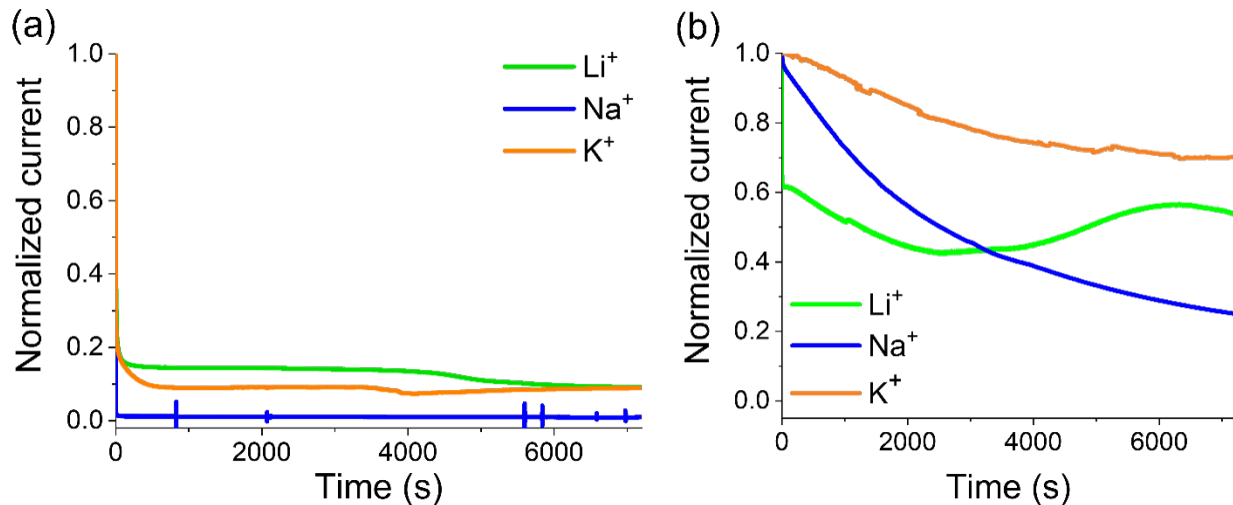


Figure B.16: Formation of the SEI on MLG at constant potential of (a) -1.4 V or (b) -3.0 V vs.  $\text{Fe}^+/\text{Fc}$ .

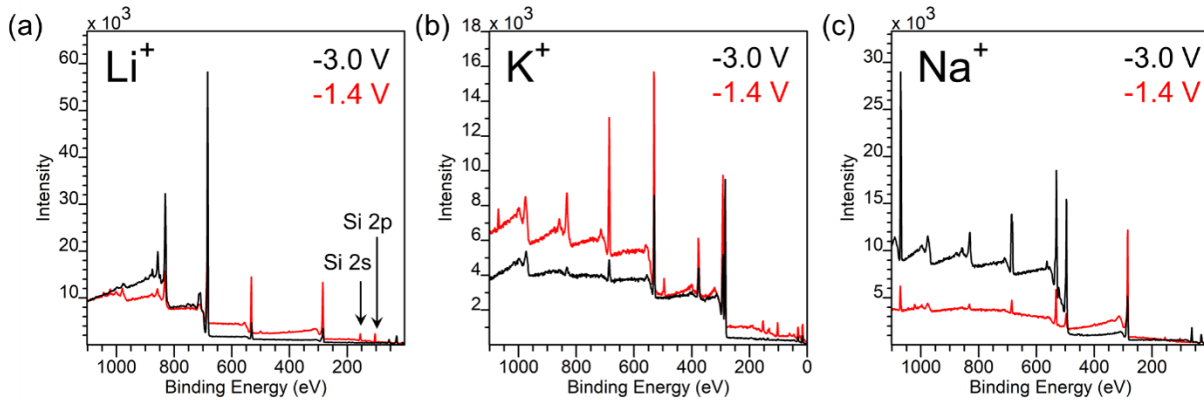


Figure B.17: Survey spectra obtained for (a)  $\text{Li}^+$ -SEI, (b)  $\text{K}^+$ -SEI and (c)  $\text{Na}^+$ -SEI. Note survey spectra reveals Si 2s and 2p peaks from SEI at -1.4 V for all three salts (from underlying  $\text{SiO}_2$  wafer substrate), which means the O 1s has contributions from  $\text{SiO}_2$  for the SEIs formed at -1.4 V.

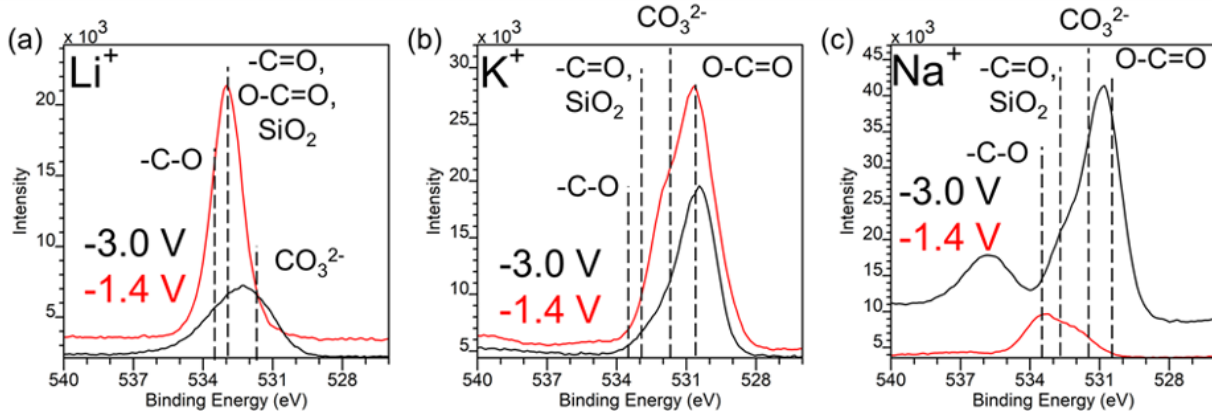


Figure B.18: High resolution spectra for O 1s for (a)  $\text{Li}^+$ -SEI, (b)  $\text{K}^+$ -SEI and (c)  $\text{Na}^+$ -SEI. Control measurements reveal O 1s contributions from underlying wafer to be at 532.9 eV.[1] Oxygen from metal carbonates arise  $\approx$  531.0-531.8 eV.[2-4] Various oxygen functional groups in hydrocarbons arise within the 532.5-533.5 eV range, as indicated in the figures.[5, 6] The broad peak at 536 eV in (c) arises from Auger peaks of sodium species.[3]

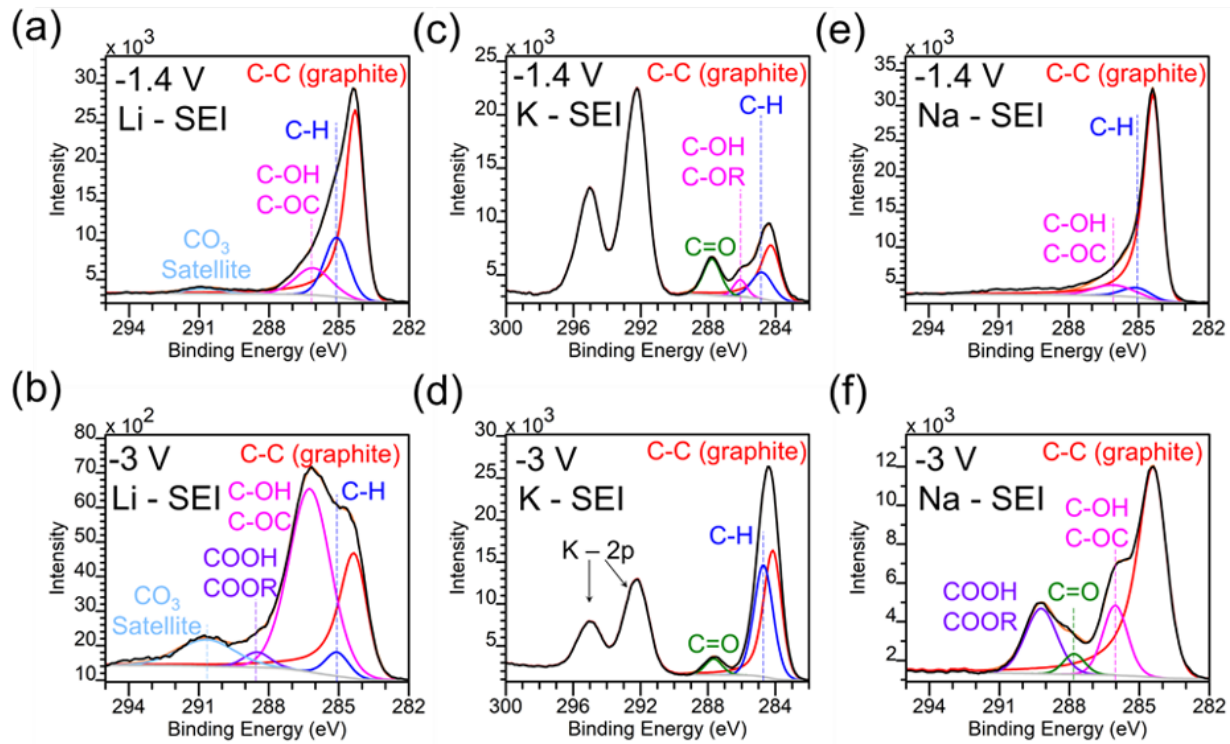


Figure B.19: High resolution spectra for C 1s for (a)  $\text{Li}^+$ -SEI, (b)  $\text{K}^+$ -SEI and (c)  $\text{Na}^+$ -SEI. Note: K 2p peaks show up within C 1s spectra for the  $\text{K}^+$ -SEI. Carbon functional groups assigned based on XPS literature of SEI on graphite,[7] fluorocarbons could contribute to peaks within the 285-294 eV range depending on the C-F bond character.[8, 9]

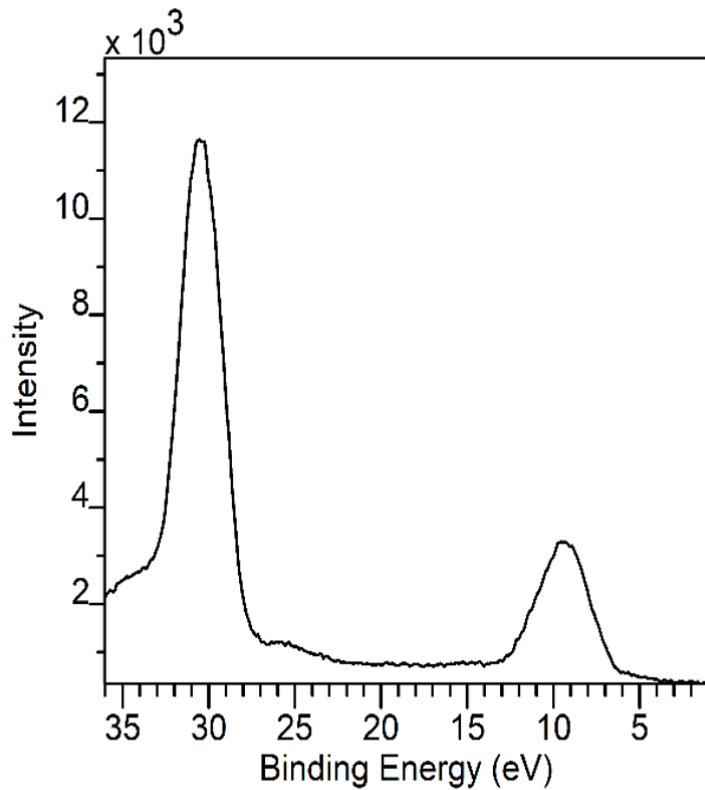


Figure B.20: Valence band spectra for  $\text{Li}^+$ -SEI. Comparison valence band XPS spectra of pure  $\text{LiF}$  species[10] reveals the dominant species in the  $\text{Li}^+$ -SEI to be  $\text{LiF}$ . Note, there appears to be no  $\text{LiBF}_4$  signals (comparing to the pure spectra),[11] so this reinforces that the peak at 686.6 eV to be B-F species incorporated within the SEI.

Table B.1: Peak assignments of components in F 1s spectra

$\text{Li}^+$ -SEI -1.4V		$\text{Li}^+$ -SEI -3.0V		Assignment	Reference
Peak Position (eV)	FHWM	Peak Position (eV)	FHWM		
685.48	1.7	684.71	1.75	LiF	[11]
686.6	1.5	686.1	1.7		
688	2.4	687.6	2.2		
$\text{K}^+$ -SEI -1.4V		$\text{K}^+$ -SEI -3.0V		KF Associated with $\text{KFP}_6$	[13] <a href="#">Figure B.18,B.19</a> [5], <a href="#">Figure B.18, B.19</a>
Peak Position (eV)	FHWM	Peak Position (eV)	FHWM		
682.4	1.4	682.5	1.7		
685.6	1.15	685	2.4	P-F	[5], <a href="#">Figure B.18, B.19</a>
686.4	2.47	686.9	2.2		
$\text{Na}^+$ -SEI -1.4V		$\text{Na}^+$ -SEI -3.0V		B-F Fluorocarbons NaF	[12] [5] [6, 14]
Peak Position (eV)	FHWM	Peak Position (eV)	FHWM		
685.75	1.6	686	1.6		
687.2	2.3	687	2.1		
		683.55	1.45	NaF	[6, 14]

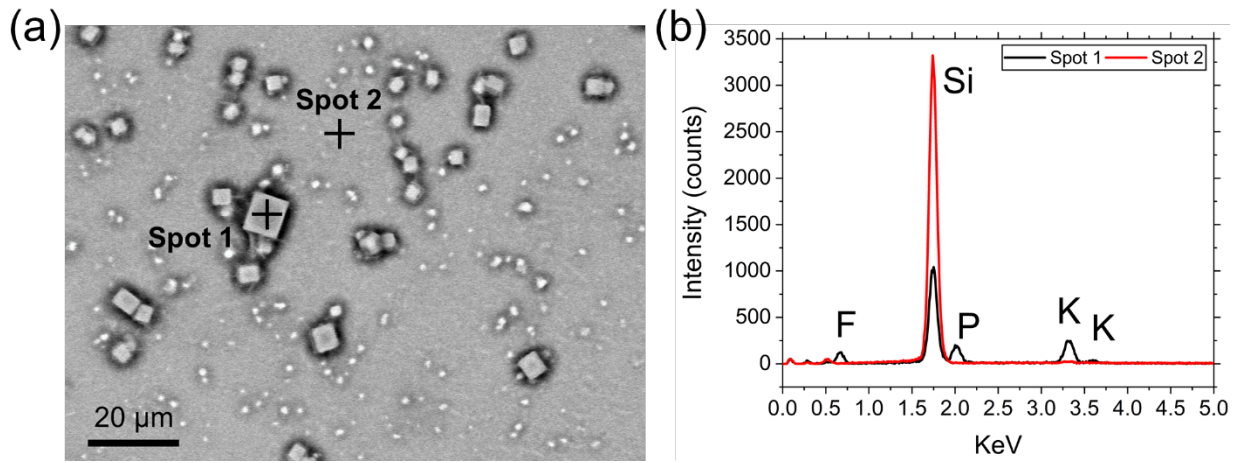


Figure B.21: SEM-EDS analysis of crystal composition in  $\text{K}^+$ -SEI at -3.0 V vs.  $\text{Fc}^+/\text{Fc}$ . (a) SEM-BSE micrograph and (b) EDS point spectra of the crystalline particles in  $\text{K}^+$ -SEI (in comparison to a crystal free region) clearly reveals the particles to be enriched in K, P and F species, indicating their identity to be  $\text{KPF}_6$  crystals.

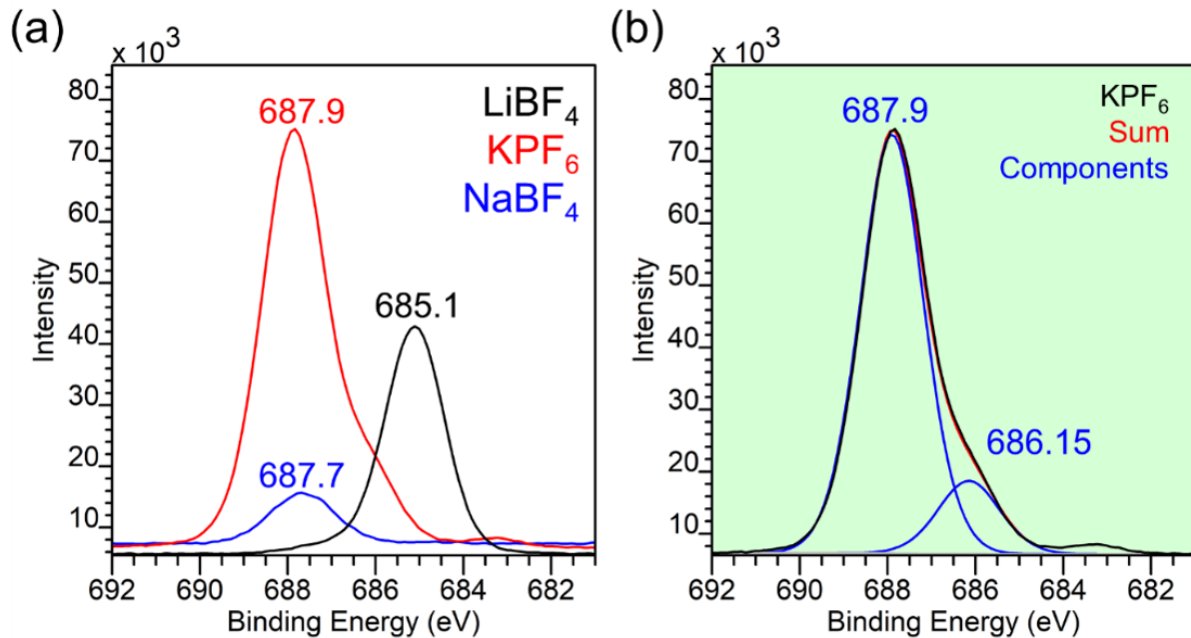


Figure B.22: XPS spectra of control salts. (a) High resolution F 1s spectra for  $\text{LiBF}_4$ ,  $\text{KPF}_6$  and  $\text{NaBF}_4$ , which reveals asymmetry in the  $\text{KPF}_6$  peak only (b) Deconvoluted F 1s for  $\text{KPF}_6$  salt, indicating a second peak at 686.15 eV, likely contributing to small peak around 685-686 eV in the F 1s spectra of  $\text{K}^+$ -SEI. We assign this peak to be associated with the  $\text{KPF}_6$  salt, most likely some impurity.

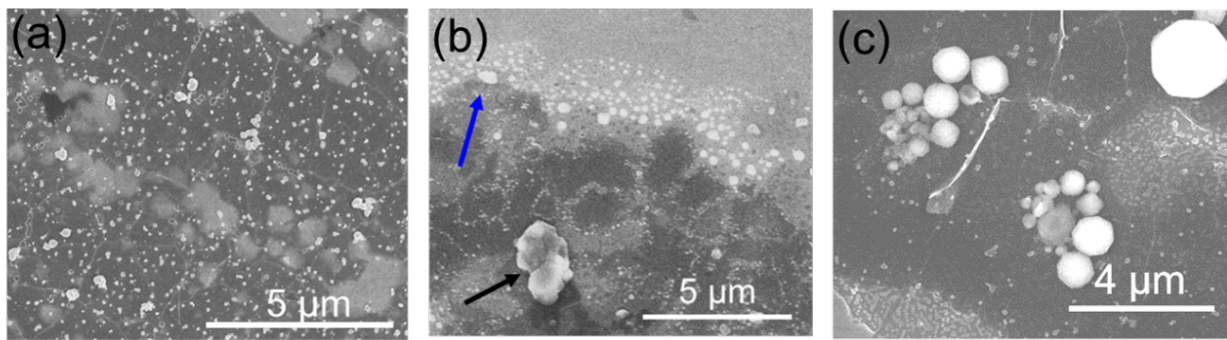


Figure B.23: SEM images of each SEI on MLG after cycling in 0.1 M (a)  $\text{LiBF}_4$ , (b)  $\text{KBF}_4$ , or (c)  $\text{NaBF}_4$ . The black and blue arrows in (b) indicate a large precipitate and select regions of SEI concentrated at the edge of the MLG electrode, respectively.

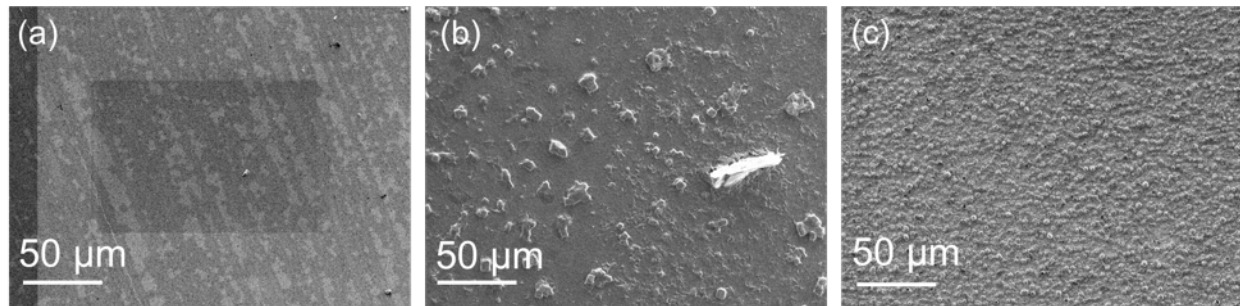


Figure B.24: SEM micrographs of (a)  $\text{Li}^+$ -SEI, (b)  $\text{K}^+$ -SEI, (c)  $\text{Na}^+$ -SEI after forming SEI at -3.0 V (same samples were used prior to SEM in XPS measurements). The Li-SEI undergoes beam damage at low accelerating voltages of 3 kV, and underlying graphene structure is visible, indicating a thin, delicate SEI forming. The other two samples do not reveal the underlying graphene, implying a thicker SEI forming. Note XPS spot size of  $300 \times 700 \mu\text{m}$  is  $\approx 4$ x larger than the  $\approx 250 \times 200 \mu\text{m}$  SEM micrographs.

## References

- (1) Armelao, L.; Barreca, D.; Bottaro, G.; Gasparotto, A.; Maragno, C.; Tondello, E. *Surface Science Spectra* **2003**, *10*, 170–181, DOI: [10.1116/11.20040901](https://doi.org/10.1116/11.20040901).
- (2) Mansour, A. *Surface Science Spectra* **1994**, *3*, 279–286, DOI: [10.1116/1.1247757](https://doi.org/10.1116/1.1247757).
- (3) Carboni, M.; Manzi, J.; Armstrong, A. R.; Billaud, J.; Brutti, S.; Younesi, R. *ChemElectroChem* **2019**, *6*, 1745–1753, DOI: [10.1002/celc.201801621](https://doi.org/10.1002/celc.201801621).
- (4) Shchukarev, A.; Korolkov, D. *Central European Journal of Chemistry* **2004**, *2*, 347–362, DOI: [10.2478/BF02475578](https://doi.org/10.2478/BF02475578).
- (5) Haasch, R. T.; Trask, S. E.; Rodrigues, M.-T.; Abraham, D. P. *Surface Science Spectra* **2020**, *27*, 016801, DOI: [10.1116/1.5130764](https://doi.org/10.1116/1.5130764).

- (6) Zheng, J.; Chen, S.; Zhao, W.; Song, J.; Engelhard, M. H.; Zhang, J.-G. *ACS Energy Letters* **2018**, *3*, 315–321, DOI: [10.1021/acsenergylett.7b01213](https://doi.org/10.1021/acsenergylett.7b01213).
- (7) Blyth, R.; Buqa, H.; Netzer, F.; Ramsey, M.; Besenhard, J.; Golob, P.; Winter, M. *Applied Surface Science* **2000**, *167*, 99–106, DOI: [10.1016/S0169-4332\(00\)00525-0](https://doi.org/10.1016/S0169-4332(00)00525-0).
- (8) Kita, Y.; Watanabe, N.; Fujii, Y. *Journal of the American Chemical Society* **1979**, *101*, 3832–3841, DOI: [10.1021/ja00508a020](https://doi.org/10.1021/ja00508a020).
- (9) Tressaud, A.; Durand, E.; Labrugère, C.; Kharitonov, A.; Kharitonova, L. *Journal of Fluorine Chemistry* **2007**, *128*, Advances in Inorganic Fluorine Chemistry, 378–391, DOI: [10.1016/j.jfluchem.2006.12.015](https://doi.org/10.1016/j.jfluchem.2006.12.015).
- (10) Dedryvère, R.; Martinez, H.; Leroy, S.; Lemordant, D.; Bonhomme, F.; Biensan, P.; Gonbeau, D. *Journal of Power Sources* **2007**, *174*, 462–468, DOI: [10.1016/j.jpowsour.2007.06.033](https://doi.org/10.1016/j.jpowsour.2007.06.033).
- (11) Leroy, S.; Martinez, H.; Dedryvère, R.; Lemordant, D.; Gonbeau, D. *Applied Surface Science* **2007**, *253*, 4895–4905, DOI: [10.1016/j.apsusc.2006.10.071](https://doi.org/10.1016/j.apsusc.2006.10.071).
- (12) Barber, M.; Connor, J. A.; Guest, M. F.; Hillier, I. H.; Schwarz, M.; Stacey, M. *Journal of the Chemical Society, Faraday Transactions 2: Molecular and Chemical Physics* **1973**, *69*, 551–558, DOI: [10.1039/F29736900551](https://doi.org/10.1039/F29736900551).
- (13) Naylor, A. J.; Carboni, M.; Valvo, M.; Younesi, R. *ACS Applied Materials & Interfaces* **2019**, *11*, 45636–45645, DOI: [10.1021/acsami.9b15453](https://doi.org/10.1021/acsami.9b15453).
- (14) Morgan, W. E.; Van Wazer, J. R.; Stec, W. J. *Journal of the American Chemical Society* **1973**, *95*, 751–755, DOI: [10.1021/ja00784a018](https://doi.org/10.1021/ja00784a018).

# Appendix C

## Supplementary Information for Chapter 5

### C.1 Materials and methods

#### C.1.1 Graphene synthesis

Graphene was grown through chemical vapor deposition (CVD) on pretreated copper foil catalyst closely following previous procedures.[1, 2] The Cu foil was treated in acetone (10 s), water (10 s), glacial acetic acid (10 min), water (10 s), acetone (10 s), and IPA (10 s) to remove any surface oxides. The Cu foil was then mounted in CVD furnace (Lindberg Blue M, Thermo Scientific) for graphene growth. A methodology from previously reported atmosphere pressure CVD graphene synthesis,[1] with no annealing step and growth at 960°C, 10 sccm CH<sub>4</sub> and 30 sccm H<sub>2</sub> for 5 min was employed to obtain the multi-layer graphene (MLG) substrates. Single layer graphene was procured commercially from GrollTex.

#### C.1.2 Graphene transfer

CVD grown graphene was transferred on SiO<sub>2</sub>/Si wafer and glass coverslips (for optical transmittance characterization) through a wet transfer method.[3] After graphene growth, one side of the Cu foil with graphene was protected with 1 layer of Poly(Bisphenol A carbonate), henceforth referred as polycarbonate, via spin-coating at 3000 rpm for 30 s. Post coating, MLG from the other side was removed using scotch tape. Oxygen plasma was used to remove SLG from the other side of the Cu foil (Harrick Plasma, 40 W power, 1 torr

$\text{O}_2$  pressure, 3 min exposure). The protected graphene was floated on top of Cu etchant for 1 h at 40°C to remove Cu foil beneath the graphene. The floating graphene/polycarbonate sheet went through 4 rinse steps with DI water, 1 h treatment with 0.1 M  $\text{Na}_2\text{EDTA}$  aqueous solution, and 4 rinse steps with DI water again to fully remove any metal residue. The clean graphene/polycarbonate sheet was finally transferred onto the desired substrate and blow dried under argon, and subsequently kept in a vacuum desiccator overnight. After drying, samples were immersed in chloroform overnight to remove polycarbonate protecting layer, and then rinsed with acetone and IPA twice. Samples were used after blow drying IPA from the final rinse step with argon.

### C.1.3 Graphene characterization

The CVD grown graphene was characterized through SEM, Raman and transmittance microscopy. The transmittance of graphene to radiation between 500-700 nm wavelengths is known to be 2.3% per layer.<sup>[4]</sup> Transmittance micrographs were obtained at 561 nm using a Leica SP8 Confocal Microscope, and it was assumed that each layer absorbs 2.3% of the light. Each individual pixel from the micrograph were individually converted to yield a no. of layers, and therefore, the resulting image now displays the spatial distribution of no. of layers of graphene. Raman spectra and images were collected using a Nanophoton Laser Raman Microscope (RAMAN-11, Japan). Scanning electron microscopy (SEM) was performed on a Hitachi S4700 field emission.

SEM micrographs (Manuscript **Figure 5.3c**) reveal full coverage of graphene on Si wafer with minimal tears. The morphology and structure of graphene is in line with what is observed for atmospheric pressure CVD synthesis of graphene.<sup>[5]</sup> There are clear dark bands of multi-layered graphene, with the lighter area around the bands clearly having fewer layers.

Raman spectro-microscopy (**Figure C.1**) confirms that the dark bands are multi-layered graphene. The lighter regions are observed to have a 2D/G peak intensity

ratio of 1 and  $>1$ , which is characteristic of bilayer (BLG) and single layer graphene (SLG) respectively.

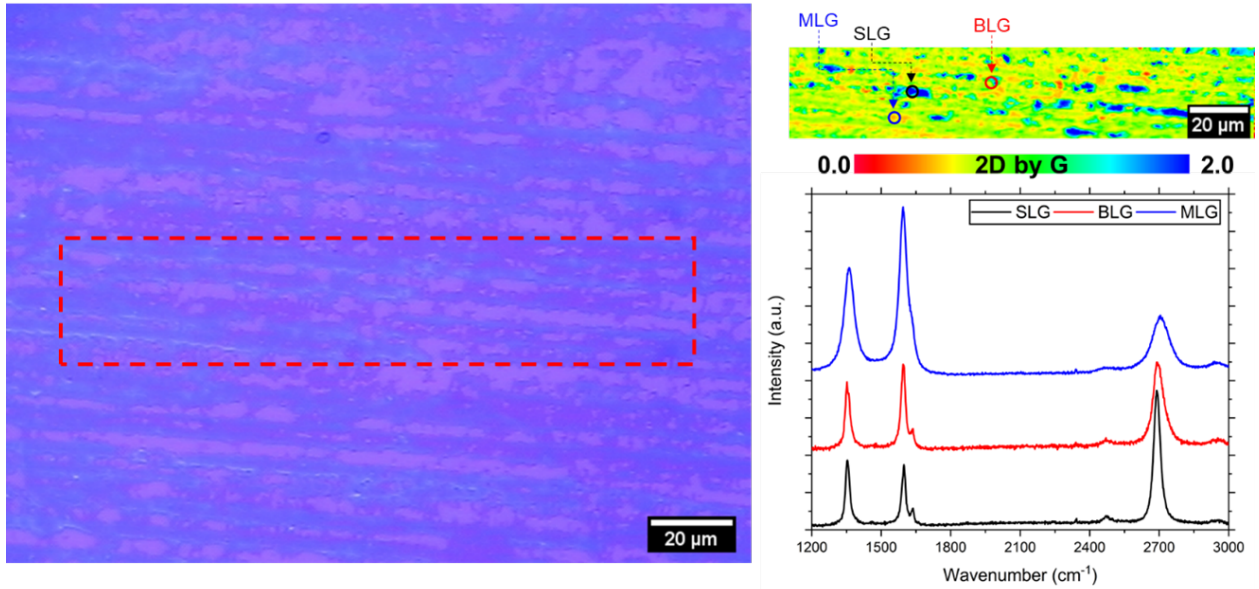


Figure C.1: Raman 2D/G peak mapping (top right) showing spatial distribution of MLG, BLG and SLG regions within the red dotted region on optical micrograph (left) of CVD-grown graphene substrates.

Transmittance micrographs in **Figure C.2** results also show the similar results, with most of the graphene appearing to be 5-15 layers thick. Single and bi-layer regions are also observed (blue areas) along with thicker graphene areas varying from 15-20 layers.

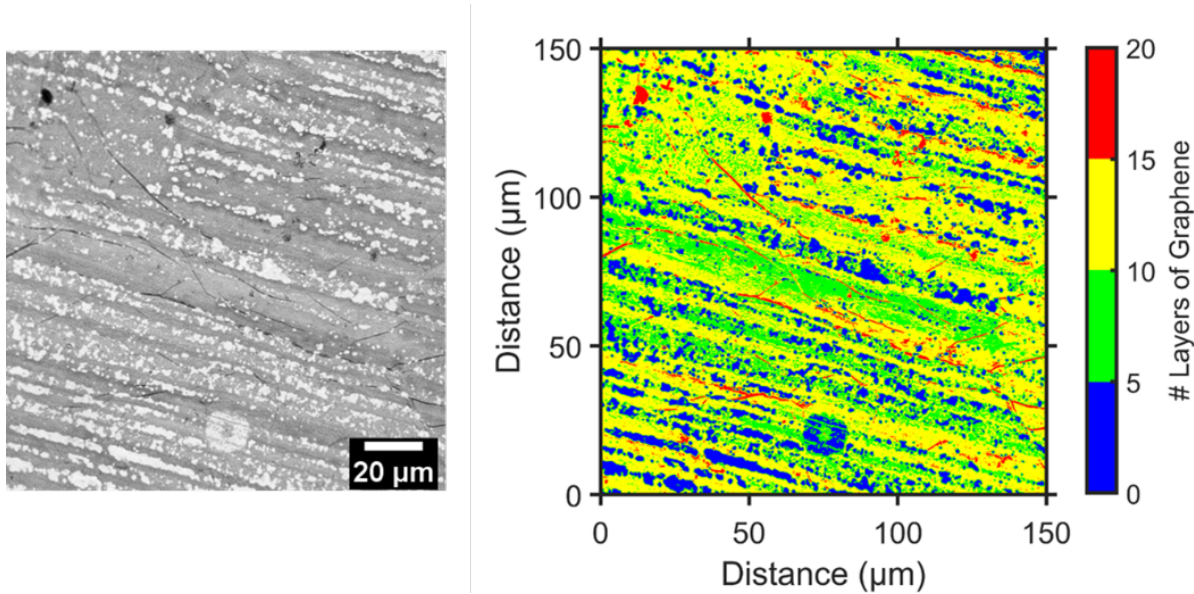


Figure C.2: Transmittance micrograph (left) of CVD graphene, and resulting number of graphene layers (right) after image analysis.

Highly oriented pyrolytic graphite (HOPG, brand grade SPI-2, SPI) and solid slabs of flexible low-density polyethylene (LDPE, 12" x 12" x 1/4" sheet from McMaster-Carr) were used for edge plane HOPG preparation, following previous work in our group.<sup>[6]</sup> HOPG sheets were peeled off using conductive Cu tape and then sealed between two pieces of LDPE. Subsequently, the setup was kept in a vacuum oven at 80°C for 2 hours and cooled under ambient air. The edge plane was then exposed by cutting and polishing with 5 μm and 1 μm SiC paper. This procedure resulted in the HOPG surface being at a lower height than the adjacent LDPE blocks as shown in **Figure C.3**. Therefore, we resorted to two methods to estimate HOPG Edge – tip distance.

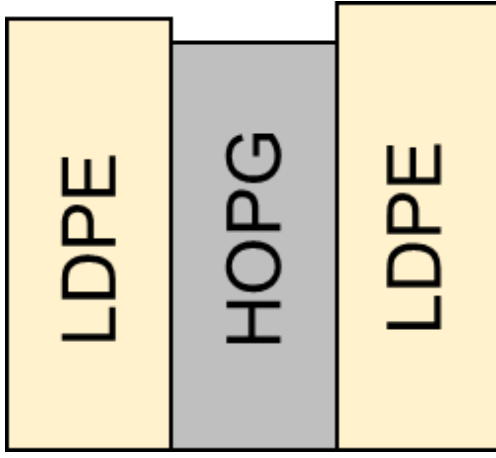


Figure C.3: Schematic of sample cross section for HOPG substrate.

#### C.1.4 HOPG height measurements

##### *Using approach curves*

We approached to 150% positive feedback over the HOPG Edge plane as shown in **Figure C.4** inset. From our  $i/i_\infty$  images, where we positioned the tip to 60% negative feedback over LDPE, the approximate positive feedback over HOPG edge was around 110% (**Figure C.4**). Therefore, using the positive feedback approach curve, we estimated that this feedback occurs at tip-substrate separation of  $\approx 2.6L$  (**Figure C.4**). Positive feedback approach curve was fit using theoretical equations laid down by Cornut and Lefrou,[7] modified to account for shifts in x and y axes.

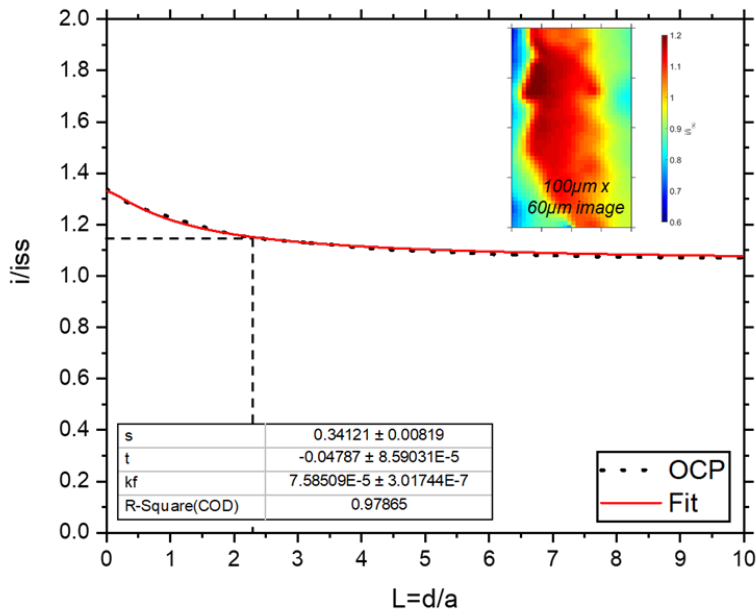


Figure C.4: Positive feedback approach to 150% (dotted line) reveal tip-substrate distance to be  $\approx 2.6L$  for a  $i/i_{ss}$  ( $i_{ss}$  is same as  $i_\infty$ ) of 1.1. Red trace is theoretical fit. Note, the fit parameter  $s$  is the tip to substrate distance for 150% positive approach, which is added to the 2.3L for getting actual tip-substrate distance.

#### Using optical profilometry

We used a Keyence VK-X1000 3D Laser Scanning Confocal Microscope to take a profile of the sample substrate after analysis, shown in **Figure C.5**. We take the average heights along every single horizontal strip of pixels and plot this average height as a function of distance in the vertical axis, as shown in **Figure C.5** inset. This reveals the HOPG edge to be slightly depressed by around 1.8-2.4  $\mu\text{m}$ . This is equivalent to around 1L to 1.4L for a tip of radius  $\approx 1.75 \mu\text{m}$ . Since the tip was estimated to be 1L from HOPG edge, this means that the tip to HOPG edge distance was around 2-2.4L, consistent with the result from positive approach feedback curves. Therefore, we resorted to calculating our  $k_f$  values at a tip-substrate distance of 2.6L for the HOPG edge samples.

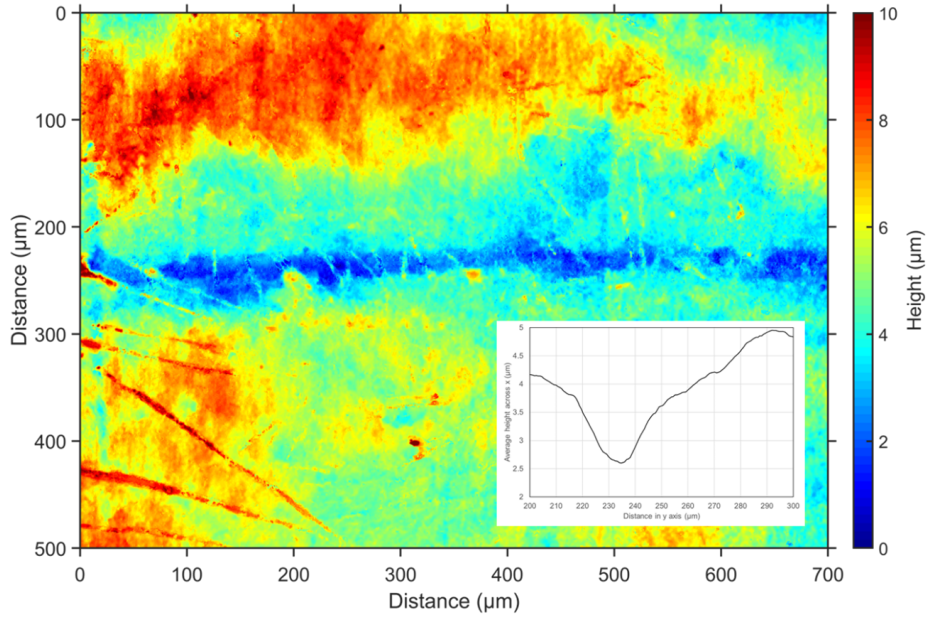


Figure C.5: Profilometry image of edge plane HOPG after testing, with average heights along x as a function of distance along y presented inset. The HOPG edge is around 1.8-2.4  $\mu\text{m}$  below the surrounding LDPE (within a 60  $\mu\text{m}$  distance, the same as that of our SECM image).

### C.1.5 SECM protocols

Cyclic voltammetry (potential sweep) and chronoamperometry (potential step) was used to cycle all substrates. All voltammograms were performed at a scan rate of 20 mV/s. In some cases, we could not reach mass transfer limited currents despite biasing to overpotentials  $>200$ -400 mV owing to solution resistance arising from the distance between reference and substrates. Chronoamperometry was performed at a mass transfer limited oxidizing potential and reduction at 0V w.r.t silver wire quasi-reference for 60s at each step. 5 sets of chronoamperometry was performed. After the 1+25 cycles of CV and 5 sets of chronoamperometry, we performed an additional potential step experiment wherein we bias the substrate at 0V for  $\approx$ 30 and 10 mins respectively. This was done to reduce the oxidized catholyte species generated by the cycling experiments and preserve the concentration of catholyte species started out with initially.

Before every set of SECM images, we took steady state current ( $i_\infty$ ) measurements by biasing the UME tip to at least 200 mV of oxidizing overpotential, at a height of 50  $\mu\text{m}$  above the substrates. The same tip potential was used for approach curves and SECM feedback imaging. Quiet time was set for 30 s, same as all SECM and approach curve measurements. The current measurement was recorded for 30 s at 0.1 s sampling interval and averaged out to get the steady state measurement. These steady state currents were subsequently used to generate normalized SECM images.

## C.2 Macrodisk electrochemistry

### C.2.1 C1, C6 (2,5-dimethyl-1,4-dialkoxybenzene), and C7 Comparison in LiBF<sub>4</sub>

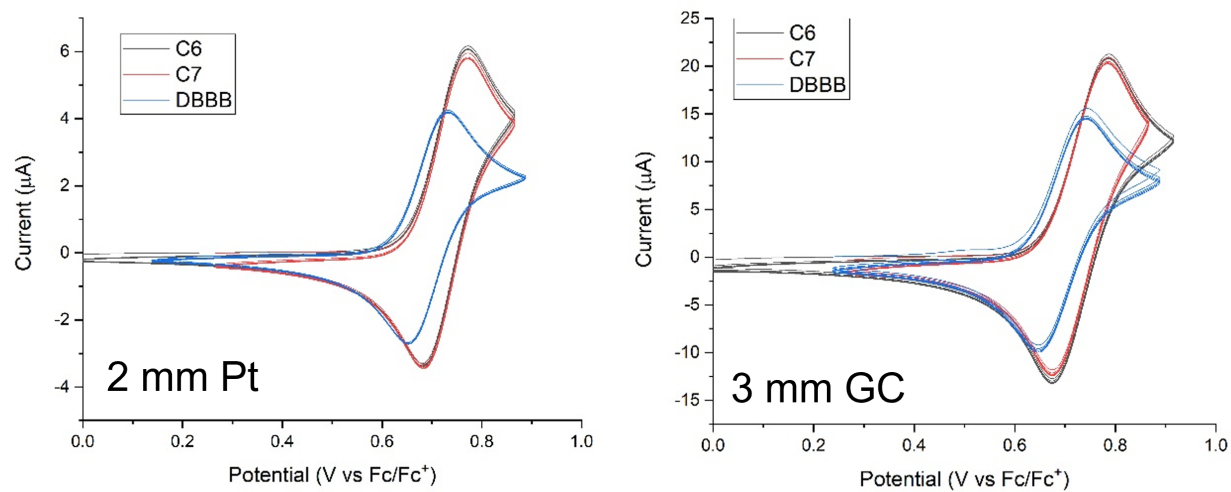


Figure C.6: Macrodisk electrochemistry comparing C1 (blue trace), C6 (black trace), and C7 (red trace) first oxidation electrochemistry. 5 mM solutions of target analyte performed on a 2 mm diameter Pt disk working electrode (left) and a 3 mm glassy carbon diameter working electrode (right). Solutions were made of 5 mM target analyte 0.1 M LiBF<sub>4</sub> in PC and evaluated using cyclic voltammetry to probe the first Faradaic oxidation at a scan rate of 10 mV/s for all samples. Electrochemistry was performed using a three electrode system with either Pt or glassy carbon working electrode, metal polypyrrole quasi-reference electrode,[8, 9] and a Pt counter electrode. Macrodisk electrochemistry displays the influence of faster diffusion coefficients of C6 and C7 with higher peak currents than C1, and the influence of less substitution with C6 and C7 having higher oxidation potentials than C1.

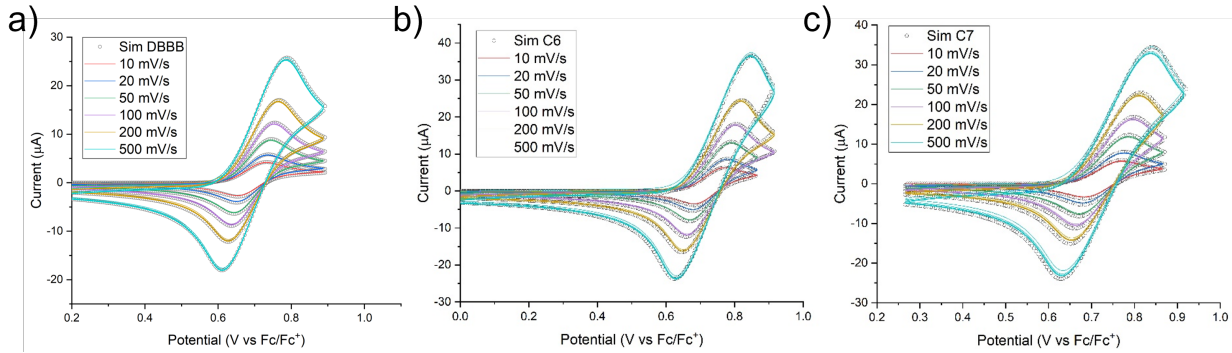


Figure C.7: Scan rate analysis performed on C1 (A), C6 (B), and C7 (C) overlaid with simulation (circles) following the progression of scan rates. A scan rate analysis was performed using a three-electrode system with a Pt working electrode, polypyrrole reference electrode and a Pt counter electrode and varying the scan rate of cyclic voltammograms from 10 mV/s up to 500 mV/s. The simulations were generated using Digi-Elch software and a fixed solution resistance of  $1800 \Omega$  and fixed capacitance of  $0.5 \mu\text{F}$  for all three analytes.

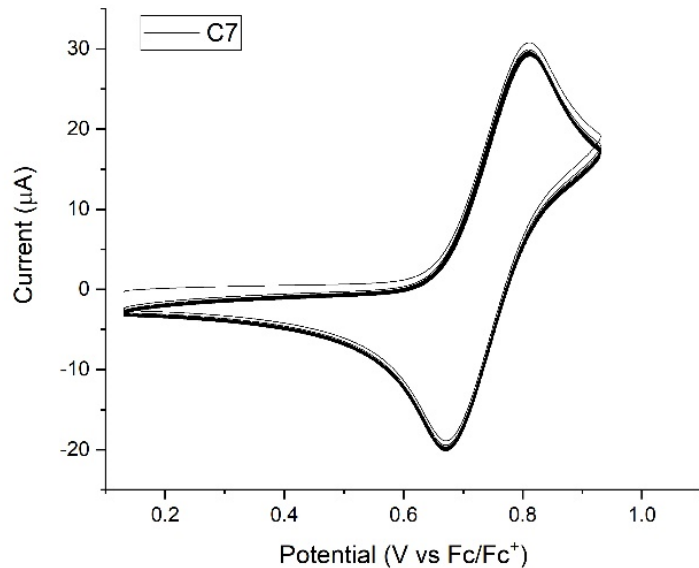


Figure C.8: C7 stability testing using macro electrode. Cyclic voltammetry performed on a solution of 5 mM C7 and 0.1 M  $\text{LiBF}_4$  in PC ramping the potentials from 0.65 V to 1.45 V to 0.65 V for 100 cycles at a scan rate of 25 mV/s. The three electrode setup used consisted of a 3 mm glassy carbon working electrode, a polypyrrole reference electrode, and a Pt counter electrode. No appreciable change in current was observed for the faradaic current of C7 over 100 cycles.

### C.2.2 C1 and C7 comparison in LiTFSI

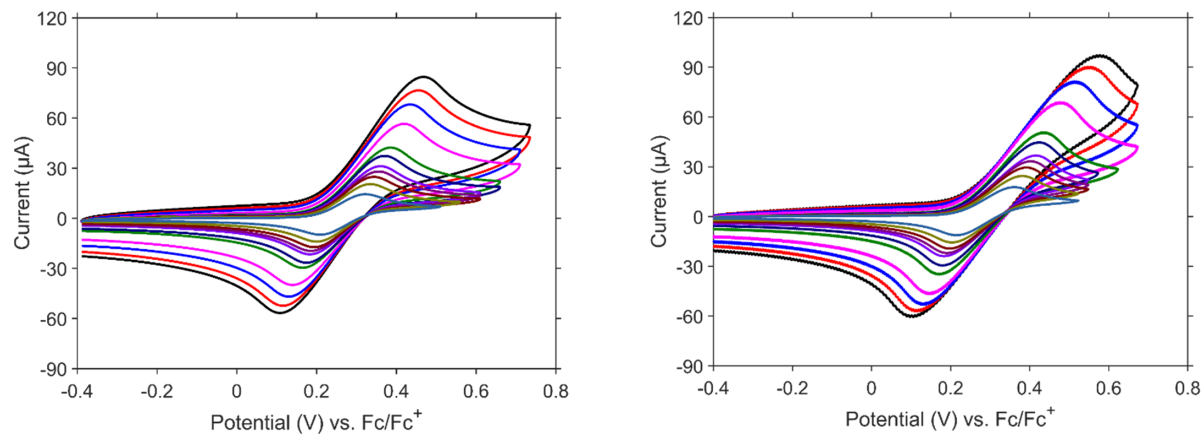


Figure C.9: Macrodisk electrochemistry comparing C1 (left), and C7 (right) first oxidation process using 0.1 M LiTFSI in PC. Electrochemistry was performed using a three-electrode system with a 3 mm glassy carbon working electrode, Ag/AgCl reference electrode (potentials adjusted to  $\text{Fc}/\text{Fc}^+$ ), and a Pt counter electrode. Scan rates used were 500, 400, 300, 200, 100, 75, 50, 40, 30, 20, 10 mV/s.

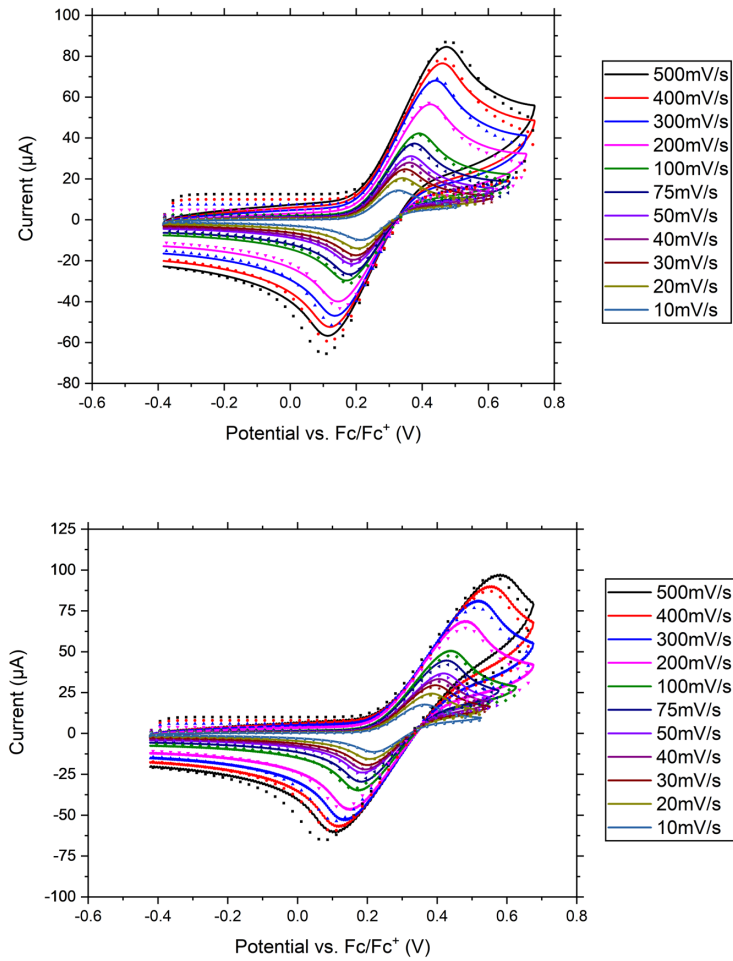


Figure C.10: Comparison of scan rate analysis with 5 mM C1 (top) and 5 mM C7 (bottom) in 0.1 M LiTFSI with simulation (dotted traces). Simulations were generated using Digi-Elch software and a solution resistance of 1500  $\Omega$  and 2000  $\Omega$  (for C1 and C7 respectively) and fixed capacitance of 0.25  $\mu\text{F}$  for both analytes.

### C.2.3 Summary of electrochemical parameters used to generate simulations

These  $k^0$  values were used exclusively as model inputs for DigiElch. The heterogeneous rate constants used to reproduce the macroelectrode cyclic voltammetry are understood to be empirically limited in their accuracy. This stems from contributions of solution resistance, capacitance, and mass transport preventing the observation and subsequent fitting of faster heterogeneous rate constants.

Table C.1: Electrochemistry parameters used to generate the simulations for C1 and C7

Parameter	C1	C7		
Electrolyte	$\text{LiBF}_4$	$\text{LiTFSI}$	$\text{LiBF}_4$	$\text{LiTFSI}$
Diffusion Coefficient ( $\text{cm}^2/\text{s}$ )	$1.08 \times 10^{-6}$	$2.3 \times 10^{-6}$	$2.23 \times 10^{-6}$	$3.6 \times 10^{-6}$
Formal Potential (V vs $\text{Fc}/\text{Fc}^+$ )	0.693	0.685	0.726	0.724
Electron Transfer Rate Constant, $k^0$ ( $\text{m/s}$ )*	$1.3 \times 10^{-4}$	$1.0 \times 10^{-4}$	$1.5 \times 10^{-4}$	$1.0 \times 10^{-4}$
Transfer Coefficient	0.5	0.5	0.53	0.5

\*These values were used exclusively as model inputs for DigiElch. The heterogeneous rate constants used to reproduce the macroelectrode cyclic voltammetry are understood to be empirically limited in their accuracy. This stems from contributions of solution resistance, capacitance, and mass transport preventing the observation and subsequent fitting of faster heterogeneous rate constants.

### C.3 SECM: Comparing C1 and C7 on MLG with LiBF<sub>4</sub>

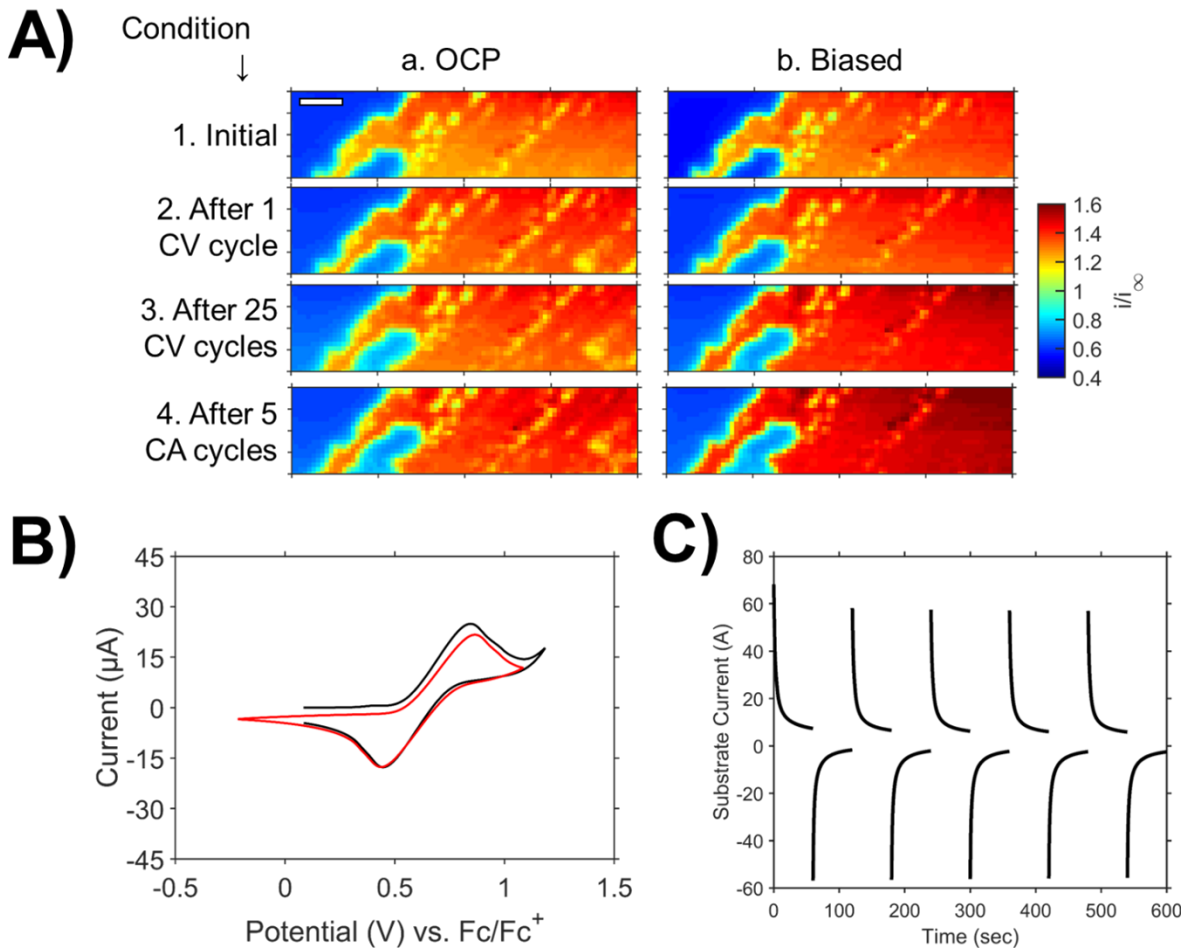


Figure C.11: A) Normalized SECM images of a MLG electrode using 5 mM C1 as catholyte mediator in 0.1 M LiBF<sub>4</sub> electrolyte in PC; image scale bars are 20  $\mu\text{m}$ . Images were taken with the substrate electrode: (i) at the initial condition before substrate biasing, (ii) after one substrate CV, (iii) after 25 more substrate CVs, and (iv) after five sets of oxidative then reductive chronoamperograms. The probe was biased at 0.88 V vs. Fc/Fc<sup>+</sup>, and the substrate was either at a) OCP or b) biased to -0.22 V vs. Fc/Fc<sup>+</sup>. B) Cyclic voltammograms with the MLG substrate. The black trace is the first cycle and red trace is the 26th total cycle. C) Chronoamperometry with MLG substrate using an oxidation potential of 1.08 V vs. Fc/Fc<sup>+</sup> and reduction potential of -0.22 V vs Fc/Fc<sup>+</sup>.

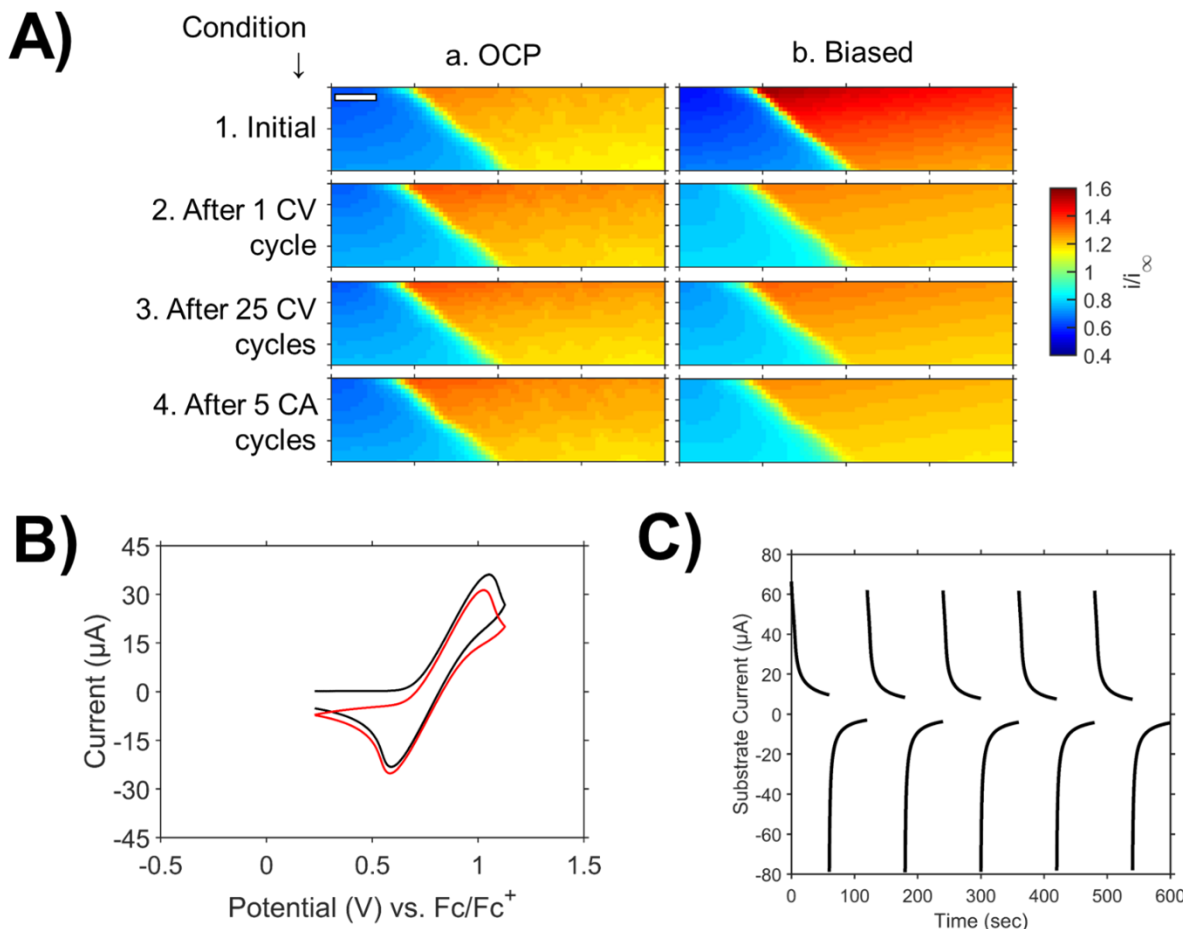


Figure C.12: A) Normalized SECM images of a MLG electrode using 5 mM C7 as catholyte mediator in 0.1 M LiBF<sub>4</sub> electrolyte in PC; image scale bars are 20  $\mu$ m. Images were taken with the substrate electrode: (i) at the initial condition before substrate biasing, (ii) after one substrate CV, (iii) after 25 more substrate CVs, and (iv) after five sets of oxidative then reductive chronoamperograms. The probe was biased at 0.926 V vs. Fc/Fc<sup>+</sup>, and the substrate was either at (a) OCP or (b) biased to -0.17 V vs. Fc/Fc<sup>+</sup>. B) Cyclic voltammograms with MLG substrate. The black trace is the first cycle and red trace is the 26th total cycle. C) Chronoamperometry with MLG substrate using an oxidation potential of 1.13 V vs. Fc/Fc<sup>+</sup> and reduction potential of -0.17 V vs Fc/Fc<sup>+</sup>.

#### C.4 Filming on MLG

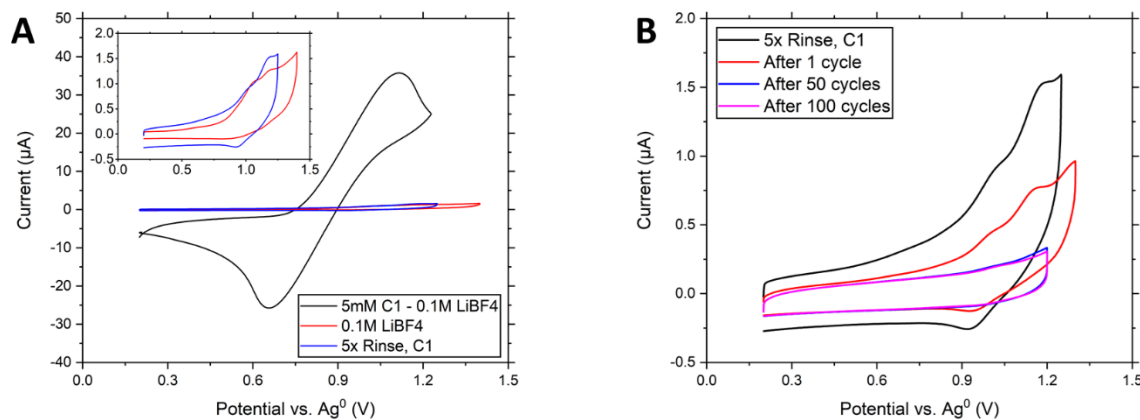


Figure C.13: A) CVs with a MLG substrate in 5 mM C1 with 0.1 M LiBF<sub>4</sub> in PC (black trace), in 0.1 M LiBF<sub>4</sub> before any addition of C1 (red trace), and after 25 CVs and 5 CAs in 5 mM C1 with 0.1 M LiBF<sub>4</sub> and rinsing five times with PC (blue trace). Inset shows zoom in of red and blue traces. B) Multiple consecutive CVs of the sample following the cycling and rinsing mentioned above for the blue trace. The decline in current indicates that any redox active film, if formed at all, desorbs from surface over time or with repetitive cycling.

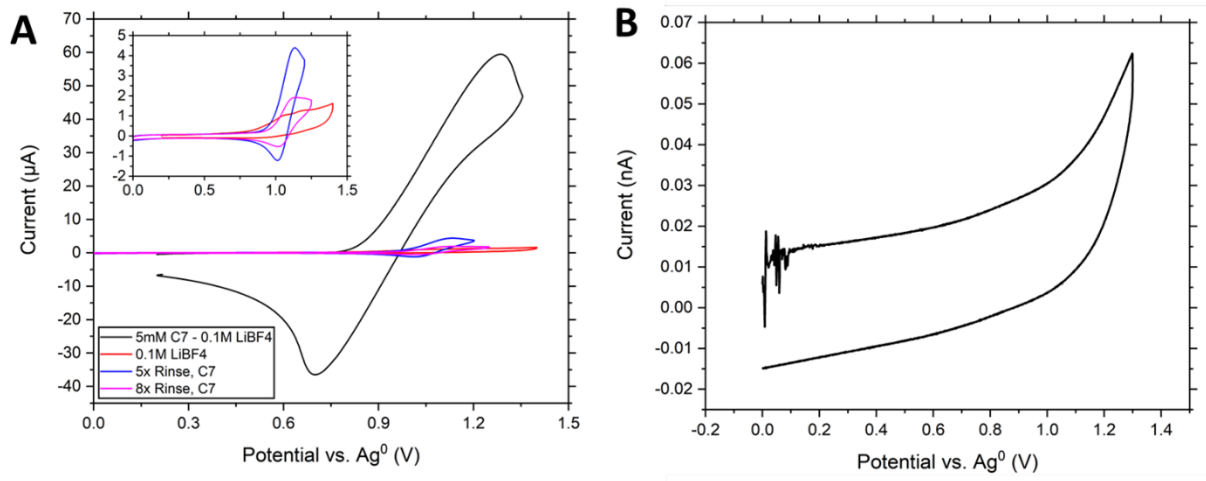


Figure C.14: A) CVs with a MLG substrate: in 5 mM C7 with 0.1 M LiBF<sub>4</sub> in PC (black trace), in 0.1 M LiBF<sub>4</sub> before any addition of C7 (red trace), after 25 CVs and 5 CAs in 5 mM C7 with 0.1 M LiBF<sub>4</sub> and rinsing five times with PC (blue trace), and after rinsing with PC a total of eight times (magenta trace). Inset shows zoom in of red, blue, and magenta traces. B) Cyclic voltammogram with an UME placed in PC approximately 1-2 mm from MLG substrate after eighth serial rinse. No faradaic signal was observed in the region anticipated for C7, which indicated the absence of solvated C7 in the post-washing MLG electrochemistry.

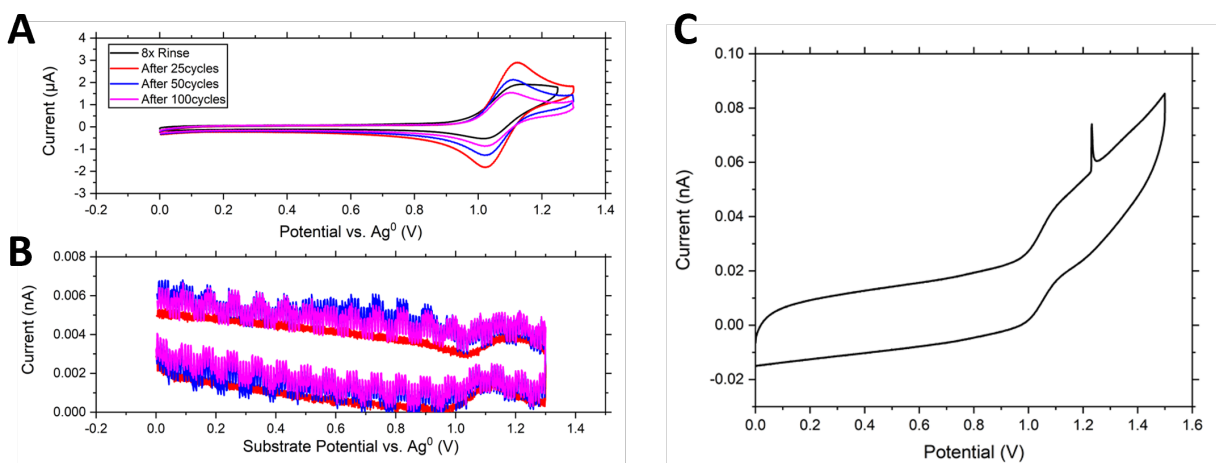


Figure C.15: A) Cyclic voltammetry of conditioned MLG sample in 0.1 M LiBF<sub>4</sub> and PC after rinsing procedure described in **Figure C.14**. The black trace represents MLG substrate after eighth serial rinse, the red trace is after a total of 25 cycles, the blue trace is after a total of 50 cycles, and the magenta trace is after a total of 100 cycles. B) UME placed above MLG substrate and biased to 0 V vs.  $\text{Ag}^0$  to collect any oxidized products generated during the MLG CVs in A). A small faradaic signal was observed when the substrate potential reached 1.1 V vs  $\text{Ag}^0$ . C) UME CV after cycling the substrate for 100 times and resting the substrate for approximately 10 h. Comparing this UME CV with a faradaic component to the initial CV where the UME was placed in solution, **Figure C.14B**, strongly indicates the presence of a desorbed redox active species in solution that was not detected earlier.

## C.5 AFM: Comparing C1 and C7 on HOPG

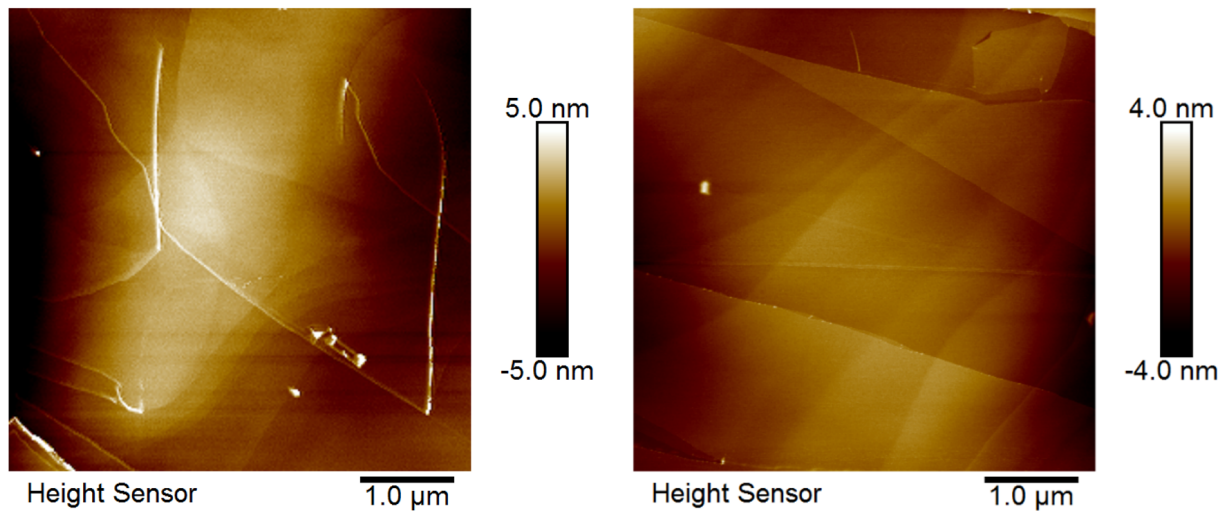


Figure C.16: AFM images of HOPG substrates, in their dry states, used in to collect the in situ data shown in **Figure 5.4a** (left) and Figure 5.4e (right) of the main text. These images emphasize the pristine nature of a freshly cleaved HOPG surface—in contrast to the often-observed low density scattering of particles when the surface is first immersed in the electrolyte.

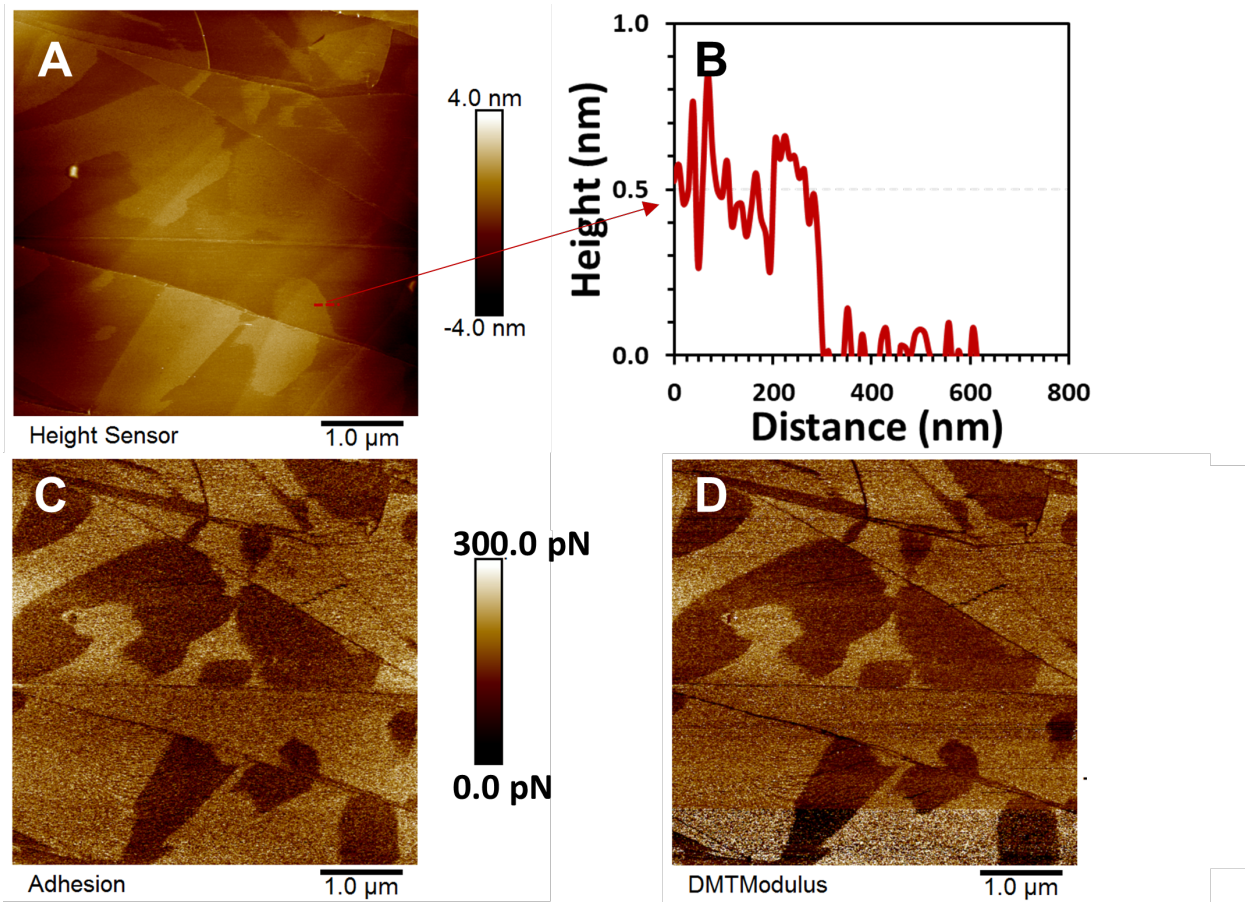


Figure C.17: Nanomechanical property maps of film formation during the reduction of  $\text{C7}^{\bullet+}$  as discussed in **Figure 5.4G**; A) Topographic image of film formation, B) Topographic profile showing a 0.5 nm film thickness, C) Relative adhesive force between the material and the tip, and D) Relative elastic modulus(Derjaguin, Muller, Toropov model).

## C.6 SECM: SLG vs. HOPG edge planes

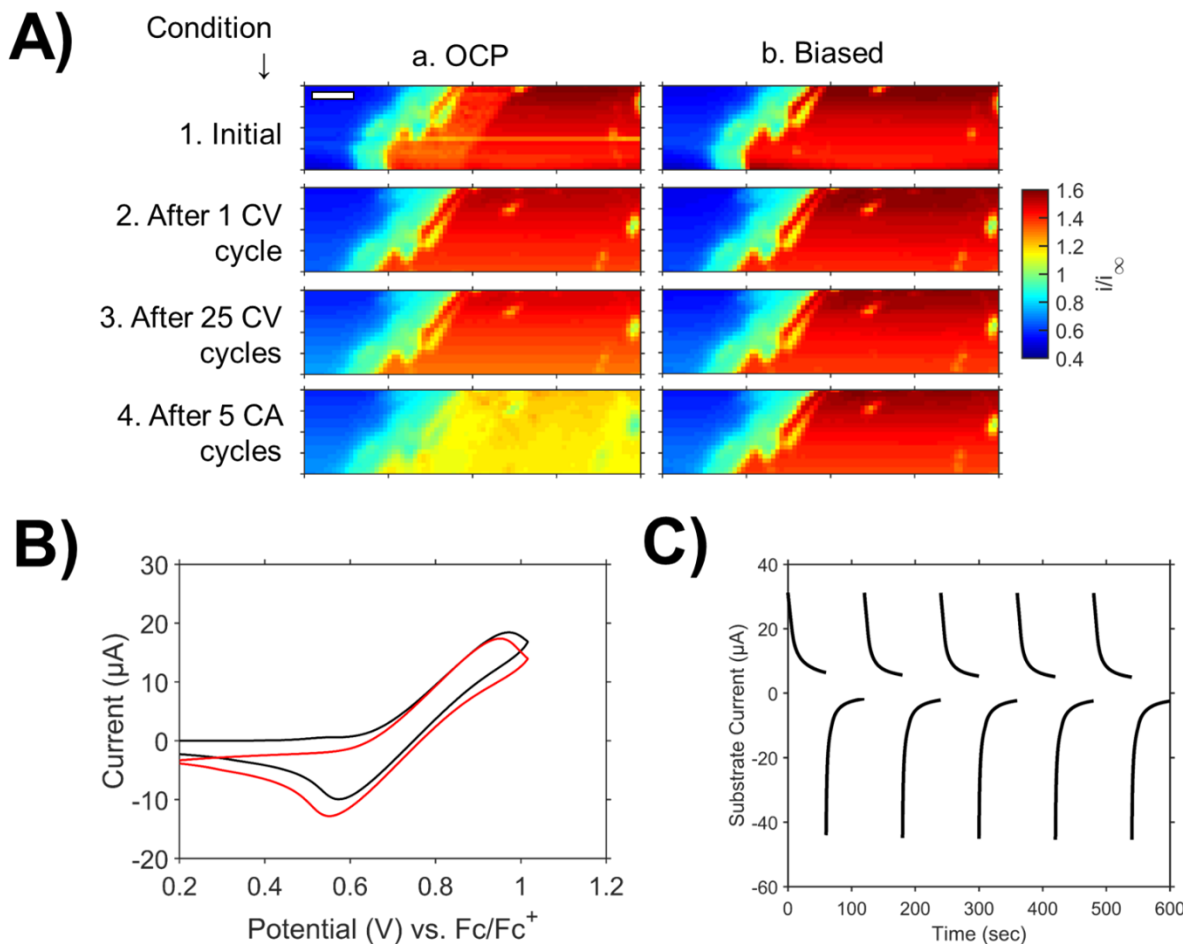


Figure C.18: A) Normalized SECM images of a SLG electrode using 5 mM C1 catholyte mediator in 0.1 M  $\text{LiBF}_4$  electrolyte in PC; image scale bars are 20  $\mu\text{m}$ . Images were taken with the substrate electrode: (i) at the initial condition before substrate biasing, (ii) after one substrate CV, (iii) after 25 more substrate CVs, and (iv) after five sets of oxidative then reductive chronoamperograms. The probe was biased at 0.97 V vs.  $\text{Fc}/\text{Fc}^+$ , and the substrate was either at a) OCP or b) biased to -0.18 V vs.  $\text{Fc}/\text{Fc}^+$ . B) Cyclic voltammograms with a SLG substrate. The black trace is the first cycle and red trace is the 26th total cycle. C) Chronoamperometry with SLG substrate using an oxidation potential of 1.02 V vs.  $\text{Fc}/\text{Fc}^+$  and reduction potential of -0.18 V vs  $\text{Fc}/\text{Fc}^+$ .

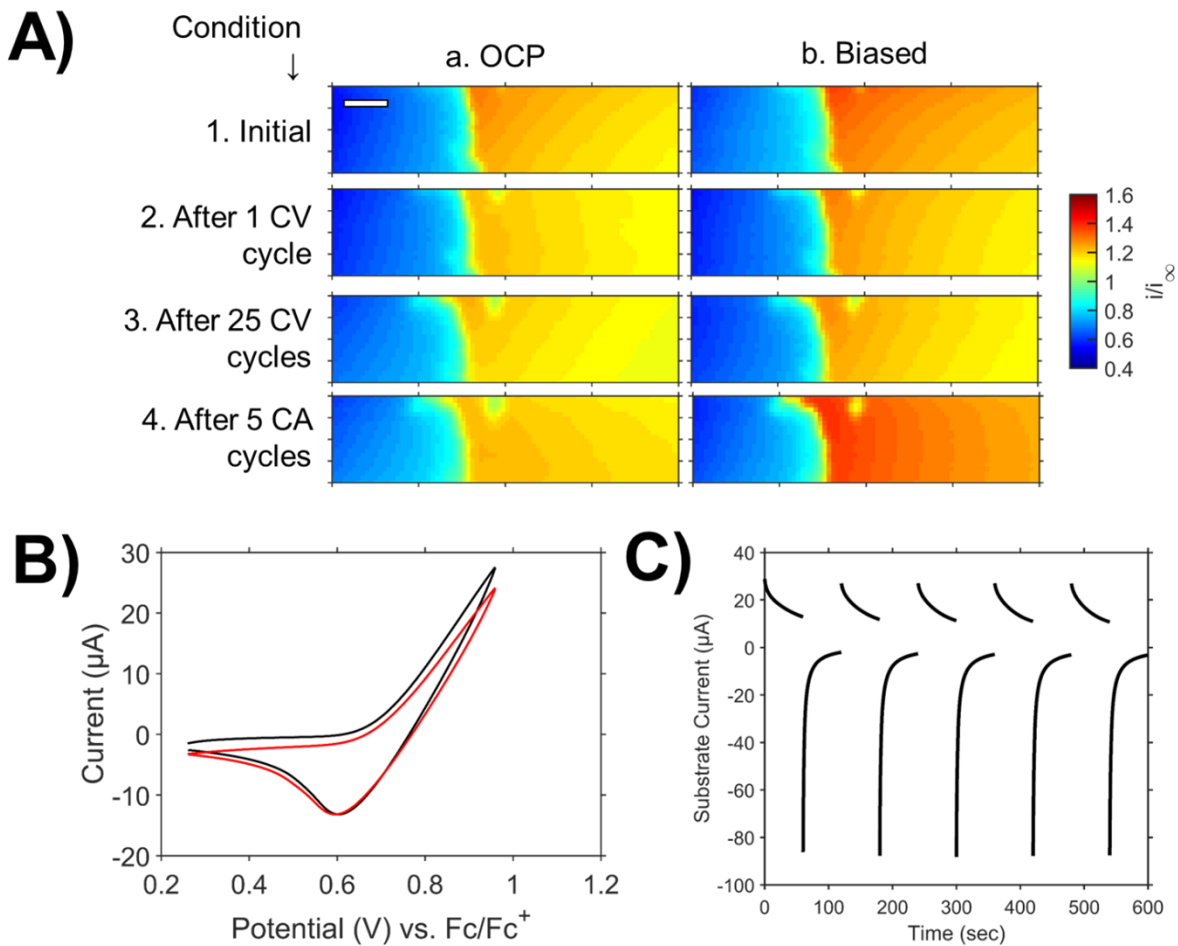


Figure C.19: A) Normalized SECM images of a SLG electrode using 5 mM C7 catholyte mediator in 0.1 M LiBF<sub>4</sub> electrolyte in PC; image scale bars are 20  $\mu$ m. Images were taken with the substrate electrode: (i) at the initial condition before substrate biasing, (ii) after one substrate CV, (iii) after 25 more substrate CVs, and (iv) after five sets of oxidative then reductive chronoamperograms. The probe was biased at 0.96 V vs. Fc/Fc<sup>+</sup>, and the substrate was either at a) OCP or b) biased to -0.24 V vs. Fc/Fc<sup>+</sup>. B) Cyclic voltammograms with a SLG substrate. The black trace is the first cycle and red trace is the 26th total cycle. C) Chronoamperometry with SLG substrate using an oxidation potential of 0.96 V vs. Fc/Fc<sup>+</sup> and reduction potential of -0.24 V vs. Fc/Fc<sup>+</sup>.

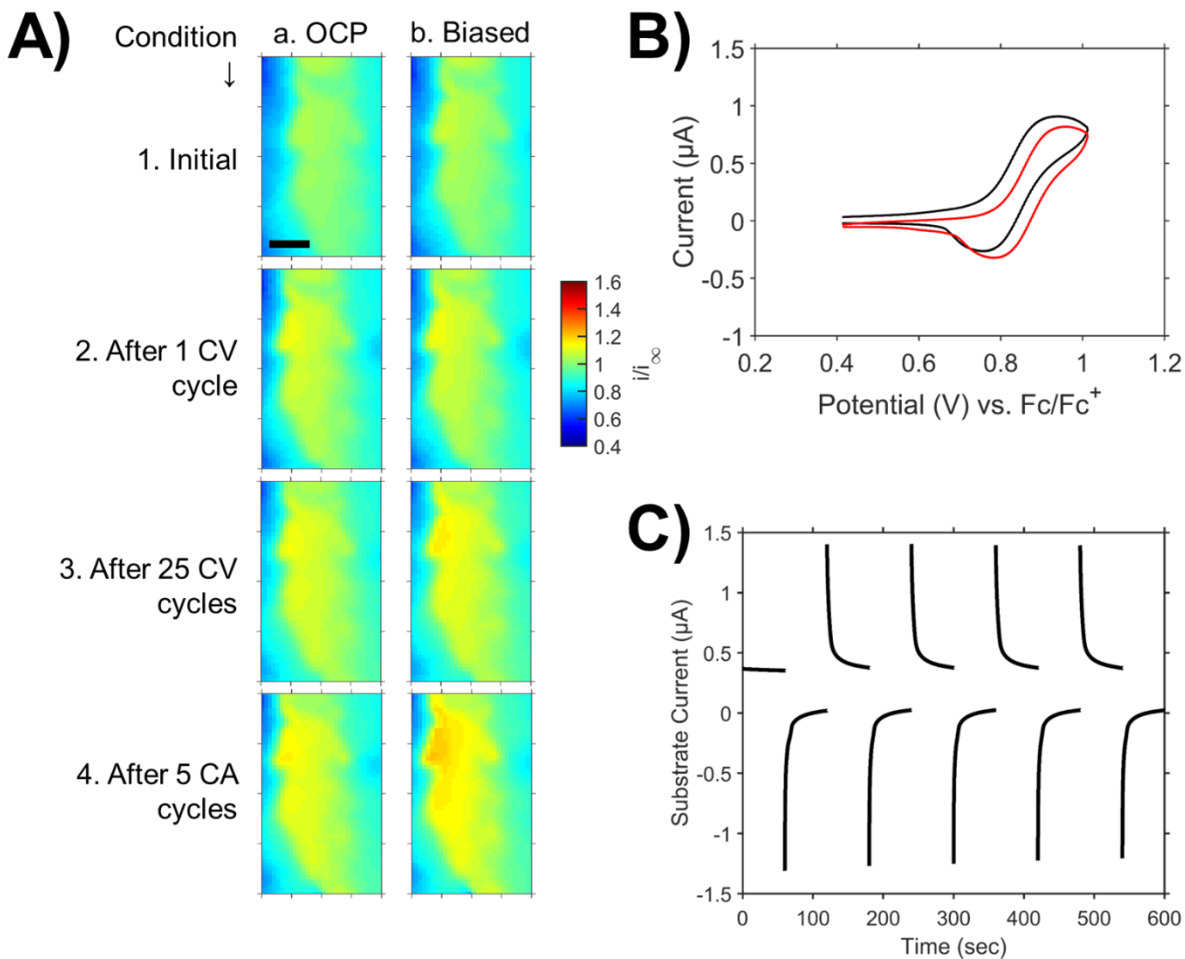


Figure C.20: A) Normalized SECM images of a HOPG edge electrode using 5 mM C1 catholyte mediator in 0.1 M  $\text{LiBF}_4$  electrolyte in PC; image scale bars are 20  $\mu\text{m}$ . Images were taken with the substrate electrode: (i) at the initial condition before substrate biasing, (ii) after one substrate CV, (iii) after 25 more substrate CVs, and (iv) after five sets of oxidative then reductive chronoamperograms. The probe was biased at 1.01 V vs.  $\text{Fc}/\text{Fc}^+$ , and the substrate was either at a) OCP or b) biased to -0.02 V vs.  $\text{Fc}/\text{Fc}^+$ . B) Cyclic voltammograms with a HOPG edge substrate. The black trace is the first cycle and red trace is the 26th total cycle. C) Chronoamperometry with HOPG edge substrate using an oxidation potential of 1.01 V vs.  $\text{Fc}/\text{Fc}^+$  and reduction potential of 0.01 V vs.  $\text{Fc}/\text{Fc}^+$ .

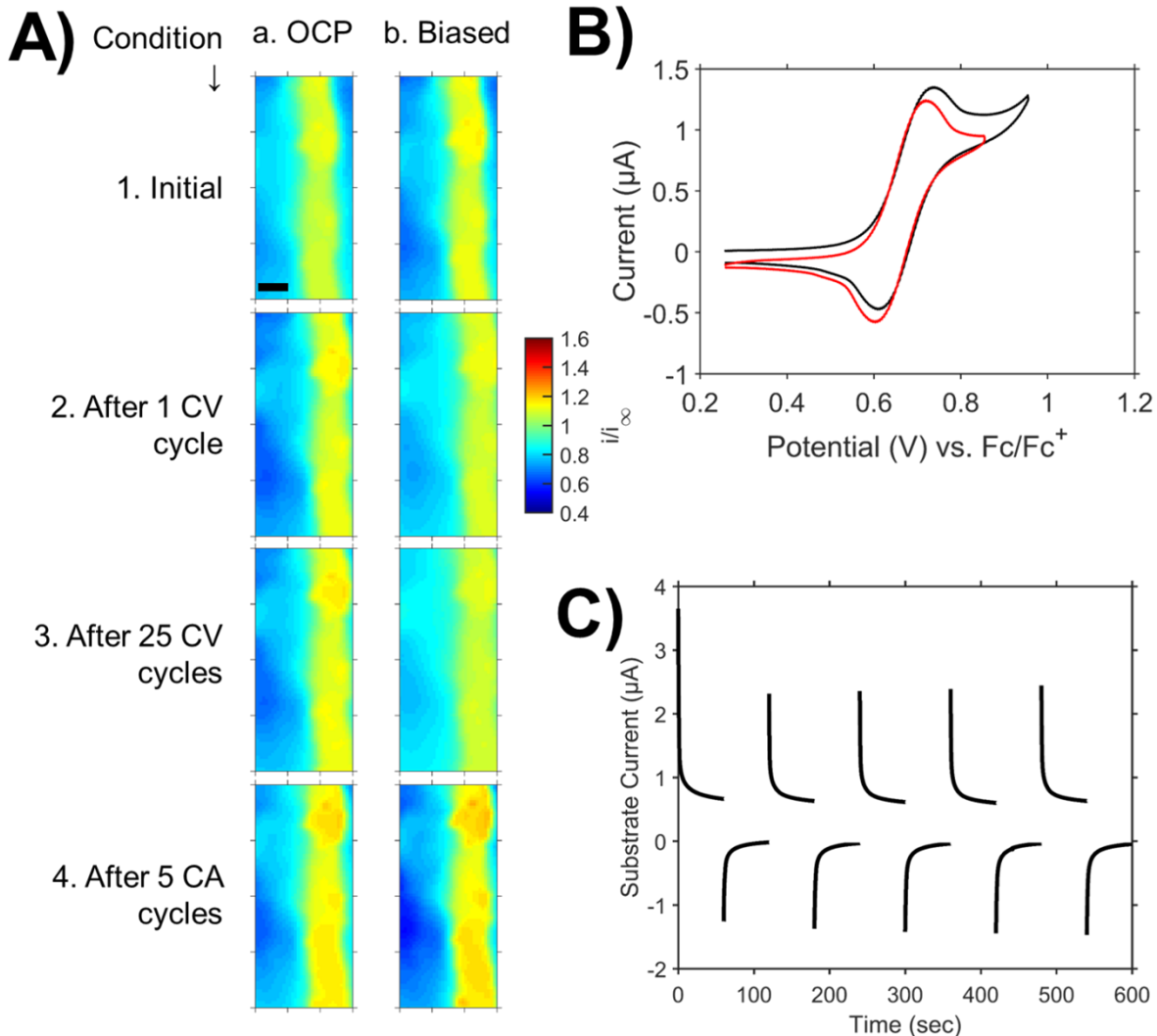


Figure C.21: A) Normalized SECM images of a HOPG edge electrode using 5 mM C7 catholyte mediator in 0.1 M LiBF<sub>4</sub> electrolyte in PC; image scale bars are 20  $\mu\text{m}$ . Images were taken with the substrate electrode: (i) at the initial condition before substrate biasing, (ii) after one substrate CV, (iii) after 25 more substrate CVs, and (iv) after five sets of oxidative then reductive chronoamperograms. The probe was biased at 0.96 V vs.  $\text{Fc}/\text{Fc}^+$ , and the substrate was either at a) OCP or b) biased to -0.35 V vs.  $\text{Fc}/\text{Fc}^+$ . B) Cyclic voltammograms with a HOPG edge substrate. The black trace is the first cycle and red trace is the 26th total cycle. C) Chronoamperometry with HOPG edge substrate using an oxidation potential of 0.86 V vs.  $\text{Fc}/\text{Fc}^+$  and reduction potential of -0.35 V vs.  $\text{Fc}/\text{Fc}^+$ .

### C.7 SECM: Comparing C1 and C7 on MLG with LiTFSI

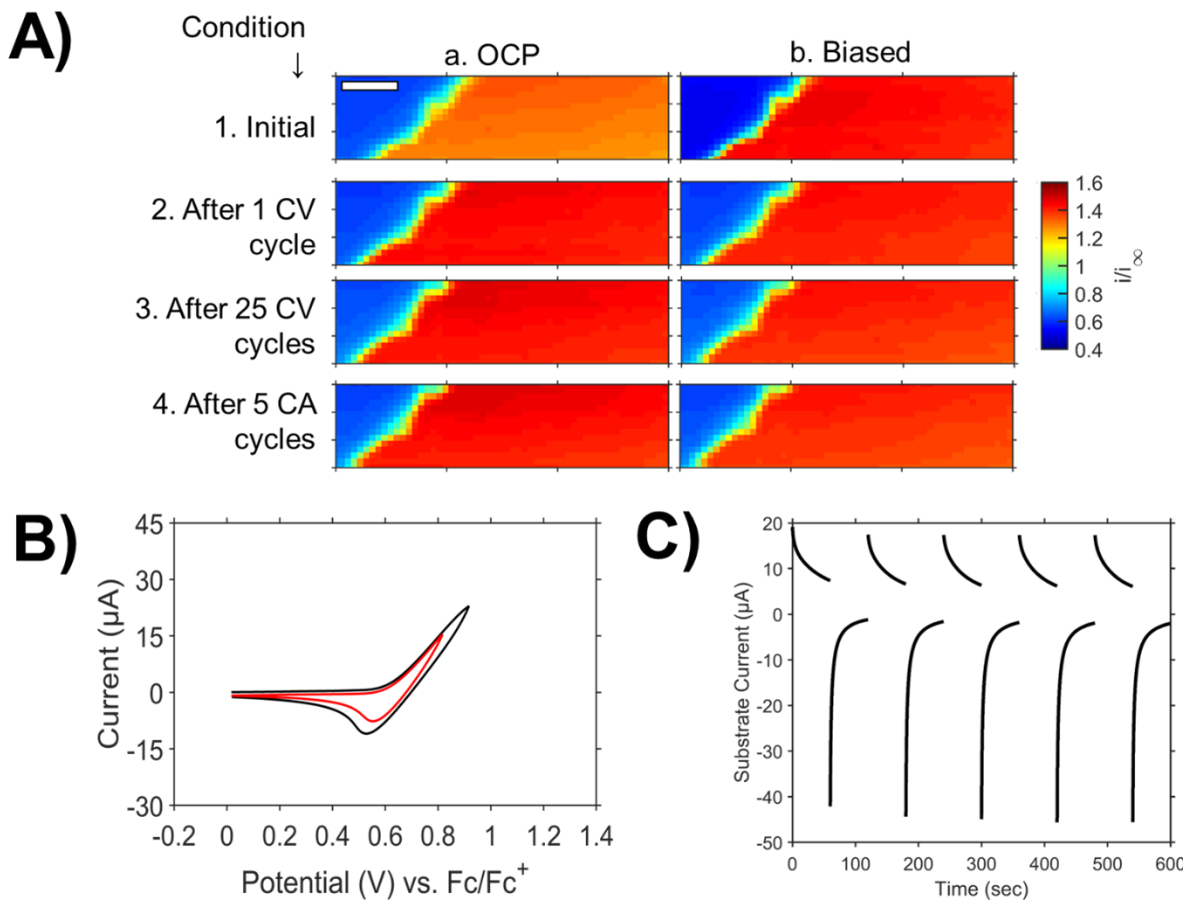


Figure C.22: A) Normalized SECM images of a MLG electrode using 5 mM C1 as catholyte mediator in 0.1 M LiTFSI electrolyte in PC; image scale bars are 20  $\mu\text{m}$ . Images were taken with the substrate electrode: (i) at the initial condition before substrate biasing, (ii) after one substrate CV, (iii) after 25 more substrate CVs, and (iv) after five sets of oxidative then reductive chronoamperograms. The probe was biased at 0.92 V vs.  $\text{Fc}/\text{Fc}^+$ , and the substrate was either at a) OCP or b) biased to -0.48 V vs.  $\text{Fc}/\text{Fc}^+$ . B) Cyclic voltammograms with the MLG substrate. The black trace is the first cycle and red trace is the 26th total cycle. C) Chronoamperometry with MLG substrate using an oxidation potential of 0.82 V vs.  $\text{Fc}/\text{Fc}^+$  and reduction potential of -0.48 V vs  $\text{Fc}/\text{Fc}^+$ .

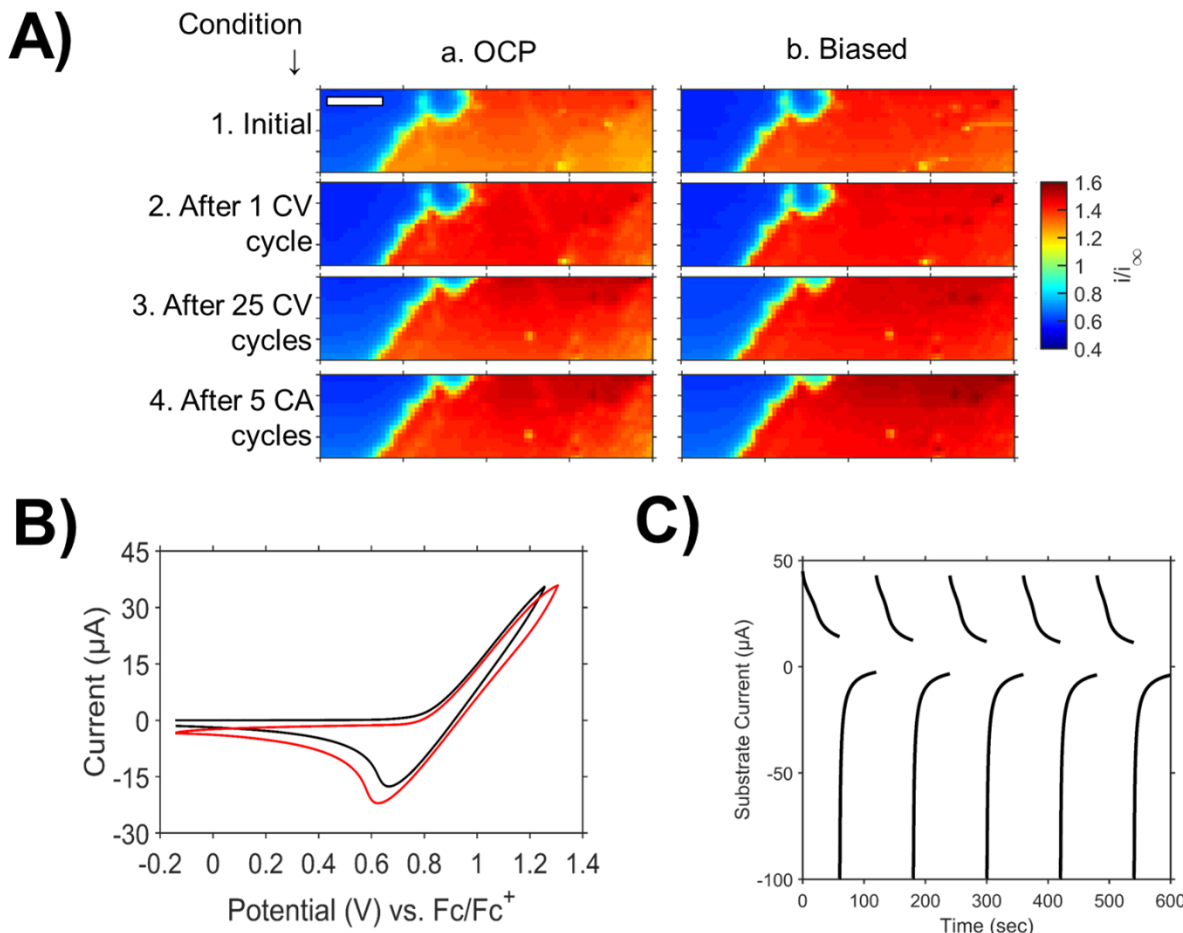


Figure C.23: A) Normalized SECM images of a MLG electrode using 5 mM C7 as catholyte mediator in 0.1 M LiTFSI electrolyte in PC; image scale bars are 20  $\mu\text{m}$ . Images were taken with the substrate electrode: (i) at the initial condition before substrate biasing, (ii) after one substrate CV, (iii) after 25 more substrate CVs, and (iv) after five sets of oxidative then reductive chronoamperograms. The probe was biased at 1.21 V vs.  $\text{Fc}/\text{Fc}^+$ , and the substrate was either a) OCP or b) biased to -0.14 V vs.  $\text{Fc}/\text{Fc}^+$ . B) Cyclic voltammograms with the MLG substrate. The black trace is the first cycle and red trace is the 26th total cycle. C) Chronoamperometry with MLG substrate using an oxidation potential of 1.26 V vs.  $\text{Fc}/\text{Fc}^+$  and reduction potential of -0.14 V vs.  $\text{Fc}/\text{Fc}^+$ .

## C.8 AFM: Comparing C1 and C7 on MLG with LiTFSI

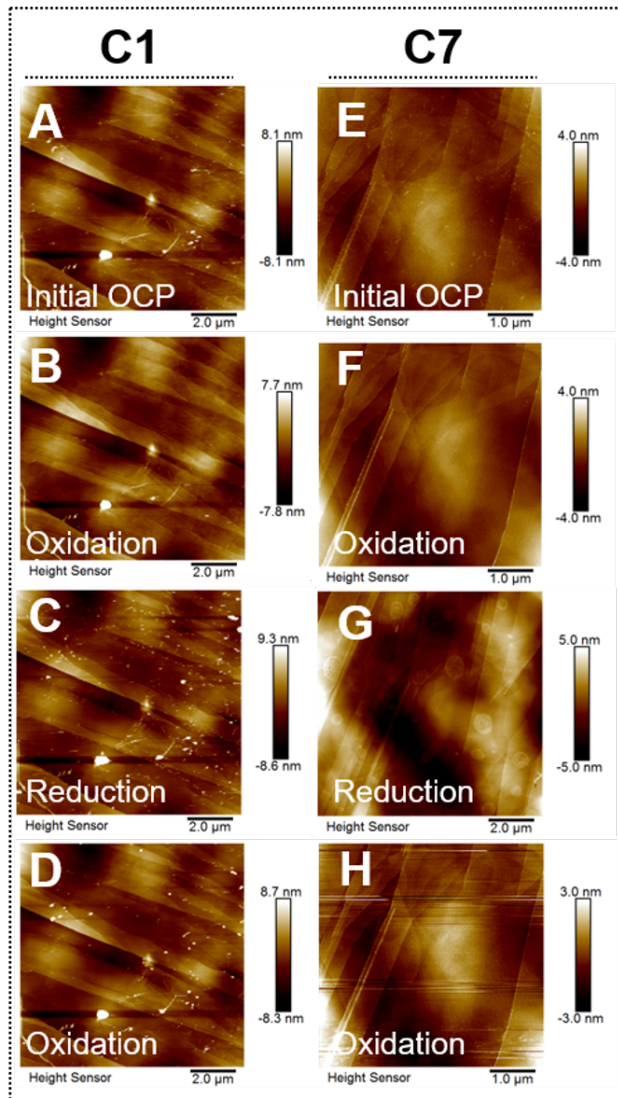


Figure C.24: In situ AFM images of the HOPG surface during experiments equivalent to those in Figure 5.4A-H of the main text, but with LiTFSI as the supporting salt. G is equivalent to **Figure 5.6F** in the main text.

### C.9 SECM $k_f$ quantification

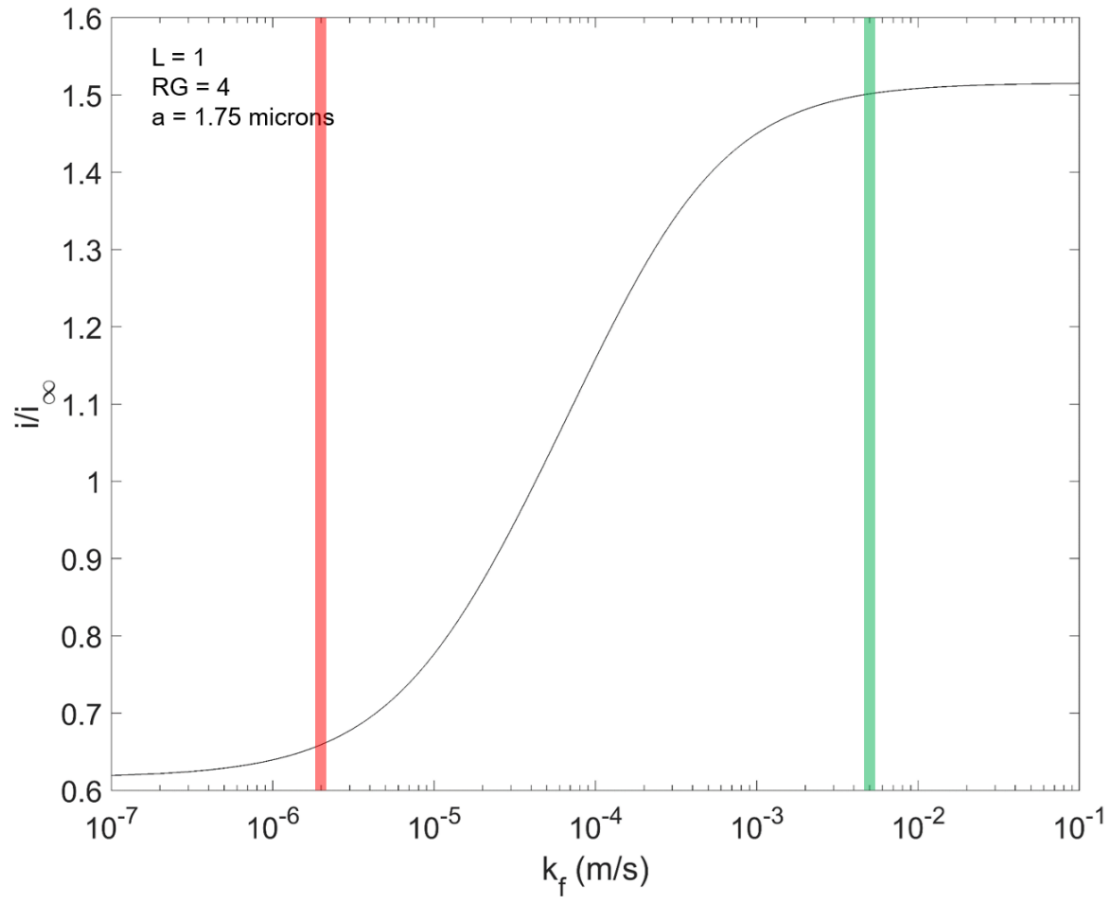


Figure C.25: Theoretical normalized tip currents versus the measured  $k_f$  from the given tip geometry and tip-substrate distance that was used in this work. The red and green lines correspond to the upper and lower limits of quantitation given in the main text.

## C.10 Summary of SECM experiments

	<b>C1</b>	<b>C7</b>
<b>MLG with LiBF<sub>4</sub></b>	Relevant Figures: Fig. 1, S11 kf at OCP (m/s) = $1.3 \times 10^{-4}$ (initial), $2.5 \times 10^{-4}$ (final) kf at Biased (m/s) = $1.8 \times 10^{-4}$ (initial), $5 \times 10^{-3}$ (final)	Relevant Figures: Fig. 1, S12 kf at OCP (m/s) = $1.3 \times 10^{-4}$ (initial), $1.6 \times 10^{-4}$ (final) kf at Biased (m/s) = $2.9 \times 10^{-4}$ (initial), $1.4 \times 10^{-4}$ (final)
	Relevant Figures: Fig. 4, S25 kf at OCP (m/s) = $1.3 \times 10^{-4}$ (initial), $3.6 \times 10^{-4}$ (final) kf at Biased (m/s) = $3.6 \times 10^{-4}$ (initial), $2.3 \times 10^{-4}$ (final)	Relevant Figures: Fig. 4, S26 kf at OCP (m/s) = $3.1 \times 10^{-4}$ (initial), $9.8 \times 10^{-4}$ (final) kf at Biased (m/s) = $5.5 \times 10^{-4}$ (initial), $3.1 \times 10^{-3}$ (final)
	Relevant Figures: Fig. 3, S20 kf at OCP (m/s) = $4.6 \times 10^{-4}$ (initial), $5.3 \times 10^{-5}$ (final) kf at Biased (m/s) = $7.1 \times 10^{-4}$ (initial), $3.8 \times 10^{-4}$ (final)	Relevant Figures: Fig. 3, S21 kf at OCP (m/s) = $1.3 \times 10^{-4}$ (initial), $1.3 \times 10^{-4}$ (final) kf at Biased (m/s) = $1.8 \times 10^{-4}$ (initial), $2.4 \times 10^{-4}$ (final)
<b>SLG</b>	Relevant Figures: Fig. 3, S22 kf at OCP (m/s) = $1.4 \times 10^{-5}$ (initial), $2.9 \times 10^{-5}$ (final) kf at Biased (m/s) = $1.8 \times 10^{-5}$ (initial), $5.5 \times 10^{-5}$ (final)	Relevant Figures: Fig. 3, S23 kf at OCP (m/s) = $6.4 \times 10^{-5}$ (initial), $3.1 \times 10^{-4}$ (final) kf at Biased (m/s) = $9.9 \times 10^{-5}$ (initial), $5.9 \times 10^{-4}$ (final)
	Relevant Figures: Fig. 3, S22 kf at OCP (m/s) = $1.4 \times 10^{-5}$ (initial), $2.9 \times 10^{-5}$ (final) kf at Biased (m/s) = $1.8 \times 10^{-5}$ (initial), $5.5 \times 10^{-5}$ (final)	Relevant Figures: Fig. 3, S23 kf at OCP (m/s) = $6.4 \times 10^{-5}$ (initial), $3.1 \times 10^{-4}$ (final) kf at Biased (m/s) = $9.9 \times 10^{-5}$ (initial), $5.9 \times 10^{-4}$ (final)
	Relevant Figures: Fig. 3, S22 kf at OCP (m/s) = $1.4 \times 10^{-5}$ (initial), $2.9 \times 10^{-5}$ (final) kf at Biased (m/s) = $1.8 \times 10^{-5}$ (initial), $5.5 \times 10^{-5}$ (final)	Relevant Figures: Fig. 3, S23 kf at OCP (m/s) = $6.4 \times 10^{-5}$ (initial), $3.1 \times 10^{-4}$ (final) kf at Biased (m/s) = $9.9 \times 10^{-5}$ (initial), $5.9 \times 10^{-4}$ (final)
<b>HOPG Edge</b>		

Figure C.26: Summary of SECM experiments with C1 and C7 catholytes with various substrates and supporting electrolytes. The reported  $k_f$  values are median values, where “initial” is the image taken before any substrate cycling and “final” is the image taken after 26 total CVs and 5 CA sets as described in the relevant figures and main text.

## References

- (1) Hui, J.; Burgess, M.; Zhang, J.; Rodríguez-López, J. *ACS Nano* **2016**, *10*, 4248–4257, DOI: [10.1021/acsnano.5b07692](https://doi.org/10.1021/acsnano.5b07692).
- (2) Hui, J.; Schorr, N. B.; Pakhira, S.; Qu, Z.; Mendoza-Cortes, J. L.; Rodríguez-López, J. *Journal of the American Chemical Society* **2018**, *140*, 13599–13603, DOI: [10.1021/jacs.8b08907](https://doi.org/10.1021/jacs.8b08907).
- (3) Wood, J. D.; Doidge, G. P.; Carrion, E. A.; Koepke, J. C.; Kaitz, J. A.; Datye, I.; Behnam, A.; Hewaparakrama, J.; Aruin, B.; Chen, Y.; Dong, H.; Haasch, R. T.; Lyding, J. W.; Pop, E. *Nanotechnology* **2015**, *26*, 055302, DOI: [10.1088/0957-4484/26/5/055302](https://doi.org/10.1088/0957-4484/26/5/055302).
- (4) Nair, R. R.; Blake, P.; Grigorenko, A. N.; Novoselov, K. S.; Booth, T. J.; Stauber, T.; Peres, N. M. R.; Geim, A. K. *Science* **2008**, *320*, 1308–1308, DOI: [10.1126/science.1156965](https://doi.org/10.1126/science.1156965).
- (5) Bhaviripudi, S.; Jia, X.; Dresselhaus, M. S.; Kong, J. *Nano Letters* **2010**, *10*, 4128–4133, DOI: [10.1021/nl102355e](https://doi.org/10.1021/nl102355e).
- (6) Gossage, Z. T.; Hui, J.; Zeng, Y.; Flores-Zuleta, H.; Rodríguez-López, J. *Chemical Science* **2019**, *10*, 10749–10754, DOI: [10.1039/C9SC03569A](https://doi.org/10.1039/C9SC03569A).
- (7) Lefrou, C.; Cornut, R. *ChemPhysChem* **2010**, *11*, 547–556, DOI: [10.1002/cphc.200900600](https://doi.org/10.1002/cphc.200900600).

- (8) Ghilane, J.; Hapiot, P.; Bard, A. J. *Analytical Chemistry* **2006**, *78*, 6868–6872, DOI: [10.1021/ac060818o](https://doi.org/10.1021/ac060818o).
- (9) Sarbapalli, D.; Mishra, A.; Rodríguez-López, J. *Analytical Chemistry* **2021**, *93*, 14048–14052, DOI: [10.1021/acs.analchem.1c03552](https://doi.org/10.1021/acs.analchem.1c03552).

## Appendix D

# Supplementary Information for Chapter 6

Table D.1: Experimental parameters used in spot analysis measurements

Figure	Redoxmer (mM)	Substrate	UME Radius, $a$ ( $\mu\text{m}$ )	$L$ ( $d/a$ )	Diffusion coefficient ( $\text{cm}^2/\text{s}$ )
4a	FcMeOH (1.5 mM)	Pt	1.2	1.05	$3.0 \times 10^{-6}$
4b	FcMeOH (1.4 mM)	MLG	1.2	1.05	$3.0 \times 10^{-6}$
4c	FcMeOH (1.2 mM)	MLG	1.2	1.05	$9.9 \times 10^{-6}$
5a, S11	Fc (2.6 mM)	MLG-Pt-Si	1.2	1.2	$3.2 \times 10^{-6}$
S15	$\text{Fc}^+\text{PF}_6^-$ (0.9 mM)	MLG-Pt-Si	1.2	1.2	$3.5 \times 10^{-6}$
6b	FcMeOH (1.2 mM)	HOPG	1.2	1.05	$3.0 \times 10^{-6}$
6c	$\text{Fc}^+\text{PF}_6^-$ (1.1 mM)	HOPG	1.2	1.05	$3.5 \times 10^{-6}$
6e	FcMeOH (1.2 mM)	GC	1.2	1.05	$3.0 \times 10^{-6}$
6f	$\text{Fc}^+\text{PF}_6^-$ (0.9 mM)	GC	1.2	1.05	$3.5 \times 10^{-6}$
7e	FcMeOH (2.8 mM)	Graphite	12.5	0.55	$3.0 \times 10^{-6}$
8a	Fc (0.1 mM)	Graphite	12.5	0.58	$3.2 \times 10^{-6}$
8b	Fc (1.5 mM)	Graphite	12.5	0.58	$3.2 \times 10^{-6}$
8c	Fc (100 mM)	Graphite	12.5	0.58	$3.2 \times 10^{-6}$
9a	$\text{Fc}^+\text{PF}_6^-$ (0.9 mM)	Graphite	12.5	0.58	$3.5 \times 10^{-6}$
9b	$\text{Fc}^+\text{PF}_6^-$ (9.5 mM)	Graphite	12.5	0.58	$3.5 \times 10^{-6}$
9c	$\text{Fc}^+\text{PF}_6^-$ (100 mM)	Graphite	12.5	0.58	$3.2 \times 10^{-6}$
S25	$\text{FcMeOH}^+$ (0.9 mM)	Graphite	12.5	0.58	$3.0 \times 10^{-6}$

All experiments were performed in Propylene carbonate (PC) as solvent and 100 mM of TBAPF<sub>6</sub> as supporting electrolyte (except for **Figure 6.4c**, which was performed in 0.1 M KNO<sub>3</sub> in H<sub>2</sub>O)

Table D.2: Parameters used in COMSOL simulations

Variable	Value [units]	Description
F	96485 [C/mol]	Faraday's constant
R	8.314 [J/(K.mol)]	Universal gas constant
T	298 [K]	Temperature
f	$F/(R \times T)$	Reduced faraday's constant
a	$1 \times 10^{-6}$ [m]	Electrode radius
RG	10	Glass to electrode radius ratio
$t_{width}$	$RG \times a$	Total tip radius
L	1	$L = d/a$
d	$L \times a$	Tip-substrate distance
red	1 [mmol/L]	R conc
ox	0 [mmol/L]	O conc
$D_{ox}$	$5 \times 10^{-10}$ [m <sup>2</sup> /s]	Diffusion coefficient of ox
$D_{red}$	$5 \times 10^{-10}$ [m <sup>2</sup> /s]	Diffusion coefficient of red
$\alpha$	0.5	Transfer coefficient for tip
$E^0$	0 [V]	Standard redox potential
$k_{tip}^0$	$1 \times 10^{-1}$ [m/s]	Standard rate constant for tip
$k_{sub}^0$	Varied between $1 \times 10^{-3}$ to $1 \times 10^{-7}$ [m/s]	Standard rate constant for substrate
$\alpha_{sub}$	Varied between 0.3 to 0.7	Transfer coefficient for substrate

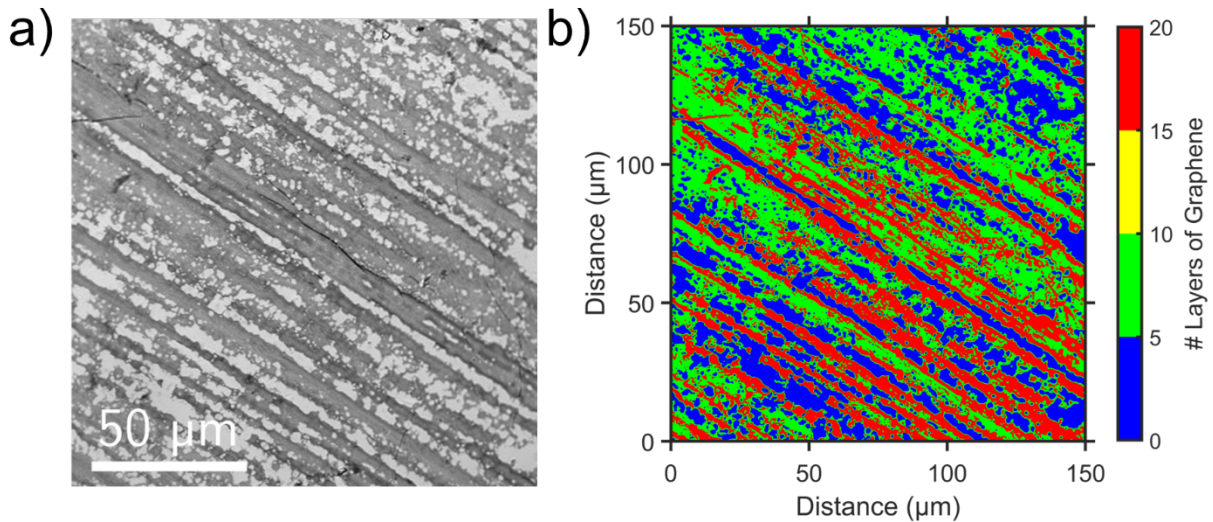


Figure D.1: Layer number distribution of MLG samples. a) Optical transmittance micrograph with 561 nm laser, b) corresponding layer number distribution assuming a single layer absorbs 2.3% of incident light.

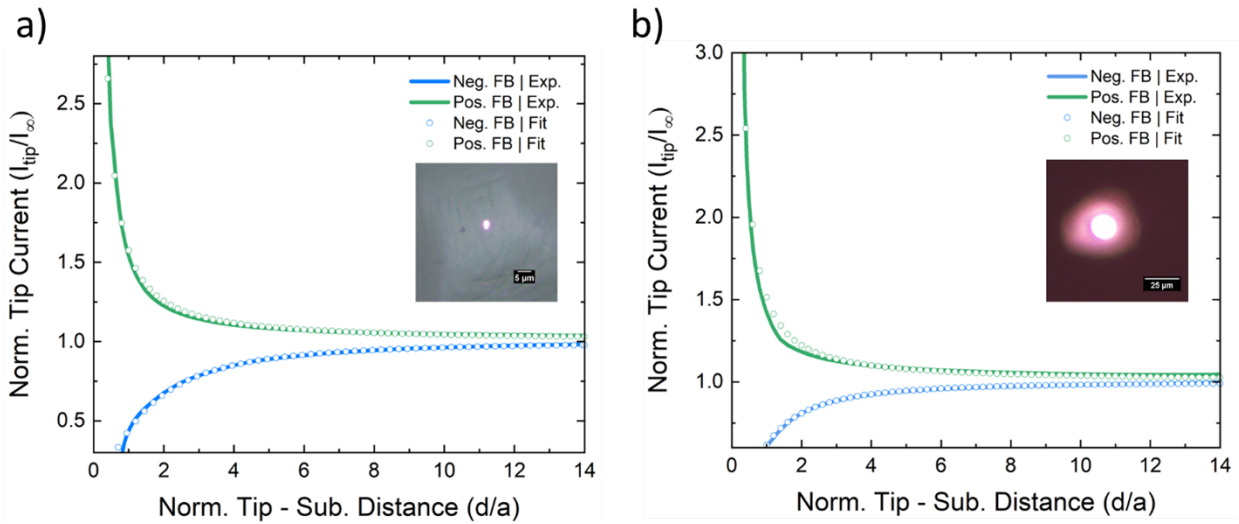


Figure D.2: Positioning SECM tip using positive feedback approach curves for spot analysis. a)  $r = 1.2 \mu\text{m}$  UME used in **Figure 6.4 – 6.6**. b)  $r = 12.5 \mu\text{m}$  used in **Figure 6.7** and **6.8**. Negative feedback approach curve (blue) performed on an insulating glass substrate in order to obtain L (Normalized tip to substrate distance) and RG (Ratio of radius of glass to electrode) of the Pt ultramicroelectrode. Positive feedback approach curve (green) performed on conducting electrodes (Pt, MLG, GC, HOPG, and Graphite) under mass transfer limited conditions to pre-defined distance ( $L = 1$  in case of  $1.2 \mu\text{m}$  UME and  $L = 0.55$  in case of  $12.5 \mu\text{m}$  UME) based on simulated positive feedback approach curve (green dot). Inset: Optical micrograph of the a)  $r = 1.2 \mu\text{m}$  UME ( $\text{RG} = 3.9$ ) b)  $r = 12.5 \mu\text{m}$  UME ( $\text{RG} = 8$ ).

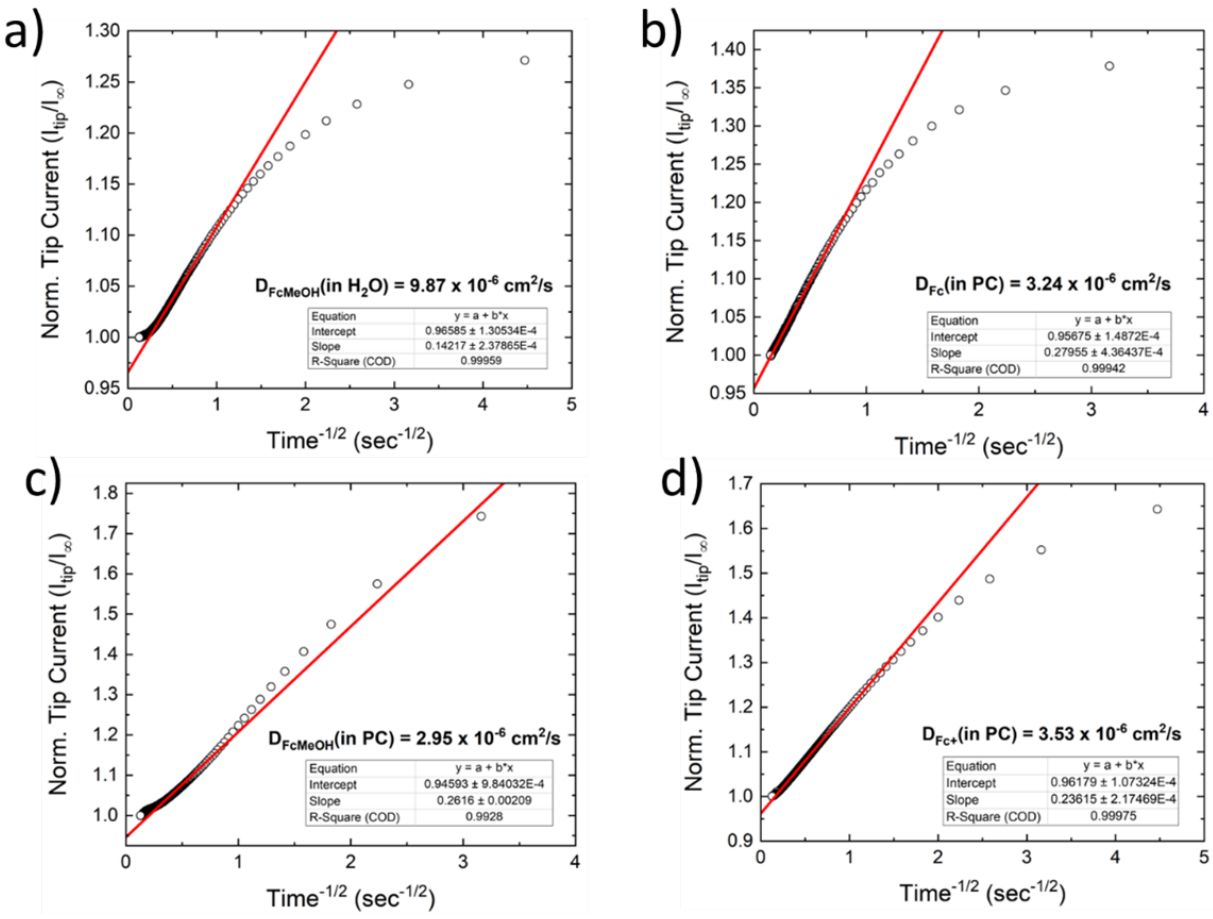


Figure D.3: i-t curves for estimation of diffusion co-efficients. a) – d) i-t curves (with quiet time = 0 sec) performed with each of the redox mediators used in **Figures 6.4 – 6.7**. We did a linear fit to a plot of the normalized tip-current vs. time $^{-1/2}$ , and the slope of the line was to obtain diffusion co-efficients.

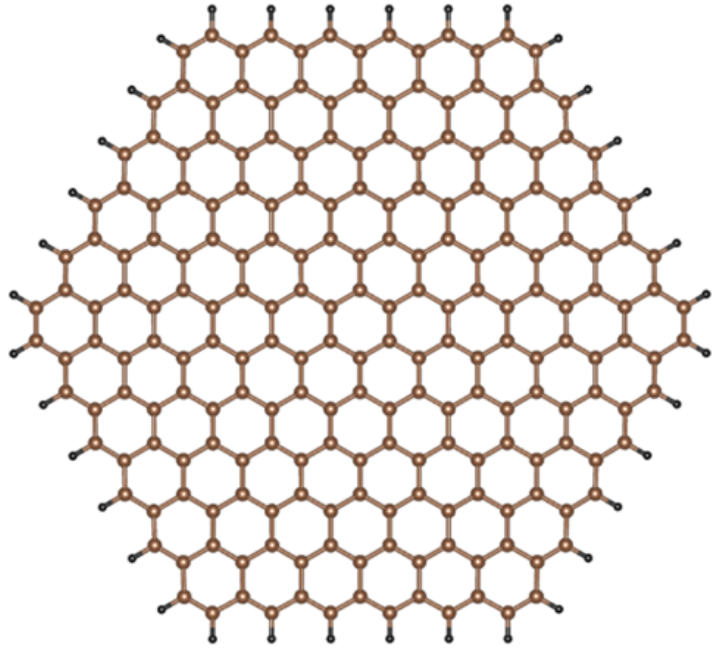


Figure D.4: Image of the hydrogen terminated hexagonal carbon cluster model used in the binding energy calculations of this work. Brown atoms are carbon and black are hydrogen.

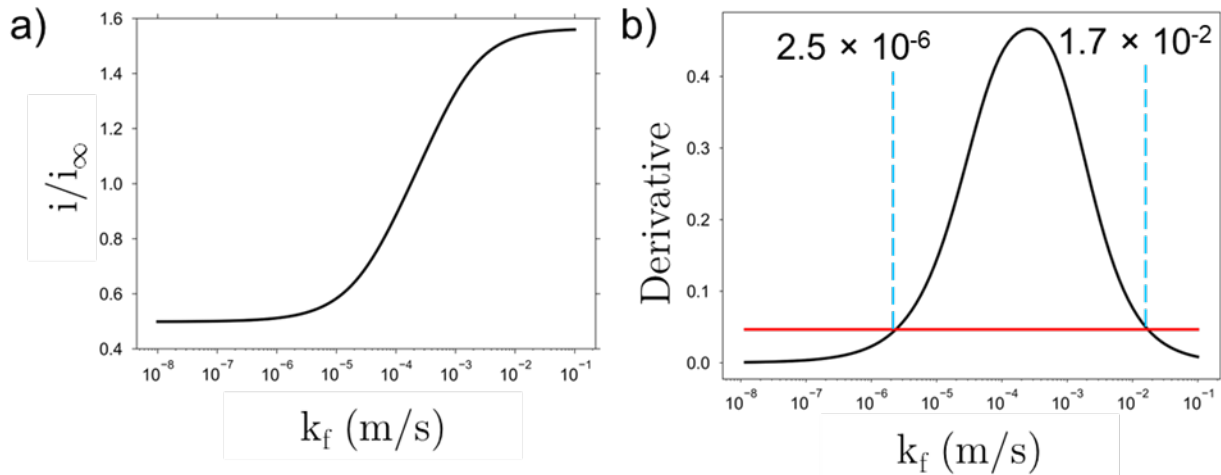


Figure D.5: Estimating practical limits of  $k_f$  measurements from SECM spot analysis measurements. a) Theoretical curve relating  $k_f$  with normalized tip current  $i/i_\infty$ . b) Derivative of a), with a horizontal red line plotted at 10% of peak value. Intersection points of the red line with the derivative are taken as the practical limits of  $k_f$  measurement, corresponding to  $2.5 \times 10^{-6}$  m/s and  $1.7 \times 10^{-2}$  m/s for negative feedback and positive feedback respectively, in this case.  $L = 1$ ,  $D = 5 \times 10^{-10}$  m $^2$ /s.  $a = 1$   $\mu\text{m}$ ,  $\text{RG} = 10$  was used to obtain the theoretical curve in a).

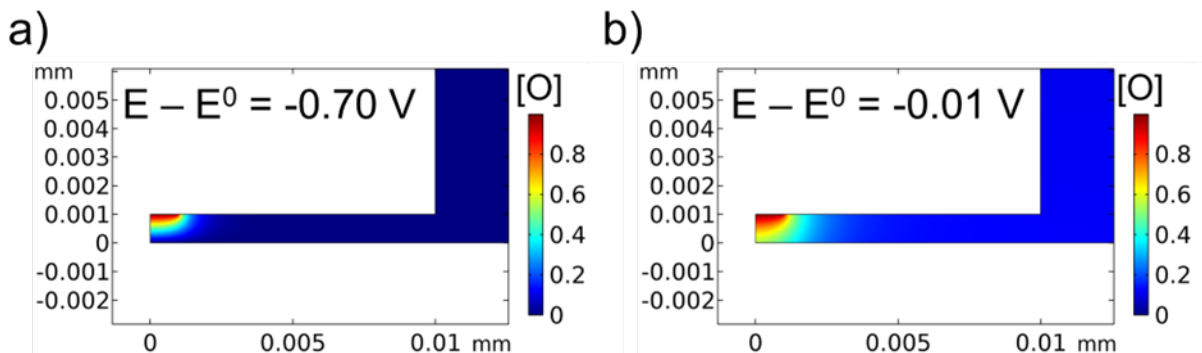


Figure D.6: 2D axisymmetric concentration plots from COMSOL simulations. Spatial variation in concentration of species O at  $E_{sub} - E^0$  of a)  $-0.70$  V and b)  $-0.01$  V, with tip biased to transform  $R \longrightarrow O$ . The result shows substrate electrode entering redox competition with the tip as  $E_{sub} - E^0$  tends to zero, leading to increasing concentration of species O in the system. Note,  $[R] + [O] = 1$  mM. COMSOL simulations carried out with  $L = 1$ ,  $D = 5 \times 10^{-10}$  m<sup>2</sup>/s.  $a = 1$   $\mu$ m, RG = 10 and initial concentration of  $[R] = 1$  mM,  $[O] = 0$  mM.

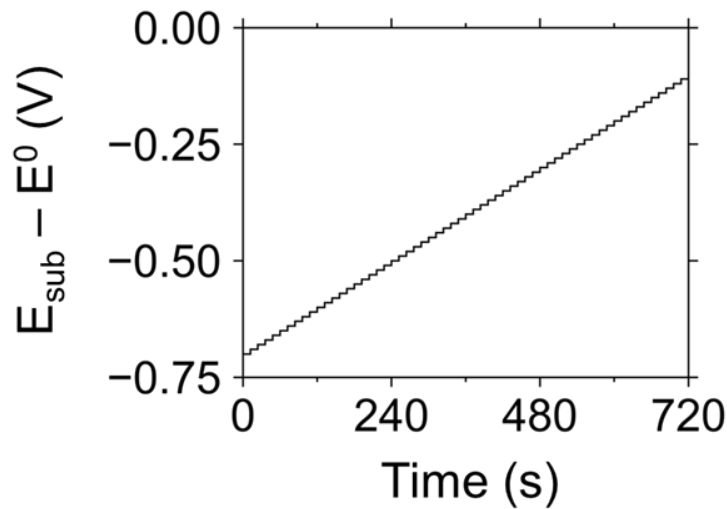


Figure D.7: Full range of potential steps used in the spot analysis method.

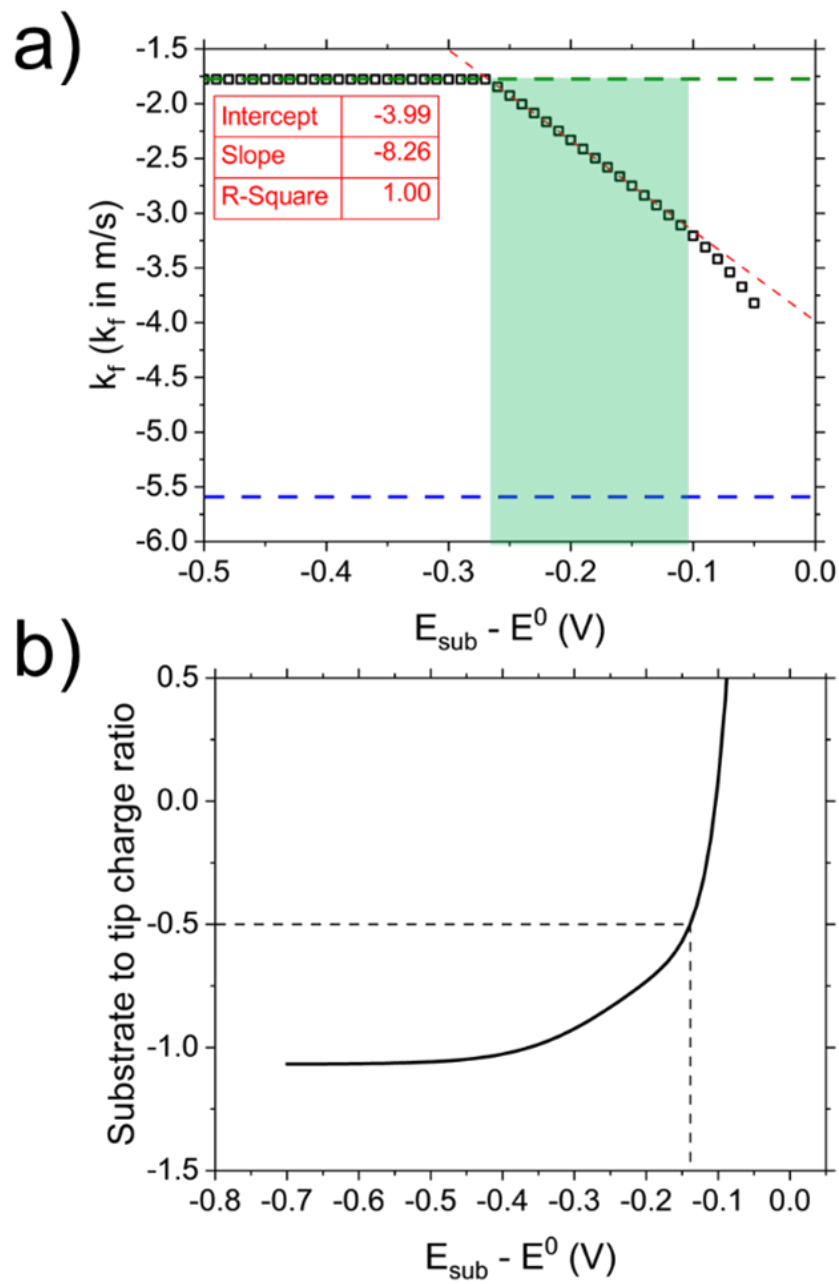


Figure D.8: Spot analysis corresponding to simulated  $k^0$  of  $1 \times 10^{-4}$  m/s and  $\alpha$  of 0.5 at the substrate in COMSOL. a) Slope and intercept from linear fit lead to an estimated  $k^0$  of  $1.02 \times 10^{-4}$  m/s and  $\alpha$  of 0.49. b) Lower  $E_{\text{sub}} - E^0$  limit for linear fit (green box in a) calculated to be the potential corresponding to substrate-to-tip charge ratio of -0.5.

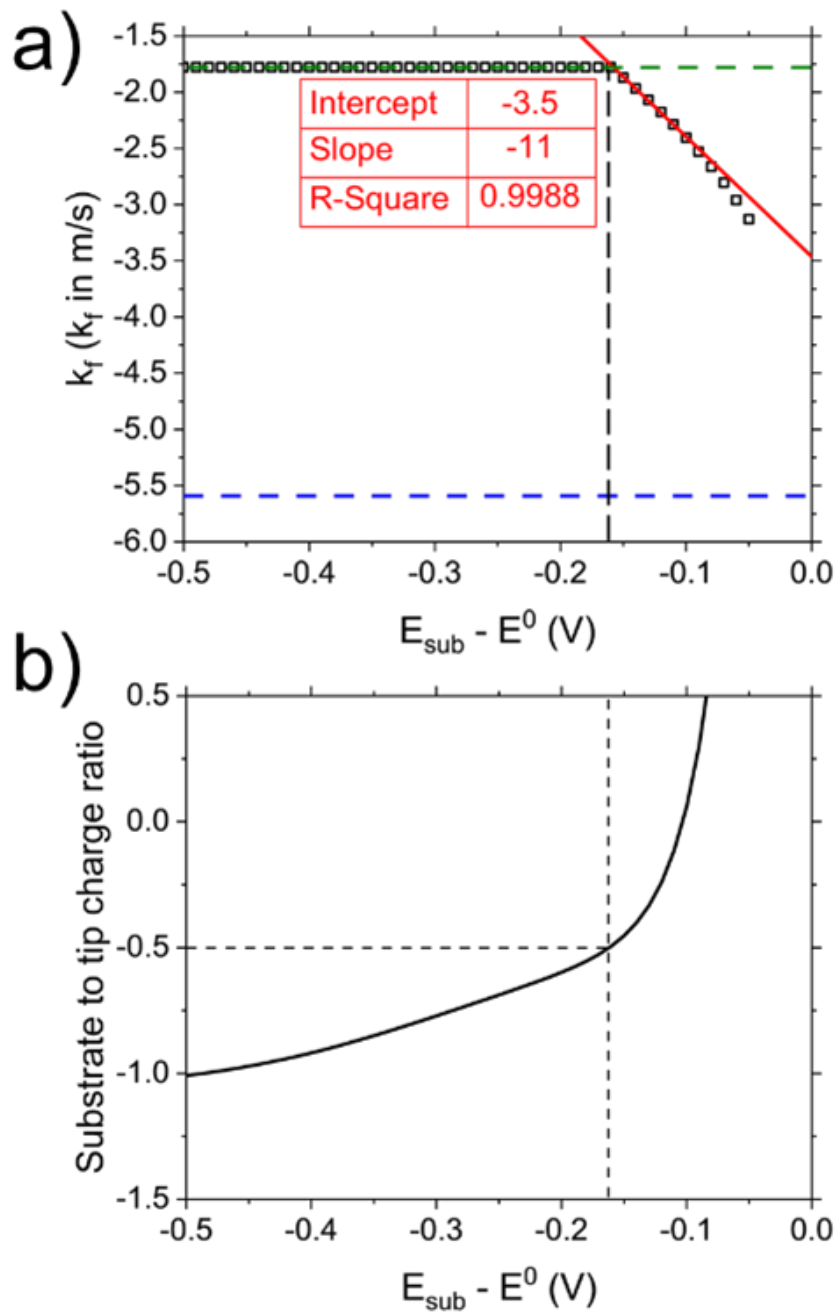


Figure D.9: Spot analysis corresponding to simulated  $k^0$  of  $1 \times 10^{-3}$  m/s and  $\alpha$  of 0.5 in COMSOL. a) Slope and intercept from linear fit lead to an estimated  $k^0$  of  $3.16 \times 10^{-4}$  m/s and  $\alpha$  of 0.65. b) Lower  $E_{sub} - E^0$  limit for linear fit calculated from the substrate to tip charge ratio; all the non-mass transfer limited values in a) observed to be under the influence of redox competition.

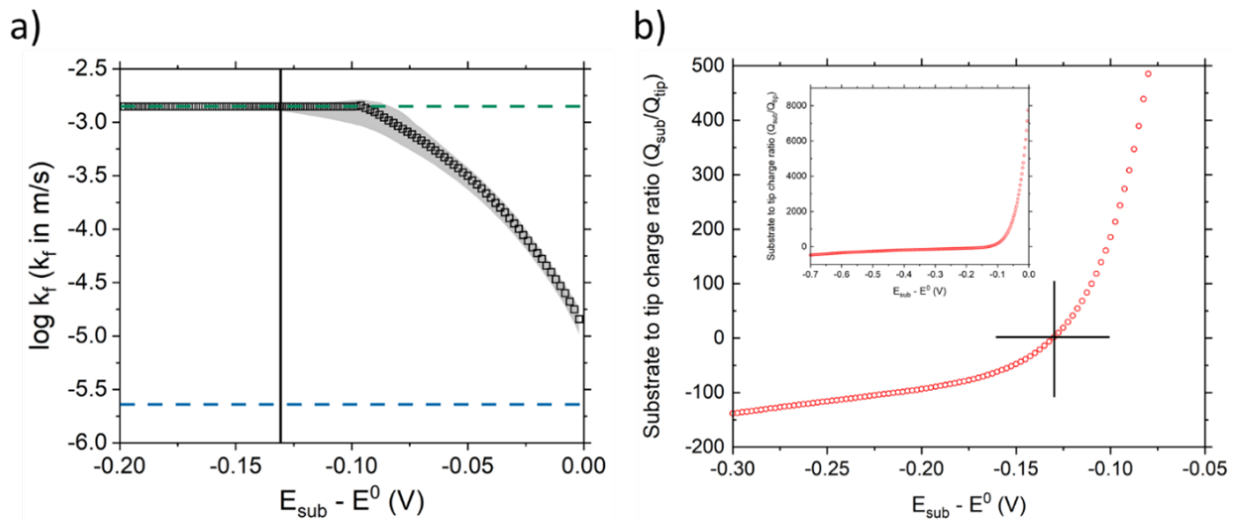


Figure D.10: Substrate response during spot analysis measurements of FcMeOH with Pt metal electrode. a) Spot analysis of FcMeOH in PC on sputtered Pt electrodes revealing redox competition influence at  $E_{\text{sub}} - E^0 > -0.13 \text{ V}$ . b) This limit was obtained from the substrate to tip charge ratio plot for **Figure 6.4a**. The crossover from a negative value for the charge ratio to a positive value is marked by the cross on the plot. Inset: Substrate to tip charge ratio over the entire extended potential window.

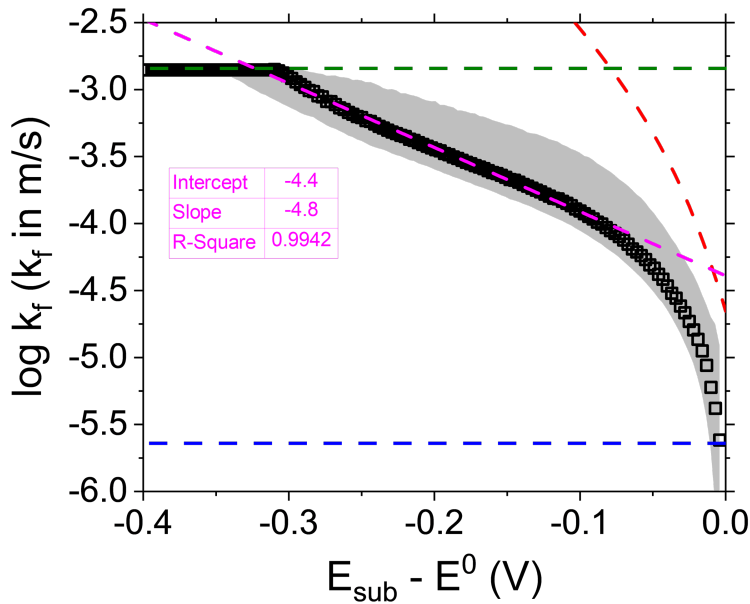


Figure D.11: Linear fit for extracting slope from ET behavior of MLG in PC with FcMeOH mediator (data same as **Figure 6.4b**). The slope corresponds to an “apparent”  $\alpha$  of 0.28.

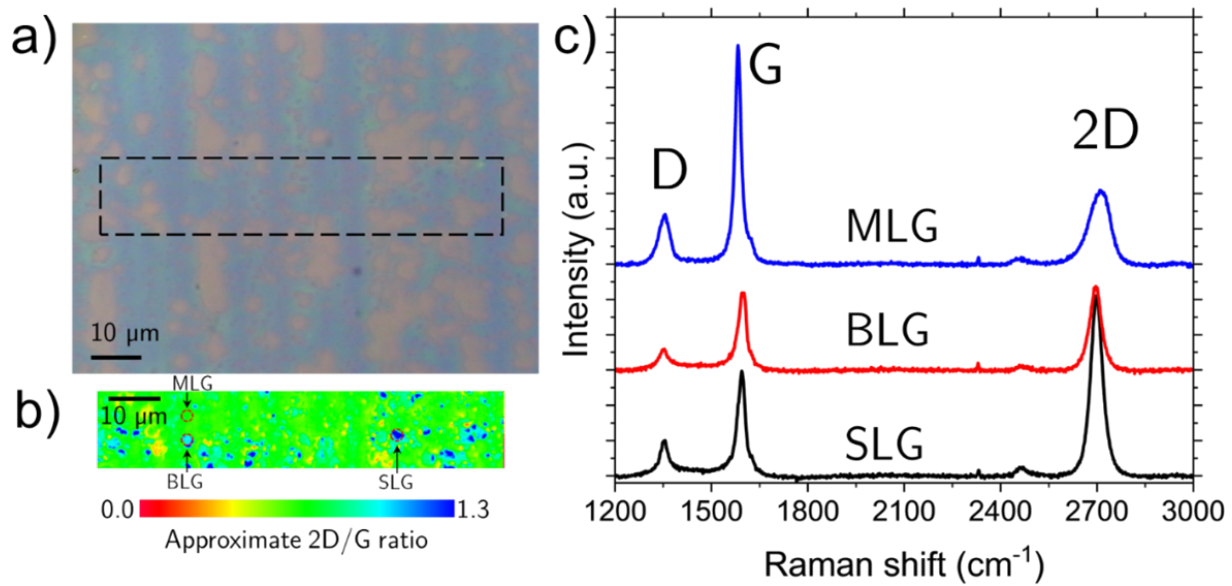


Figure D.12: Raman spectral maps of MLG samples illustrating areas with SLG, BLG and MLG coverage. a) Optical micrograph of MLG, b) Raman 2D/G spectral map without baseline correction, with select spots showing baseline-corrected spectra from c) SLG, BLG and MLG.

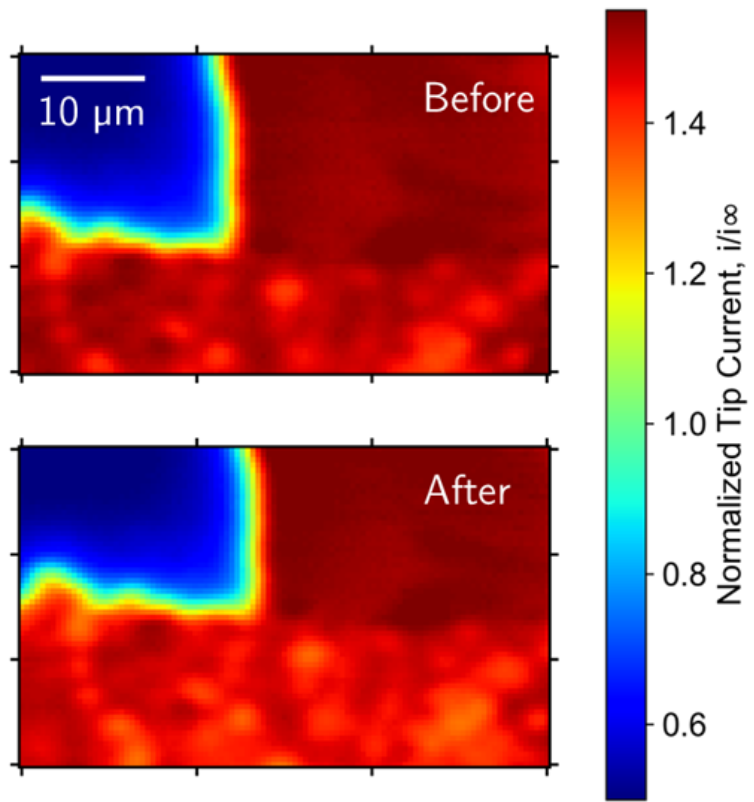


Figure D.13: SECM feedback imaging at OCP of  $\text{Fc}^+$  reduction before and after biased feedback imaging. A clear decrease in feedback is noted over the thinner MLG areas after biased feedback imaging, indicating that ET kinetics is inhibited over time.

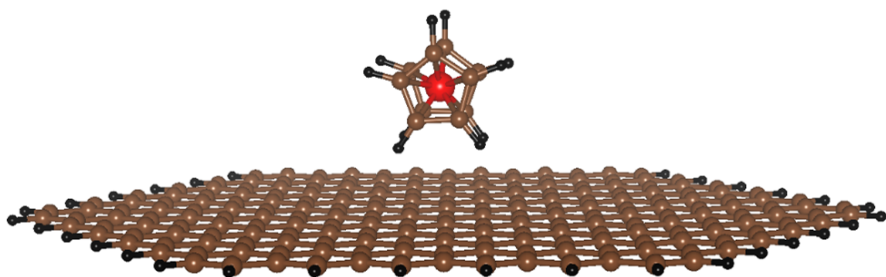


Figure D.14: Figure depicting the geometry of Fc at the surface of the graphene cluster model. Brown atoms are carbon, black hydrogen, and the single red atom is iron.

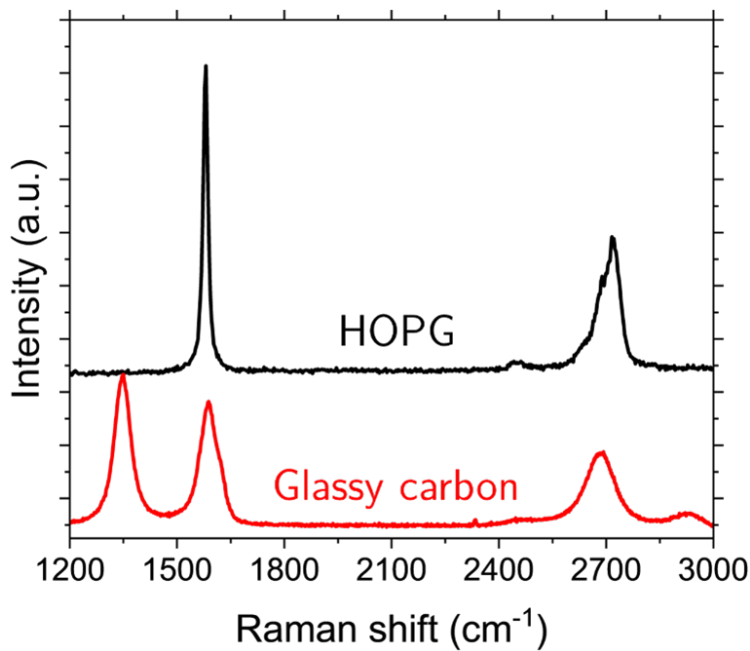


Figure D.15: Raman spectra of basal plane HOPG and glassy carbon.

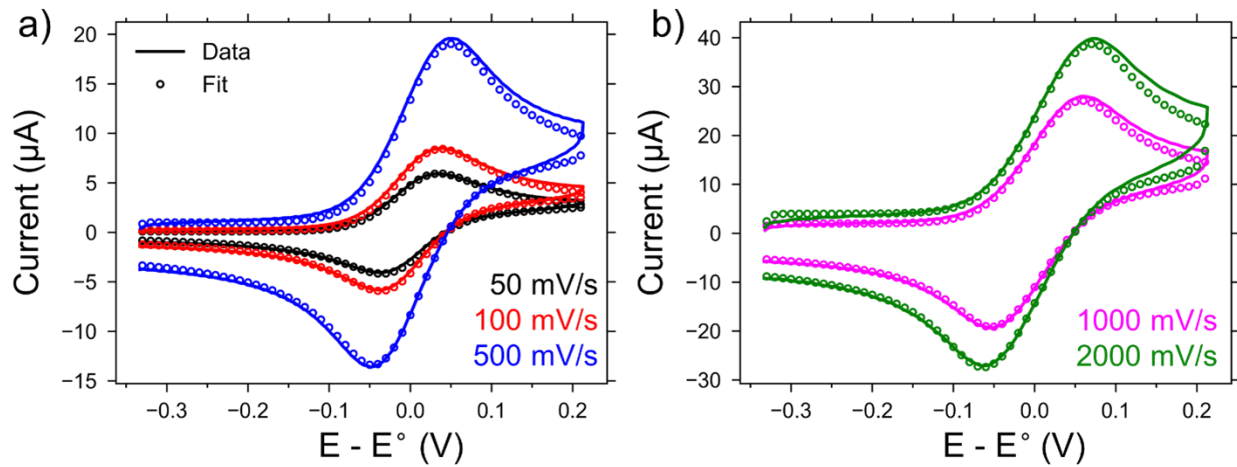


Figure D.16: Scan rate dependence CV measurements with  $0.83 \text{ mM } \text{Fc}^+\text{PF}_6^-$  with  $0.1 \text{ M }$  TBAPF<sub>6</sub> dissolved in PC. DigiElch simulations are overlaid, with simulation parameters:  $\alpha = 0.5$ ,  $k^0 = 10 \text{ cm/s}$ ,  $R_u = 800 \Omega$ ,  $D = 3.5 \times 10^{-10} \text{ m}^2/\text{s}$ ,  $C_{dl} = 5 \mu\text{F}$ , Electrode area =  $0.071 \text{ cm}^2$ . No distinct adsorption features are observable. Working electrode: glassy carbon, reference electrode: graphite quasi-reference, counter electrode: Pt wire.

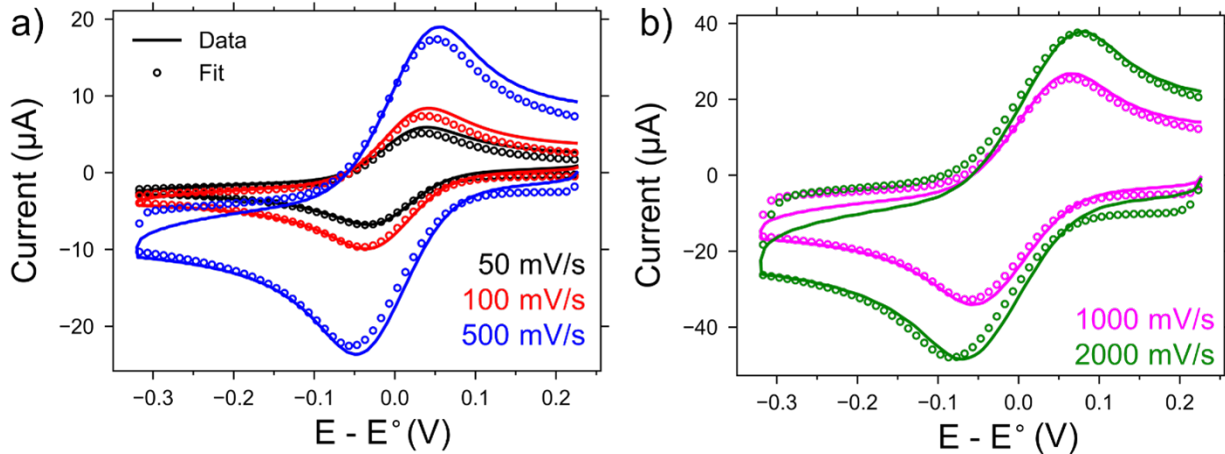


Figure D.17: Scan rate dependence CV measurements with 0.8 mM Fc in 0.1 M TBAPF<sub>6</sub> electrolyte solution with PC. DigiElch simulations are overlaid, with simulation parameters:  $\alpha = 0.5$ ,  $k^0 = 10 \text{ cm/s}$ ,  $R_u = 700 \Omega$ ,  $D = 3.0 \times 10^{-10} \text{ m}^2/\text{s}$ ,  $C_{dl} = 2 \mu\text{F}$ , Electrode area = 0.071 cm<sup>2</sup>. No distinct adsorption features are observable. Working electrode: glassy carbon, reference electrode: graphite quasi-reference, counter electrode: Pt wire.

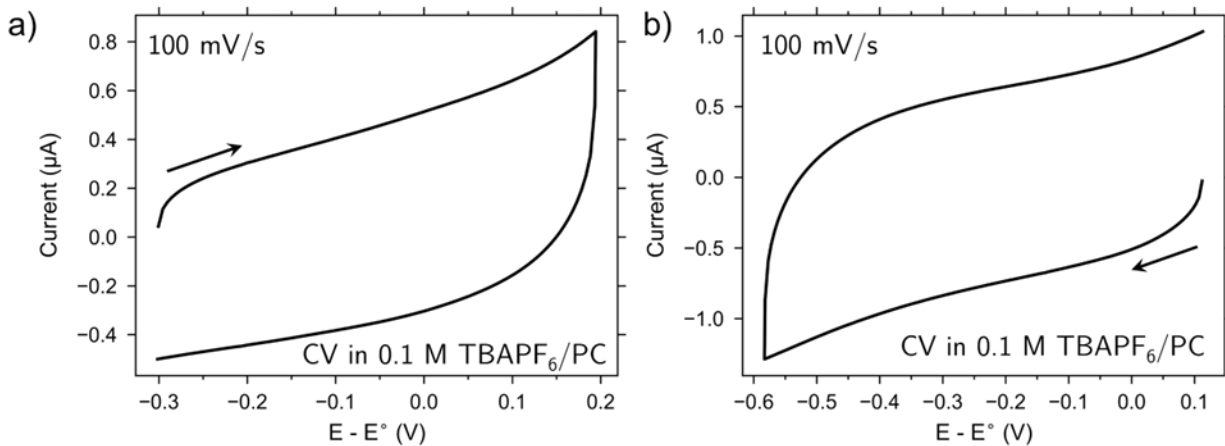


Figure D.18: CVs obtained after soaking GC electrode post cycling a) Fc (**Figure D.17**) and b) Fc<sup>+</sup>PF<sub>6</sub><sup>-</sup> (**Figure D.18**) in blank electrolyte. No redox signatures are observed, indicating no surface-bound Fc species are present.

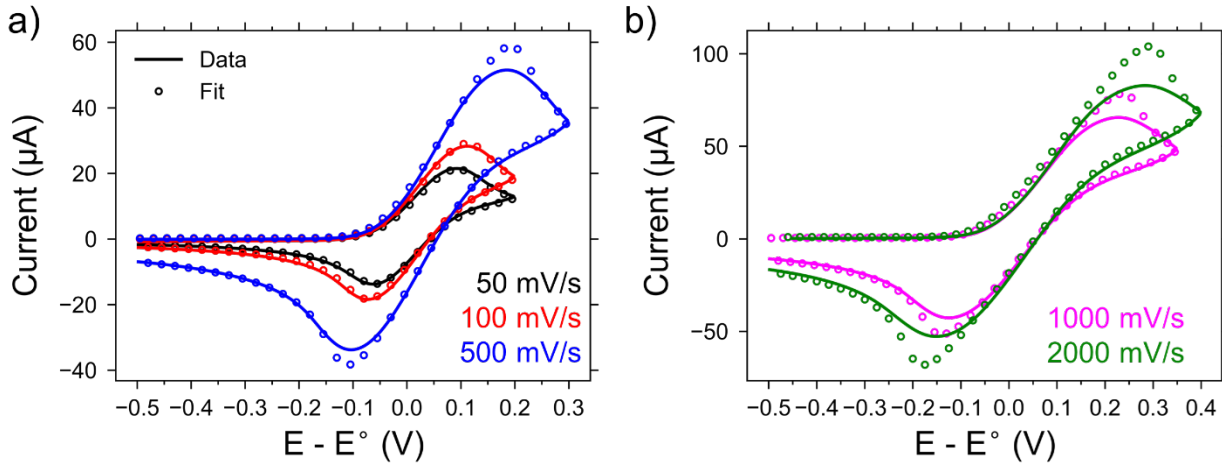


Figure D.19: Scan rate measurements with 0.95 mM Fc in 0.1 M TBAPF<sub>6</sub> dissolved in PC. Digielch simulations are overlaid, with simulation parameters:  $\alpha = 0.5$ ,  $k^0 = 10$  cm/s,  $R_u = 2000 \Omega$ ,  $D = 3.0 \times 10^{-10} \text{ m}^2/\text{s}$   $C_{dl} = 5 \mu\text{F}$ , Electrode area = 0.2374 cm<sup>2</sup>. No distinct adsorption features are observable. Working electrode: multi-layer graphene, reference electrode: polypyrrole quasi-reference, counter electrode: Pt wire.

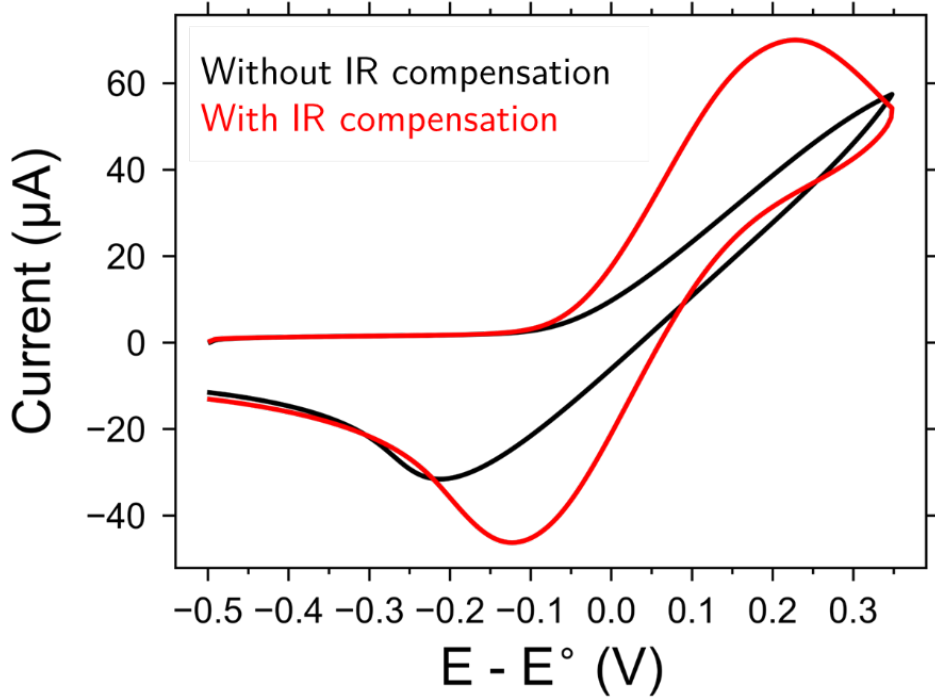


Figure D.20: CV with and without IR compensation from CHI760e potentiostat. Scan rate 1 V/s, working electrode: multi-layer graphene, reference electrode: polypyrrole quasi-reference, counter electrode: Pt wire. Applied IR compensation ( $3000 \Omega$ ) causes artificial distortion of CV, leading to mismatch with Digielch simulations in **Figure D.19**.

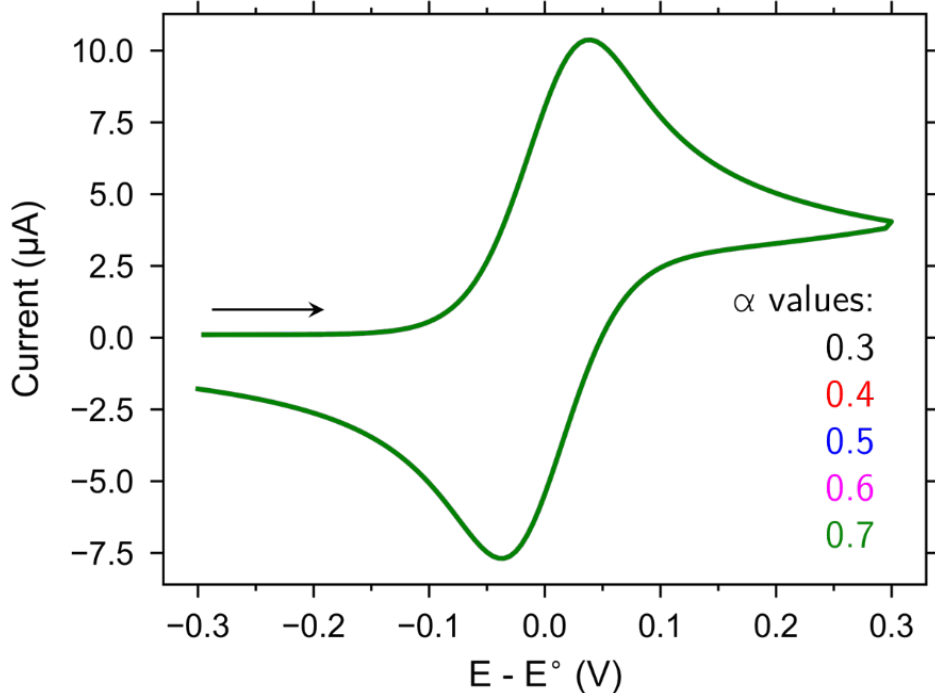


Figure D.21: Digielch simulation for  $R \rightleftharpoons O$  redox reaction at various  $\alpha$ . Simulation parameters were similar to those reported in **Figure D.16** and **D.17**;  $[R]_{initial} = 1 \text{ mM}$ ,  $[O]_{initial} = 0 \text{ mM}$ ,  $\alpha = \text{varies}$ ,  $k^0 = 10 \text{ cm/s}$ ,  $R_u = 700 \Omega$ ,  $D = 3.0 \times 10^{-10} \text{ m}^2/\text{s}$ ,  $C_{dl} = 1 \mu\text{F}$ , Electrode area =  $0.071 \text{ cm}^2$ . No change in CV profiles is observed and all the five traces are on top of each other.

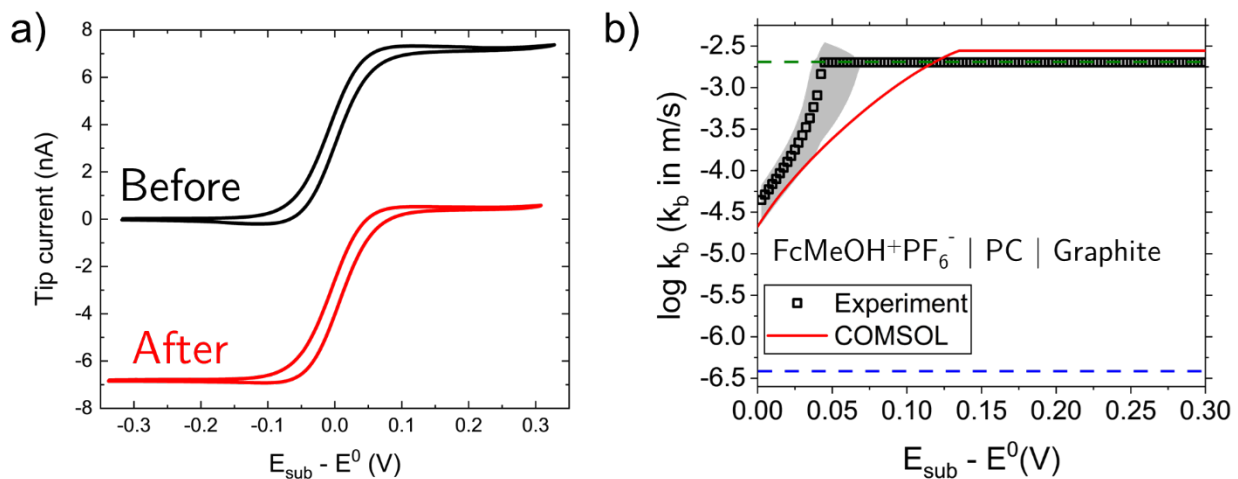


Figure D.22: Spot analysis measurements on graphite electrode with  $\text{FcMeOH}^+\text{PF}_6^-$ . a) UME CVs at 20 mV/s illustrating bulk electrolysis of  $\text{FcMeOH}$  species to obtain  $\text{FcMeOH}^+\text{PF}_6^-$ . b) Spot analysis measurement of  $\text{FcMeOH}$  oxidation at substrate. Bulk electrolysis measurements were carried out in a W-cell using a Pt flag as the working electrode, carbon rod as the RE, and a Pt mesh as the counter electrode.

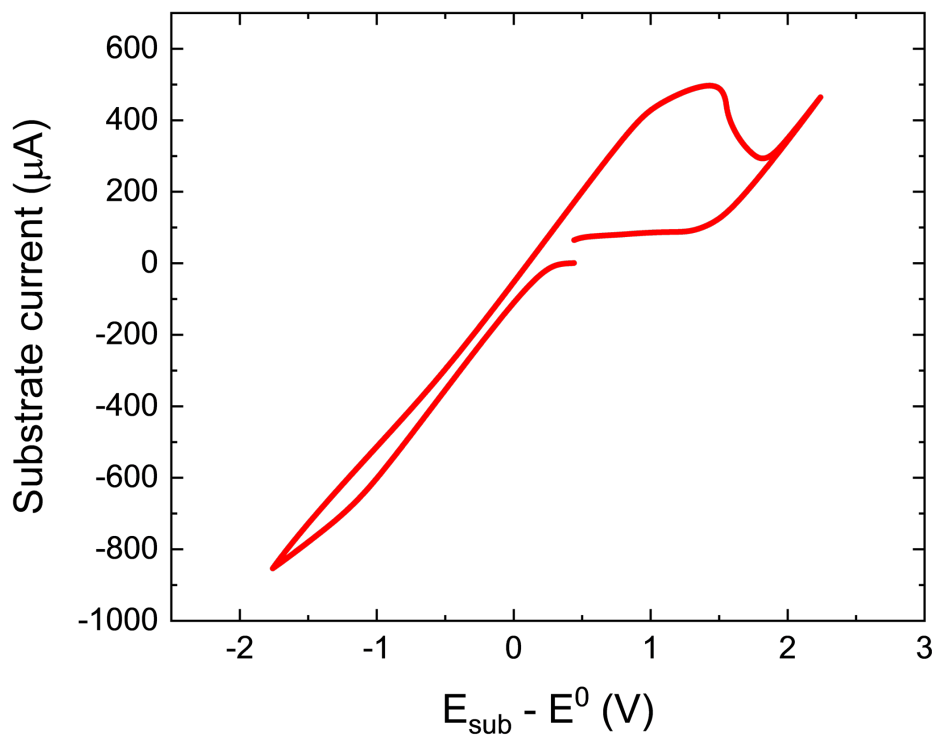


Figure D.23: Cyclic voltammogram of 100 mM  $\text{Fc}^+\text{PF}_6^-$ . Combination of high solution resistance and currents lead to linear ohmic response observable. Working electrode: Graphite ( $r = 1.5$  mm), counter electrode: Pt wire, reference electrode: Carbon rod, electrolyte: 100 mM  $\text{Fc}^+\text{PF}_6^-$ , supporting electrolyte: 100 mM TBAPF<sub>6</sub>, solvent: PC, scan-rate: 100 mV/s.